Rosette Nanotubes: Supramolecular Scaffolds for Organic Optoelectronics

by

Liang Shuai

A thesis submitted in partial fulfillment of the requirements for the degree of

Doctor of Philosophy

Department of Chemistry
University of Alberta

Abstract

Supramolecular rosette nanotubes (RNTs) are obtained by the hierarchical self-assembly of mono and twin G∧C building blocks. The mono G∧C motif is a fused bicyclic ring of guanine and cytosine with six self-complementary sets of hydrogen bonding sites, while the twin G∧C motif is a covalently linked dimer of two mono G∧C motifs. The modification of G∧C motifs with various functional groups offers an attractive pathway to build surface-functionalized RNTs for different applications.

To explore the potential applications of RNTs in the field of organic optoelectronics, three porphyrin- and three oligothiophene-functionalized G∧C modules were synthesized. The solubility, self-assembly ability and optical properties of these building blocks were tuned by chemical modification. The porphyrin-mono G∧C module **G∧C-Por 1** formed long RNTs in $MeNO_2$ with a moderate solubility. The porphyrin-twin G∧C modules **$(G\wedge C)_2$-Por 2** and **$(G\wedge C)_2$-Por 3** both displayed good solubility and self-assembly ability in the mixed solvent of 1,2-DCB and MeOH. The porphyrin groups on the RNTs were identified as J-type aggregates in all cases. In comparison, the terthiophene-twin G∧C module **$(G\wedge C)_2$-3T** did not form well-dispersed nanostructures in most organic solvents due to the poor solubility. The sexithiophene-mono G∧C module **G∧C-6T** displayed a good solubility in 1,2-DCB and DCM but the self-assembly ability was found to be poor. The sexithiophene-twin G∧C module **$(G\wedge C)_2$-6T** displayed a good solubility in nonpolar solvents and formed well-dispersed long RNTs. The oligothiophene units on the RNTs were identified as H-type aggregates upon the formation of RNTs.

These porphyrin- and oligothiophene-functionalized G∧C RNTs were characterized by SEM, TEM, AFM and STM. The diameters of the individual RNTs were measured to be in the range of 4–8 nm, which were in good agreement with the values from the molecular modeling simulations. The length of the RNTs varied from a few hundreds of nanometers to several micrometers, which was controlled by different self-assembly conditions. At high concentrations, these RNTs formed interconnected networks alone or with $PC_{61}BM$ in the mixed blends. In all the blended thin films of porphyrin-functionalized RNTs:$PC_{61}BM$, the fluorescence emissions of porphyrin groups were sufficiently quenched. The phase-separated nanoscale morphology and sufficient photoinduced electron transfer in the blended thin films are highly desired when spin-casting the active layers of bulk-heterojunction organic photovoltaic (OPV) devices.

The HOMO and LUMO energy levels of the RNTs of **G∧C-Por 1**, **$(G\wedge C)_2$-Por 2**, **$(G\wedge C)_2$-Por 3** and **$(G\wedge C)_2$-6T** were characterized by UPS and UV-Vis. The energy-level alignments of all these materials and $PC_{61}BM$ indicate they are potential electron donor-acceptor pairs for OPVs. The *I–V* properties and conductivity of the thin films of these functional RNTs were measured and were found to display significant improvements in conductivity compared to the nonconductive unassembled counterparts. The conductivity of the RNTs is comparable to those of the conducting polymers.

These RNTs may contribute to the repertoire of electron donor materials in solution-processed OPVs and organic semiconductors.

Acknowledgements

Foremost, I would like to thank my supervisor Professor Hicham Fenniri for his guidance, trust and support during the period of my PhD program. With the freedom in research that he gave to me, I was delighted to deal with a number of projects that I truly love. His encouragement and help enabled me to overcome the scientific challenges that I met during the past five years. His kindness and sense of humor made our discussions relaxed and joyful.

I am grateful to Professor Todd L. Lowary and Professor Robert E. Campbell for serving on my supervisory committee. In particular, Dr. Lowary took the role as my co-supervisor and offered me a lot of help during the last one and a half years. I also want to thank Professor Alexander Brown and Professor Jon R. Parquette for taking the time to review my thesis and serve on the examining committee.

I am thankful to all the previous members in the Supramolecular Nanoscale Assembly Group (SNAG) led by Professor Fenniri during his time at the National Institute for Nanotechnology (NINT) and the University of Alberta. It was a great pleasant to work with these lovely and helpful people in an enjoyable work environment throughout the years. For many of them we were colleagues and soon became lifelong friends. I own an enormous debt to Dr. Jae-Young Cho for performing all the TEM, AFM and STM characterizations. Dr. Takeshi Yamazaki performed all the molecular modeling simulations and provided helpful discussions. Dr. Rachel Beingessner, Dr. Venkatakrishnan Parthasarathy, Dr. Zhimin Yan, Dr. Weizhen Shen, Dr. Mounir El-Bakkari, Dr. Usha Hermraz and Dr. Christophe Danumah all offered me enormous helps in the lab. In particular, Rachel was

generous and considerate to do the proofreading job of my thesis and provided invaluable suggestions. I want to thank Zhaoyi Qin, Rahul Agrawal, Uyen Ho and Belete Legesse for cheering me up during the hard times.

I was very fortunate to finish most of my research work in NINT, as the researchers there were very helpful. Particularly, Professor Richard L. McCreery granted me the access to the instruments in his lab to carry out the electronic characterizations. Dr. Amr M. Mohamed provided a lot of assistance in preparing the two-electrode devices. Dr. Wenjuan Huang helped me in generating the molecular 3D drawings. The personnel from the Department of Chemistry, NanoFab and Alberta Center for Surface Engineering and Science (ACSES) at the University of Alberta also provided technical support and helpful discussions.

I also want to thank my friends Mengyuan Zhu, Meijing Wang, Xiaoyu Tu and Wei Peng for their stimulating words throughout the years.

I know I am deeply indebted to my parents. Without their continuous support, encouragement and love, I could not have focused on my studies and pursued my goals. Over the years, they supported me in good times and bad. I would like to take this opportunity to express my gratitude and share the joy with them.

Table of Contents

Page

Chapter 4. Self-Assembly and Characterization of Oligothiophene-Functionalized Guanine–Cytosine Building Blocks

List of Tables

List of Figures

List of Abbreviations

°C	Degree Celsius
1,2-DCB	1,2-dichlorobenzene
1,2-DCE	1,2-Dichloroethane
1D	One-dimensional
2D	Two-dimensional
3D	Three-dimensional
AFM	Atomic force microscopy
Alq_3	8-Hydroxyquinoline
BChl	Bacteriochlorophyll
BE	Binding energy
BHJ	Bulk heterojunction
Boc	tert-Butyloxycarbonyl protecting group
br s	Broad singlet
br t	Broad triplet
C_{60}	Buckminsterfullerene
c-AFM	Conductive atomic force microscopy
CD	Circular dichroism
CH_3CN	Acetonitrile
Chl	Chlorophyll
CRT	Cathode ray tube
c-Si	Crystalline silicon

CV	Cyclic voltammetry
d	Day(s) (unit of time) or Doublet (only used for NMR data)
DAQ	Data acquisition
DCC	*N*,*N*′-dicyclohexylcarbodiimide
DCM	Dichloromethane
DDQ	2,3-Dichloro-5,6-dicyano-1,4-benzoquinone
DFT	Density functional theory
DIPEA	Diisopropylethylamine
DME	1,2- Dimethoxyethane
DMF	Dimethylformamide
DMSO	Dimethyl sulfoxide
DPP	Diketopyrrolopyrrole
DSC	Differential scanning calorimetry
DSSC	Dye-sensitized solar cell
EDC	1-ethyl-3-(3-dimethylaminopropyl)carbodiimide
EL	Electroluminescence
ESI	Electrospray ionization
Et_2O	Diethyl ether
Et_3N	Triethylamine
EtOAc	Ethyl acetate
FET	Field effect transistor
FF	Filled factor
FT-IR	Fourier transform infrared

G∧C	A fused bicyclic ring of guanine and cytosine
GAFF	General AMBER force field
h	Hour(s)
HBC	Hexabenzocoronene
HOBy	Hydroxybenzotriazole
HOMO	Highest occupied molecular orbital
HOPG	Highly ordered pyrolitic graphite
HRMS	High resolution mass spectrometry
HSQC	Heteronuclear single quantum coherence
IPES	Inverse photoemission spectroscopy
$Ir(ppy)_3$	Tris[2-phenylpyridinato-C^2,*N*]iridium(III)
ITO	Indium tin oxide
LH1	Light-harvesting complex I
LH2	Light harvesting complex II
LRMS	Low resolution mass spectrometry
LUMO	Lowest unoccupied molecular orbital
m	Multiplet
MD	Molecular dynamics
$MeNO_2$	Nitromethane
MeOH	Methanol
min	Minute(s)
$NaBH(OAc)_3$	Sodium triacetoxyborohydride
NBS	*N*-bromosuccinimide

NDI	Naphthalene diimide
$Ni(dppp)Cl_2$	Dichloro[1,3-bis(diphenylphosphino)propane]nickel
NIS	*N*-iodosuccinimide
nm	Nanometer
NMR	Nuclear magnetic resonance
OFET	Organic field-effect transistor
OLED	Organic light-emitting diode
OPVs	Organic photovoltaics
P3HT	Poly(3-hexylthiophene)
$PC_{61}BM$	Henyl-C_{61}-butyric acid methyl ester
$PC_{71}BM$	Phenyl-C_{71}-butyric acid methyl ester
PCE	Power conversion efficiency
$Pd(PPh_3)_4$	Tetrakis(triphenylphosphine)palladium(0)
PDI	Perylene diimde
PEDOT:PSS	Poly-(3,4-ethylenedioxythiophene) : polystyrene sulfonate
PES	Photoemission spectroscopy
Ph_3P	Triphenylphosphine
PL	Photoluminescence
POM	Polarizing optical microscopy
ppm	Parts per million
PPV	Poly(*p*-phenylene vinylene)
RESP	Restrained electrostatic potential
RNT	Rosette nanotube

rpm	Revolutions per minute
rt	Room temperature
s	Second(s) (unit of time) or Singlet (only used for NMR data)
SCE	Saturate calomel electrode
SEM	Scanning electron microscopy
STM	Scanning tunneling microscopy
SWNT	Single-walled carbon tube
t	Triplet
TEM	Transmission electron microscopy
TFA	Trifluoroacetic acid
THF	Tetrahydrofuran
TLC	Thin layer chromatography
TPP	Tetraphenylporphyrin
UPS	Ultraviolet photoelectron spectroscopy
UV-Vis	Ultraviolet-Visible
VDW	van der Waals
Vis-NIR	Visible-Near infrared
VT	Variable temperature
WF	Work function
XPS	X-ray photoelectron spectroscopy
XRD	X-ray diffraction
μm	Micrometer

Chapter 1

Pi-conjugated Supramolecular Assemblies for Organic Optoelectronics

1.1 Introduction

Although the discovery of electrical conduction in metals could be dated to 1752 when Benjamin Franklin passed lightning through a metallic rod, it was not until the 1970s when researchers began reporting on conducting organic aromatic compounds. Since then, the field of organic electronics has attracted a surge of interest in both academia and industry. In 1987, the first organic light-emitting diode (OLED) device using 8-hydroxyquinoline (Alq_3) as the electroluminescent film was reported by Ching W. Tang and Steven VanSlyke from the Eastman Kodak Company.[1] In the same year, the first organic field-effect transistor (OFET) device using a polythiophene thin film was reported by researchers from Mitsubishi Electric Coorporation.[2] In 1991, the first dye-sensitized solar cell (DSSC) device using organoruthenium dye was reported by Brian O'Regan and Michael Grätzel.[3] In the middle of the 1990s, solution-processed polymer solar cells became popular since the device performance was drastically improved by introducing the morphology of bulk heterojunction (BHJ).[4] The merits of organic electronics were also emphasized by the 2000 Nobel Prize in Chemistry, which was awarded to Alan J. Heeger, Alan G. MacDiarmid and Hideki Shirakawa for their discovery and development of conductive polymers.[5]

Compared to electronic devices based on inorganic or metallic materials, organic electronic devices feature low-cost, highly flexible, light-weight and solution processable properties.[6] As a major branch in the ensemble of organic electronics, organic optoelectronics have been extensively studied along with the development of conducting

organic materials, simply because the efficient conversion of energy from sunlight to electricity and the opposite form of converting electricity into high-output light are highly demanded. A few organic optoelectronic devices have been commercialized and are changing our lives. The most famous example would be the OLED displays, which are an excellent alternative to the conventional cathode ray tube (CRT). Now OLED displays are widely used as the high-power-efficiency screens in electronic devices such as smart phones, laptops and televisions. Although the electroluminescence of organic materials has been successfully commercialized, organic photovoltaics (OPVs) have not been employed in real devices for light harvesting, as the power conversion efficiency (PCE) of the OPV devices remains low compared to conventional silicon-based solar cells. Nevertheless, silicon-based solar cells are heavy and inflexible, the fabrication process requires a high-consumption of energy and is unfriendly to the environment, and the installation cost is high. Thus, the development of low-cost and solution-processed OPV devices has garnered a great deal of interest and enthusiasm in both academia and industry.

As mentioned above, the efficient BHJ morphology of the light absorption active layer is the key to improve the OPV device performance, because the charge carrier (electron and hole) mobility can be greatly improved when the materials are highly ordered in the active layer.[7] However, organic compounds are generally amorphous and have a lack of ordering in thin films. The exception to this case is liquid crystalline materials, which have been used to enhance the performance of OPV devices because of high mesoscopic structural organization. On the other hand, supramolecular self-assemblies have programmed orders at all dimensions — from one-dimensional (1D) nanotubes and fibers, two-dimensional (2D) sheets and layers, to three-dimensional (3D) metal- or carbon organic frameworks.[8] In

addition, all these supramolecular architectures are composed of elemental building blocks — the monomers. The advantages of the supramolecular self-assembly strategy include i) relatively easy preparation of the building block, ii) commanded self-assembly with precise programming from a molecular level, iii) generation of the most thermodynamically stable supramolecular nanostructure, and iv) compatibility in favor of solution-processed devices.[9] Hence, supramolecular nanoscale self-assembly is a powerful tool to impose well-defined ordering to otherwise ill-defined organic materials. In fact, the emerging field of supramolecular polymers has received significant attention for numerous applications.[10]

In this chapter, an overview on how supramolecular assemblies were employed in organic optoelectronics is presented, with the focus on OPVs. The natural light-harvesting system in purple bacteria is also discussed, as it is a wealth of inspiration that has been resorted to for the design of new OPV systems. Different types of constructions of OPV devices are described, with the emphasis on the solution-processed devices featuring the BHJ morphology. Finally, the self-assembly building blocks called the guanine–cytosine (G∧C) motifs and their applications are reviewed.

1.2 Light-harvesting complexes in photosynthetic bacteria

Plants, algae and photosynthetic bacteria can absorb light and transform the energy into chemical energy by photosynthesis. In this process, the light reactions occur in photosystems I and II (PSI and PSII) for all organisms performing oxygenic photosynthesis, and in light-harvesting complexes LH1 and LH2 for bacteria that do not produce oxygen. Nevertheless, all of these antennas are assemblies of proteins and self-organized pigment arrays on the photosynthetic membranes.[11] As the main light-harvesting pigments, all

chlorophylls (Chl) and bacteriochlorophylls (BChl) are structurally similar to porphyrins, with the differences in the extent of the conjugation and substituents on the cores. These pigments have different light absorption properties to adapt different organisms under different light conditions.

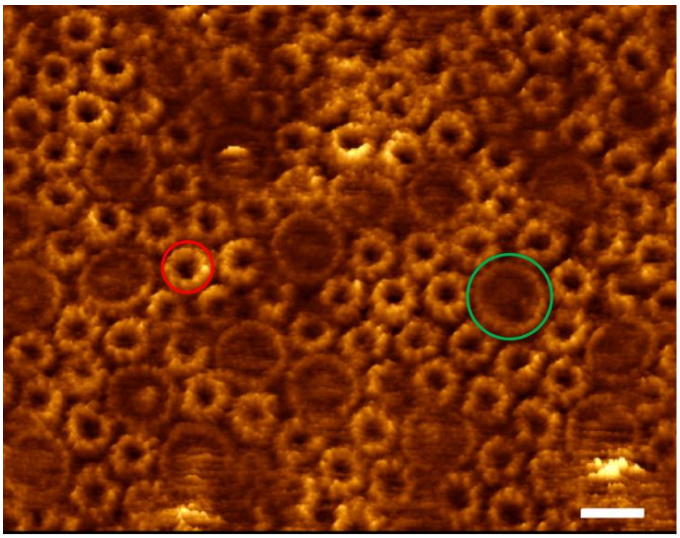

Figure 1.1. AFM image of photosynthetic complexes in the photosynthetic membrane of *Rhodospirillum photometricum*. Encircled are a LH1(green) and a LH2 (red). Scale bar: 10 nm. Figure adapted with permission from Ref. 12, © 2009 Elsevier.

In purple bacteria, both LH1 and LH2 are ring-shaped (Figure 1.1),[12] and the protein scaffolds position BChl molecules in a precise and specific arrangement to allow efficient cooperation between the pigments in the array. X-ray analysis has revealed the two radial arrays of Bchl *a* molecules in the well-resolved crystal structure of the LH2 complex of *Rhodopseudomonas acidophila*. The LH2 complex is a double-walled concentric hollow cylinder, with a height of 4.0 nm. The inner and outer diameters are 3.6 nm and 6.8 nm.[13] Nine Bchl *a* molecules locate between the helices of the transmembrane β-apoproteins to

form the outer cylindrical wall, and they adopt the geometry in which their bacteriochlorin planes are aligned parallel to the photosynthetic membrane surface. The lower array consists of 18 Bchl *a* molecules sandwiched between the helices of the α- and β-apoproteins in a more compact layout, and their bacteriochlorin planes are perpendicular to the membrane surface (Figure 1.2).

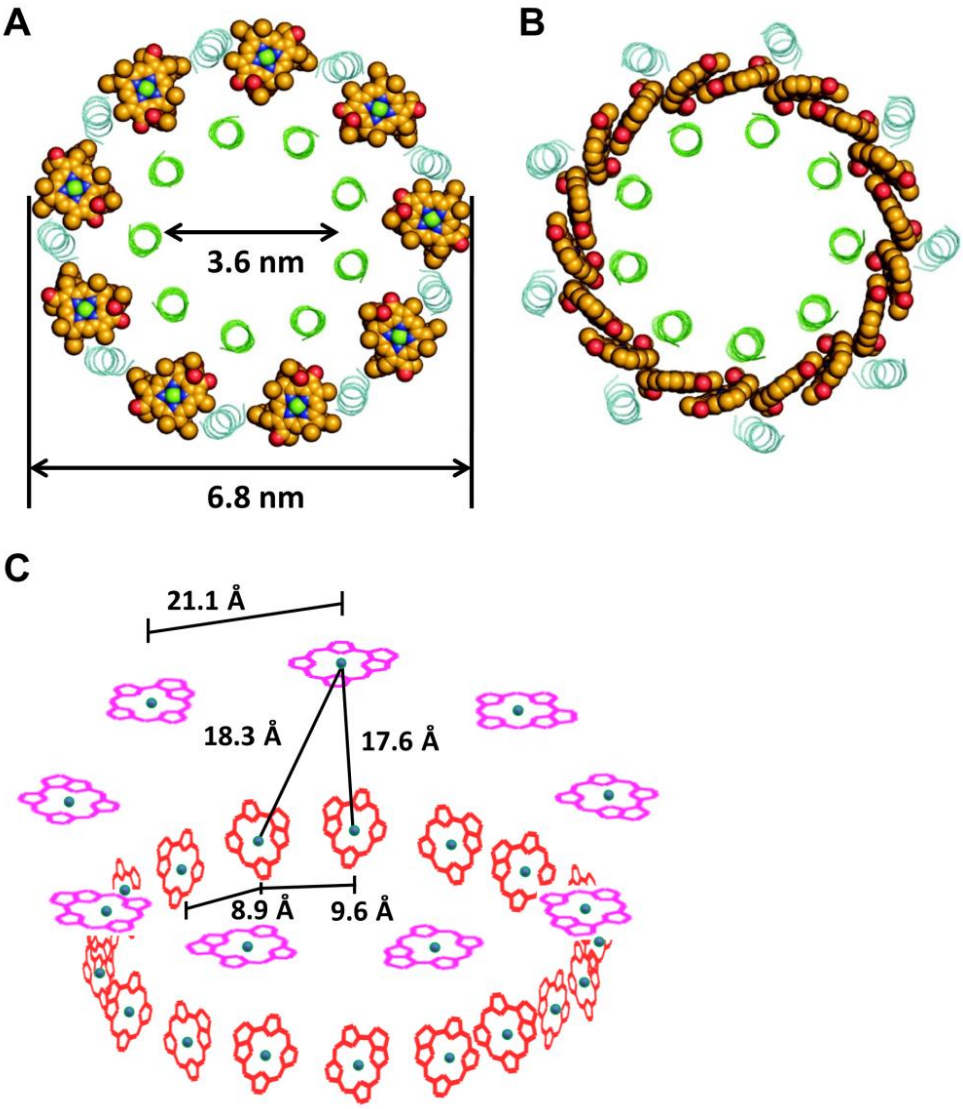

Figure 1.2. (A and B) Models for the LH2 complex of *Rhodopseudomonas acidophila* (viewed looking in a direction along the concentric axis perpendicular to the photosynthetic membrane). Atom and helix colors: yellow/grey, C; green, Mg and α-apoproteins; cyan, β-apoproteins; blue, N; red, O. The phytol chains of the BChl *a* molecules are removed for clarity. (C) The ring-shaped arrays of the BChl *a* molecules in the LH2 complex in a tilted side-view. The numbers indicate the center-to-center distances between the pigments. The substituents on the core of the pigment are removed for clarity. Figure (A) and (B) adapted with permission from Ref. 13c, © 2006 Cambridge University Press.

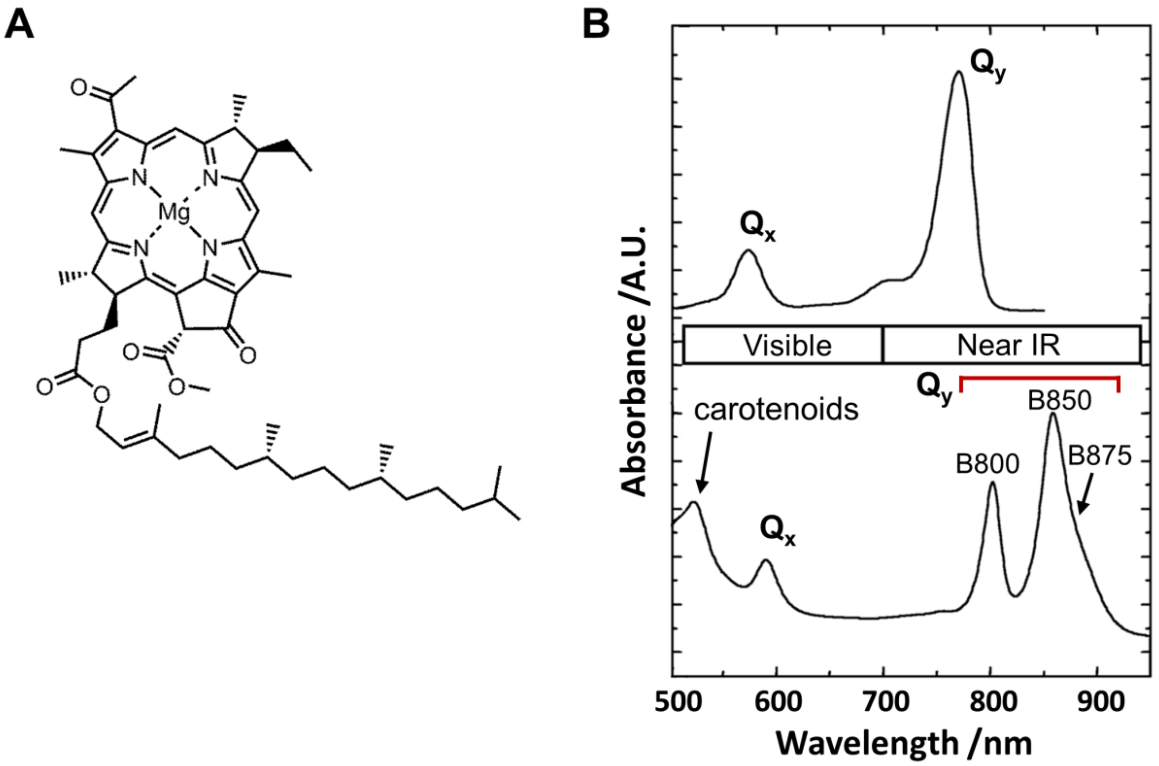

Figure 1.3. (A) Molecular structure of BChl *a*; (B) Absorption spectrum of BChl *a* in 7:2 (v/v) acetone:methanol (top), and *in* vivo absorption spectrum of isolated photosynthetic membranes from *Rhodopseudomonas acidophila* (bottom). Figure B adapted with permission from Ref. 13c, © 2006 Cambridge University Press.

The protein scaffolds are extremely important to tune the absorption spectra of the pigments in the photosynthetic complexes. For example, BChl *a in vivo* displays three different Q_y absorption maxima: 800 nm and 850 nm from LH2, and 875 nm from LH1. All three bands correspond to the same pigment, herein B800, B850 and B875 are used to differentiate the same BChl *a* molecules but in three different ring-shaped arrays. In comparison, the monomeric BChl *a* in organic solvent has a Q_y band at 772 nm (Figure 1.3). The red shifts of the Q_y band originate from the coordination and hydrogen bonds between

the pigments and the proteins, and the intermolecular interaction between the pigments. The importance of the same molecule having three Q_y bands is that, the process of excitation energy transfer is set in a fixed direction by the gradient of energy levels. The electronic excitation energy is passed from B800→B850 (in LH2)→B875 (in LH1), and finally to the reaction center to power the photosynthetic redox reaction. The ring-shaped supramolecular structure of the pigment arrays is essential to stabilize the excited electron, as the electron can be delocalized over the rings.

1.3 Solar irradiation spectrum and crystalline silicon-based photovoltaic device

It has been estimated that the energy delivered from the sunlight arriving on the surface of the earth accounts for 10 000 times the world energy demand.[14] The energy distribution of solar irradiation counts for 5% in the ultraviolet region, 46% in the visible light region and 49% in the infrared region.[15] Figure 1.4 shows a solar simulation spectrum at Air Mass 1.5 global (AM 1.5G, 1000 W/m^2), which covers a broad range of wavelengths (280–2500 nm), corresponding to a photon energy of 0.5–4.4 eV.[16] It is a dream for scientists to develop novel materials that have a broad absorption range and large absorption coefficient to make good use of the solar energy. Crystalline silicon (c-Si) has an absorption range approximately from 300 nm to 1200 nm, with a band gap of 1.12 eV.[16b] Due to the Shockley-Queisser limit (the sum of energy loss due to unabsorbed photons, thermalization and extraction losses), the theoretical maximum power conversion efficiency (PCE) of a photovoltaic device based on c-Si is about 41%.[17] Other inorganic semiconductors such as Ge, GsAs, CdTe and CdS are also good candidates in the application of photovoltaics, as they have excellent absorption range and efficiency.[18] However, due to the low element

abundance in the earth, the fabrication cost of the devices based on these semiconductors is much higher than that of the silicon-based devices. In addition, Cd and Te are highly toxic, which also limits their applications.

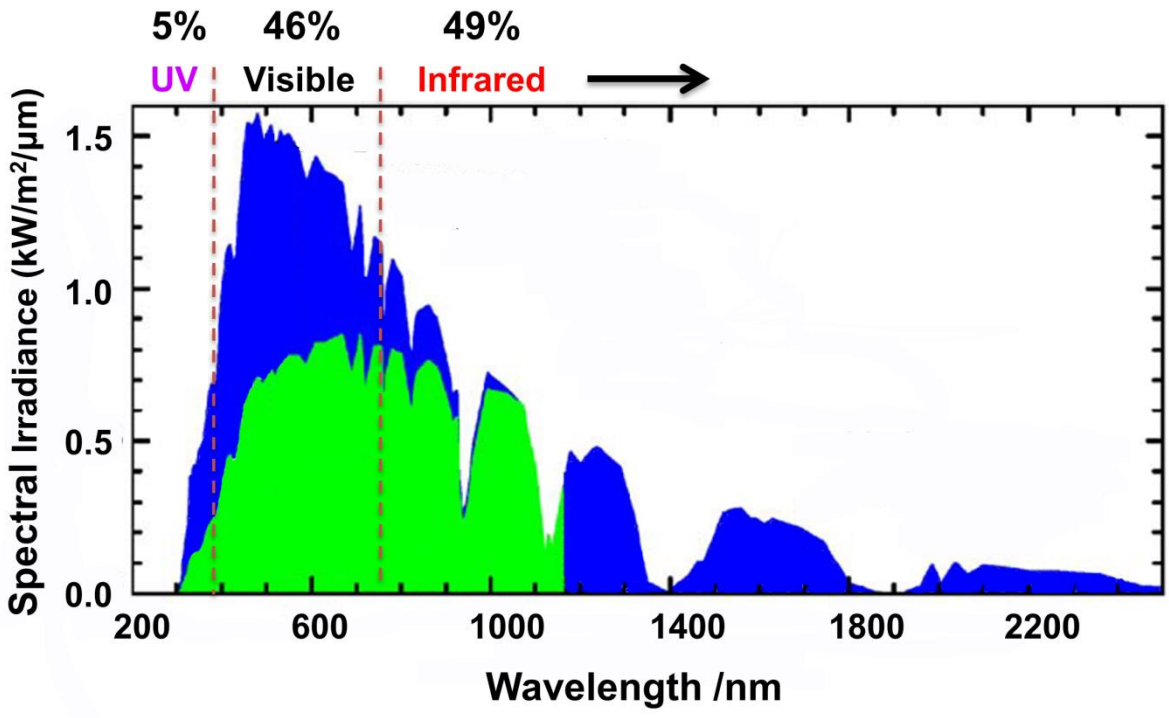

Figure 1.4. Solar irradiation (AM 1.5G, 1000 W/m^2) spectrum (blue area) and the maximum fraction that is absorbed by a typical crystalline silicon-based solar cell (green area). Figure adapted with permission from Ref. 16a, © 2005 Elsevier.

1.4 Investigation of the photovoltaic device performance

For all solar cells, the most important parameter is the power conversion efficiency (PCE), which is normally denoted as η and defined as the quotient of dividing the maximum output electrical power from the device (P_{out}) by the light intensity shining on the device (P_{in}). PCE is a parameter widely used to evaluate the performance of a solar cell in the literature.

For a given photovoltaic device with a known effective surface area, PCE can be calculated using the following equation (**E1**).[19]

$$\eta = \frac{P_{\text{out}}}{P_{\text{in}}} = \text{FF}\frac{V_{\text{OC}}J_{SC}}{P_{\text{in}}} \qquad \textbf{E1}$$

V_{OC} is the open circuit voltage, and J_{SC} is the short circuit current density. For convenience in the calculation, all the parameters are transformed into values with standard units. Herein, both P_{out} and P_{in} have the unit (W/m^2), V_{OC} has the unit (V) and J_{SC} has the unit (A/m^2). The last parameter FF is the filled factor, which is defined by **E2**.[19]

$$\text{FF} = \frac{V_{\text{m}}J_{\text{m}}}{V_{\text{OC}}J_{SC}} \qquad \textbf{E2}$$

V_{m} and J_{m} are the respective voltage and current density when the device is at the maximum output electrical power point. Both V_{m} and J_{m} can be obtained from the *J–V* curve of the device. Figure 1.5 shows a typical *J–V* curve of a solar cell. V_{OC} is the absolute value when the current density is zero, and J_{SC} is the absolute value when the voltage is zero. The product of $V_{\text{OC}} \times J_{\text{SC}}$ is the theoretical maximum output electrical power. The product of $V_{\text{m}} \times J_{\text{m}}$ can be viewed as the area of the maximum rectangle that can be drawn inside the area of the *J–V* curve.[20]

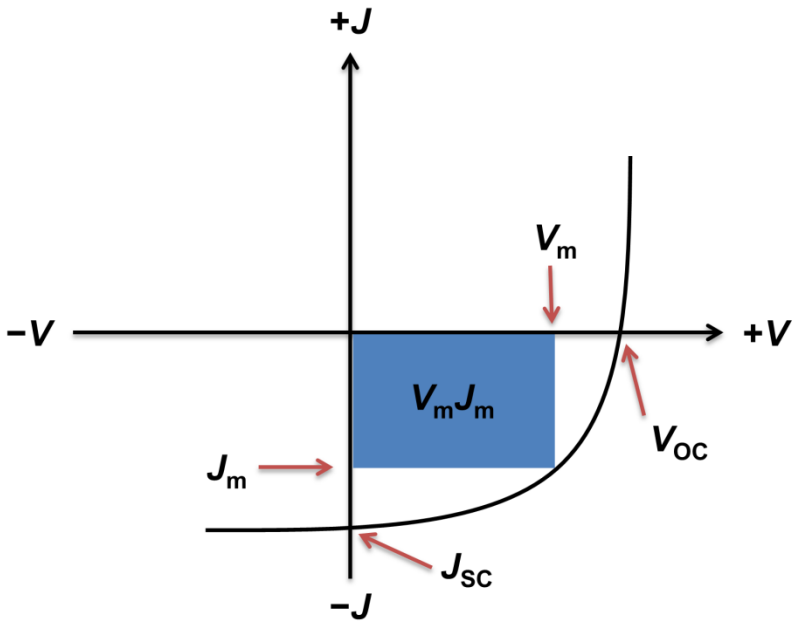

Figure 1.5. The typical *J*–*V* curve of a solar cell. The blue area indicates the product of V_m × J_m.

1.5 Organic photovoltaics

1.5.1 Principle and materials

In an organic photovoltaic device, the photoactive layer is composed of two types of organic materials, called the electron donor (D) and the electron acceptor (A).[19,20] When the ground-state electron in the HOMO energy level of the donor molecule is excited by absorbing the energy of a photon, it is promoted to the LUMO energy level, leaving a hole (positive charge) in the HOMO (Figure 1.6). The excited-state electron and the hole together form an exciton. Due to the energy difference between the LUMO energy levels of the donor and acceptor, the excited-state electron transfers from the LUMO of the donor to the LUMO of the acceptor. Since the energy difference of the LUMO energy levels is the driving force for efficient electron transfer, a large value means more possibility for the

successful electron transfer, but also means more energy loss. Generally, a value of ~0.3 eV is enough for the electron transfer.[19b,21] Once the photoinduced electron transfer occurs before the radiative or nonradioactive decay of photoexcitations, the free electron and the hole (also called charge carriers) move to the respective cathode and anode via a hopping mechanism.[20,22] The electron collected at the cathode then flows to the anode, completing a light-to-electricity circle. Although various metals can be used as the cathode material, such as Al, Ag, Mg, Ba and Ca, Al is the most common since it is inexpensive and comparatively stable. With regard to the anode material, indium tin oxide (ITO) is the most widely used, as it is highly conductive and optically transparent. The ITO is commonly coated on a glass substrate. Between the photoactive layer and the anode, a solution-processed hole-transporting layer of poly(3,4-ethylenedioxythiophene) and polystyrene sulfonate (PEDOT:PSS) is commonly inserted to block the electrons, since the direct contact of the active layer with the anode is known to lead to current leakage and the recombination of charge carriers, which are detrimental to the device performance.[23] Beside PEDOT:PSS, transition metal oxides such as NiO, MoO_3, V_2O_5, and WO_3 have been successfully demonstrated as alternative anode interfacial layers for hole-transporting, although the vacuum evaporation technique was employed to cast these layers.[24] In some cases, an insertion layer of lithium fluoride (LiF) or titanium oxide (TiO_x) between the photoactive layer and the anode layer was used to reduce the electron junction barrier at the acceptor-anode interface and enhance the device performance.[25]

The primary site for exciton dissociation is at the electrode interface. However, for the excitons formed in the middle of the organic photoactive layer, they cannot reach the electrode interfaces due to charge recombination if the layer is too thick, since the exciton

diffusion length is on the order of 10 nm.[20] Hence, the photoactive layer is relatively thin and the thickness is in the range of several tens to a few hundreds of nanometers. If the layer is too thin, the light absorption is inefficient. A compromise regarding the thickness of the photoactive layer has to be found since efficient exciton diffusion and efficient light absorption cannot be simultaneously achieved at all times.[26] This is a common process in the OPV device optimization.

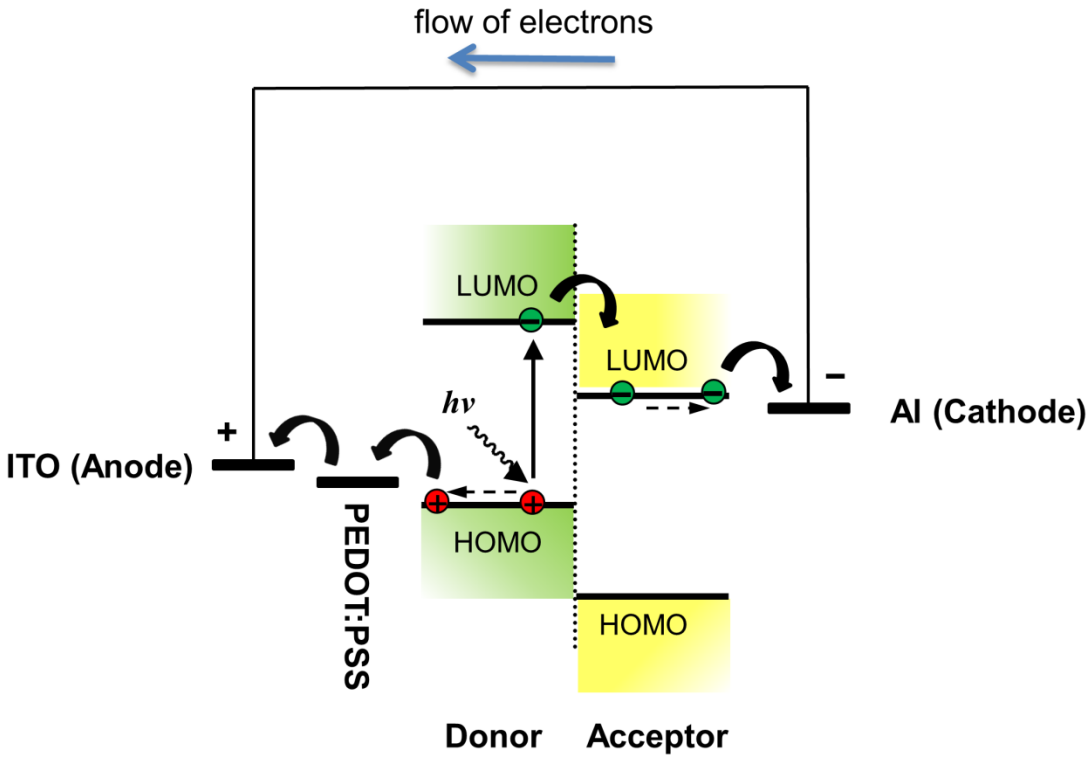

Figure 1.6. Schematic illustration of the energy levels and light-harvesting process in an organic thin-film solar cell.

1.5.2 The concept of "heterojunction" and structures of OPV devices

In inorganic semiconductors, free charge carriers (electrons and holes) are created upon light absorption and migrate fast in opposite directions.[20] In contrast, the excited electron is still bound to the hole (at room temperature) before the exciton dissociation, which is a relatively slow process in most organic semiconductors. On the other hand, the charge carrier mobility of organic semiconductors is much slower than inorganic semiconductors. The basis of a heterojunction is to use the energy difference in the HOMO−LUMO energy levels of two materials — the electron donor (D) and acceptor (A). The energy gap between the LUMO of the donor and the LUMO of the acceptor favors the exciton dissociation by the photoinduced electron transfer from the donor to the acceptor. The initial observations caused by heterojunctions were reported in the 1950s. For example, Nelson found that the photoconductivity of CdS was increased when a cyanine dye was added and sensitized in the red spectral range. He argued that the LUMO energy level of the dye was above the LUMO energy level of CdS. The excited electron in the LUMO of the dye would be transferred to the LUMO of CdS and thereby improved the conductivity.[27] In 1979, Ching. W. Tang first used the concept of heterojunction to design a bilayer organic photovoltaic device consisting of copper phthalocyanine and a perylene derivative, and an unprecedented PCE of ~1% was recorded.[20,28] Now the idea of heterojunction is widely recognized and used by researchers to develop novel organic solar cells.

Figure 1.7 shows three typical structures of organic solar cells. In a planar heterojunction (also called a bilayer heterojunction) device (Figure 1.7A), the electron donor layer and the electron acceptor layer are in contact with a planar interface. Charge separation (exciton dissociation) occurs at the heterojunction interface.[29] Electrons then migrate to the cathode

and holes migrate to the anode. However, the electron donor layer cannot be thick, as the exciton diffusion length is on the order of 10 nm. The excitons cannot diffuse across a thick film to reach the D−A interface. This is the main disadvantage of planar heterojunction devices. In a bulk heterojunction (BHJ) device (Figure 1.7B), the electron donor and acceptor are mixed in a blended film with an interpenetrating network morphology.[7,30] Compared to the planar heterojunction configuration, the BHJ configuration offers a larger interface area for the dissociation of excitons, and thereby improves the device performance. Recently, the tandem cell has attracted significant attention. In a tandem cell (Figure 1.7C), two or more sub-cells with different absorption ranges are stacked in series. The photon utilization efficiency is significantly enhanced in a tandem cell, which benefits the PCE of the device.[31]

The photoactive layer of an OPV device can be solution-processed or processed by thermal deposition in high-vacuum.[32] As a solid-phase processing technique, thermal deposition is not applicable for organic materials with low volatility and saturated vapor pressure, especially for polymers. In addition, thermal deposition is more expensive and cannot be used for large-area fabrication. In contrast, the solution-processing technique is easy, low-cost and compatible with the idea of roll-to-roll printing. Currently the spin-casting technique is widely used in academia for OPV device fabrication.

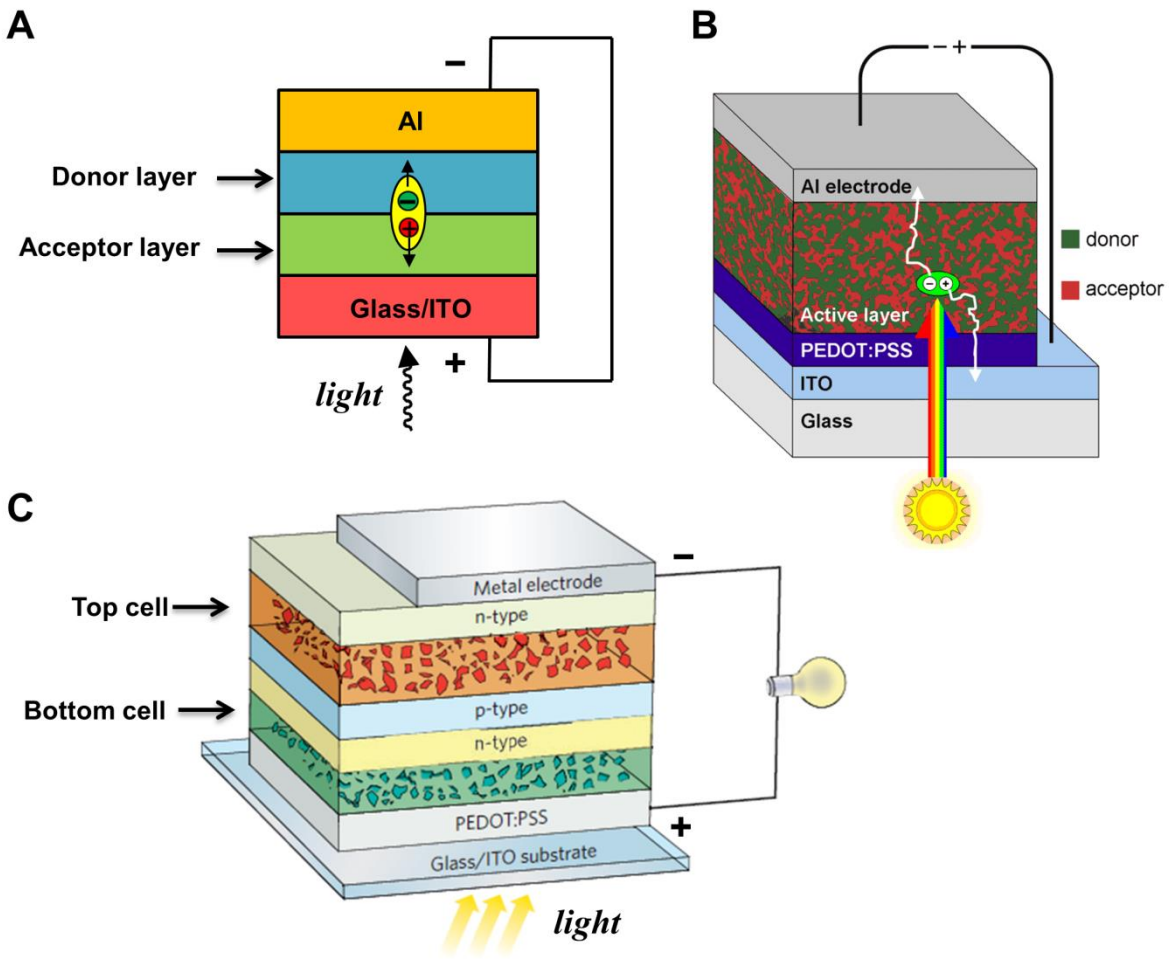

Figure 1.7. Structures of three types of organic solar cells. (A) a planar heterojunction cell; (B) a bulk heterojunction cell; (C) a tandem cell. Figure B courtesy of Stanford Synchrotron Radiation Lightsource, 2011; Figure C adapted with permission from Ref. 31a © 2012 Nature Publishing Group.

1.5.3 Electron donor and acceptor materials

Numerous conjugated molecules have been used as electron donor and acceptor materials in OPV devices. Generally, these molecules display intense and broad absorption bands, as well as moderate charge carrier mobility.[26]

Figure 1.8 shows the chemical structures of a few representitive electron donor materials. Conducting polymers having long conjugation length and good hole mobility have been extensively investigated as the electron donor materials in solution-process OPV devices. Generally, the constitutional repeating units in conducting polymers are composed of aromatic rings with solubilizing alkyl substituents. These polymers tend to form well-organized crystalline nanostructures in films due to interchain interactions and form interconnected network structures that are favorable for charge separation and transport. Poly(3-hexylthiophene) (P3HT) has good hole mobility. The OPV devices using P3HT and fullerene derivatives (electron acceptors) have been reported with reproducible PCE approaching 5%.[33] Poly(*p*-phenylene vinylene) (PPV) is another well-known electron donor species. Solar cells based on poly[2-methoxy-5-(2'-ethylhexyloxy)-*p*-phenylene vinylene] (MEH-PPV) and fullerene derivatives have been reported with a PCE more than 3%.[4,34] Recently, more conducting polymers have been synthesized for the application in OPVs. A copolymer of benzo[1,2-b:4,5-b']dithiophene and thieno[3,4-b]thiophene (PBDTTT) was synthesized by Yu *et al.* and a PCE of 5.6% was achieved.[35] The high efficiency was attributed to the broad and strong absorption of this material, especially in the range of 600–800 nm. A PCE of 6.77% was achieved by modifications on the substituents of PBDTTT and morphology optimization.[36] Leclerc *et al.* reported poly[N-9''-hepta-decanyl-2,7-carbazole-alt-5,5-(4',7'-di-2-thienyl-2',1',3'-benzothiadiazole)] (PCDTBT) with a PCE of 3.6%.[37] The PCE was further improved to 6.1% by the insertion of a titanium oxide (TiO_x) layer as an optical spacer and as a hole blocker between the photoactive layer and the cathode.[38]

Semiconducting oligomers have also been used as electron donors (Figure 1.8). Compared to polymers, oligomers are easy to purify. Oligothiophenes are among the most-studied oligomers, due to their good charge transport properties and chemical tunability. Sakai *et al.* prepared a planar heterojunction solar cell using sexithiophene and C_{60} as the photoactive layers, and a PCE of 0.8% was achieved.[39] The PCE was further improved to 1.5% using the same materials in a BHJ solar cell. Chen *et al.* synthesized a 2,2'-dicyanovinyl capped octyl-substituted septithiophene (DCN7T), and blended it with a fullerene derivative to fabricate a BHJ solar cell which generated a PCE of 3.7%.[40]

Beside polymers and oligomers, many small-molecule dyes such as porphyrins, phthalocyanines, merocyanines have also been used as the electron donors in OPVs (Figure 1.8). Nakamura *et al.* used an in-situ formed tetrabenzoporphyrin as the electron donor and a fullerene derivative as the electron acceptor to construct a solar cell and a PCE of 5.2% was achieved.[41] Kippelen *rt al.* used pentacene and C_{60} to construct a planar heterojunction solar cell, and a PCE of 2.7% (± 0.4%) was achieved.[42]

Generally, OPV devices using conducting polymers as the electron donor materials display higher PCE than the devices using conducting oligomers or other small molecules. This is mainly due to the tendency of forming a well-organized interconnection network morphology of the polymers in the thin films. In contrast, small molecules usually lack ordering in the solid state, although they have many advantages such as monodispersity and well-defined chemical structures.

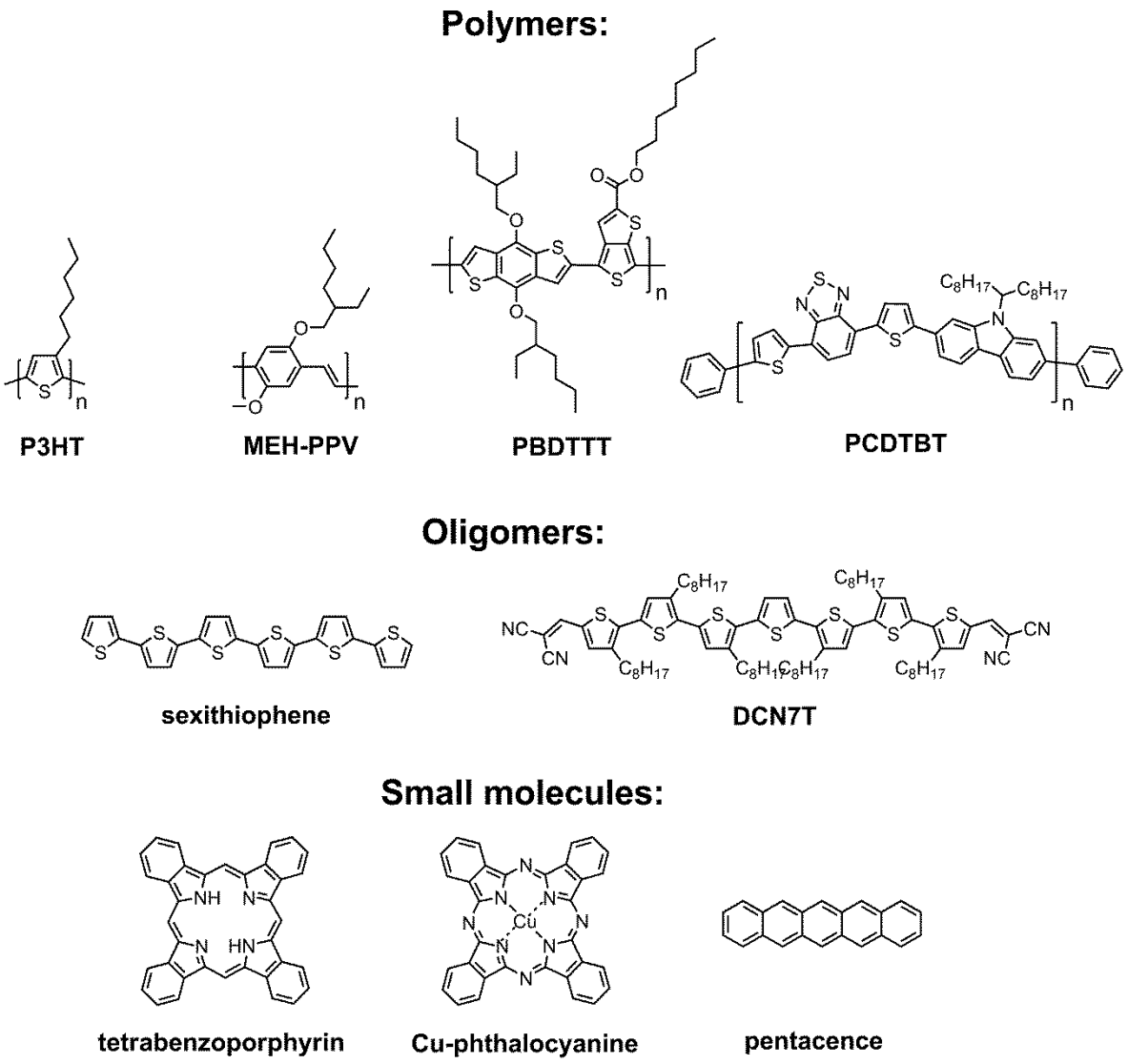

Figure 1.8. Chemical structures of some representative electron donor materials used in OPV devices.

Compared to electron donor materials, the electron acceptor materials are much less in number. Figure 1.9 shows the chemical structures of some well-studied electron acceptor materials. Fullerenes are excellent electron donor materials, because they display high electron mobility and the photoinduced electron transfer from organic electron donors to fullerenes is ultrafast.[4, 43] The main disadvantage of fullerenes is their low solubility. Modification of fullerenes is an attractive way to improve the solubility. In 1995, Wudl *et al*. first reported the synthesis of phenyl-C_{61}-butyric acid methyl ester ($PC_{61}BM$), which is still the most promising electron acceptor for the application in OPVs due to the good solubility in many organic solvents and high electron mobility.[44] Later, more fullerene derivatives were developed to improve the absorption in the visible region and tune the HOMO–LUMO energy levels.[45] For example, Li *et al.* synthesized an indene-C_{60} bisadduct (ICBA), and the device based on P_3HT:ICBA displayed a PCE of 5.44%, compared to 3.88% of a device based on P_3HT:$PC_{61}BM$ under the same conditions.[46]

A few non-fullerene electron acceptors have also been used in OPVs, such as perylene diimide,[47] oligothiophene-*S*,*S*-dioxide,[48] diketopyrrolopyrrol,[49] 9,9'-bifluorenylidene[50] and dicyano-substituted quinacridone (Figure 1.9).[51] However, none of these molecules have displayed superior electron mobility compared to fullerene derivatives, and the PCEs of the devices based on non-fullerene electron acceptors are relatively low.[45]

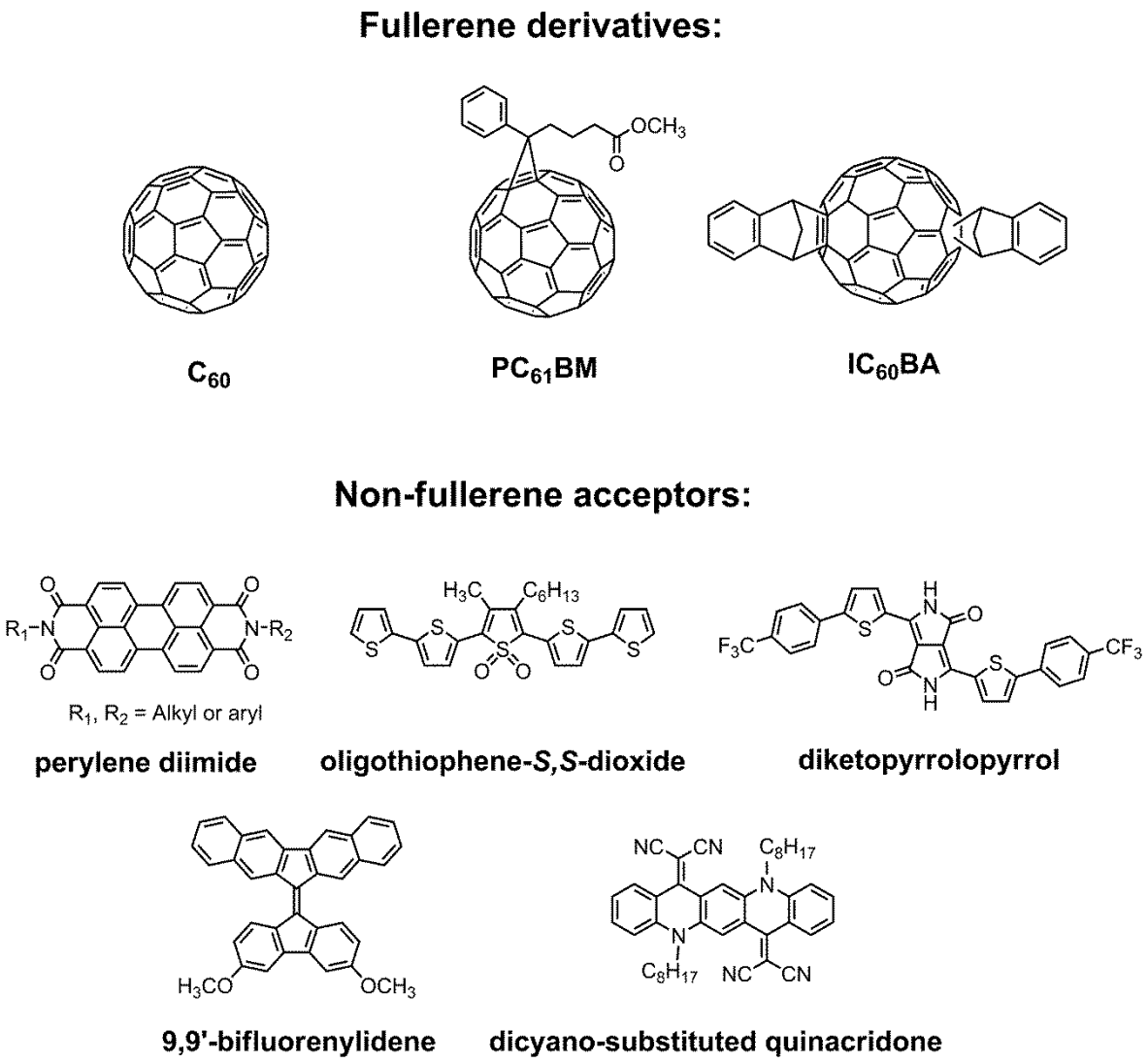

Figure 1.9. Chemical structures of some representative electron acceptor materials used in OPV devices.

Recently, a new design strategy of linking the electron donor and acceptor together (D–A) by covalent bonds or non-covalent interactions have attracted some interest. The idea is to facilitate the exciton dissociation and homogeneous distribution of the materials in thin films.[52] Small-molecule D–A dyads, D–A oligomers and D–A polymers have been used to fabricate the one-component OPV devices. Two examples are shown in Figure 1.10. The

first molecule is a phthalocyanine-fullerence (Pc-C_{60}) dyad synthesized by Torres *et al.*, and an OPV device based on this dyad displayed a PCE of 0.02%.[53] The second material is a D–A polymer poly(bithiophene-C_{60}) synthesized by Li *et al.*, and an OPC device based on this material displayed a PCE of 0.52%.[54] The relatively low efficiencies of these one-component OPV devices were attributed to the ill-defined morphology in the films and inefficient charge transport.[55] Nevertheless, the one-component strategy is still a credible approach towards efficient OPVs if morphological control of the photoactive layers is achieved.[52,56]

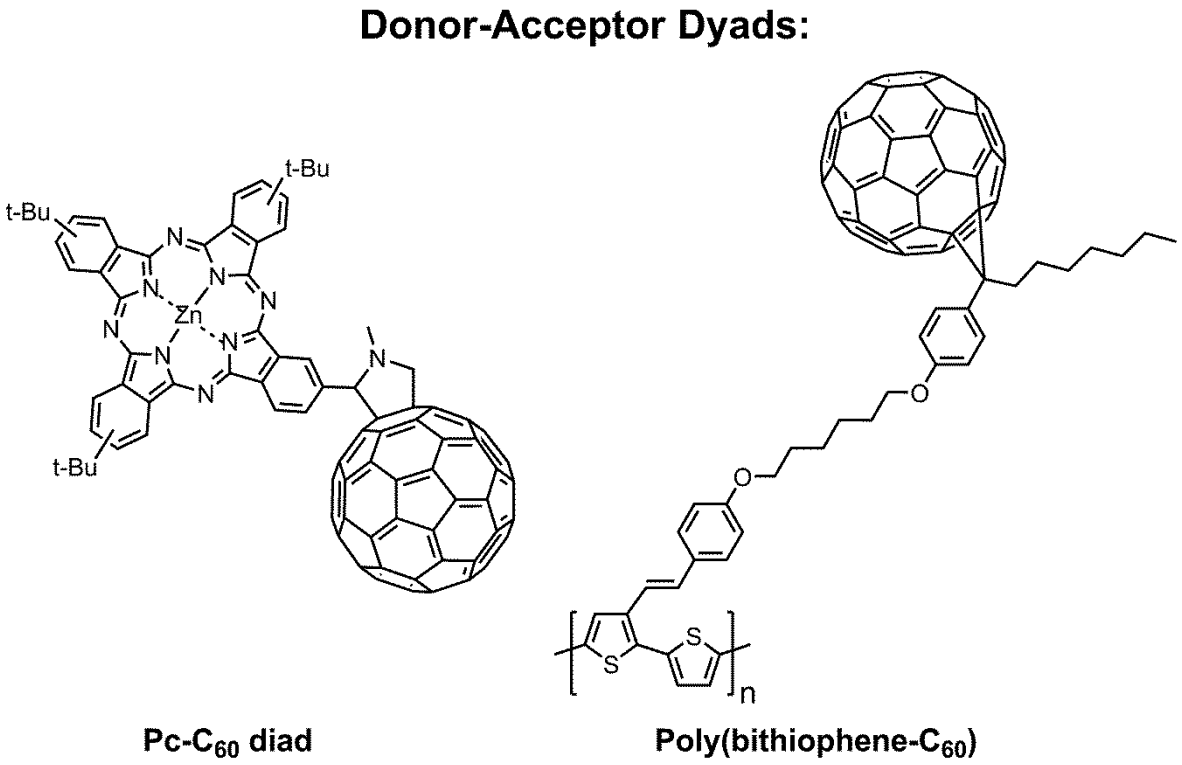

Figure 1.10. Chemical structures of two electron donor-acceptor complexes used in one-component OPV devices.

1.5.4 Effects of nanoscale morphology on power conversion efficiency

As discussed above, the chemical and physical properties of the electron donor and acceptor such as the alignment of the HOMO–LUMO energy levels, the charge carrier mobility and the absorption range are important to the PCE of an OPV device. More importantly, the nanoscale morphology of the photoactive layer is strongly related to the device performance. The concept of bulk heterojunction has been widely used to improve the PCE, as it favors charge separation and transport.

OPV devices based on P3HT:$PC_{61}BM$ have been set as a benchmark.[57] It has been demonstrated that the highly ordered nanoscale morphology of the blended thin films of P3HT:$PC_{61}BM$ is the key to enhance the device performance.[57, 58] On the other hand, devices based on poly(3-butylthiophene) (P3BT) and $PC_{61}BM$ displayed low PCEs.[59] The poor efficiency was attributed to poor solubility, poor crystallinity and low hole mobility.[60] Jenekhe *et al.* reported that high efficiencies could also be achieved in solar cells based on P3BT:$PC_{61}BM$ where P3BT formed well-defined 1D nanowires.[61] The nanowires of P3BT were generated by heating a solution of P3BT to 90–100 °C followed by a slow cooling process. The nanowire suspension and a $PC_{61}BM$ solution were then mixed together. TEM and AFM images of the mixed composite showed that the nanowires formed an interconnected network surrounded by a continuous $PC_{61}BM$ phase (Figure 1.11), and the width of the nanowires was ~10 nm. A solution-processed OPV device based on this composite displayed a hole mobility of 8.0×10^{-3} $cm^2V^{-1}s^{-1}$ and a PCE of 2.2%, which were comparable to a device based on P3HT:$PC_{61}BM$. In contrast, a P3BT solution that was not treated with heating did not form nanowires. An OPV device based on the untreated P3BT:$PC_{61}BM$ displayed a hole mobility of 3.8×10^{-5} $cm^2V^{-1}s^{-1}$ and a PCE of 1.0%.

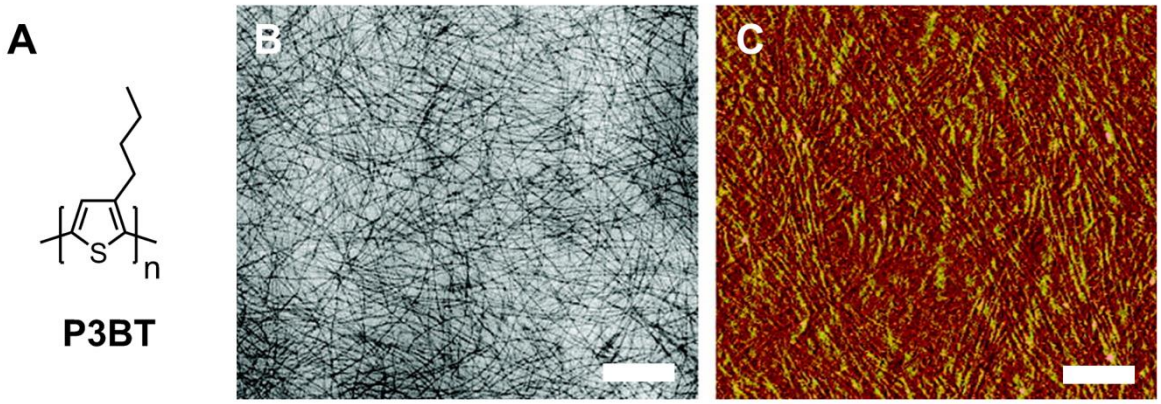

Figure 1.11. (A) Chemical structure of P3BT; (B–C) TEM (B) and AFM (C) images of P3BT nanowires/$PC_{61}BM$ (1:1, w/w ratio). Scale bars: 500 nm. Figure B and C adapted with permission from Ref. 60, © 2008 American Chemistry Society.

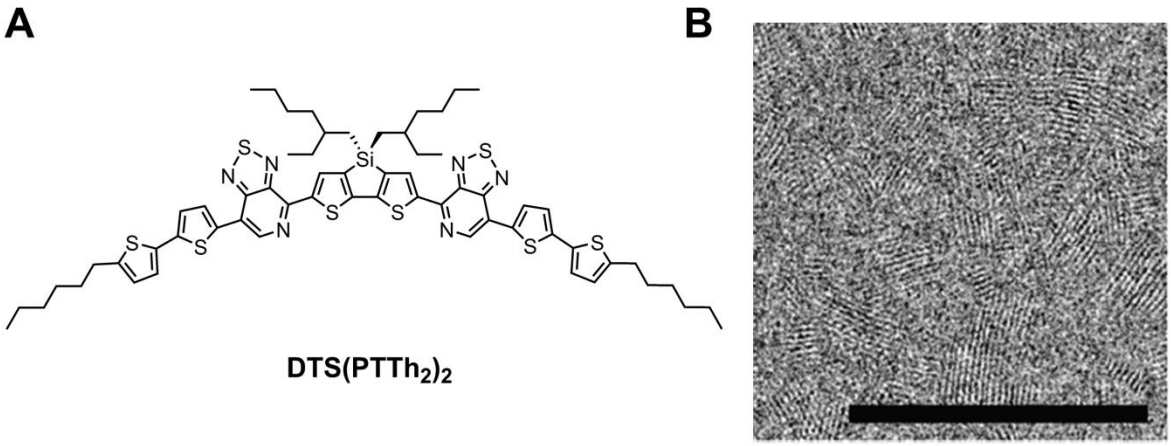

Figure 1.12. (A) $DTS(PTTh_2)_2$; (B) High-magnification TEM image of a BHJ thin film of $DTS(PTTh_2)_2$:$PC_{71}BM$. Scale bar: 100 nm. Figure B adapted with permission from Ref. 61 © 2012 Nature Publishing Group.

Bazan and Heeger *et al.* synthesized a small-molecule donor $DTS(PTTh_2)_2$, and the OPV device based on $DTS(PTTh_2)_2$ and a fullerene derivative $PC_{71}BM$ displayed a high PCE of

6.7%.[62] The unprecedented high efficiency of the device was attributed to the highly ordered nanocrystalline morphology of the material in the blended BHJ thin film with $PC_{71}BM$ (Figure 1.12). The nanocrystalline morphology was imposed by an annealing process. The addition of 1,8-diiodooctane as a solvent additive during the film-forming process further led to reduced domain sizes in the BHJ layer.

1.6 Supramolecular assemblies in organic photovoltaics

Since highly ordered nanoscale morphologies of the BHJ layers are eagerly sought in the development of high efficient OPVs, supramolecular self-assembly is an obvious attractive pathway to introduce ordering at all dimensions to shape the desired nanoscale morphology. In addition, the building blocks in supramolecular assemblies ubiquitously adopt well-organized spatial arrangements since the assemblies are precisely programmed at a molecular level.[8b,63] The molecular arrangements may lead to changes in the absorption spectra due to uniform aggregation patterns of chromophores, and promote charge transfer and transport between the photoactive moieties in the assemblies, which is beneficial for the performance of an OPV device. This strategy has been cleverly employed by the natural light-harvesting systems (see details in Section 1.2). Chemists also use the strategy to build supramolecular assemblies for the application in OPVs.

1.6.1 Assemblies of electron donor

Hasobe *et al.* synthesized a porphyrin-peptide oligomer of 16 units [$\mathbf{P(H_2P)_{16}}$] and mixed it with C_{60} in solution (Figure 1.13).[64] Efficient porphyrin fluorescence quenching was observed in the benzonitrile solution of the mixture, indicating the C_{60} molecules strongly

interacted with the porphyrin pendants (Figure 1.13B). In the binary solvent system of acetonitrile-toluene, the complexes of the porphyrin-peptide oligomer and C_{60} formed self-assembled clusters with well-defined shapes and sizes (a diameter of 100–200 nm), as revealed by TEM imaging (Figure 1.13C). The composite clusters can be electrochemically deposited on nanostructured SnO_2 electrodes. A photovoltaic device based on these clusters displayed a PCE of ~1.6%. In contrast, the monomer of porphyrin-amino acid [$\mathbf{P(H_2P)_1}$] did not form well-defined clusters with C_{60}. A photovoltaic device based on the composite of the monomer and C_{60} displayed a low PCE of 0.043%. The near 40 times increment in PCE of the device based on the clusters of [$\mathbf{P(H_2P)_{16}}$–C_{60}] was ascribed to the enhancement of photoinduced electron transfer in the supramolecular assemblies.

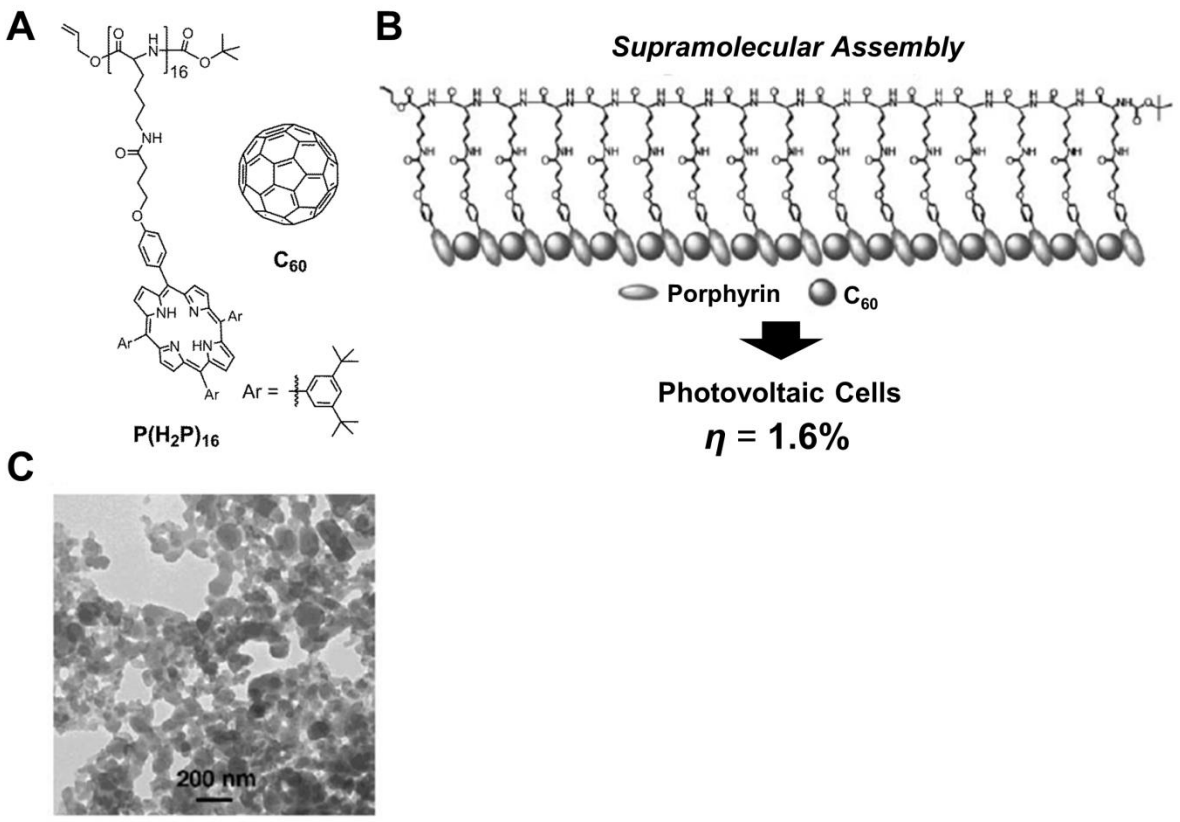

Figure 1.13. (A) Molecular structures of $P(H_2P)_{16}$ and C_{60}; (B) schematic illustration of the supramolecular organization between $P(H_2P)_{16}$ and C_{60}; (C) TEM image of the clusters of $P(H_2P)_{16}$–C_{60}. Figure B and C adapted with permission from Ref. 64 © 2007 Royal Society of Chemistry.

Kumar *et al.* synthesized a sexithiophene functionalized peptide (**1**) (Figure 1.14A).[65] From the measurement using size exclusion chromatography, peptide **1** was estimated to contain approximately 23 repeat units in length. FT-IR and variable-temperature CD studies revealed that the peptide adopts an α-helix conformation. In cyclohexane, peptide **1** self-assembled into a highly branched mesh-like network (Figure 1.14A). Similar nanostructures were also found in chlorobenzene. The chlorobenzene solution of peptide **1**

was mixed with $PC_{61}BM$ and the mixture was spin-cast to form the BHJ active layer in the OPV device, which displayed a PCE of 0.22% (± 0.017%). The hole mobility of the nanocomposite of peptide **1** was measured to be 1.9×10^{-7} $cm^2V^{-1}s^{-1}$. Meanwhile, two control molecules **2** and **3** were also synthesized (Figure 1.14B). None of these control molecules could form well-organized nanostructures in cyclohexane or chlorobenzene. The OPV devices based on **2**:$PC_{61}BM$ and **3**:$PC_{61}BM$ displayed respective PCEs of 0.14% (± 0.018%) and 0.12% (± 0.007%). The hole mobility of **2** and **3** were both too low to be measured (instrument detection limit 1.0×10^{-8} $cm^2V^{-1}s^{-1}$). The improved PCE and hole mobility in the case of peptide **1** were ascribed to the self-assembled highly ordered nanostructures.

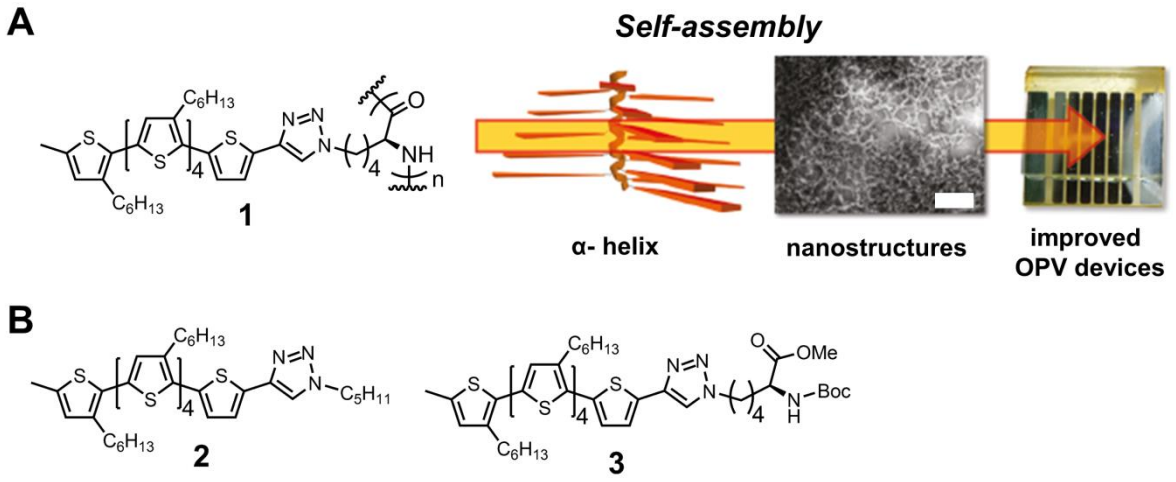

Figure 1.14. (A) Chemical structure of peptide **1** and a schematic illustration of the self-assembly process (TEM scale bar: 500 nm); (B) Chemical structures of the control molecule **2** and **3**. Figure A adapted with permission from Ref. 65 © 2011 American Chemistry Society.

1.6.2 Assemblies of electron acceptor

Wang *et al.* synthesized a fullerene molecule bearing a cyanobiphenyl tail (a mesogen) linked by a short alkyl spacer (**C_{60}-bp-CN**) (Figure 1.15).[66] This material displayed the nature of smectic liquid-crystalline phase revealed by polarizing optical microscopy (POM) and differential scanning calorimetry (DSC), as two exothermic transitions were observed. The thin film of **C_{60}-bp-CN** showed the patterns of lamellar ordering after thermal annealing from 180 °C. X-ray diffraction (XRD) analysis of the thin film revealed that the cyanobiphenyl tails were interdigitated and closely packed, with the fullerene groups flanking on the sides (Figure 1.15B). A blended thin film of P3HT:**C_{60}-bp-CN** after annealing from 180° C showed well-aligned nanocrystalline structures. Interestingly, the UV-Vis spectrum of the blended thin film of P3HT:**C_{60}-bp-CN** showed a large red shift (~70 nm) and stronger absorption shoulders, compared to the spectrum of the blended thin film of P3HT:C_{60} treated with the same annealing protocol. A PCE of 0.65% was recorded on the OPV device based on the P3HT:**C_{60}-bp-CN**. In contrast, a device based on P3HT:C_{60} showed a PCE of 0.22%, which was due to the degraded continuous morphology of C_{60} at such a high temperature (180 °C).

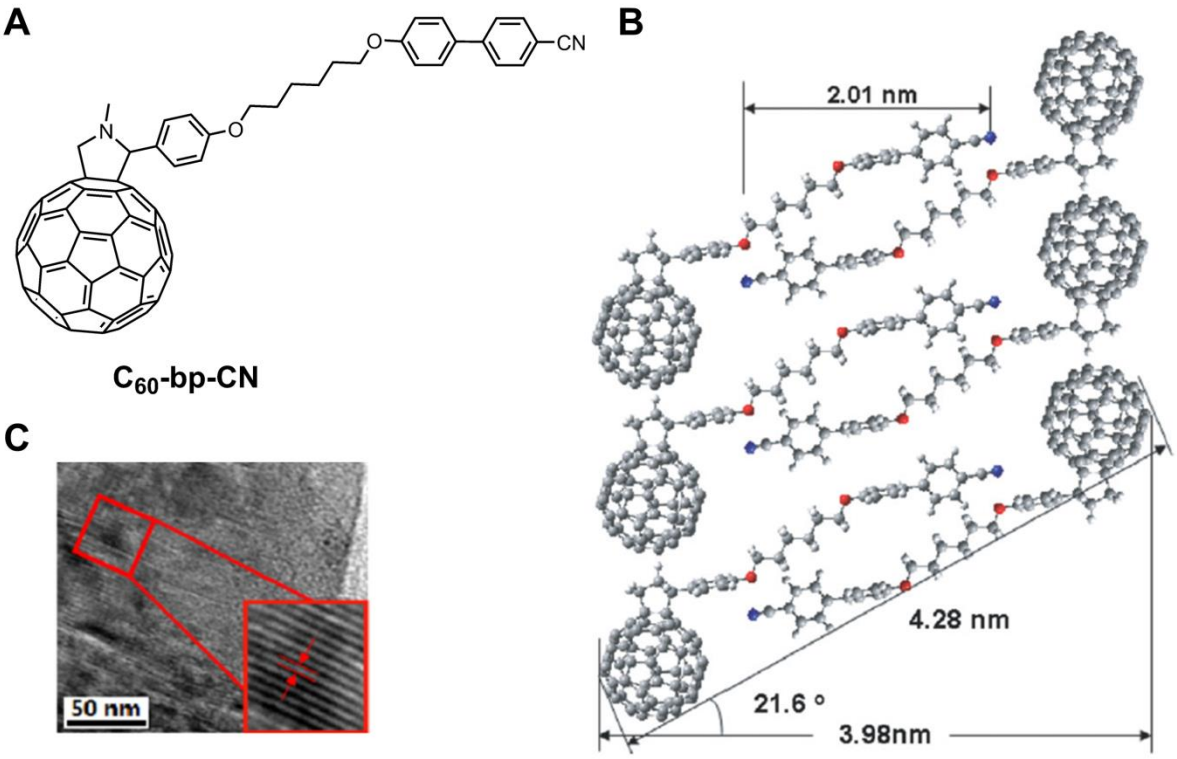

Figure 1.15. (A) Molecular structure of **C_{60}-bp-CN**; (B) a proposed arrangement of **C_{60}-bp-CN**; (C) high resolution cryo-TEM image of P3HT:**C_{60}-bp-CN** film after heating at 180 °C for 30 min. Figure B and C adapted with permission from Ref. 66 © 2012 Elsevier.

1.6.3 Assemblies of one-component electron donor-acceptor complex

Geng *et al.* synthesized a one-component D–A cooligomer (**F5T8-hP**), where the moiety of alternating fluorene-bithiophene served as the electron donor and the *N*-hexyl perylene diimide (PDI) served as the electron acceptor (Figure 1.15A).[67] **F5T8-hP** displayed smectic liquid-crystalline properties, and formed highly ordered alternative lamellar nanostructures with the persistent length in the range of 100–400 nm after solvent-vapor annealing (Figure 1.16B). The formation of these well-defined lamellar nanostructures was driven by the intermolecular π–π stacking interactions between the homotropic donor units and the

acceptor units. The OPV device based on **F5T8-hP** showed a J_{SC} of 4.49 mA/cm^2, V_{OC} of 0.87 V, FF of 0.38 and PCE of 1.5%.

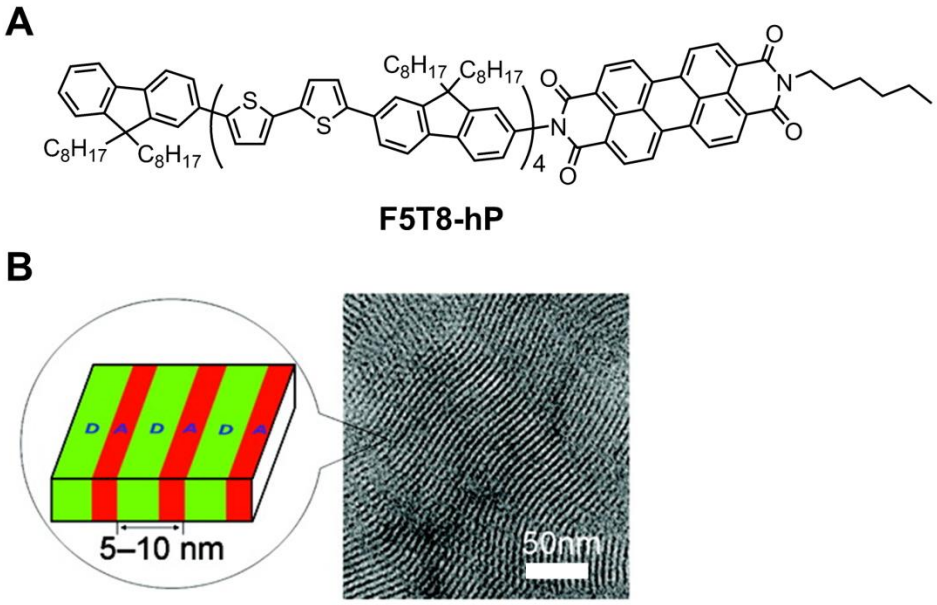

Figure 1.16. (A) Molecular structure of **F5T8-hP**; (B) TEM image of a **F5T8-hP** thin film after solvent-vapor annealing and a schematic illustration of the lamellar nanostructures in the film. Figure B adapted with permission from Ref. 67 © 2009 American Chemical Society.

Aida *et al.* synthesized two metalloporphyrin-fullerene D-A dyads (**P_{Zn}-C_{60} 1** and **P_{Zn}-C_{60} 2**) which both have a hydrophilic oligoethyleneglycol tail (Figure 1.17A).[68] Adding MeOH (65% in volume) to a toluene solution of **P_{Zn}-C_{60} 1** changed the solution color from pink to pale orange. After aging for 4 h, well-defined nanotubes with a uniform diameter of 32 nm and a wall thickness of 5.5 nm were found in the TEM samples prepared from this solution (Figure 1.17B). Similarly, adding MeOH (55% in volume) to a toluene solution of **P_{Zn}-C_{60} 2** led to the formation of nanotubes with a uniform diameter (7–8 nm) and wall

thickness (1.7–1.8 nm) (Figure 1.17C). XRD analysis revealed that the nanotubes of **P_{Zn}-C_{60} 1** adopt a bilayer pattern while the nanotubes of **P_{Zn}-C_{60} 2** adopt a monolayer pattern. The nanotubes of **P_{Zn}-C_{60} 1** and **P_{Zn}-C_{60} 2** both displayed a photocurrent upon light illumination (Figure 1.17E).

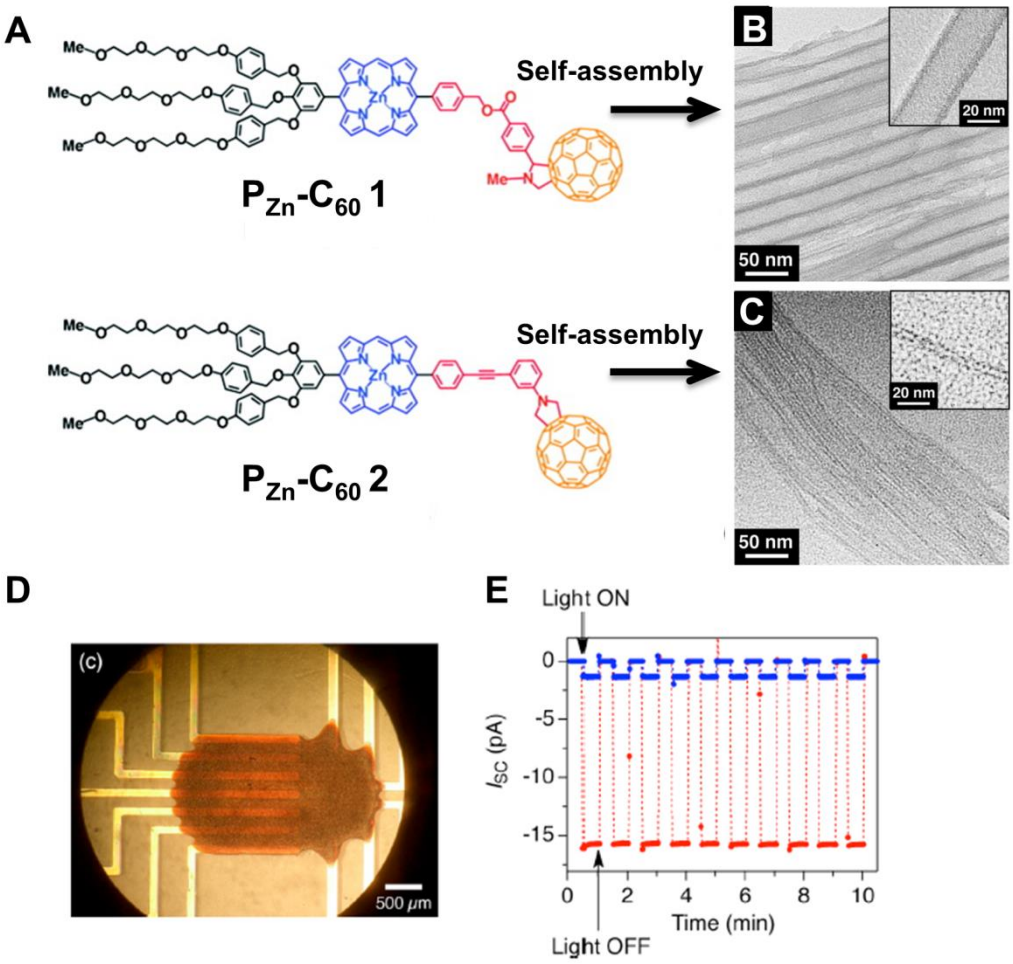

Figure 1.17. (A) Molecular structures of **P_{Zn}-C_{60} 1** and **P_{Zn}-C_{60} 2**; (B) TEM image of **P_{Zn}-C_{60} 1** nanotubes; (C) TEM image of **P_{Zn}-C_{60} 2** nanotubes; (D) optical image of the OPV cell with a drop cast film of **P_{Zn}-C_{60} 1** nanotubes; (E) changes in I_{SC} of OPV devices based on **P_{Zn}-C_{60} 1** nanotubes and **P_{Zn}-C_{60} 2** nanotubes upon turning on and off the light (46 mW/cm^2). Figure adapted with permission from Ref. 68 © 2012 American Chemical Society.

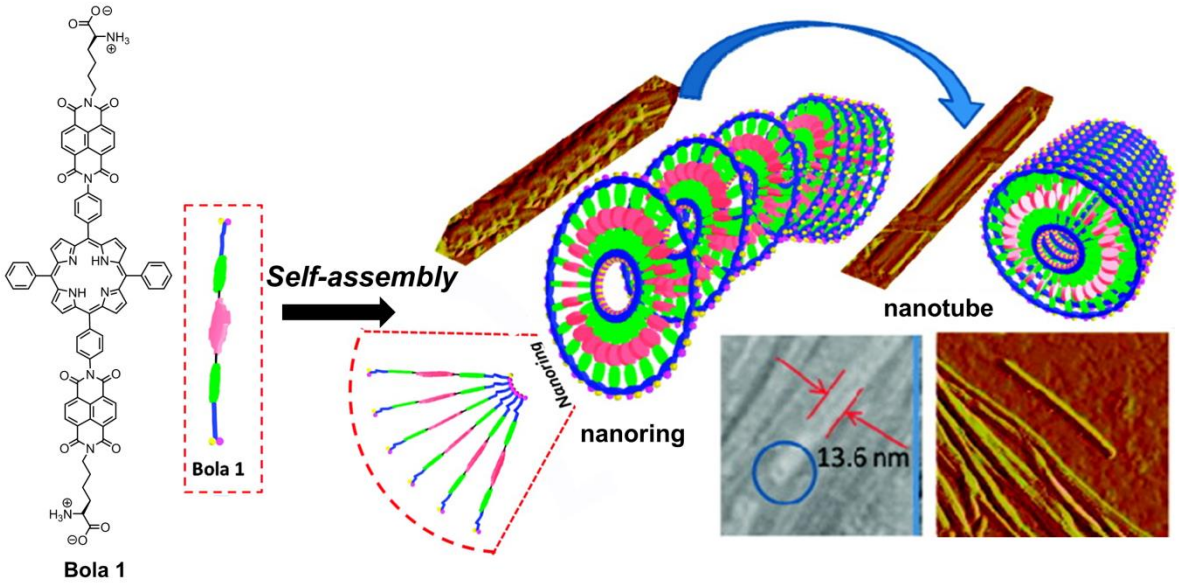

Figure 1.18. Molecular structure of **Bola 1** and schematic illustration of the hierarchical self-assembly process. Figure adapted with permission from Ref. 69 © 2011 American Chemical Society.

Parquette *et al.* synthesized a bolaamphiphile D–A–D triad complex (**Bola 1**), where the tetraphenylporphyrin donor was flanked by two L-lysine-substituted naphthalene diimide (NDI) acceptors on the sides (Figure 1.18).[69] In 10% MeOH/H_2O, **Bola 1** formed well-organized, micrometer-long nanotubes with an outer diameter of 13.6 nm and a wall thickness of 4.6 nm. A few bundles of single nanotubes were also presented and the bundles grew larger and formed precipitates after aging for 2–3 days. In addition to the nanotubes, short stacks of discrete nanorings were also identified by AFM, and the stacks of nanorings were found to fuse together into nanotubes on the smooth surface of mica. The hierarchical self-assembly of **Bola 1** into nanorings and nanotubes was driven by amphiphilic interactions and π–π interactions. The assembly solution of **bola 1** in 10% MeOH/H_2O showed red shifts both in the porphyrin Soret bands and the NDI bands,

indicating both of the porphyin groups and the NDI groups are J-type aggregates in the assemblies. The steady-state and time-resolved fluorescence spectra of the assembly solution showed fast and near complete fluorescence quenching of the porphyrin emission bands, indicating the efficient photoinduced electron transfer from porphyrin to NDI. Although not mentioned by the authors, it would be interesting to see whether **Bola 1** is suitable for the applications in OPVs and organic semiconductors.

1.6.4 Coassemblies of electron donor and acceptor

Schmidt-Mende *et al.* used hexaphenyl-substituted hexabenzocoronene (**HBC-PhC$_{12}$**) as the electron donor and a perylene diimide derivative (**PDI-1**) as the electron acceptor to construct a solution-processed OPV device (Figure 1.19).[70] A spin-cast thin film of pure **HBC-PhC$_{12}$** displayed discotic liquid-crystalline properties and exhibited a smooth textured surface by AFM imaging, while the film of **PDI-1** showed micrometer-long crystallites driven by π–π stacking interactions. A thin film spin-cast from a solution blend of **HBC-PhC$_{12}$**:**PDI-1** (40:60) showed well-organized, vertically segregated nanostructures in the AFM image (Figure 1.19B). The solution-processed OPV device based on this mixture displayed a J_{SC} of 33.5 μA/cm^2, V_{OC} of 0.69 V and a PCE of 1.95% under illumination at 490 nm. It was seen that the high interfacial area between the electron donor and acceptor in the photoactive layer gave rise to efficient photoinduced electron transfer and favored the charge transport.

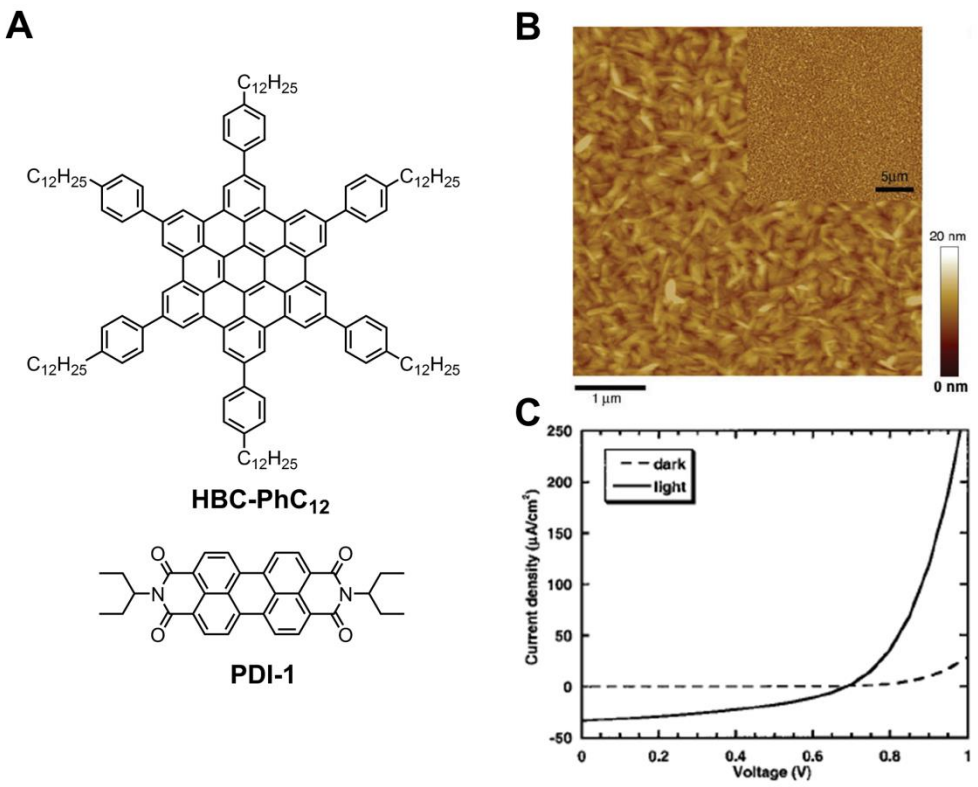

Figure 1.19. (A) Molecular structures of **HBC-PhC$_{12}$** and **PDI-1**; (B) tapping mode AFM image of a thin film spin-cast from a 40:60 blend solution of **HBC-PhC$_{12}$** and **PDI-1**. Figure B adapted with permission from Ref. 70 © 2001 American Association for the Advancement of Science.

Aida *et al.* used the coassembly strategy to tune the optoelectronic properities of self-assembled nanotubes that were composed of π-stacked hexabenzocoronene-fullerene dyad **HBC-C$_{60}$** and the unmodified hexabenzocoronene derivative **HBC-2** (Figure 1.20).[71] Both **HBC-C$_{60}$** and **HBC-2** formed highly ordered homotropic nanotubes when the respective toluene suspensions were applied to sonication and heating (Figure 1.20 C–E). Interestingly, when the toluene suspensions of **HBC-C$_{60}$** and **HBC-2** were mixed at different molar ratios and applied to the same self-assembling condition, coassembled nanotubes with a coaxial

configuration were found. These coassembled nanotubes were uniform in diameter (22 nm) and wall thickness (4.5 nm), and showed different charge carrier mobility at different molar ratios of **HBC-C_{60}** and **HBC-2**. OPV devices were fabricated based on the coassembled nanotubes and two homotropic nanotubes. When the molar fraction of **HBC-C_{60}** was increased, the short circuit current (I_{SC}) increased first and then slightly decreased, and V_{OC} decreased, while the FF values were almost unchanged (0.25–0.30).

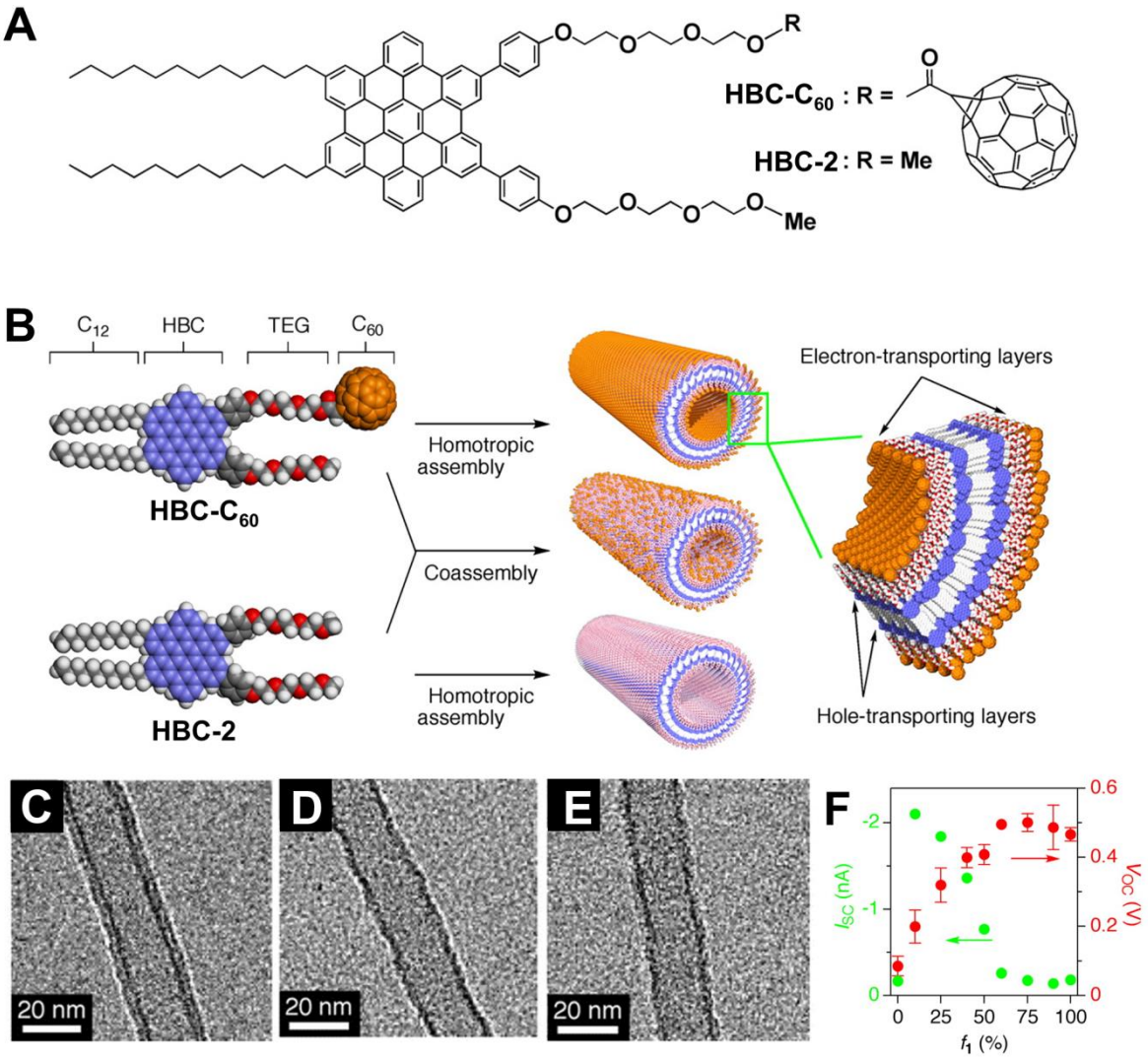

Figure 1.20. (A) Molecular structures of **HBC-C$_{60}$** and **HBC-2**; (B) schematic illustration of homotropic assembly and coassembly; (C) TEM image of a homotropic nanotube of **HBC-C$_{60}$**; (D) TEM image of a homotropic nanotube of **HBC-2**; (E) TEM image of a coassembled nanotube of **HBC-C$_{60}$** and **HBC-2**; (F) plots of V_{OC} (red) and I_{SC} (green) versus the molar fraction of **HBC-C$_{60}$**. Figure adapted with permission from Ref. 71 © 2009 American Association for the Advancement of Science.

1.7 Supramolecular assemblies in semiconductors

Highly ordered spatial arrangements of π-conjugated chromophores may favor the charge hopping process between the adjacent chromophores, especially in the cases of 1D aggregates, which provide continuous pathways for charge carries.[8b,63] For example, regioirregular P3HT without defined interchain interactions normally display low charge-carrier mobility (10^{-6} to 10^{-4} $cm^2V^{-1}s^{-1}$), while the charge carrier mobility of regioregular P3HT with highly ordered lamellar morphology could be as high as 0.1 $cm^2V^{-1}s^{-1}$.[72] Introducing ordering into thin films of conducting polymers normally requires an annealing process. In contrast, supramolecular self-assembly in solution represents a convenient method to build molecular architectures with desired dimensions. This strategy has been employed by researchers to build organic semiconductors.

Würthner and Chi *et al.* reported self-assembled nanotubes from a derivative of Bacteriochlorophyll *c* bearing a hydrophilic oligoethyleneglycol tail (**ZnBChl-1**).[73] In a mixed solvent of H_2O/MeOH (100:1, v/v), **ZnBChl-1** formed well-defined nanotubes with an outer diameter of 6.0 ± 0.5 nm and an inner diameter of ~2 nm, driven by hydrophobic effect between the oligoethyleneglycol tails and π–π stacking interaction between the bacteriochlorophyll pigments (Figure 1.21). The nanotube solution was very stable under ambient condition and did not form precipitates over several months. Interestingly, the nanotubes of **ZnBChl-1** were semiconductive, with a measured conductivity of 0.48 ± 0.07 S/m revealed by conductive AFM (c-AFM). The exceptional charge-transport properties of these nanotubes were ascribed to the closely packed dye groups in the 1D tubular nanostructures.

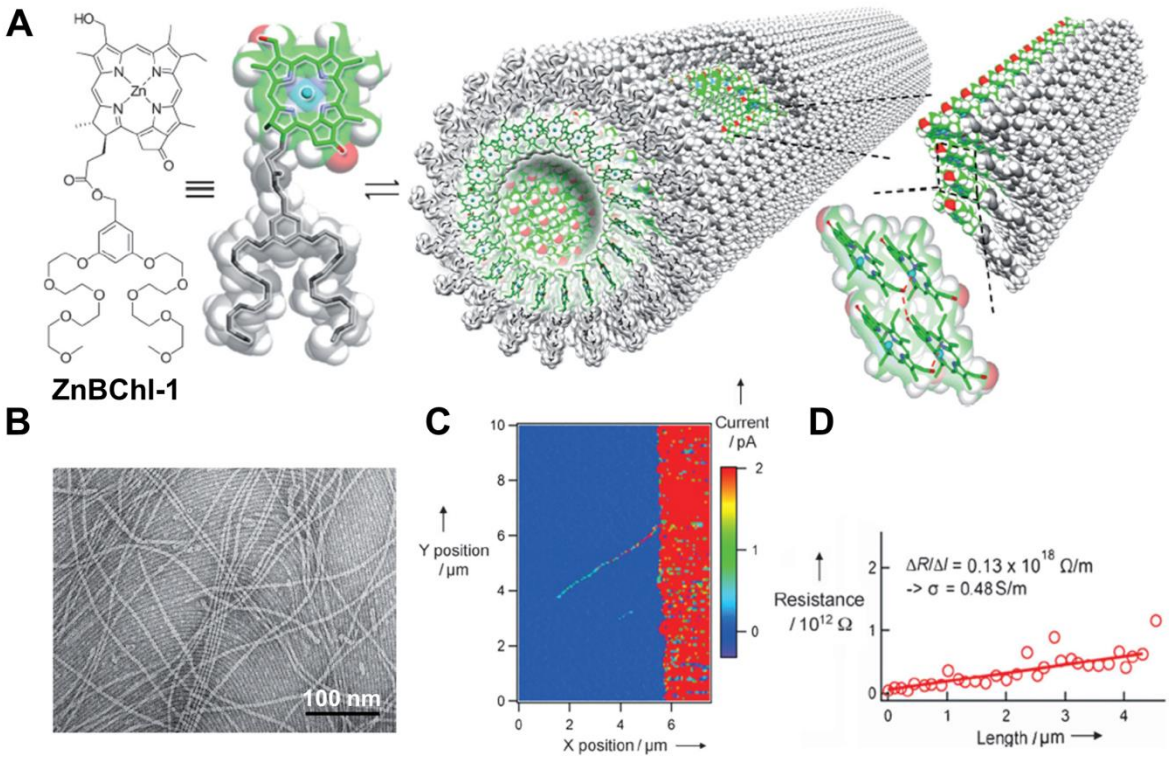

Figure 1.21. (A) Molecular structure of **ZnBChl-1** and space-filling models of self-assembled nanotubes; (B) TEM image of **ZnBChl-1** nanotubes drop-cast from H_2O/MeOH (100:1, v/v); (C) c-AFM image of a single nanotube connected to a thin layer of PEDOT:PSS on the right side; (D) resistance of the nanotube as a function of its length. Figure adapted with permission from Ref. 73 © 2012 Wiley-VCH.

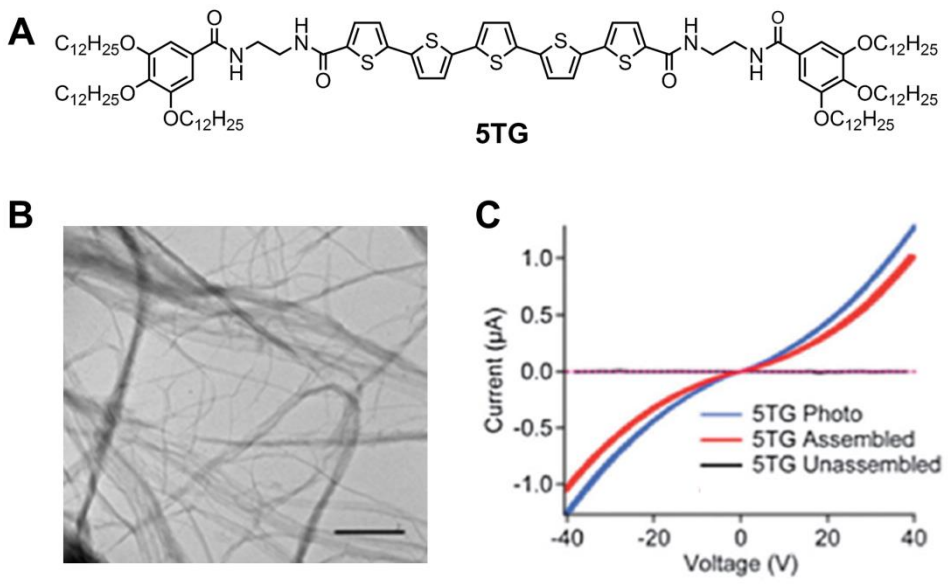

Figure 1.22. (A) Molecular structure of **5TG**; (B) TEM image of a thin film of **5TG** drop-cast from a chlorocyclohexane solution of **5TG** (scale bar: 500 nm); (C) *I–V* curves of thin films of assembled and unassembled **5TG** and the signal changes upon photoirradiation at 354 nm (7.32 mW/cm^2). Figure B and C adapted with permission from Ref. 74 © 2011 Royal Society of Chemistry.

Stupp *et al.* synthesized a quinquethiophene molecule flanked with amide-linked oligoethyleneglycol groups on the sides (5**TG**) (Figure 1.22).[74] The chlorocyclohexane solution of **5TG** formed an organogel at a low concentration (~0.1 wt%) when the solution was heated close to the boiling point of the solvent and allowed to cool to room temperature. Nanofibers with a length of several micrometers and width in 40−300 nm were found in the SEM and TEM samples prepared from a diluted solution of this organogel (Figure 1.22B). Adding MeOH to the organogel led to disassembly, indicating that the formation of nanofibers was mainly driven by the intermolecular hydrogen-bonding interactions between the amide groups. Interestingly, the drop-cast thin films of self-assembled **5TG** and

unassembled **5TG** differed in conductivity (Figure 1.22C). The conductivity of the thin film of self-assembled **5TG** was measured to be $9.9 \pm 1.7 \times 10^{-4}$ S/m. In contrast, the thin film of unassembled **5TG** did not display any detectable conductivity above the instrument detection limit. Shining UV light on the thin film led to increased current, indicating that the semiconducting quinquethiophene units in the nanofibers are responsible for charge transport.

1.8 Supramolecular assemblies in OLED

An Organic Light-emitting diode (OLED) is an electroluminescent (EL) device, which can be viewed as the inversed version of an OPV device, since the working mechanism of an OLED device is the relaxation of high-energy electrons from the LUMO to the HOMO of an organic compound accompanied with the energy released in the form of emitting light.[75] Beside organometallic compounds such as Alq_3 and $Ir(ppy)_3$, conductive polymers such as poly(*p*-phenylene vinylene) (PPV) and polyfluorene can also be used as the active-layer materials in OLED devices.[76] Recently, a few supramolecular assemblies have been explored as potential materials for application in OLEDs.[8b]

Meijer and Schenning *et al*. synthesized three fluorophore oligomers equipped with quadruple hydrogen bonding 2-ureido-4[1*H*]- pyrimidinone (UPy) end groups (**UPy-OF3-UPy**, **UPy-OPV5-UPy** and **UPy-Pery-UPy**) (Figure 1.23A).[77] All these molecules could form strong linear supramolecular assemblies in many organic solvents. More interestingly, supramolecular coassemblies could also be obtained by dissolving them in a single solution. Chloroform solutions of pure **UPy-OF3-UPy**, **UPy-OPV5-UPy** and **UPy-Pery-UPy** emitted blue, green and orange light, respectively, upon photoirradiation at 365 nm. A

three-component mixed solution with an optimized molar ratio emitted near white light (Figure 1.23B). Spin-cast thin films of these molecules on quartz plates displayed similar fluorescence emissions (Figure 1.23C). The AFM image of the spin-cast film of the three-component mixture showed a very smooth and continuous surface that closely resembled those of the pure components (Figure 1.23D). The solution-processed OLED devices using three pure components as the active-layer materials displayed EL properties, with the blue light for **UPy-OF3-UPy**, green light for **UPy-OPV5-UPy** and red light for **UPy-Pery-UPy** (Figure 1.23E). The OLED device based on the three-component mixture with an optimized molar ratio emitted near white light (Figure 1.23F).

As shown in the example above, supramolecular assemblies may represent a new catalog of materials for OLEDs.

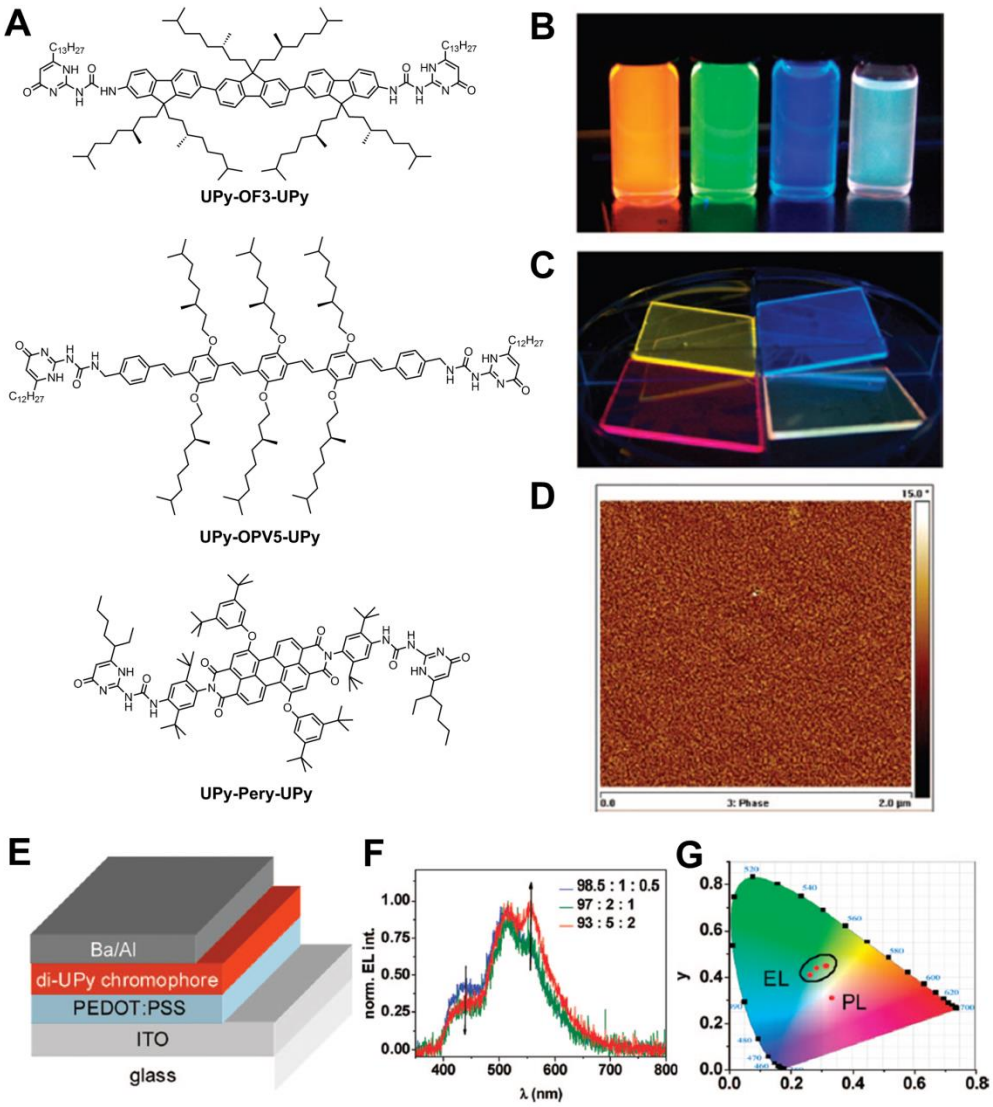

Figure 1.23. (A) Molecular structure of **UPy-OF3-UPy**, **UPy-OPV5-UPy** and **UPy-Pery-UPy**; (B) chloroform solutions of pure **UPy-OF3-UPy** (blue), **UPy-OPV5-UPy** (green) and **UPy-Pery-UPy** (orange) and a three-component solution (59:33:8) excited at 365 nm; (C) spin-cast thin films of three pure components and a mixture (84:10:6) (D) TEM image of a thin film spin-cast from a 80:20:10 mixture of the three components; (E) architecture of the OLED devices; (F) normalized EL spectra of mixtures with different ratios at 24 V; (G) positions of the EL and PL spectra of the mixtures in the CIE color space. Figure B–G adapted with permission from Ref. 77 © 2008 American Chemical Society.

1.9 Supramolecular assemblies in OFET

The field-effect transistor (FET) is an electrical device that uses an electric field to control the conductivity of a channel of one type charge carrier in a semiconducting material. A FET device normally consists of a source, a drain and a gate. Depending on the signs of the applied bias voltage between the gate and the source or the applied voltage between the gate and the semiconducting layer (body), the flow of charge carriers between the source and the gate can be controlled.[78] Hence, the FET is a useful tool to measure the charge carrier mobility of organic semiconducting materials. The organic field-effect transistor (OFET) is a device that uses organic semiconducting materials as the body. A few conducting polymers have been used in OFETs, including P3HT, polyfluorene and poly (*p*-phenylene vinylene) (PPV), due to their high conductivity.[79] π-conjugated small molecules have also been used in OFETs, especially rubrene and pentacene. Some semiconducting supramolecular assemblies have also been reported as promising materials for the application in OFETs, such as assemblies of conducting oligomers, oligoarenes, arene diimides and phthalocyannines.[80]

1.10 Guanine–Cytosine motifs and self-assembled rosette nanotubes

G∧C motifs are fused bicyclic rings of guanine and cytosine with self-complementary sets of hydrogen bonding sites. In 1996, Lehn and Mascal reported that G∧C type motifs can form hexamers (rosettes) by intermolecular hydrogen bonding.[81] Later on, the Fenniri group reported that G∧C motifs functionalized with amino acids not only form hexamers but they also undergo hierarchical self-assembly into rosette nanotubes (RNTs) in water via π–π stacking and hydrophobic effects (Figure 1.24).[82] The G∧C motif featuring an aldehyde

moiety can be functionalized with a broad range of molecules bearing an active primary or secondary amino group through reductive amination. Over the past 15 years, our group continuously developed variants of G∧C modules with different functional groups, including single amino acids,[82] short peptides,[83] crown ethers,[84] aromatic groups[85] and electroactive small molecules (unpublished data). The G∧C modules functionalized with chiral molecules displayed unique chiroptical properties which can be tuned by using different self-assembly protocols.[83a,86]

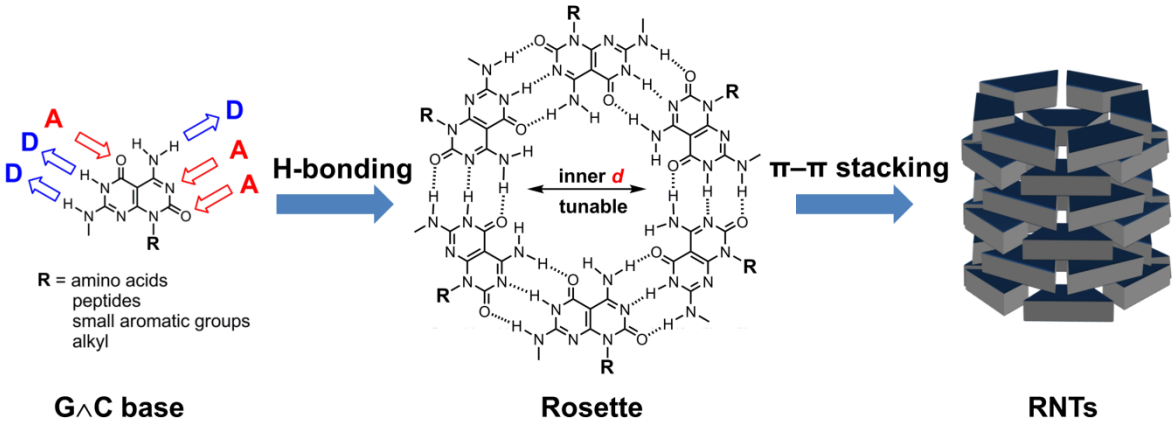

Figure 1.24. Schematic illustration of the hierarchical self-assembly process of G∧C modules into 1D RNTs.

A new type of building block called twin G∧C motif was also designed and synthesized. It differs from the original mono G∧C by a covalent bridging of two individual G∧C modules with a short spacer (Figure 1.25).[87] The self-assembled RNTs from twin G∧C motifs are more stable than those from mono G∧C motifs. This is attributed to the increased (double) number of hydrogen bonds per self-assembling module (12 instead of 6), reduced steric demand and electrostatic repulsion.

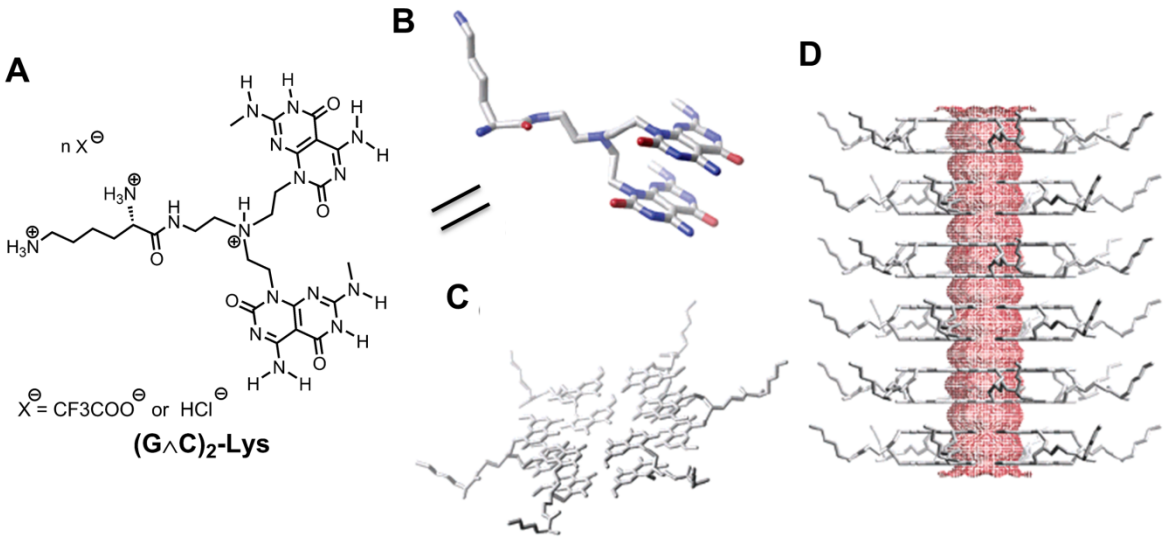

Figure 1.25. (A) Chemical structure of a twin G∧C module **(G∧C)$_2$-Lys**; (B) model of **(G∧C)$_2$-Lys**; (C) model of a rosette of **(G∧C)$_2$-Lys**; (D) model of a **(G∧C)$_2$-Lys** RNT. Figure B–D adapted with permission from Ref. 87 © 2005 American Chemical Society.

Beside the bicyclic system, the G∧C motif was expanded to tricyclic and tetracyclic rings via a synthetic strategy of inserting one or two 6-membered rings between the guanine and cytosine sides of the G∧C motif (Figure 1.26).[88] By extending the core of the G∧C molecule, the inner and outer diameters of the RNTs can be tuned in a range of several angstroms to nanometers. Small molecules such as dexamethasone (a pharmaceutical active ingredient) can be encapsulated in the cavity of the RNTs.[89] All these functionalized RNTs have different applications in nanomedicine,[90] tissue engineering[91] and catalysis[92].

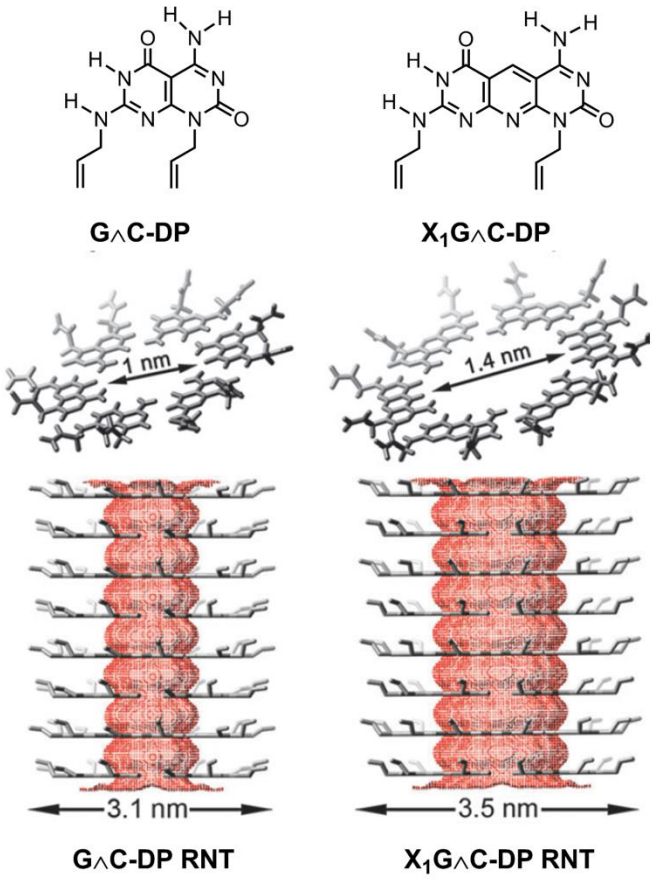

Figure 1.26. Chemical structures of a bicyclic motif **G∧C-DP** and a tricyclic motif **X_1G∧C-DP** and models of corresponding RNTs. Figure adapted with permission from Ref. 88a © 2005 American Chemistry Society.

By far, most of the functionalized G∧C motifs developed in our group were found to form self-assembled RNTs in polar solvents, especially in H_2O, which is beneficial for applications in the fields of health and biology. On the other hand, developing functionalized G∧C building blocks which can form highly ordered nanostructures in low-polarity solvents is highly desired for exploiting the potential application of these materials in organic optoelectronics. In fact, by the time I joined the research group led by Prof.

Fenniri, a few G∧C modules with haloarene substituents had been synthesized by previous colleagues.[85] Recent studies indicate that some of these molecules can form short RNTs and nanofibers in polar organic solvent such as DMSO and DMF, although the solubilities are low (unpublished data included in Zhaoyi Qin's master thesis Sept. 2014). A few alkyl substituted G∧C modules had also been synthesized, and only the G∧C modules bearing a dodecyl tail were found to be able to form well-dispersed RNTs in a nonpolar solvent (cyclohexane).[93] I was intrigued to design and synthesize some novel G∧C building blocks that could form RNTs in low-polarity solvents to explore their potential applications in organic optoelectronics, due to the lack of attempts in this field and the fact that G∧C modules are good scaffolds to pack the photo- and electroactive molecules in well-organized patterns.

1.11 Summary

In this chapter, an overview on the applications of various supramolecular assemblies in the field of organic optoelectronics was preented, with the focus on OPVs and organic semiconductors. As shown in many examples, the nanoscale ordering imposed by the supramolecular assemblies improved the device performance. However, in order to generate self-assembled nanostructures with the desired architecture and geometry, it is imperative that the building blocks are delicately designed. As an emerging field, there is still plenty of room for the utilization of supramolecular chemistry for clean energy and sustainable development.

1.12 References

(1) Tang, C. W.; VanSlyke, S. A. *Appl. Phys. Lett.* **1987**, *51*, 913–915.

(2) Koezuka, H. S.; Tsumuta, A.; Ando, T. *Synth. Met.* **1987**, *18*, 699–704.

(3) O'Regan, B.; Grätzel, M. *Nature* **1991**, *353*, 737–740.

(4) Yu, G.; Gao, J.; Hummelen, J. C.; Wudl, F.; Heeger, A. J.; *Nature* **1995**, *270*, 1789–1791.

(5) "The Nobel Prize in Chemistry 2000". *Nobelprize.org.* Nobel Media AB 2014. http://www.nobelprize.org/nobel_prizes/chemistry/laureates/2000/ (Accessed Oct 10, 2014).

(6) Arias, A. C.; MacKenzie, J. D.; McCulloch, I.; Rivnay, J.; Salleo, A. *Chem. Rev.* **2010**, *110*, 3–24.

(7) Beaujuge, P. M.; Frechet, J. M. *J. Am. Chem. Soc.* **2011**, *133*, 20009–20029.

(8) (a) Würthner, F. *Nat. Chem.* **2014**, *6*, 171–173. (b) Hoeben, F. J. M.; Jonkheijm, P.; Meijer, E. W.; Schenning, A. P. H. J. *Chem. Rev.* **2005**, *105*, 1491−1546.

(9) Elemans, J. A. A. W., van Hameren, R., Nolte, R. J. M.; Rowan, A. E. *Adv. Mater.* **2006**, *18*, 1251–1266.

(10) Brunsveld, L.; Folmer, B. J. B.; Meijer, E. W.; Sijbesma, R. P. *Chem. Rev.* **2001**, *101*, 4071–4097.

(11) (a) Croce, R.; van Amerongen, H. *Nat. Chem. Biol.* **2014**, *10*, 492–501. (b) Scholes, G. D.; Fleming, G. R.; Olaya-Castro, A.; van Grondelle R. *Nature Chem.*, **2011**, *3*, 763–774.

(12) Fassioli, F.; Olaya-Castro, A.; Scheuring, S.; Sturgis, J. N.; Johnson, N. F. *Biophys. J.* **2009**, *97*, 2464–2473.

(13) (a) Mcdermott, G.; Prince, S. M.; Freer, A. A.; Hawthornthwaite-Lawless, A. M.; Paplz, M. Z.; Cogdell, R. J. *Nature*, **1995**, *374*, 517–521. (b) Hong, X.; Weng, Y.-X.; Li, M.

Biophys J. **2004**, *86*, 1082–1088. (c) Cogdell, R. J.; Gall, A.; Köhler, J. *Q. Rev. Biophysics* **2006**, 39, 227–324.

(14) Aguas, H.; Ram, S. K.; Araujo, A.; Gaspar, D.; Vicente, A.; Filonovich, S. A.; Fortunato, E.; Martins, R.; Ferreira, I.; *Energy Environ. Sci.* **2011**, *4*, 4620–4632.

(15) Department of Astronomy, University of Washington. Astronomy 150: Light. http://www.astro.washington.edu/users/smith/Astro150/Tutorials/EM/ (accessed Oct 10, 2014.)

(16) (a) Richards, B. S. *Sol. Energy Mater. Sol. Cells* **2006**, *90*, 2329–2337. (b) Huang, X.; Han, S.; Huang, W.; Liu, X. *Chem. Soc. Rev.* **2013**, *42*, 173–201.

(17) Shockley, W.; Queisser, H. J. *J. Appl. Phys.* **1961**, *32*, 510–519.

(18) Goetzberger, A.; Hebling, C.; Schock, H.-W. *Mater. Sci. Eng. R-Rep.* **2003**, *40*, 1–46.

(19) (a) Li, C.; Liu, M.; Pschirer, N. G.; Baumgarten, M.; Müllen, K. *Chem. Rev.* **2010**, *110*, 6817–6855. (b) Thompson, B. C.; Fréchet, J. M. J. *Angew. Chem., Int. Ed.* **2008**, *47*, 58–77.

(20) Spanggaard, H.; Krebs, F. C. *Sol. Energy Mater. Sol. Cells* **2004**, *83*, 125−146.

(21) Brabec, C. J.; Winder, C.; Sariciftci, N. S. Hummelen, J. C.; Dhanabalan, A.; van Hal, P. A.; Janssen, R. A. J. *Adv. Funct. Mater.* **2002**, *12*, 709−712.

(22) Clarke, T. M.; Durrant, J. R. *Chem. Rev.* **2010**, *110*, 6736–6767.

(23) (a) Choi, J. K.; Jin, M. L.; An, C. J.; Kim, D. W.; Jung, H.-T. *ACS Appl. Mater. Interfaces* **2014**, *6*, 11047–11053. (b) Cao, Y.; Yu, G.; Zhang, C.; Menon, R.; Heeger, A. J. *Synth. Met.* **1997**, *87*, 171–174.

(24) Sun, Y.; Takacs, C. J.; Cowan, S. R.; Seo, J. H.; Gong, X.; Roy, A.; Heeger, A. J. *Adv. Mater.* **2011**, *23*, 2226–2230.

(25) (a) Gao, Y. Interface Electronic Structure and Organic Photovoltaic Devices. In *Optical Science and Engineering*; Sun, S.-S. and Sariciftci, N. S. Eds.; CRC Press: Boca Raton, FL, 2005; Vol. 99, pp 421–448. (b) Hau, S. K.; Yip, H.-L.; Acton, O.; Baek, N. S.; Ma, H.; Jen, A. K.-Y. *J. Mater. Chem.* **2008**, *18*, 5113–5119. (c) Ahlswede, E.; Hanisch, J.; Powalla, M. *Appl. Phys. Lett.* **2007**, *90*, 163504.

(26) (a) Brédas, J.-L.; Norton, J. E.; Cornil, J.; Coropceanu, V. *Acc. Chem. Res.* **2009**, *42*, 1691–1699. (b) Brabec, C. J.; Dyakonov, V.; Parisi, J.; Sariciftci, N. S. *Organic Photovoltaics: Concepts and Realization* 1st ed.; Springer-Verlag: Berlin, 2003.

(27) Nelson, R. C. *J. Opt. Soc. Am.* **1956**, *46*, 13–16.

(28) Tang, C. W. *Appl. Phys. Lett.* 1986, *48*, 183–185.

(29) McGehee, M. D.; Topinka, M. A. *Nat. Mater.* **2006**, 5, 675–676.

(30) Brabec, C. J.; Sariciftci, N. S.; Hummelen, J. C. *Adv. Funct. Mater.* **2001**, *11*, 15−26.

(31) (a) Li, G.; Zhu, R.; Yang, Y. *Nat. Photonics* **2012**, 6, 153–161. (b) Sista, S.; Park, M.-H.; Hong, Z.; Wu, Y.; Hou, J.; Kwan, W. L.; Li, G.; Yang, Y. *Adv. Mater.* **2010**, *22*, 380–383. (c) Kim, J. Y.; Lee, K.; Coates, N. E.; Moses, D.; Nguyen, T.-Q.; Dante, M.; Heeger, A. J. *Science* **2007**, *317*, 222−225. (d) Dennler, G.; Scharber, M. C.; Brabec, C. J. *Adv. Mater.* **2009**, *21*, 1323–1338.

(32) Ostroverkhova, O. *Handbook of Organic Materials for Optical and (Opto)Electronic Devices: Properties and Applications* 1st ed.; Woodhead Publishing Limited: Cambridge, UK, 2013.

(33) (a) Zhao, G.; He, Y.; Li, Y. *Adv. Mater.* **2010**, *22*, 4355–4358. (b) Chen, Li.-M.; Hong, Z.; Li, G.; Yang, Y. *Adv. Mater.* **2009**, *21*, 1434–1449.

(34) (a) Wienk, M. M.; Kroon, J. M.; Verhees, W. J. H.; Knol, J.; Hummelen, J. C.; van Hal, P. A.; Janssen, R. A. J. *Angew. Chem., Int. Ed.* **2003**, *42*, 3371–3375. (b) Brabec, C. J.; Shaheen, S. E.; Winder, C.; Sariciftci, N. S.; Denk, P. *Appl. Phys. Lett.* **2002**, *80*, 1288–1290.

(35) Liang, Y.; Wu, Y.; Feng, D.; Tsai, S. T.; Son, H. J.; Li, G.; Yu, L. *J. Am. Chem. Soc.* **2009**, *131*, 56–57.

(36) Chen, H.-Y.; Hou, J.; Zhang, S.; Liang, Y.; Yang, G.; Yang, Y.; Yu, L.; Wu, Y.; Li, G. *Nat. Photonics* **2009**, *3*, 649–653.

(37) Blouin, N.; Michaud, A.; Leclerc, M. *Adv. Mater.* **2007**, *19*, 2295–2300.

(38) Park, S. H.; Roy, A.; Beaupre, S.; Cho, S.; Coates, N.; Moon, J. S.; Moses, D.; Leclerc, M.; Lee, K.; H., A. J. *Nat. Photonics* **2009**, *3*, 297–302.

(39) Sakai, J.; Taima, T.; Saito, K. *Org. Electron.* **2008**, *9*, 582–590.

(40) Liu, Y.; Zhou, J.; Wan, X.; Chen, Y. *Tetrahedron* **2009**, 65, 5209–5215. (b) Yin, B.; Yang, L.; Liu, Y.; Chen, Y.; Qi, Q.; Zhang, F.; Yin, S. *Appl. Phys. Lett.* **2010**, 97, 023303.

(41) Matsuo, Y.; Sato, Y.; Niinomi, T.; Soga, I.; Tanaka, H.; Nakamura, E. *J. Am. Chem. Soc.* **2009**, *131*, 16048–16050.

(42) Yoo, S.; Domerq, B.; Kippelen, B. *Appl. Phys. Lett.* **2004**, *85*, 5427–5429.

(43) Sariciftci, N. S.; Smilowitz, L.; Heeger, A. J.; Wudl, F. *Science* **1992**, *258*, 1474–1476.

(44) Hummelen, J. C.; Knight, B. W.; LePeq, F.; Wudl, F.; Yao, J.; Wilkins, C. L. *J. Org. Chem.* **1995**, *60*, 532–538.

(45) (a) He, Y.; Li, Y. *Phys. Chem. Chem. Phys.* **2011**, *13*, 1970–1983. (b) Li, C.-Z.; Yip, H.-L.; Jen, A. K. Y. *J. Mater. Chem.* 2012, *22*, 4161–4177.

(46) He, Y.; Chen, H.-Y.; Hou, J.; Li, Y. *J. Am. Chem. Soc.* **2010**, *132*, 1377–1382.

(47) Kim, I.; Haverinen, H. M.; Wang, Z. X.; Madakuni, S.; Li, J.; Jabbour, G. E. *Appl. Phys. Lett.* **2009**, *95*, 023305.

(48) Camaioni, N.; Ridolfi, G.; Fattori, V.; Favaretto, L.; Barbarella, G. *Appl. Phys. Lett.* **2004**, *84*, 1901–1903.

(49) Sonar, P.; Ng, G.-M.; Lin, T. T.; Dodabalapur, A.; Chen, Z.-K. *J. Mater. Chem.* **2010**, *20*, 3626–3636.

(50) Brunetti, F. G.; Gong, X.; Tong, M.; Heeger, A. J.; Fred, W. *Angew. Chem., Int. Ed.* **2010**, *49*, 532–536.

(51) Zhou, T.; Jia, T.; Kang, B.; Li, F.; Fahlman, M.; Wang, Y. *Adv. Energy Mater.* **2011**, *1*, 431–439.

(52) Roncali, J. *Adv. Energy Mater.* **2011**, *1*, 147–160.

(53) Loi, M. A.; Denk, P.; Hoppe, H.; Neugebauer, H.; Winder, C.; Meissner, D.; Brabec, C.; Sariciftci, N. S.; Gouloumis, A.; Vazquez P.; Torres, T. *J. Mater. Chem.* **2003**, *13*, 700–704.

(54) Tan, Z.; Hou, J.; He, Y.; Zhou, E.; Yang, C.; Li, Y. *Macromolecules* **2007**, *40*, 1868–1873.

(55) Lin, Y. Z.; Li, Y. F.; Zhan, X. W. *Chem. Soc. Rev.* **2012**, *41*, 4245–4272.

(56) Martínez-Díaz, M. V.; de la Torre, G.; Torres, T. *Chem. Commun.* **2010**, *46*, 7090–7108.

(57) Dang, M. T.; Hirsch, L.; Wantz, G.; Wuest, J. D. *Chem. Rev.* **2013**, 113, 3734–3765.

(58) (a) Vanlaeke, P.; Swinnen, A.; Haeldermans, I.; Vanhoyland, G.; Aernouts, T.; Cheyns, D.; Deibel, C.; D'Haen, J.; Heremans, P.; Poortmans, J.; Manca, J. V. *Sol. Energy Mater.*

Sol. Cells **2006**, *90*, 2150–2158. (b) Chen, D.; Nakahara, A.; Wei, D.; Nordlund, D.; Russell, T. P. *Nano Lett.* **2011**, *11*, 561–567.

(59) (a) Hiorns, R. C.; De Bettignies, R.; Leroy, J.; Bailly, S.; Firon, M.; Sentein, C.; Khoukh, A.; Preud'homme, H.; Dagron-Lartigau, C. *Adv. Funct. Mater.* **2006**, *16*, 2263–2273. (b) Nguyen, L. H.; Hoppe, H.; Erb, T.; Günes, S.; Gobsch, G.; Sariciftci, N. S. *Adv. Funct. Mater.* **2007**, *17*, 1071–1078.

(60) (a) Yang, X. N.; Loos, J.; Veenstra, S. C.; Verhees, W. J. H.; Wienk, M. M.; Kroon, J. M.; Michels, M. A. J.; Janssen, R. A. J. *Nano Lett.* **2005**, *5*, 579–583. (b) Babel, A.; Jenekhe, S. A. *Synth. Met.* **2005**, *148*, 169–173.

(61) Xin, H.; Kim, F. S.; Jenekhe, S. A. *J. Am. Chem. Soc.* **2008**, *130*, 5424–5425.

(62) Sun, Y.; Welch, G. C.; Leong, W. L.; Takacs, C. T.; Bazan, G. C.; Heeger, A. J. *Nat. Mater.* **2012**, *11*, 44–48.

(63) Schenning, A. P. H. J.; Meijer, E. W. *Chem. Commun.* **2005**, *26*, 3245–3258.

(64) Hasobe, T.; Saito, K.; Kamat, P. V.; Troiani, V.; Qiu, H.; Solladié, N.; Kim, K. S.; Park, J. K.; Kim, D.; D'Souza, F.; Fukuzumi, S. *J. Mater. Chem.* **2007**, *17*, 4160–4170.

(65) Kumar, R. J.; MacDonald, J. M.; Singh, T. B.; Waddington, L. J.; Holmes, A. B. *J. Am. Chem. Soc.* **2011**, *133*, 8564–8573.

(66) Wang, P.; Yao, K.; Chen, L.; Chen, Y.; Li, F.; Wang, H.; Yu, S. *Sol. Energy Mater. Sol. Cells* **2012**, *97*, 34–42.

(67) Bu, L.; Guo, X.; Yu, B.; Qu, Y.; Xie, Z.; Yan, D.; Geng, Y.; Wang, F. *J. Am. Chem. Soc.* **2009**, *131*, 13242–13243.

(68) Charvet, R.; Yamamoto, Y.; Sasaki, T.; Kim, J.; Kato, K.; Takata, M.; Saeki, A.; Seki, S.; Aida, T. *J. Am. Chem. Soc.* **2012**, *134*, 2524–2527.

(69) Tu, S. Y.; Kim, S. H.; Joseph, J.; Modarelli, D. A.; Parquette, J. R. *J. Am. Chem. Soc.* **2011**, *133*, 19125–19130.

(70) Schmidt-Mende, L.; Fechtenkötter, A.; Müllen, K.; Moons, E.; Friend, R. H.; MacKenzie, J. D. *Science* **2001**, *293*, 1119–1122.

(71) Yamamoto, Y.; Zhang, G. X.; Jin, W. S.; Fukushima, T.; Ishii, N.; Saeki, A.; Seki, S.; Tagawa, S.; Minari, T.; Tsukagoshi, K.; Aida, T. *Proc. Natl. Acad. Sci. U.S.A.* **2009**, *106*, 21051–21056.

(72) (a) Sirringhaus, H.; Tessler, N.; Friend, R. H. *Science* **1998**, *280*, 1741–1744. (b) Sirringhaus, H.; Brown, P. J.; Friend, R. H.; Nielen, M. M.; Bechgaard, K.; Langeveld-Voss, B. M. W.; Spiering, A. J. H.; Janssen, R. A. J.; Meijer, E. W.; Herwig, P.; de Leeuw, D. M. *Nature*, **1999**, *401*, 685−688.

(73) Sengupta, S.; Ebeling, D.; Patwardhan, S.; Zhang, X.; von Berlepsch, H.; Böttcher, C.; Stepanenko, V.; Uemura, S.; Hentschel, C.; Fuchs, H.; Grozema, F. C.; Siebbeles, L. D. A.; Holzwarth, A. R.; Chi, L.; Würthner, F. *Angew. Chem., Int. Ed.* **2012**, *51*, 6378–6382.

(74) Stone, D. A.; Tayi, A. S.; Goldberger, J. E.; Palmer, L. C.; Stupp, S. I. *Chem. Commun.* **2011**, *47*, 5702–5704.

(75) Tsujimura, T. *OLED Display Fundamentals and Applications* 1st ed.; Wiley: Hoboken, USA, 2012.

(76) Buckley, A. *Organic Light-Emitting Diodes (OLEDs): Materials, Devices and Applications* 1st ed.; Woodhead Publishing Limited: Cambridge, UK, 2013.

(77) Abbel, R.; Grenier, C.; Pouderoijen, M. J.; Stouwdam, J. W.; Leclère, P. E. L. G.; Sijbesma, R. P.; Meijer, E. W.; Schenning, A. P. H. J. *J. Am. Chem. Soc.* **2009**, *131*, 833–843.

(78) Boylestad, R. L.; Nashelsky, L. *Electronic Devices and Circuit Theory* 10th ed.; Upper Saddle River, USA, 2009.

(79) Hu, W.; Bai, F.; Xiong, G.; Zhan, X.; Fu, H.; Bjornholm, T. *Organic optoelectronics* 1st ed.; Wiley-VCH: Weinheim, Germany, 2013.

(80) Busseron, E.; Ruff, Y.; Moulin, E.; Giuseppone, N. *Nanoscale* **2013**, 5, 7098–7140.

(81) Marsh, A.; Silvestri, M.; Lehn, J.-M. *Chem. Commun.* **1996**, *13*, 1527–1528.

(82) Fenniri, H.; Mathivanan, P.; Vidale, K. L.; Sherman, D. M.; Hallenga, K.; Wood, K. V.; Stowell, J. G. *J. Am. Chem. Soc.* **2001**, *12*, 3854–3855.

(83) (a) Fenniri, H.; Deng, B.-L.; Ribbe, A. E. *J. Am. Chem. Soc.* **2002**, *124*, 11064–11072. (b) Zhang, L. J.; Rodriguez, J.; Raez, J.; Myles, A. J.; Fenniri, H.; Webster, T. J. *Nanotechnology* **2009**, *20*¸175101.

(84) Fenniri, H.; Deng, B.-L.; Ribbe, A. E.; Hallenga, K.; Jacob, J.; Thiyagarajan, O. *Proc. Natl. Acad. Sci. U.S.A.* **2002**, *99*, 6487–6492.

(85) Beingessner, R. L.; Deng, B.-L.; Fanwick, P. E.; Fenniri, H. *J. Org. Chem.* **2008**, *73*, 931–939.

(86) Hemraz, U. D.; El-Bakkari, M.; Yamazaki, T.; Cho, J.-Y.; Beingessner, R. L.; Fenniri, H. *Nanoscale* **2014**, *6*, 9421–9427.

(87) Moralez, J.; Raez, J.; Yamazaki, T.; Motkuri, R.; Kovalenko, A.; Fenniri, H. *J. Am. Chem. Soc.* **2005**, *127*, 8307–8309.

(88) Borzsonyi, G.; Johnson, R. S.; Myles, A. J.; Cho, J. Y.; Yamazaki, T.; Beingessner, R. L.; Kovalenko, A.; Fenniri, H. *Chem. Commun*. **2010**, *46*, 6527–6529. (b) Borzsonyi, G.; Alsbaiee, A.; Beingessner, R. L.; Fenniri, H. *J. Org. Chem.* **2010**, *75*, 7233–7239.

(89) Chen, Y. P.; Song, S.; Yan, Z. M.; Fenniri, H.; Webster, T. J. *Int. J. Nanomedicine* 2011, *6*, 1035–1044.

(90) (a) Suri, S. S.; Rakotondradany, F.; Myles, A. J.; Fenniri, H.; Singh, B. *Biomaterials* **2009**, *30*, 3084–3090. (b) Journeay, W. S.; Suri, S. S.; Moralez, J. G.; Fenniri, H.; Singh, B. *Small*, **2009**, *5*, 1446–1452. (c) Farah, A. A.; Bravo-Vasquez, J. P.; Alvarez-Puebla R. A.; Cho, J.-Y.; Fenniri, H. *Small* **2009**, *5*, 1283–1286. (d) Chen, Y.; Song, S.; Yan, Z.; Fenniri, H.; Webster, T. J. *Int. J. Nanomed.* **2011**, *6*, 101–107.

(91) (a) Zhang, L.; Ramsaywack, S.; Fenniri, H.; Webster, T. J. *Tissue Eng. Pt. A* **2008**, *14*, 1353–1364. (b) Zhang, L.; Rakotondradany, F.; Myles, A. J.; Fenniri, H.; Webster, T. J. *Biomaterials* **2009**, *30*, 1309–1320. (c) Chun, A. L.; Moralez, J. G.; Webster, T. J.; Fenniri, H. *Biomaterials* **2005**, *26*, 7304–7309.

(92) Chhabra, R.; Moralez, J. G.; Raez, J.; Yamazaki, T.; Cho, J.-Y.; Myles, A. J.; Kovalenko, A.; Fenniri, H. *J. Am. Chem. Soc.* **2010**, *132*, 32–33.

(93) (a) Tikhomirov, G.; Yamazaki, H.; Kovalenko, A.; Fenniri, H. *Langmuir* **2008**, *24,* 4447–4450. (b) Tikhomirov, G.; Oderinde, M.; Makeiff, D.; Mansouri, A.; Weibing, L.; Heirtzler, F. R.; Kwok, D. Y.; Fenniri, H. *J. Org. Chem.* **2008**, *73*, 4248–4251.

Chapter 2

Design, Synthesis and Self-Assembly of Porphyrin-Functionalized Guanine–Cytosine Building Blocks

2.1 Introduction

Porphyrins are a group of organic π-conjugated macrocycles. The parent molecule of all porphyrins is porphin, which is comprised of four pyrrole subunits interconnected by four methine bridges. The positions of the methine groups are commonly labeled as the *meso* carbons (5, 10, 15, 20) (Figure 2.1A). The inner conjugation path contains 16 carbon and 2 nitrogen atoms. Each of these contributes one π electron for a total of 18 electrons, which follows Hückel's rule of aromaticity. All bonds in the conjugation path have a fixed length of 0.136-0.137 nm.[1] From a synthetic prospective, porphin is difficult to prepare and almost insoluble in all solvents, because of the endless molecular stacks of the planar macrocycles.

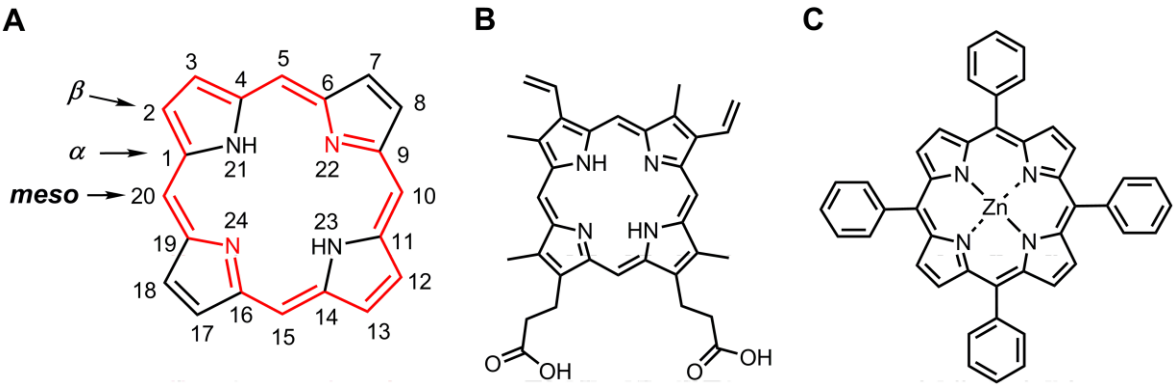

Figure 2.1. Molecular structures of (A) porphin, (B) protoporphyrin IX and (C) zinc-(5,10,15,20)-tetraphenylporphyrin.

For the natural porphyrins in biological systems such as protoporphyrin IX (Figure 2.1B), the substituents mostly occur on the β carbons of the pyrrole rings. Vinyl and propionic acid are the two typical active substituents that can be extended to longer side chains, or covalently connected to protein scaffolds.[2] In synthetic porphyrins, *meso* carbons are the most accessible sites for introducing substituents. Mono-, di-, tri- or tetra-substituted porphyrins can be simply obtained via the one-pot synthesis of specific pyrrole derivatives and aldehydes under different reaction conditions. Among them, *meso*-tetraphenylporphyrins (TPPs) are the most favored porphyrins (Figure 2.1C), mainly on account of the ease of synthesis and diverse functionality of the phenyl rings. In addition, the substituted phenyl rings are positioned at a dihedral angle to the plane of porphin macrocycle.[3] Hence the extended functional groups can be in, above, or below the porphin plane.[1] The free rotation of all four phenyl rings largely improves the solubility and reduces intermolecular stacking.

Another fascinating aspect of porphyrin is that the two NH protons can be replaced by almost all the metal ions in the periodic table. The metal-containing form is called metalloporphyrin or a porphyrin metal salt. For example, magnesium and iron are ubiquitous in the natural porphyrins, from the photoreceptor chlorophylls in the natural light-harvesting complexes, to the oxygen-transporter hemes in the hemoglobin of mammals. It must be pointed out that none of the porphyrins alone could function without the associated protein scaffolds and the environments in the biological systems. In addition, the two basic pyrrole N bearing a lone pair in porphyrins are feasible to form the acid form upon protonation. There are two acid forms which are called porphyrin diacid and monoacid, depending on the number of protons abstracted by pyrrole nitrogen atoms.

Although the two nitrogen atoms have a similar basicity,[4] a few studies have claimed that porphyrin monoacid may exist.[5] However, few direct characteristics were discussed, as the monoacids are unstable and difficult to isolate. In particular, for *meso*-substituted porphyrins, a one-step protonation occurs simultaneously to give the diacids without any detectable intermediates, since the addition of a second proton is energetically favored.[6] The porphyrin diacid differs from the free base form by a saddle-distorted geometry of the porphin core.[7]

The absorption spectra of all free base porphyrins feature an extremely strong band in the near ultraviolet region, called the Soret band, and four moderate bands in the visible region, called the Q bands. These bands originate from the singlet-singlet or triplet-singlet π–π^* transitions. In C=O substituted porphyrins, n–π^* transition may arise. Introducing a metal ion or protons to the porphyrin leads to changes in the band intensity and location. The number of Q bands also decreases, due to the change in degree of molecular symmetry.[8] Substituents, counterions and aggregation also change the absorption properties of porphyrins, especially the wavelength of the absorption maxima.[9] Many porphyrins can form ordered aggregates.[10] In general, the bathochromic shift (red shift) of the absorption bands upon dye self-organization is attributed to J-type aggregation, and H-type aggregation commonly leads to hypsochromic shift (blue shift) of the bands.[11]

Porphyrins have been intensively studied over a wide range of applications in the fields of photodynamic therapy,[12] catalysis,[13] molecular device[14] and organic photovoltaics (OPVs).[15] Among these, highly ordered porphyrin arrays at the nanoscale level attract a great deal of attention, since many of them display interesting electronic and optoelectronic properties. This chapter focuses on the design, synthesis and self-assembly studies of three

porphyrin-functionalized guanine-cytosine molecules **G∧C-Por 1**, **(G∧C)$_2$-Por 2** and **(G∧C)$_2$-Por 3** (Figure 2.2), which are semiconductors and potential electron-donor materials for solution-processed OPV devices. The optoelectronic properties of these porphyrin-functionalized RNTs are discussed in Chapter 3.

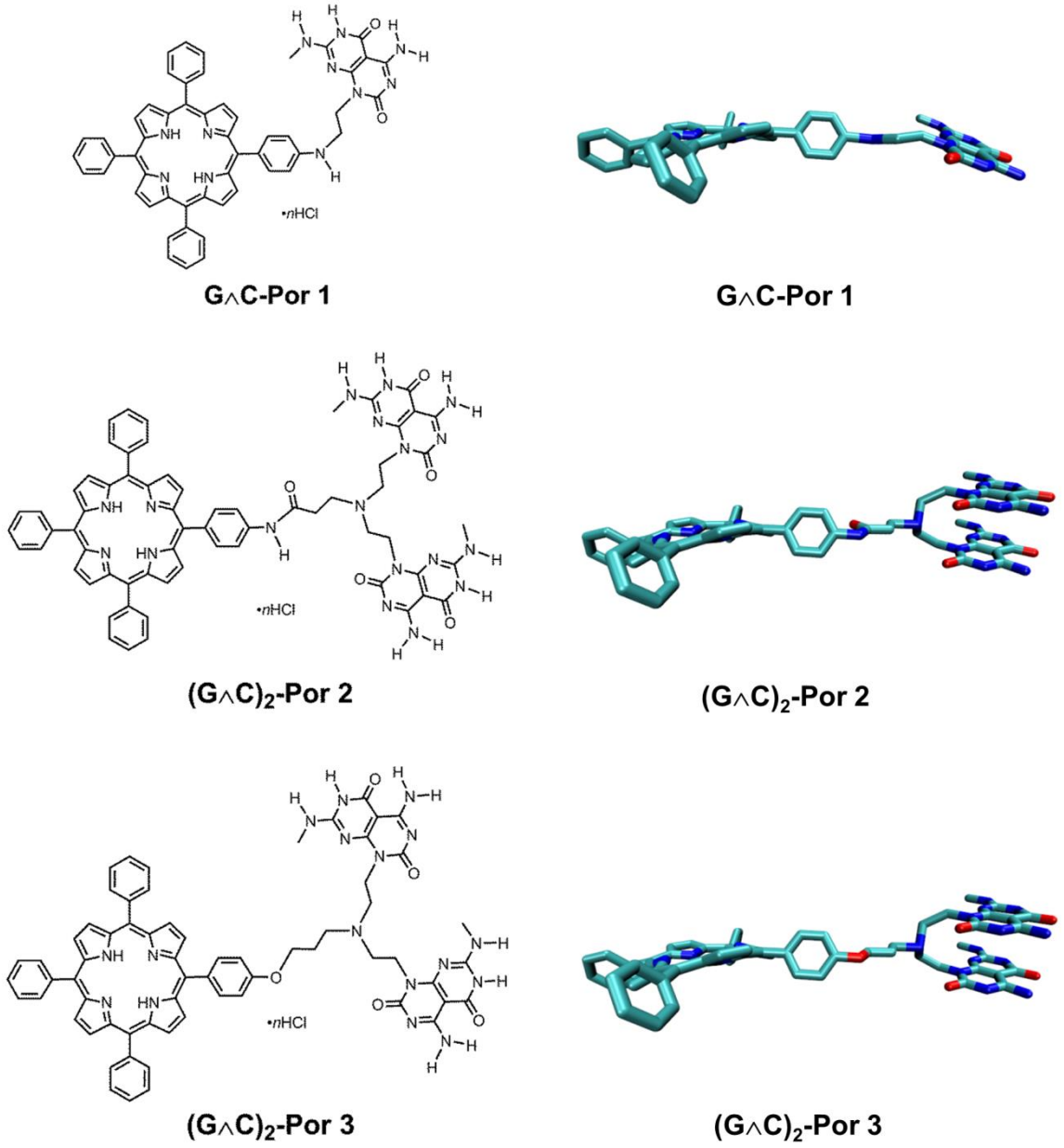

Figure 2.2. Molecular structures and models of **G∧C-Por 1**, **(G∧C)$_2$-Por 2** and **(G∧C)$_2$-Por 3**.

2.2 Strategies for building one-dimensional porphyrin arrays

Although the light-harvesting complexes can be isolated and analyzed, they cannot be copied in the laboratories. On the other hand, artificial 1D porphyrin arrays could be built by different strategies, including axial metalloporphyrin coordination,[16] porphyrin ionic self-assembly,[17] and attaching the chromophores to a scaffold via covalent bond or non-covalent interaction.[18] These arrays demonstrate unique optoelectronic properties, resulting from the special arrangements of porphyrins in close proximity.

Among various types of scaffolds such as peptides,[18a-b] single-walled carbon nanotubes (SWNT),[18c] DNA[18d] and polymer surfactants,[18e] a building block that can form bottom-up hierarchical self-assembly by noncovalent intermolecular interactions (e.g. hydrogen bonding,[18f] electrostatic interactions,[17] hydrophobic interaction,[18g-h] π–π stacking[18f,i] and host/guest interaction[18j]) represents an emerging approach that can advance the process of building 1D porphyrin arrays. The advantages of this approach include i) relatively easy preparation of the building block, ii) commanded self-assembly with precise programming from a molecular level, iii) generation of the most thermodynamically stable supramolecular nanostructure, and iv) compatibility in favor of solution-processed devices. However, in order to generate self-assembled nanostructures with the desired architecture and geometry, it is imperative that the monomer building blocks are delicately designed.

2.3 Synthesis of G∧C-Por 1

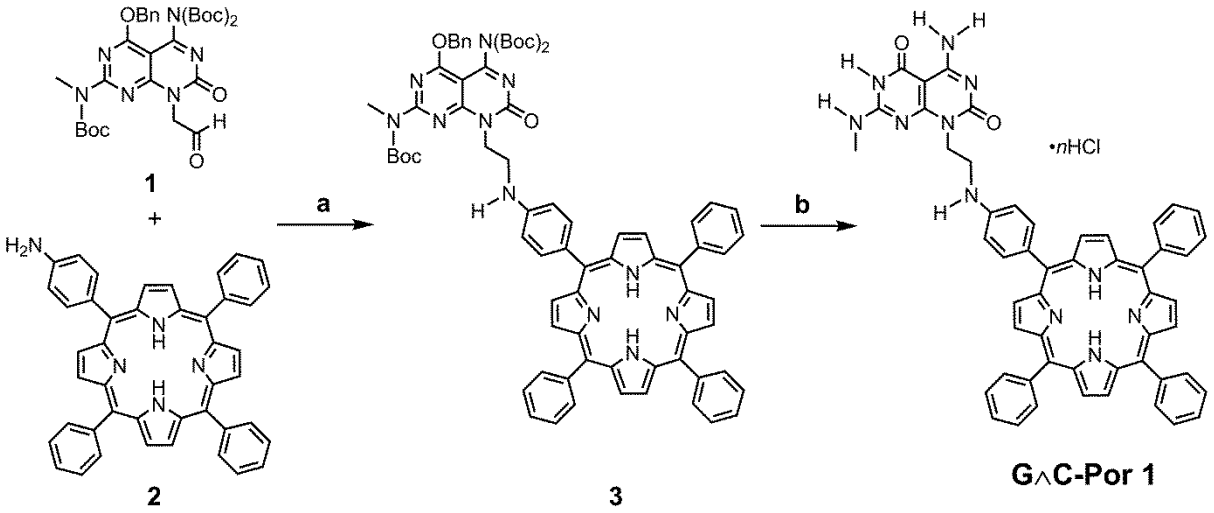

Figure 2.3. Synthesis Route of **G∧C-Por 1**. Reagents and conditions: (a) $NaBH(OAc)_3$, 1,2-DCE, 25 °C, 7 d, 40%; (b) HCl (4 M in 1,4-dioxane), 80 °C, 4 h, quantitative yield.

G∧C aldehyde **1** was synthesized following a 12-step route as previously reported with an overall yield 8.8%.[19] 5,10,15,20-tetraphenylporphyrin was applied to nitration with $NaNO_2$ in TFA, and then reduced by $SnCl_2•2H_2O$ in concentrated hydrochloric acid. 5-(4-aminophenyl)-10,15,20-triphenylporphyrin (ATPP) **2** was obtained after work-up and column chromatography with an overall yield 39%.[20] As shown in Figure 2.3, G∧C aldehyde **1** and ATPP **2** were treated with $NaBH(OAc)_3$, which is an mild reducing agent in the reductive amination reaction.[21] Triethylamine and DIPEA were avoided as they are detrimental to this reaction and normally lead to low yield. Although porphyrin **2** is a primary amine, the di-alkylated product was not observed even under the condition of a significant excess amount of $NaBH(OAc)_3$. This is mainly due to the low nucleophilicity of the amino group on the benzene ring (aniline). For this reason, only the porphyrin-mono

G∧C motif **3** was obtained as the product (Figure 2.3). The purification of **3** was a challenge. The column chromatography with silica gel led to decomposition, as the compounds with a loss of one or two Boc protecting groups were identified in the fractions. In addition, the color of **3** gradually changed from claret-red to deep green after being loaded to the stationary phase, indicating the protonation occurred on the pyrrole NH of the porphyrin unit. Adding mobile phase modifiers such as triethylamine did not improve the separation. Neutral and basic alumina were then chosen as the stationary phase. They worked well but needed to be deactivated to Brockmann II or III grade. **G∧C-Por 1** was obtained quantitatively after the deprotection of **3** in HCl (4 M in 1,4-dioxane) and work-up. The TFA salt of **G∧C-Por 1** was also obtained either by using TFA and thioanisole in the deprotection reaction, or by dissolving **G∧C-Por 1** in TFA for anion exchanging. **G∧C-Por 1** is a green solid, whereas **G∧C-Por 1** (TFA) is a dark brown solid.

2.4 Self-Assembly of G∧C-Por 1 (TFA)

The solubility of **G∧C-Por 1** (TFA) is poor in most common solvents such as DCM, acetone and DMF. Fibers were found in the amber aqueous solution at a concentration of 0.02 mM by SEM (Figure 2.4A), and amorphous aggregates were present in the brown 1,2-DCB suspension (Figure 2.4B). **G∧C-Por 1** (TFA) becomes soluble when it is heated in DCM and $MeNO_2$ at a low concentration. Large sheet-form layers were observed in DCM (Figure 2.4C), and tubular bundles were present in $MeNO_2$ (Figure 2.4D). **G∧C-Por 1** (TFA) can be freely dissolved in MeOH to form a dark brown solution. Small round-shape and worm-shape aggregates were found in the fresh solution by SEM (Figure 2.4E). However, the solution formed a precipitate over time. Large aggregates were observed in the MeOH solution aged for 2 h (Figure 2.4F). Although different processing conditions were examined on this compound, well dispersed RNTs could not be obtained. With regard to building well-organized 1D porphyrin arrays, **G∧C-Por 1** (TFA) is not suitable.

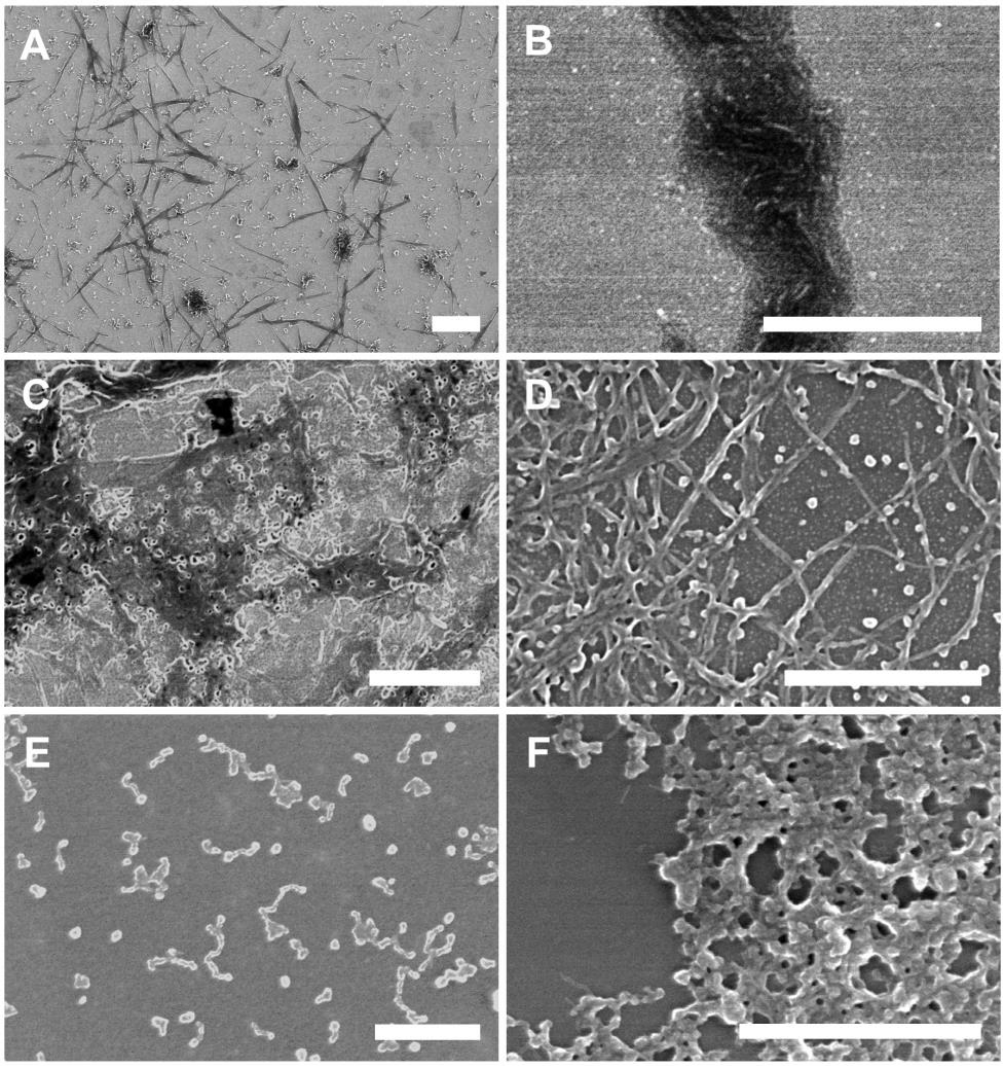

Figure 2.4. SEM images of **G∧C-Por 1** (TFA) in different solvents. (A) H_2O; (B) 1,2-DCB; (C) DCM; (D) $MeNO_2$; (E) MeOH (fresh solution); (F) MeOH (2h aging). Concentration: A–C, 0.02 mM; D, 0.05 mM; E–F, 0.1 mM. Condition: all samples were applied to sonication for 1 min; B and D were heated at 100 °C and 70 °C for 3 min respectively; A–D were aged for 24 h. Scale bars: 500 nm.

2.5 Self-Assembly of G∧C-Por 1

2.5.1 Optimization of the self-assembly conditions

G∧C-Por 1 has a similar solubility as the TFA salt in H_2O, 1,2-DCB and DCM. No single RNTs were observed in these solutions by SEM. Small particles were found in a hot fresh MeOH solution, and large aggregates with a clean background were seen in the SEM image as the precipitate formed with aging (Figure 2.5).

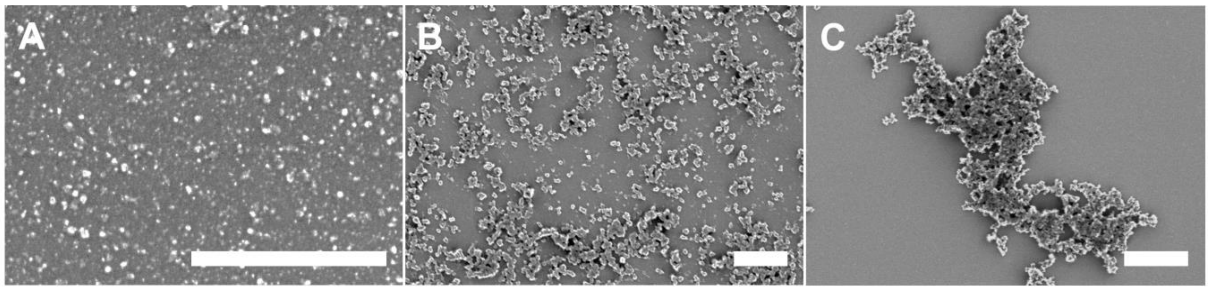

Figure 2.5. SEM images of **G∧C-Por 1** (0.1 mM in MeOH) at different aging time. (A) Fresh hot solution after heating at 60 °C for 3 min; (B) solution at 25 °C after 10 min aging; (C) solution at 25 °C after 2 h aging. Scale bars: 500 nm.

In $MeNO_2$, **G∧C-Por 1** can be gradually dissolved after repeated cycles of sonication and gentle heating (< 70°C) to form a green solution at a maximum concentration of 0.5 mM. SEM images of this solution show tubular architectures after 1 h of aging, which remained stable in solution at room temperature over a period of 1 year (Figure 2.6). The solution was clear and did not form a precipitate. The length of the RNTs varies from a few hundred nanometers to tens of micrometers, depending on aging time and cycles of sonication and heating.

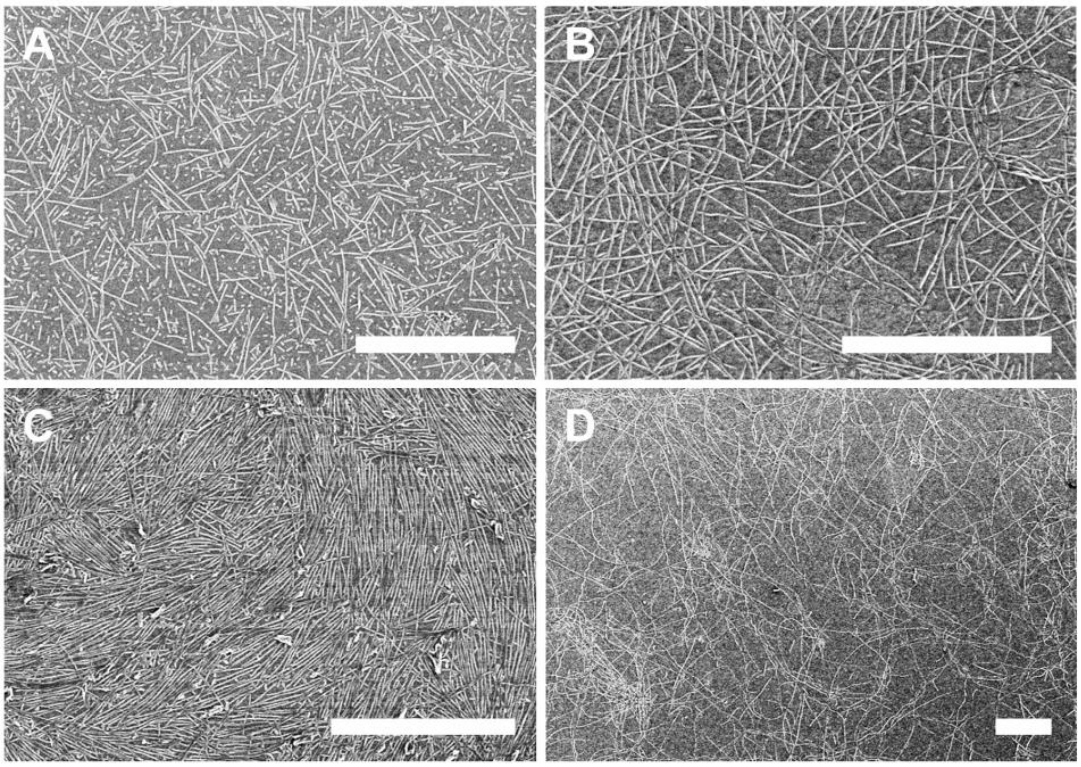

Figure 2.6. SEM images of **G∧C-Por 1** RNTs (0.16 mM in $MeNO_2$) at different aging times. (A) 1 h; (B) 6 h; (C) 21 d; (D) 450 d. Self-assembly condition: alternate sonication (30 s × 3) and heating (50 °C, 2 min × 3). Scale bars: 1 μm.

Alternating between sonication and heating is crucial to the formation of the RNTs. Under the condition of sonication only, the solubility of **G∧C-Por 1** in $MeNO_2$ is limited up to 0.1 mM, and the self-assembly process of **G∧C-Por 1** is very slow (Figure 2.7A). The RNTs are short even after a period of aging for 30 d. Gentle heating (< 70°C) without sonication does not improve the solubility, and only produces short RNTs and bundles (Figure 2.7B). Although heating at a higher temperature could improve the solubility, the color of the solution changed from green to dark green. SEM images show only amorphous particles in this solution (Figure 2.7C).

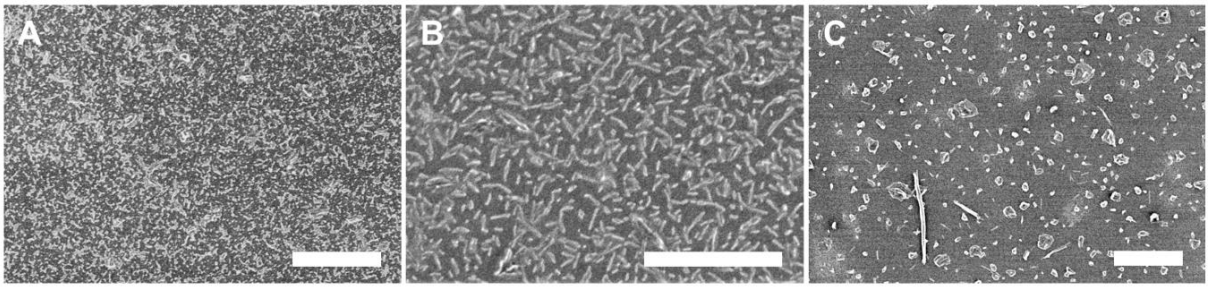

Figure 2.7. SEM images of **G∧C-Por 1** (0.1 mM in $MeNO_2$) processed under different conditions. (A) sonication at 25 °C for 20 min; (B) heating at 55 °C for 30 min; (C) heating at 90 °C for 5 min. Aging: 3 d. Scale bars: 500 nm.

2.5.2 Control studies of the self-assembly

Since some well-established ionic porphyrins can form self-organized tubular architectures,[17] the observed nanotubes of **G∧C-Por 1** by SEM need to be identified. Herein 5-(4-aminophenyl)-10,15,20-triphenylporphyrin hydrochloride (**ATPP-HCl**) was used as a control. It can be prepared by dissolving the free base of 5-(4-aminophenyl)-10,15,20-triphenylporphyrin in HCl (4 M in 1,4-dioxane) followed by work-up in the same manner used to synthesize **G∧C-Por 1**. **ATPP-HCl** is a green flaky solid, whereas **G∧C-Por 1** is a powder.

A $MeNO_2$ solution of **ATPP-HCl** was applied to repeated cycles of sonication and gentle heating, just in the same manner that **G∧C-Por 1** was processed. The SEM images show only a few amorphous aggregates, even after the solution was aged for 7 d (Figure 2.8). This suggests that the observed tubular architectures in the case of **G∧C-Por 1** are due to the self-assembly of the G∧C motif, rather than the ionic assembly or hydrophobic interactions of the porphyrin molecules.

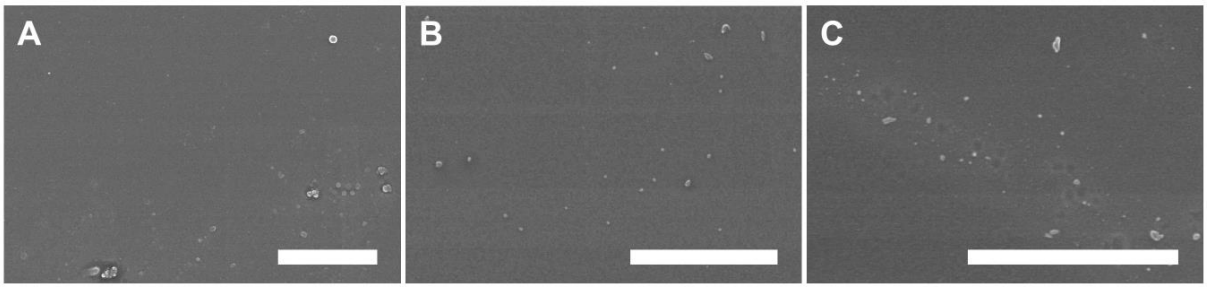

Figure 2.8. SEM images of **ATPP-HCl** (0.1 mM in $MeNO_2$) at different aging time. (A) 1 h; (B) 3 d; (C) 7 d. Condition: alternate sonication (30 s × 3) and heating (50 °C, 2 min × 3). Scale bars: 500 nm.

2.5.3 UV-Vis absorption spectra of G∧C-Por 1 RNTs

Since **G∧C-Por 1** can only be dissolved in $MeNO_2$ with sonication and heating, and the formation of RNTs occurs immediately under these conditions, it is impossible to track the changes in the absorption spectrum of the solution during the course of self-assembly. Interestingly, it was found that RNTs formed from **G∧C-Por 1** in $MeNO_2$ cannot tolerate high temperature. More specifically, heating a stock solution of **G∧C-Por 1** RNTs to 95 °C for 3 min followed by re-cooling to 25 °C leads to a noticeable color change in the solution from green to brown. The presence of only short stacks in the SEM images of the brown solution is indicative of the disassembly of the RNTs (Figure 2.9A and B). We utilized this behavior to study the spectroscopic changes of the RNTs solution upon disassembly. A $MeNO_2$ solution of **ATPP-HCl** was used as a control and processed under the same condition. No tubular architectures were found in this control solution before or after heating (Figure 2.9C and D).

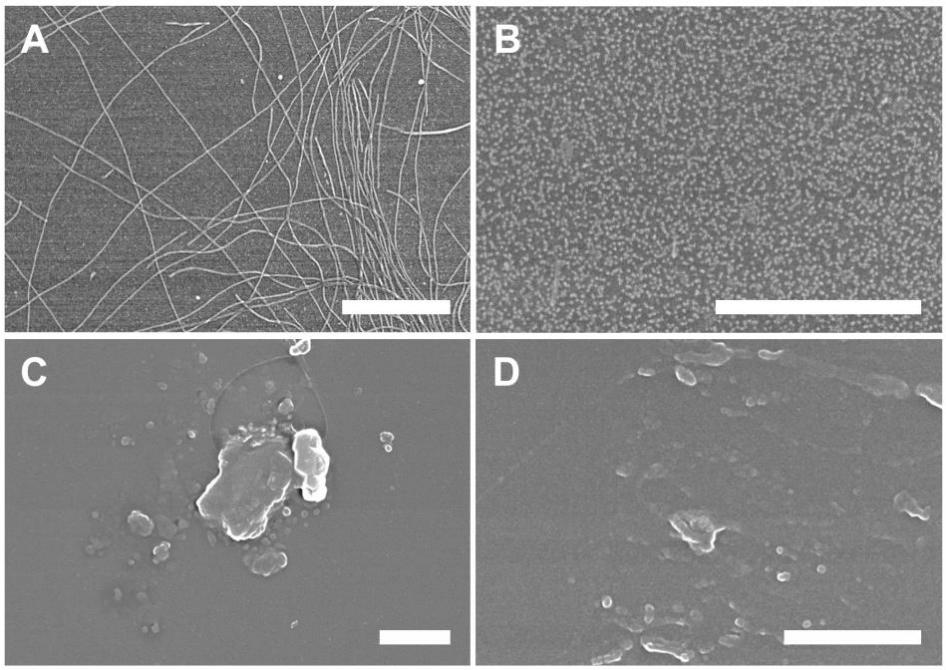

Figure 2.9. SEM images of **G∧C-Por 1** and **ATPP-HCl** (0.16 mM in $MeNO_2$) on heating. (A–B) **G∧C-Por 1** RNTs before and after heating; (C–D) **ATPP-HCl** before and after heating. Condition: 95 °C, 3 min. Scale bars: 500 nm.

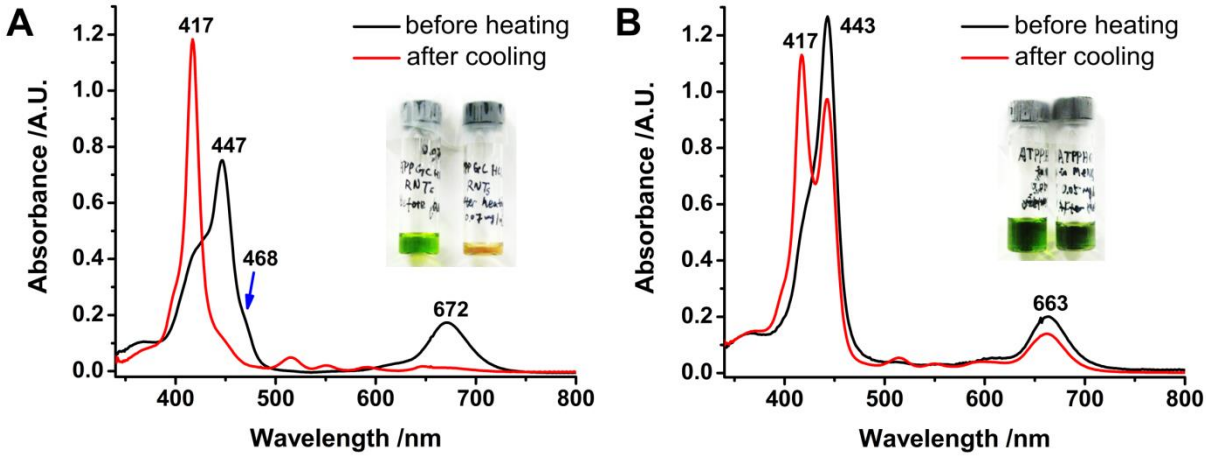

Figure 2.10. Absorption spectra of **G∧C-Por 1** RNTs (A) and **ATPP-HCl** (B) before and after heating. Insets show the solutions before and after heating. Concentration: 0.07 mM in $MeNO_2$. Heating condition: 95 °C for 3 min. Path length: 1 mm.

Figure 2.10 shows the absorption spectra of **G∧C-Por 1** and **ATPP-HCl** before and after heating. In the spectrum of **ATPP-HCl** in $MeNO_2$, the characteristic absorption bands of porphyrin diacid were observed. After cooling, the Soret band at 417 nm increased, and the band at 443 nm decreased. The broad Q band at 663 nm also slightly decreased. These changes might be attributed to minor structure fluctuation of the amorphous aggregates. In the spectrum of **G∧C-Por 1** RNTs in $MeNO_2$ before heating, the broad Soret bands consist of a peak at 447 nm and two shoulders at 417 nm and 468 nm, and the single Q band is at 672 nm. After cooling, the bands at 468 nm and 672 nm almost disappeared, and the band at 417 nm increased. These spectroscopic changes are correlated to the self-assembly induced intermolecular interaction between the porphyrin groups on the outer periphery of the RNTs. The red shifts and broader bandwidth of both Soret and Q bands, along with the increased absorbance of the Q band, indicate that the organization pattern of the porphyrin groups is a typical J-type.[22]

2.5.4 Dilution effect on G∧C-Por 1 RNTs

The well-organized structure of **G∧C-Por 1** RNTs in solution is maintained by the hydrogen bonds and π–π stacking between the elemental building blocks. Although the intermolecular hydrogen bonds are strong, π–π stacking might not be, since it is a type of weak interactions that can be largely affected by the solvent polarity and the concentration. Herein the stability of **G∧C-Por 1** RNTs upon dilution was investigated.

A dilute solution (0.01 mM in $MeNO_2$) of **G∧C-Por 1** RNTs was prepared from a concentrated stock solution (0.16 mM in $MeNO_2$). SEM images of this dilute solution at different aging times showed the disassembly process of the long RNTs (Figure 2.11).

When the solution was freshly prepared, RNTs with a length over several micrometers were widely present. After 1 d of aging, the long RNTs disappeared. Instead, short ones with the length of a few hundred nanometers were observed. After 7 d, only very short stacks of rosettes were found. The short stacks are stable in solution even for one year, and do not undergo further disassembly. The changes in the absorption spectra of this solution also signify the disassembly process (Figure 2.12). The strong absorption band at 447 nm and the shoulder at 468 nm gradually disappeared over time, leaving a single Soret band at 417 nm. On the other hand, the broad Q band at 672 nm decreased and shifted to 647 nm. These spectroscopic changes are similar to those observed in the disassembly process of **G∧C-Por 1** RNTs by heating.

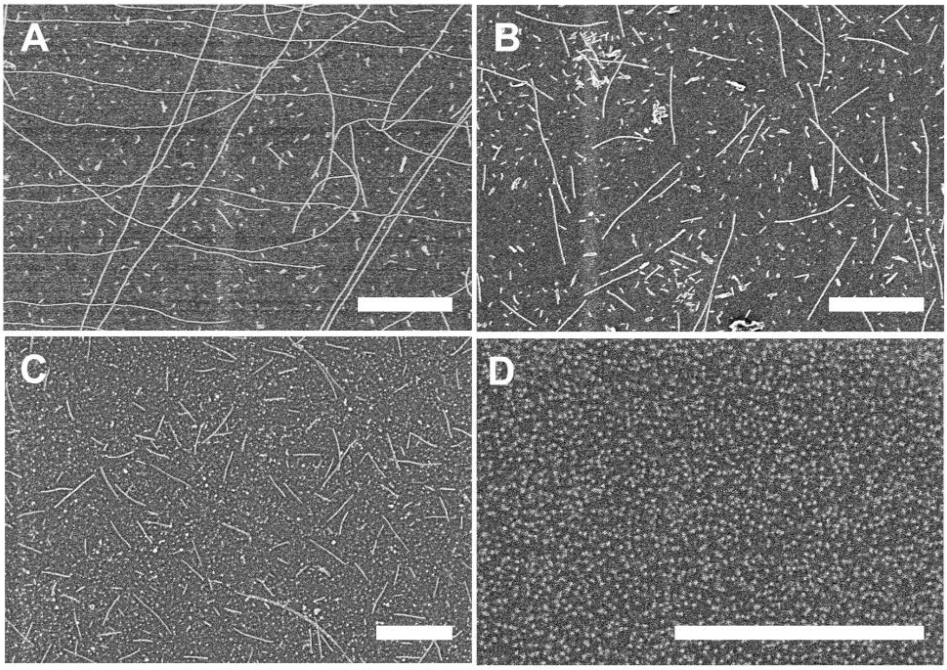

Figure 2.11. SEM images of a dilute solution of **G∧C-Por 1** RNTs (0.01 mM in $MeNO_2$) at different aging times. (A) 30 s; (B) 2 h; (C) 1 d; (D) 7 d. Condition: diluted from a concentrated stock solution (0.16 mM). Scale bars: 500 nm.

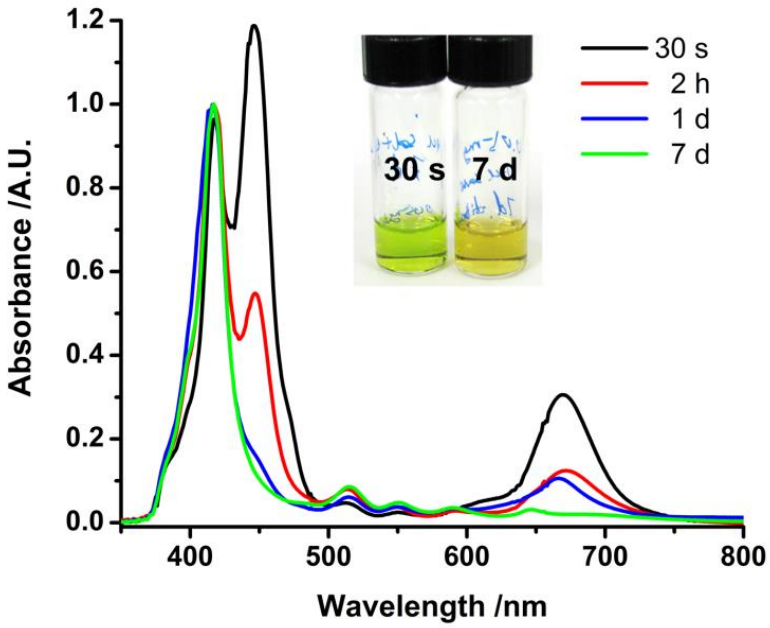

Figure 2.12. Normalized absorption spectra of **G∧C-Por 1** RNTs at different aging times. Inset shows the solution before and after dilution (0.01 mM in $MeNO_2$). Path length: 10 mm.

2.5.5 TEM imaging of G∧C-Por 1 RNTs

TEM is a well-established technique that can produce high-resolution images and display delicate structures of nanomaterials. In particular, it is a powerful tool to measure the diameters of the RNTs. To enhance contrast, TEM samples need to be stained by compounds of heavy metals prior to imaging. The stains can absorb electrons and scatter part of the electron beam, so the objects can be easily contoured by the sharp boundaries against the background.

Uranyl acetate is a commonly used negative stain, and so far is the best one for almost all types of RNTs in our previous studies. For a well-stained sample, under the scanning electron (SE) mode of SEM, RNTs are dark and boundaries are bright, due to the strong

secondary electron flow emitted by uranyl ions excited by the electron beam. In contrast, under the transmission electron (TE) mode RNTs are bright and boundaries are dark, due to the less deflection of the electron beam through RNTs than that through the stain-rich boundaries. Uranyl acetate is often dissolved in H_2O or MeOH at a concentration up to 2% (w/v). However, RNTs of **G∧C-Por 1** cannot be stained by these solutions. Unfortunately, when the aqueous stain solution of uranyl acetate was drop-cast onto the carbon coated TEM grid of **G∧C-Por 1**, the RNTs were not stained, as shown in the SEM images (Figure 2.13A and B). In another staining method, the sample grid was dipped in the uranyl acetate stain for 1 min and then blotted by filter paper. Although it seems that a few RNTs are stained under the TE mode of SEM, the contrast of RNTs against background is still poor in TEM imaging, making the diameter measurement inaccurate (Figure 2.13C and D). The failure of the sample staining was probably due to the hydrophobic nature of the porphyin groups on the RNTs, as the aqueous stain solution does not have a good contact with RNTs.

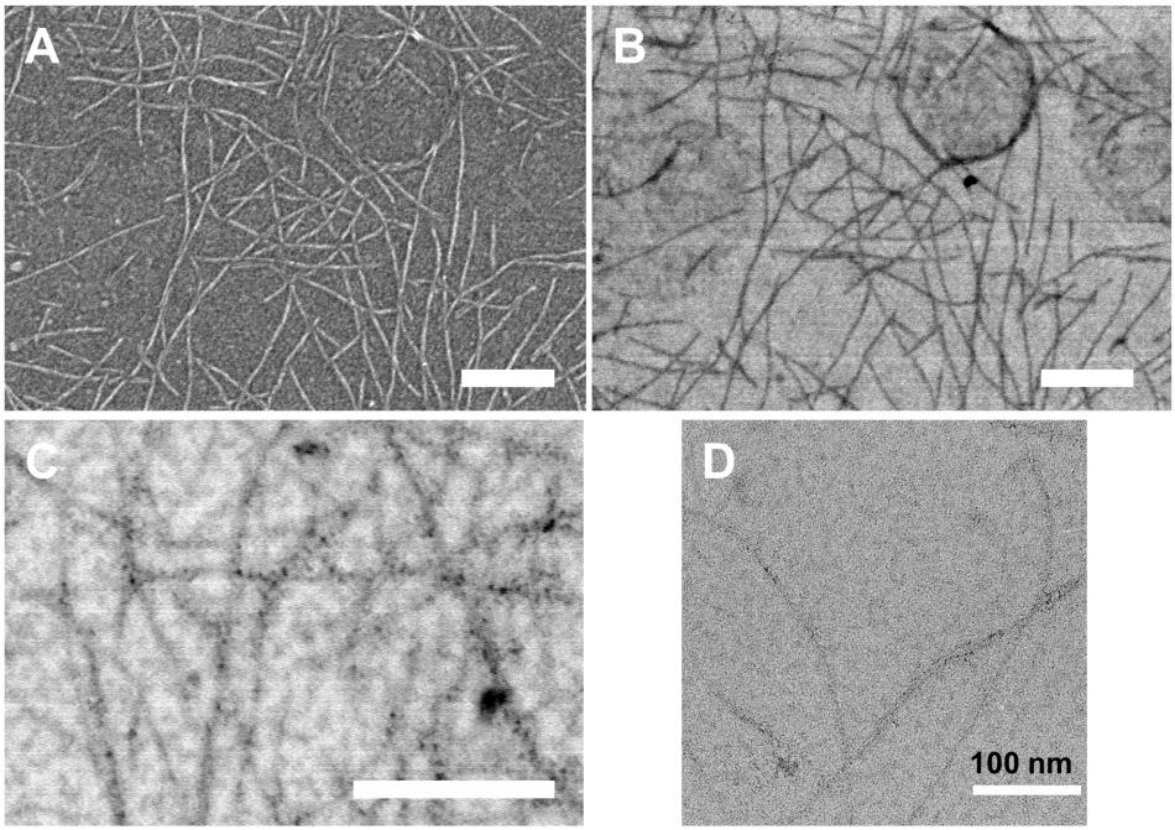

Figure 2.13. SEM and TEM images of poorly-stained **G∧C-Por 1** RNTs. (A–B), images taken under SE mode (A) and TE mode (B) of SEM show the same area; (C–D), images taken under SE mode of SEM (C) and by TEM (D). Stain: 2% uranyl acetate in H_2O. Stain condition: (A–B), the stain was drop-cast onto the TEM grid; (C–D), the TEM grid was dipped in the stain. SEM scale bars: 200 nm.

The solution of uranyl acetate in MeOH also did not stain the RNTs. In fact, a patterned layer was seen by SEM after the sample was treated with this solution (Figure 2.14A). Interestingly, when MeOH was drop-cast onto a sample grid and then immediately blotted, the long RNTs broke into short pieces as shown in the SEM image (Figure 2.14B).

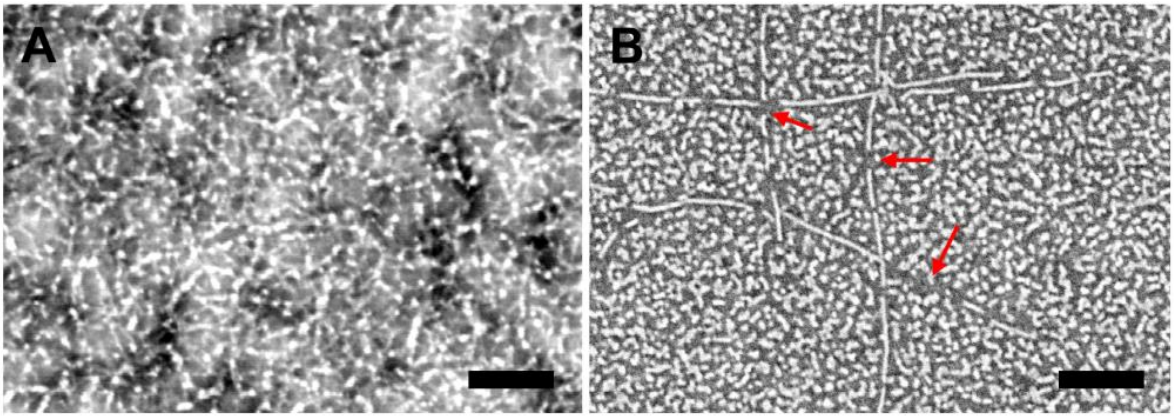

Figure 2.14. SEM images of **G∧C-Por 1** RNTs after contact with stain (A) and MeOH (B). The arrows indicate the disconnection of the RNTs. Stain: 1% uranyl acetate in MeOH. Scale bars: 100 nm.

The trick for sample staining is that uranyl acetate needs to be dissolved in a solvent that is miscible with $MeNO_2$ and does not affect the intact structure of **G∧C-Por 1** RNTs. After screening many solvents, CH_3CN and acetone were found to work well. After sonication and heating, uranyl acetate can be dissolved at a maximum concentration of 0.3% in acetone, and 0.2% in CH_3CN. To dissolve it in CH_3CN, more care is needed, because high temperature or a long period of sonication is detrimental, as the freshly dissolved uranyl acetate crashes out of the solution. In addition, the stains need to be used when they are fresh, because the clear solution gets cloudy over time. In particular, the stain in CH_3CN should be used within 1 h after preparation.

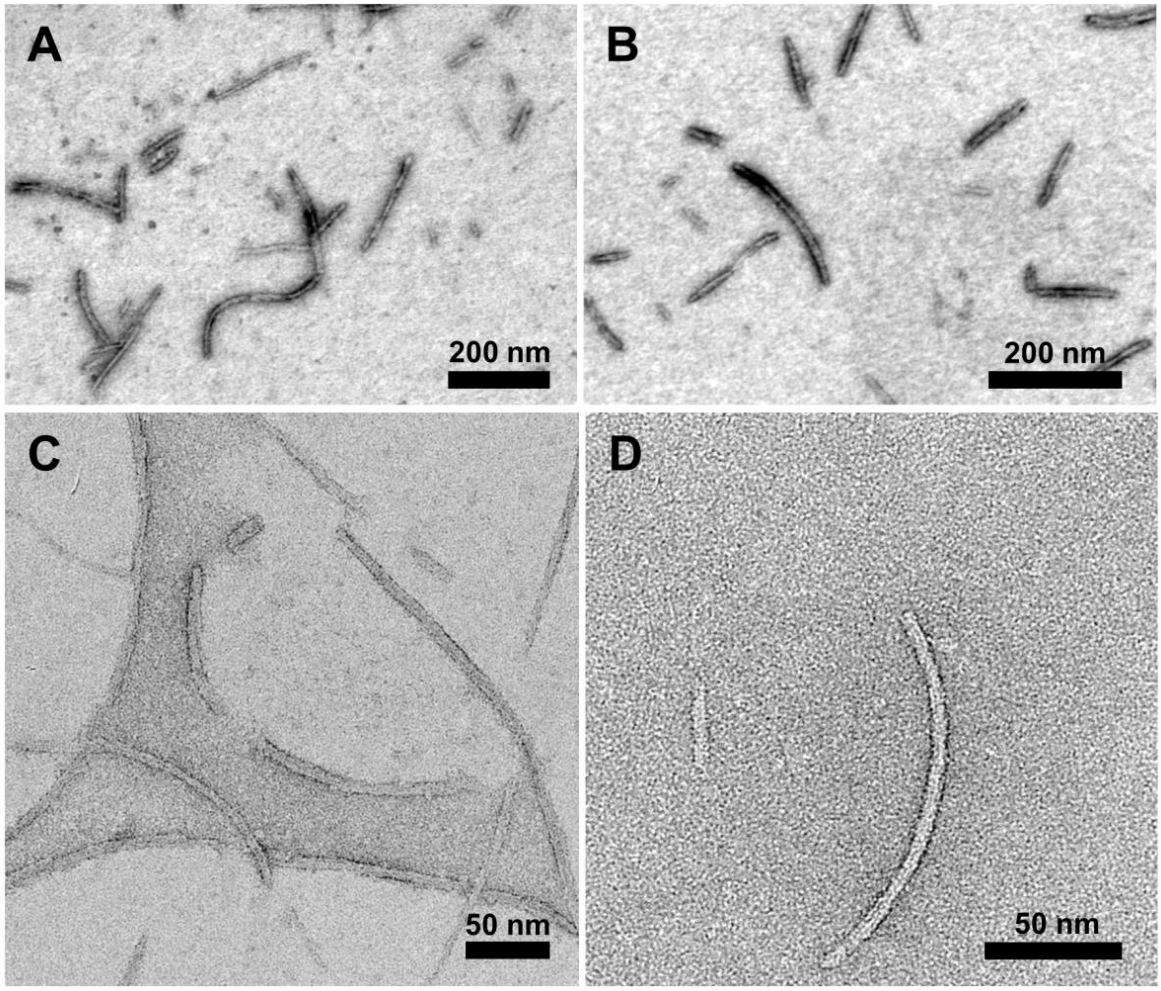

Figure 2.15. TE mode SEM (A–B) and high resolution TEM (C–D) images of well-stained **G∧C-Por 1** RNTs. Concentration: 0.01 mM in $MeNO_2$. Stain: 0.2% uranyl acetate in CH_3CN.

A well-stained sample of **G∧C-Por 1** RNTs shows clear boundaries and good contrast against the background both in SEM and TEM imaging (Figure 2.15). Interestingly, we found most of the tubular structures in the TEM images are bundles of two single RNTs. This is probably due to the intermolecular interaction between the porphyrin groups on the surface of the RNTs, which is also confirmed by STM. The diameter of a single RNT was

averaged from the cross-sectional value of the binary bundle. The single RNT has a diameter of 5.4 ± 0.7 nm based on 25 TEM measurements.

Technically, an unstained specimen can be analyzed by cryo-TEM which is developing popularity in structural biology. With cryo-TEM the biological samples are displayed in their native environment with minimum conformational changes derived from no use of heavy-metal stains. However, the cost of low resolution limits its application. Recently the state-of-the-art Zernike phase contrast technique that utilizes phase plates has been applied to cryo-TEM. In many cases, it effectively increases the contrast of the sample and provides 3D reconstructions with higher resolution.[23] Phase contrast was invented by the Dutch Nobel laureate Fritz Zernike during World War II, and now has been prevalently used in the optical microscope. It takes advantage of the phase differences of light caused by differences in refractive index between components of the object, and the phase differences are transformed into amplitude differences of light that can be directly observed. In the Zernike phase contrast TEM, a phase plate is placed in the back focal of the objective lens to reconcile contrast and resolution. The commonly used phase plate is a continuous amorphous carbon film of appropriate thickness with a small hole in the center. The electrons passing through this hole and those scattered are different in phase and lead to different contrast in imaging.

The characterization of an unstained sample of **G∧C-Por 1** RNTs using a phase-plate cryo-TEM was done by Dr. Jae-Young Cho at the National Institute for Nanotechnology (NINT). Figure 2.16 depicts the TEM images of the RNTs with some 3D features. The diameter of a single RNT measured from these images is similar to the value measured from images using a conventional TEM. However, the resolution of the phase-plate cryo-

TEM is a bit lower, so we take the diameter measured from the stained sample, which has a resolution at 0.1 nm.

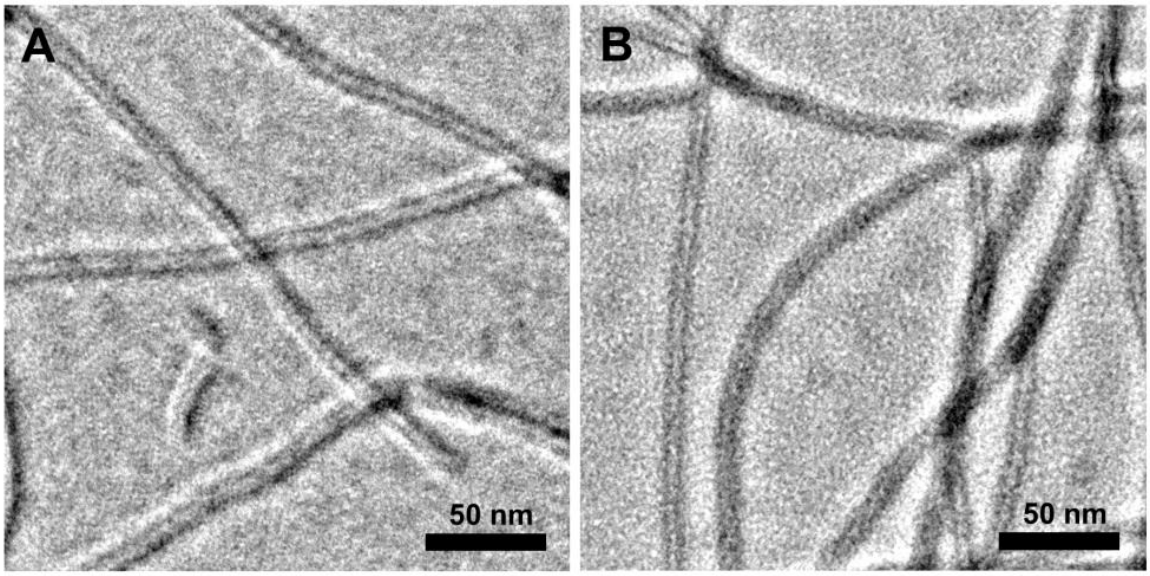

Figure 2.16. Phase-plate cryo-TEM images of an unstained sample of **G∧C-Por 1** RNTs.

2.5.6 AFM imaging of G∧C-Por 1 RNTs

AFM can generate a 3D surface profile of a sample with a high resolution which is comparable or even better than that of TEM. During imaging, the AFM probe scans across the sample surface. The atomic interactions between the tip of the probe and the sample give rise to the deflection of the reflective cantilever, which causes the position changes of the reflected laser beam on the position sensitive photodiode detector. The cantilever deflection information is then transferred to the piezoelectric scanner which controls the movement of the probe, and the amount of the movement is recorded by the computer to produce the topographic image.[24] Tapping mode is the most commonly used technique of operation of an AFM, because it provides high resolution with minimum sample damage based on a feedback mechanism of constant oscillation amplitude. Height and amplitude

are the two most common image types of tapping mode AFM. Height profile provides a vertical topographic image, from where both lateral and height measurements can be estimated. Amplitude profile is also commonly shown as it often displays the shape of the sample more easily. In terms of AFM sample preparation, a solution sample can be drop-cast or spin-cast on HOPG or mica. Both of them are commonly used substrates because of the flatness of the surface.

Figure 2.17 depicts the tapping mode AFM images of **G∧C-Por 1** RNTs on mica and HOPG. The RNTs form a 3D network that consists of both single RNTs and binary bundles. In the image of a more dilute sample, short RNTs are found instead of long ones (Figure 2.18A). However, both single RNTs and bundles are present (Figure 2.18B). The internal interaction of the bundles seems to be strong, as the bundles cannot be broken up even after the solution was applied to sonication for 30 min. The height of a single RNT is considered to be equivalent to its outer diameter, and the value is 4.3 ± 0.4 nm based on 20 measurements (Figure 2.18C). Although the value is slightly lower than those from TEM measurement and molecular modeling simulation, the discrepancy is quite common in most types of RNTs developed in our group. This phenomenon is attributed to two reasons. First, since the AFM imaging is taken at ambient condition, moisture in air can form a sub-nanometer water layer on the sample surface which results in a smaller measured value than the actual height of the object. Second, in tapping mode the tip of the AFM probe actually compresses the sample and may cause subtle deformation, especially in the cases of soft materials.[25]

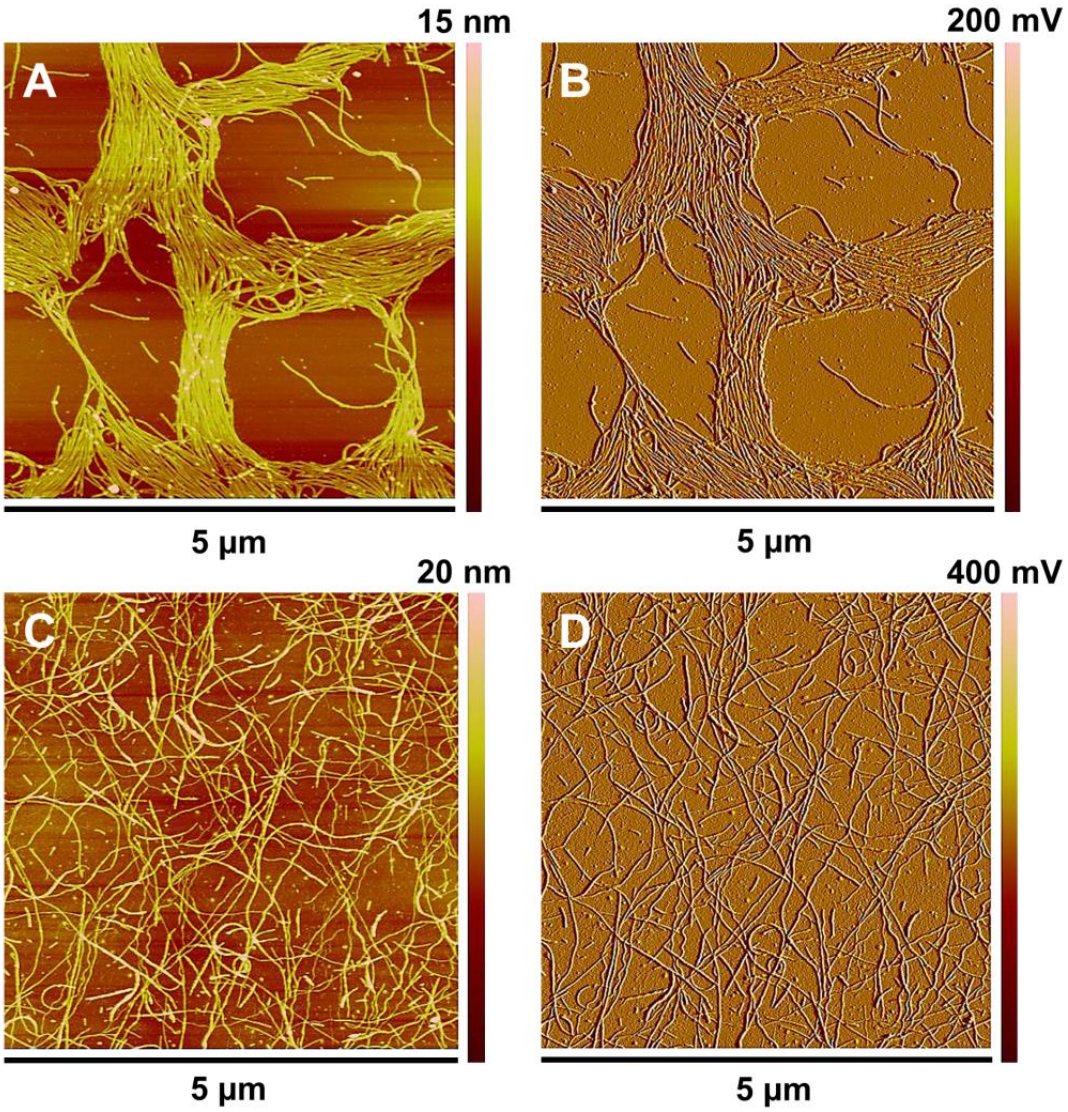

Figure 2.17. Tapping mode AFM images of **G∧C-Por 1** RNTs on mica (A–B) and HOPG (C–D). (A) and (C) are height profiles, (B) and (D) are amplitude profiles. Concentration: 0.05 mM in $MeNO_2$.

In high-resolution AFM imaging, the surface of **G∧C-Por 1** RNT periodically shows a bumpy topography (Figure 2.18C). The difference between the height values from the peak and valley is ~ 1.2 nm, which is similar to the size of a porphyrin group. This is also confirmed by STM.

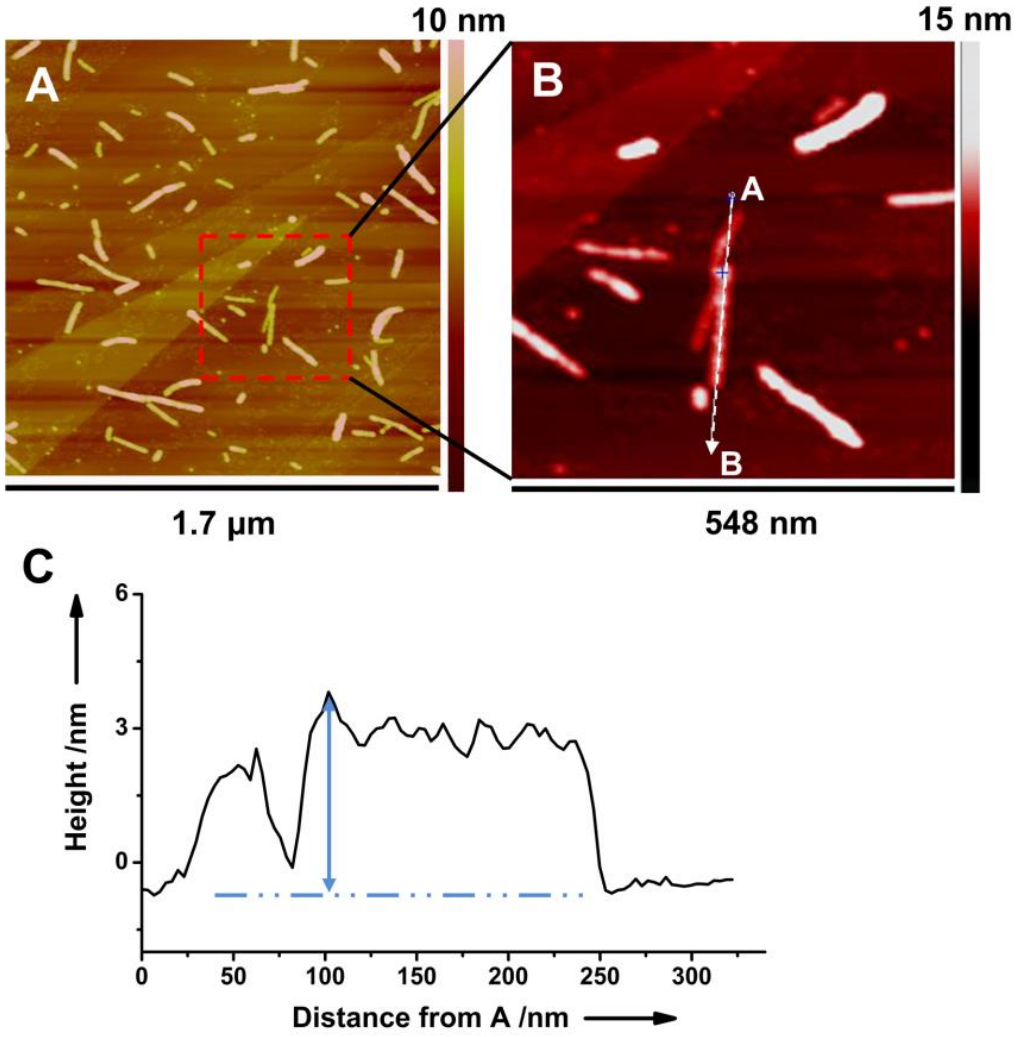

Figure 2.18. Height measurement of a single **G∧C-Por 1** RNT by tapping mode AFM. (A) AFM image of a dilute sample (0.005 mM in $MeNO_2$); (B) enlargement of the squared area in (A); (C) height profile along the arrow in (B), the two-headed arrow shows the height value from a peak.

2.5.7 STM imaging of G∧C-Por 1 RNTs

Different from AFM, the principle of STM is based on the distance-dependent quantum mechanical tunneling effect between the outermost atom of the STM tip and the topmost atom of the sample surface. In addition, both of the STM tip and the sample should be conducting. If the tip-sample distance is small enough, usually within a few angstroms, the electrons at the Fermi energy level of the sample can overcome the energy barrier, known as the work function Φ, and tunnel into the empty state of the tip, or vice versa. When a bias voltage is applied between the sample and the tip, the tunneling effect results in a feeble electron current that can be amplified and transferred to the scanning control unit, herein the distance between the tip and the topmost atom of the sample can be constant in the constant current mode of STM. Because the tunneling current depends exponentially on the tip-sample distance, and only the outermost atom of the tip and the topmost atom of the sample are directly involved, single atom imaging can be observed by STM. On account of these features, STM is an important technique that has been applied to surface structure analysis, catalysis research, atomic molecular manipulation and single molecular electronics.[26]

The delicate structures of many well-organized assemblies of porphyrins have been revealed by STM at the submolecular level, as these porphyrins display a strong electron tunneling effect with the tip.[27] When the tip is modified with a single fullerene molecule, the HOMO of porphyrin can be spatially visualized by STM, due to the efficient electron transfer from the HOMO of porphyrin to the LUMO of fullerene.[28]

We used STM to probe the delicate structure of **G∧C-Por 1** RNT. High-resolution images of a bundle of two single RNTs are shown in Figure 2.19. The size of a porphyrin

group is measured to be 1.18 ± 0.13 nm. The distance between two horizontally adjacent porphyrin groups on the same hexameric rosette is 0.97 nm, and the distance between two vertically adjacent porphyrin groups along the long axis of the RNT is 3.47 nm. The diameter of a single RNT is 6.17 ± 0.42 nm, which is in good agreement with the values obtained from TEM measurements and molecular modeling simulation. Interestingly, the porphyrin groups on the interface of two single RNTs interlace with each other and form a compact and almost continuous array. From the STM images, we propose that the porphyin groups on the interface of the bundle adopt a slipped cofacial J-aggregate arrangement, which is in good agreement with the red-shifted Soret and Q bands in the absorption spectrum of the **G∧C-Por 1** RNTs solution.

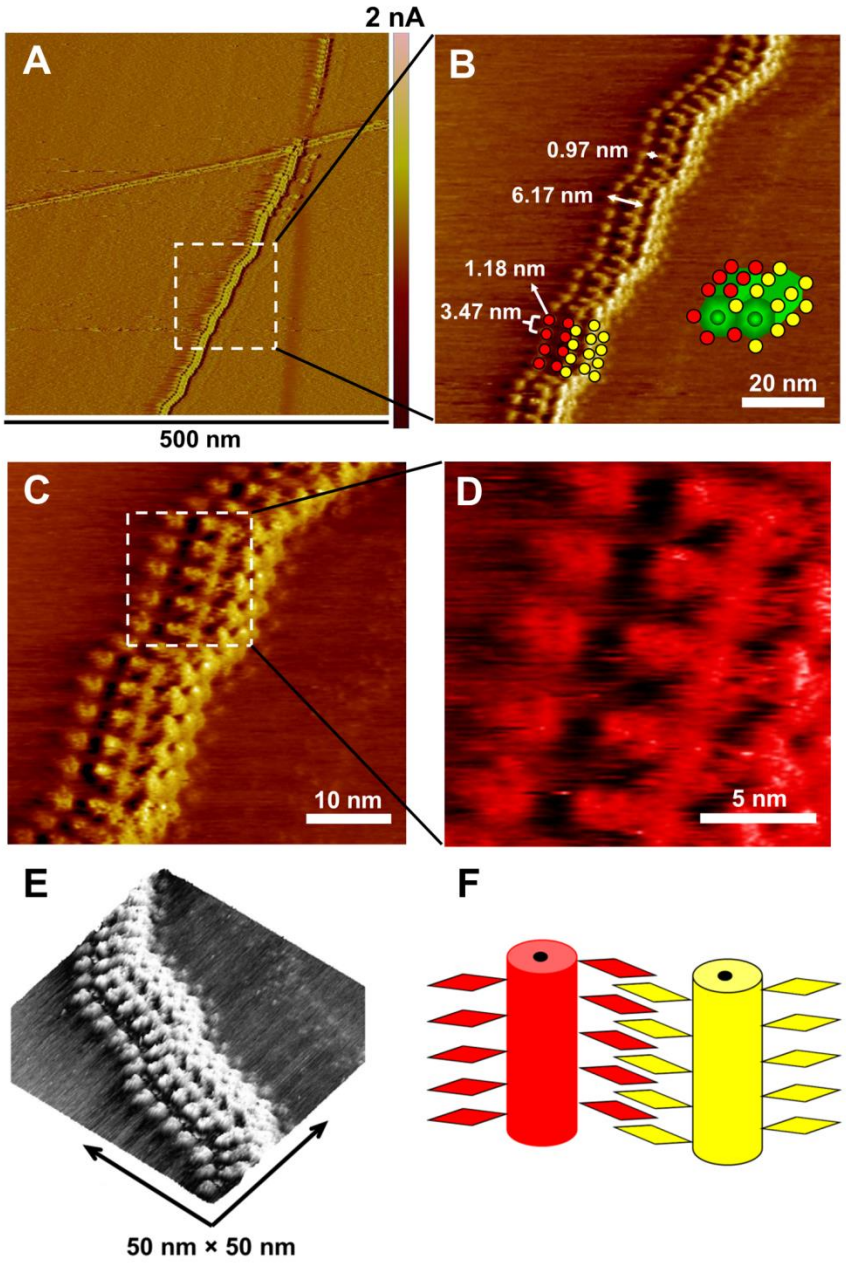

Figure 2.19. (A) STM images of a bundle of two single **G∧C-Por 1** RNTs; (B) enlargement of the squared area in (A), inset is a schematic illustration, the red and yellow circles represent porphyrin groups; (C–D) enlarged segments; (E) three dimensional topography of the bundle; (F) side-view illustration of the bundle, porphyrin groups are represented as colored diamonds, only porphyrin groups on the edges are shown for clarity. STM conditions: current setpoint: 500 pA; bias voltage: 1000 mV.

2.5.8 The importance of proton and chloride ion on the supramolecular structure of G∧C-Por 1 RNTs

G∧C-Por 1 is in the form of porphyrin dication, with the molecular formula $(C_{53}H_{41}N_{11}O_2)$•4.2(HCl) deduced from elemental analysis. Similar to other porphyrin dications, **G∧C-Por 1** has an emerald green color. The proton and Cl^- ion are critical to the supramolecular structure of **G∧C-Por 1** RNTs.

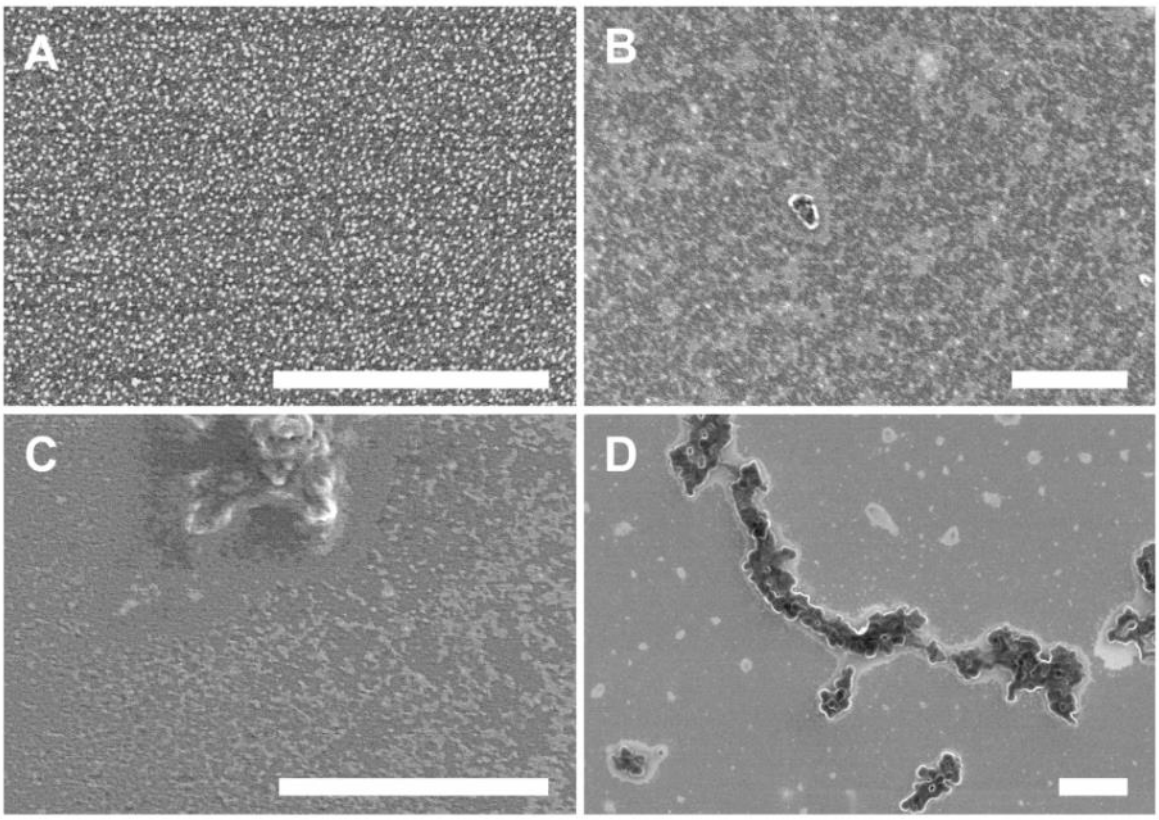

Figure 2.20. SEM images of the free base of **G∧C-Por 1** in $MeNO_2$ (A), 1,2-DCB (B), toluene (C), and THF (D). Concentration: 0.05 mg/mL. Condition: alternate sonication (30 s × 3) and heating (50 °C, 2 min × 3). Scale bars: 500 nm.

The free base form of **G∧C-Por 1** was prepared by washing **G∧C-Por 1** with aqueous K_2CO_3 (10%). The free base is a purple powder, and can be dissolved at a low concentration in $MeNO_2$, 1,2-DCB, toluene and THF. These solutions were treated under the same condition as that optimized for the self-assembly of **G∧C-Por 1**. As shown in Figure 2.20, only short stacks of rosettes were observed in $MeNO_2$. In 1,2-DCB and toluene, short stacks of rosettes and a few amorphous aggregates were present. In THF, large aggregates were observed.

In another experiment, triethylamine was quantitatively added to a stock solution of **G∧C-Por 1** RNTs, and the changes in the spectra and SEM images were recorded (Figure 2.21). When one equiv. of triethylamine was added to the RNTs solution, the color of the solution instantly changed from light green to brown, and a flocky precipitate was observed. Large aggregates were found in the SEM image, which are thought to be debris of the RNTs. In the absorption spectrum, the characteristic bands of **G∧C-Por 1** RNTs at 468 nm and 672 nm disappeared. Appearance of the four small Q bands signifies that the porphyin groups are in the form of free base. The Soret band has a shoulder at 431 nm, and is broader than that of 5-(4-aminophenyl)-10,15,20-triphenylporphyrin (ATPP). The broad Soret band may be correlated to the amorphous aggregates observed in the SEM imaging.

These observations indicate that extra protons are important for the self-assembly and supramolecular structure of RNTs, but may not have an effect on the intermolecular H-bonding interaction.

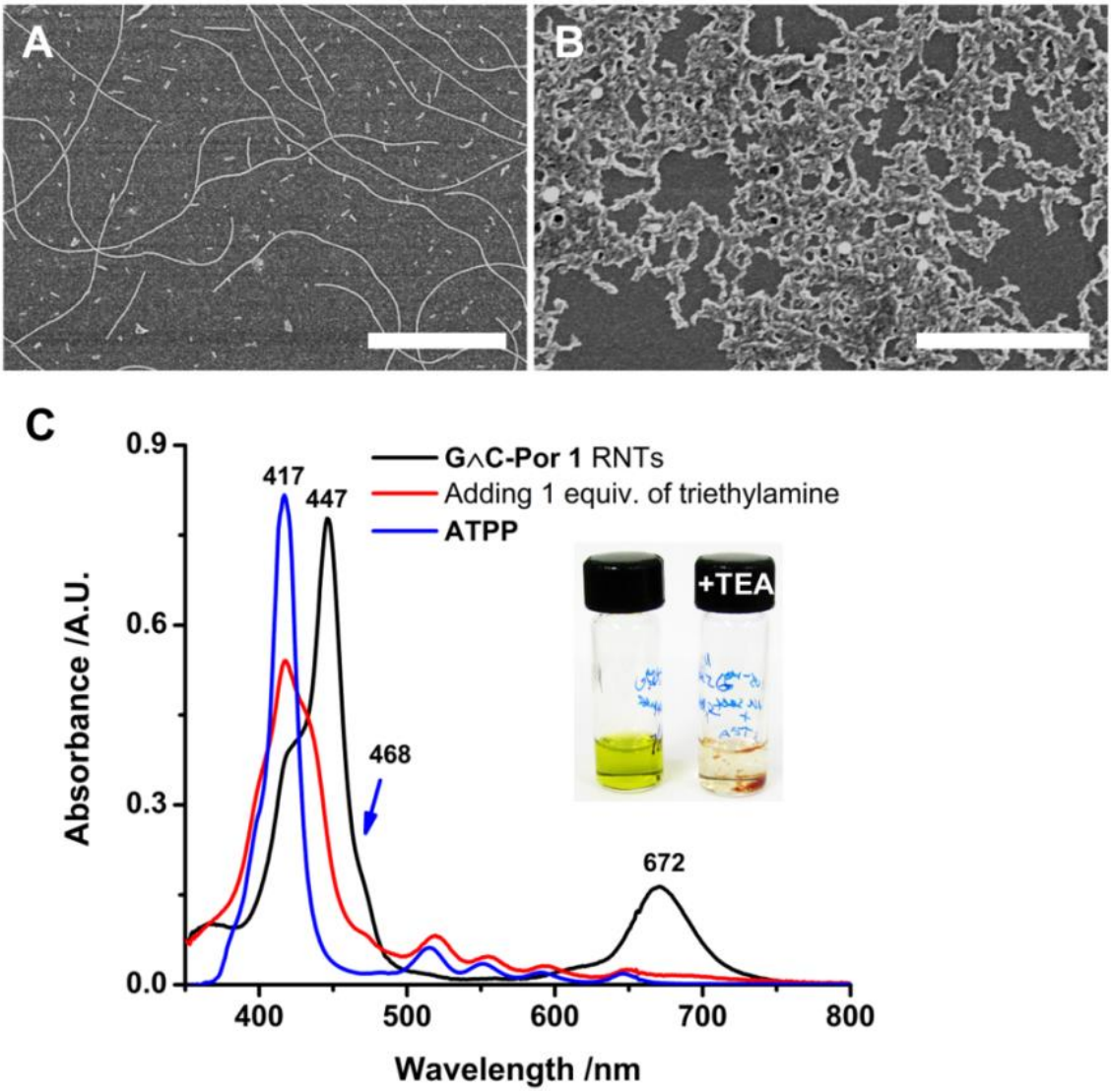

Figure 2.21. SEM images of a $MeNO_2$ solution (0.05 mM) of **G∧C-Por 1** RNTs before (A) and after (B) adding one equiv. of triethylamine; (C) absorption spectra. Inset shows the solution before and after adding one equiv. of triethylamine. Path length: 1 mm. Scale bars: 500 nm.

On the other hand, the Cl^- ion is also essential to the tubular nanostructure, since no RNTs were observed in the case of **G∧C-Por 1** (TFA). The all-atom molecular dynamics (MD) simulation for **G∧C-Por 1** in $MeNO_2$ shows that many Cl^- ions are positioned above

and below the macrocycle planes of the porphyrin groups and stay there during the MD simulation time conducted (Figure 2.22). These Cl^- ions interact with the abstracted protons on the basic pyrrole N. Considering that the porphyrin group in the present modeling study carries two positive charges, the presence of Cl^- ions would be extremely important to reduce the electrostatic repulsion between the porphyin groups on the RNT surface and stabilize the supramolecular structure. In fact, during the solvent equilibration step in the present MD simulation, we noticed that the equilibration of Cl^- ions strongly affects the RNT structure. Disruption of the RNT supramolecular structure was observed when we did not equilibrate Cl^- ions well and did not allow them to distribute on the RNT surface. More details about the modeling study are given in the following section.

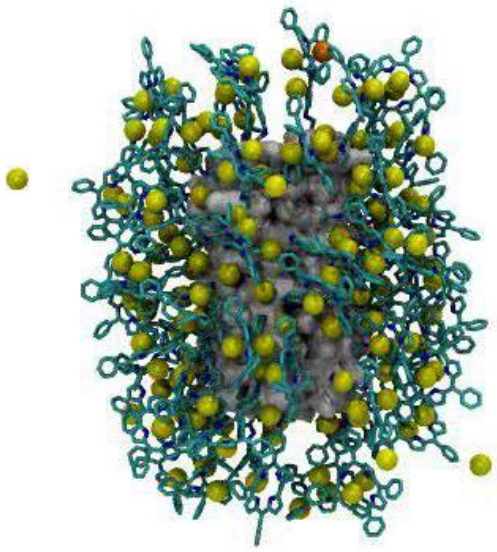

Figure 2.22. A snapshot at 10 ns in the MD simulation for a single **G∧C-Por 1** RNT in $MeNO_2$. The core of the RNT is shown as the white surface representation, the porphyrin groups are shown as the tube representation, the Cl^- ions are presented as a VDW sphere, and colored in yellow except one that is colored in orange. $MeNO_2$ molecules are omitted for clarity.

2.5.9 Molecular modeling study for a single G∧C-Por 1 RNT

The molecular modeling study for a single **G∧C-Por 1** RNT was carried out by Dr. Takeshi Yamazaki. In the present modeling study, the two basic pyrrole N in the porphyrin group of **G∧C-Por 1** are protonated to form the dication, since the compound was obtained from deprotection of the precursor in HCl (4 M in 1,4-dioxane) without a basification work-up. The emerald green color of **G∧C-Por 1** is indicative of the porphyrin dication.[29] In fact, adding an organic base like triethylamine to a solution of the G∧C-porphyrin renders the appearance of the 4 characteristic Q bands of the porphyrin free-base form.[30]

Figure 2.23 shows a schematic illustration of the hierarchical self-assembly of **G∧C-Por 1**. Six **G∧C-Por 1** molecules form a hexameric rosette via intermolecular H-bonding interaction. The rosettes self-organize further to form a nanotube via π–π stacking. The staggered angle between two rosettes is 30°. The porphyrin groups on the nanotube surface form 12 continuous linear arrays. These figures were generated with VMD.[31]

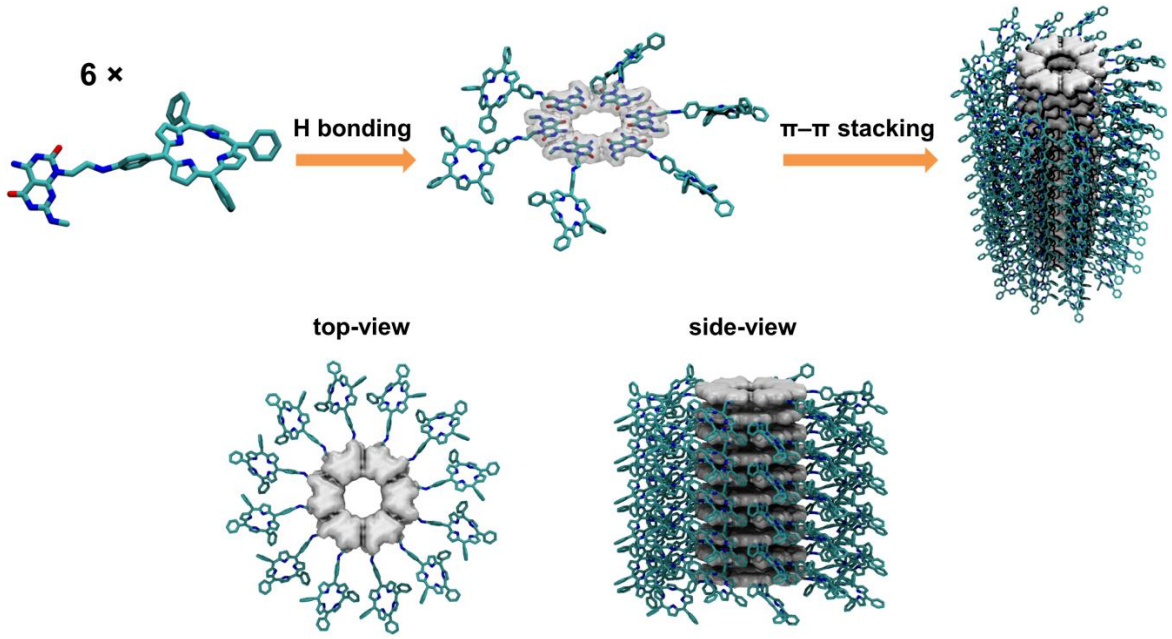

Figure 2.23. Schematic illustration of hierarchical self-assembly of **G∧C-Por 1**.

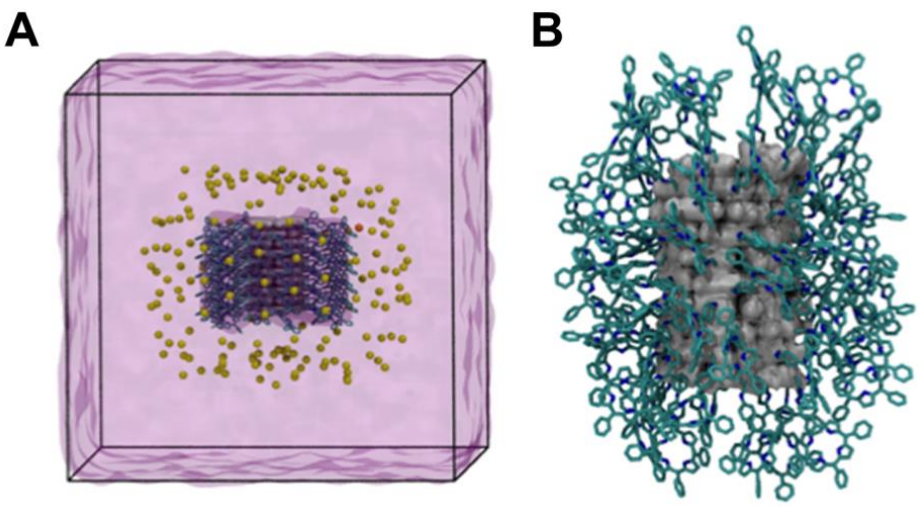

Figure 2.24. MD simulation of a single **G∧C-Por 1** RNT. (A) a single RNT of 10 rosette stacks in $MeNO_2$; (B) a snapshot of the RNT at 100 ns, the Cl^- ions are omitted for clarity.

The MD simulation was set up and run for a single RNT that is comprised of 10 rosette stacks, based on our previous modeling study.[32] The **G∧C-Por 1** RNT was modeled by the general AMBER force field (GAFF)[33] complemented with the partial charges taken from OPLS2005 force field[34]. The $MeNO_2$ molecule was modeled by GAFF with the partial charges determined by the restrained electrostatic potential (RESP)[35] at the HF/6-31G* level using the Gaussian 09 program[36]. MD simulations were run in Amber12.[37] The RNT was solvated in 20,000 $MeNO_2$ molecules and 180 chloride ions, as shown in Figure 2.24A. In this figure, the core of the RNT is shown as the white surface representation and the porphyrins are shown as the tube representation. The Cl^- ions are presented as a VDW sphere, and colored in yellow except one that is colored in orange. $MeNO_2$ molecules are represented as a purple transparent surface. The solvent environment was first equilibrated at 298 K with a pressure of 1 atm for 2 ns with harmonic positional restraints on the RNT.

Then, the positional restraints of the RNT were removed from the edge rosette rings to the middle rings in the stepwise manner for every 200 ps, and finally a 100 ns simulation was performed at 298 K with a pressure of 1 atm as a production run. The time step was 2 fs, and all bonds involving hydrogen were constrained by SHAKE.[38] A cutoff of 8 Å was used for non-bonded interactions, and the long-range electrostatic interactions were treated with the particle mesh Ewald method.[39] Figure 2.24B shows the snapshot of the RNT at 100 ns, suggesting the structural stability of the RNT scaffold in $MeNO_2$ and Cl^- solution.

Based on the MD trajectory of a single RNT, we measured the width of the RNT along the X-direction as the diameter. Figure 2.25 shows the measurement of the RNT width as a function of the MD simulation time. The average over 100 ns was calculated to be 6.05 nm, which is consistent with the values from our TEM and STM measurements. This suggests that the present molecular modeling describes the RNT reasonably well. We can see a small fluctuation (~ 1 Å difference) around 47 ns in Figure 2.25. This is because one of the porphyrin groups changed its orientation. Nevertheless, there was no significant supramolecular structural change observed associated with this fluctuation.

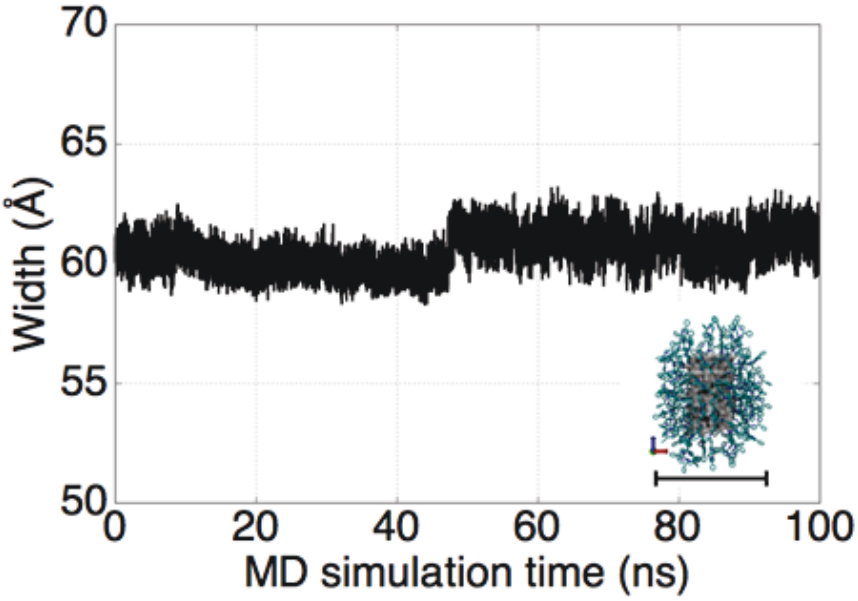

Figure 2.25. Measurement of the width of a single **G∧C-Por 1** RNT as a function of MD simulation time.

2.6 Limitation of G∧C-Por 1

Although **G∧C-Por 1** can form RNTs in $MeNO_2$, the solubility constraint (max. 0.5 mmol) may limit its application in OPV device fabrication.

Spin-casting and thermo deposition are the two most used techniques for fabricating thin films of organic materials. As a solid-phase processing technique, thermo deposition is mainly used for small molecules that have moderate volatility and saturated vapor pressure, and it has been successfully used in a few cases. However, to date most of electron-donor materials are polymers and they are only suitable for spin-casting. As a wet-processing technique, spin-casting is cost-efficient and more important on the transition to the yet unachieved ultimate goal of "printable OPVs", in which the mixed solution of both

electron-donor and electron-acceptor materials can be evenly sprayed to a substrate and form the so called bulk heterojunction[40] active layer with a proper thickness. We can simply take this process as an analogue to inkjet printing. The thickness of the active layer directly affects the performance of OPV devices. When the layer is too thin, the light absorption efficiency is low, and a thick layer is detrimental to charge separation and charge transport. In most of the cases, the thickness of the active layer varies in a range from a few tens to several hundreds of nanometers. In a solution-processed OPV device, the thickness of the active layer is determined by the concentration of the solution and the rate of spin-casting. In general, a high concentration is desired, because it can ensure the thickness of active layer and save the solvent. For the devices fabricated in the lab, the concentration normally ranges between 10 to 40 mg/mL.[41] Although a lower spin-casting rate generates a thicker layer, it cannot be too low, otherwise the spin-cast film is uneven and it is detrimental to the device performance. For this reason the spin-casting rate is commonly set as more than 1,000 rpm.

In terms of the solvent for solution-processed OPV device fabrication, chlorobenzene and 1,2-DCB are the most common, as they can largely dissolve many polymeric and small-molecule electron donors. In addition, fullerene derivatives, which are extensively exploited as the electron-acceptor materials, can also be dissolved at a high concentration in these haloaromatics. Among these electron acceptors, $PC_{61}BM$ is a benchmark. This is mainly attributed to its good electron-accepting ability and high electron mobility.[42] However, it is insoluble in $MeNO_2$.[43] Although 1,2-DCB and $MeNO_2$ are miscible and the mixture can dissolve $PC_{61}BM$ at a concentration up to a few mg/mL, the fabrication of solution-processed OPV devices based on **G∧C-Por 1** and $PC_{61}BM$ may be a challenge.

This is because the binary solvent system does not improve the solubility of **G∧C-Por 1**, which means the spin-cast active layer of the two may be too thin for efficient light absorption due to the solubility constraint.

In view of the above mentioned considerations, I planned to synthesize porphyin-functionalized G∧C building blocks that are highly soluble in chlorobenzene or 1,2-DCB, and the self-assembled RNTs from them feature a superior structural stability. This is the starting point for the synthesis of **$(G\wedge C)_2$-Por 2** and **$(G\wedge C)_2$-Por 3**.

2.7 Synthesis of $(G\wedge C)_2$-Por 2

As shown in Figure 2.26, di-N-alkylation was not observed in the reaction of ATPP and G∧C aldehyde, so I chose to modify the ATPP with a short spacer that has a terminal primary amino group. The spacer should be short so that the porphyrin groups have a restricted rotation, and the intact highly ordered arrangement of the porphyrin is not affected to a large extent. 3-(Boc-amino)-1-propanol was first tried with ATPP following a reported method of direct N-alkylation of aromatic amines with alcohols.[44] However, this reaction did not proceed and no expected product was observed. A trial of nucleophilic substitution reaction between ATPP and 3-(Boc-amino)propyl bromide was not successful, probably due to the low nucleophilicity of the aromatic amino group.

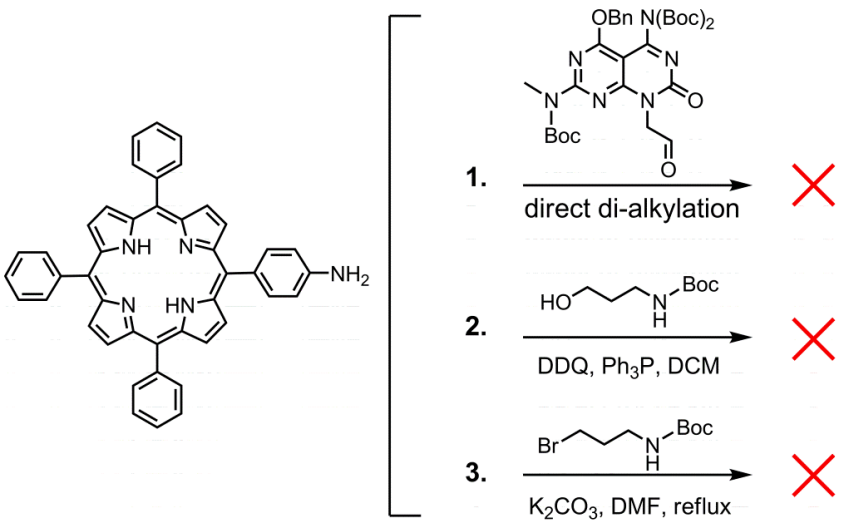

Figure 2.26. Failed attempts to obtain porphyrin-twin G∧C and modified porphyrin with a spacer bearing a primary amino group.

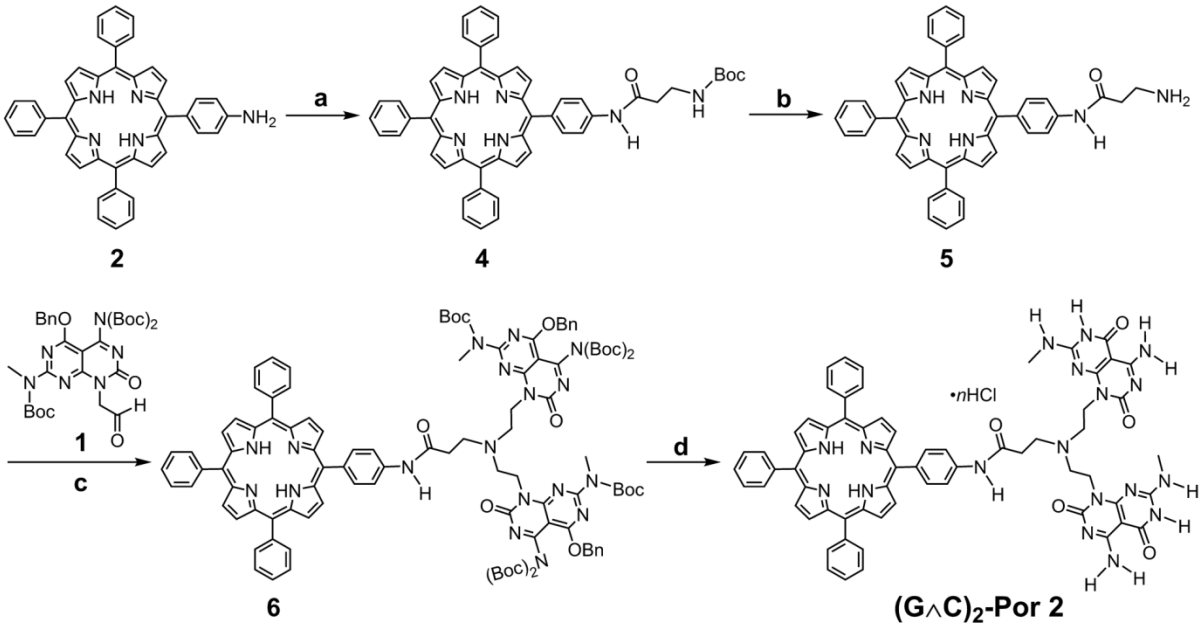

Figure 2.27. Synthesis route of **(G∧C)$_2$-Por 2**. Reagents and conditions: (a) Boc-*β*-alanine, EDC•HCl, DIPEA, DCM, 25 °C, 24 h, 92%; (b) DCM/TFA (1:1), 25 °C, 2 h, followed by work-up with $NaHCO_3$, 96%; (c) $NaBH(OAc)_3$, triethylamine, THF, 25 °C, 4 d, 42%; (d) HCl (4 M in 1,4-dioxane), 80 °C, 4 h, quantitative yield.

Boc-*β*-alanine was then chosen as the spacer as it can form an amide bond with ATPP through a coupling reaction (Figure 2.27). Carbodiimides are used in the amide coupling reaction as they can activate carboxylic acids for the amide formation. In the first trial, *N*,*N*′-dicyclohexylcarbodiimide (DCC) was used and the reaction proceeded to completion after 24 h at 25 °C. Although the byproduct N,N'-dicyclohexylurea can be filtered off as it is insoluble in most solvents, trace amounts still remain and complicate the NMR and MS spectra of the desired product. This drawback leads to tedious purification and a low yield. DCC was then replaced by 1-ethyl-3-(3-dimethylaminopropyl)carbodiimide (EDC) and pure compound **4** was obtained after work-up without further purification, as the byproduct urea is very soluble in water and can be easily removed. In amide coupling reactions, hydroxybenzotriazole (HOBt) is commonly used as an additive to suppress side reactions. However, the addition of this reagent was found to be unnecessary, as compound **4** was obtained quantitatively without HOBt. Deprotection of **4** followed by work-up produced compound **5**. Interestingly, only the di-alkylation product **6** was observed in the reductive amination between **5** and G∧C aldehyde **1** as shown in Figure 2.27. The yield of **6** can be improved by dissolving the dried reaction mixture in fresh solvent and adding more reducing agent to repeat the reaction. A proper solvent for this reaction is very important. Although 1,2-DCE is a common solvent for reductive amination using $NaBH(OAc)_3$ as the reducing agent and it works in the synthesis of **G∧C-Por 1**, it should not be used in the synthesis of **6**. When the reaction was run in 1,2-DCE, no product was observed at all. Instead, G∧C aldehyde **1** was reduced to the alcohol exclusively when the temperature was elevated to 50 °C. THF was found to be the best solvent for this reaction. **$(G\wedge C)_2$-Por 2** was quantitatively obtained after deprotection of **6** in HCl (4 M in 1,4-dioxane).

2.8 Self-assembly of $(G\wedge C)_2$-Por 2

2.8.1 $(G\wedge C)_2$-Por 2 in single-solvent systems

The solubility test and self-assembly study of **$(G\wedge C)_2$-Por 2** in different solvents are summarized in Table 2.1 and Figure 2.28. In general, the solubility is poor in most of solvents, with the exception of MeOH and DMF, in which **$(G\wedge C)_2$-Por 2** can be readily dissolved with no need for heating. To improve the solubility and investigate the self-assembly capability in indifferent solvents, these solutions were heated to the boiling point for 1 min and then slowly cooled to room temperature. At a concentration of 0.5 mM, only the MeOH and DMF solutions are clear, others are cloudy and slowly form precipitates. In $MeNO_2$ and 1,2-DCB, very short stacks of rosettes are found in SEM imaging. In CH_3CN, short RNTs are found, with an average length of a few tens of nanometers. Nevertheless, the RNTs do not elongate over time. The DMF solution has a unique charet-red color. Worm-like nanostructures are found in the SEM image, but nothing is found in the fresh solution before heating. In the absorption spectra of **$(G\wedge C)_2$-Por 2** in DMF, a broad new band at 328 nm emerges after heating, which might be correlated to the nanostructures of aggregates found in the SEM image (Figure 2.29). No tubular nanostructure was seen in the THF solution, and only large particles were present in the acetone solution. In MeOH, long RNTs were found and the background was clear in the SEM image. Herein more detailed studies are done for the self-assembly of **$(G\wedge C)_2$-Por 2** in MeOH.

Table 2.1. Summary of the self-assembly study of **(G∧C)$_2$-Por 2** in single-solvent systems.

Solvent	Solubility	Color	RNTs
$MeNO_2$	slightly	green	short stacks
DMF	good	claret-red	×
CH_3CN	poor	light green	< 100 nm
THF	slightly	light brown	×
Acetone	poor	light green	×
1,2-DCB	slightly	brown	short stacks
MeOH	good	bright cyan	> 1 μm

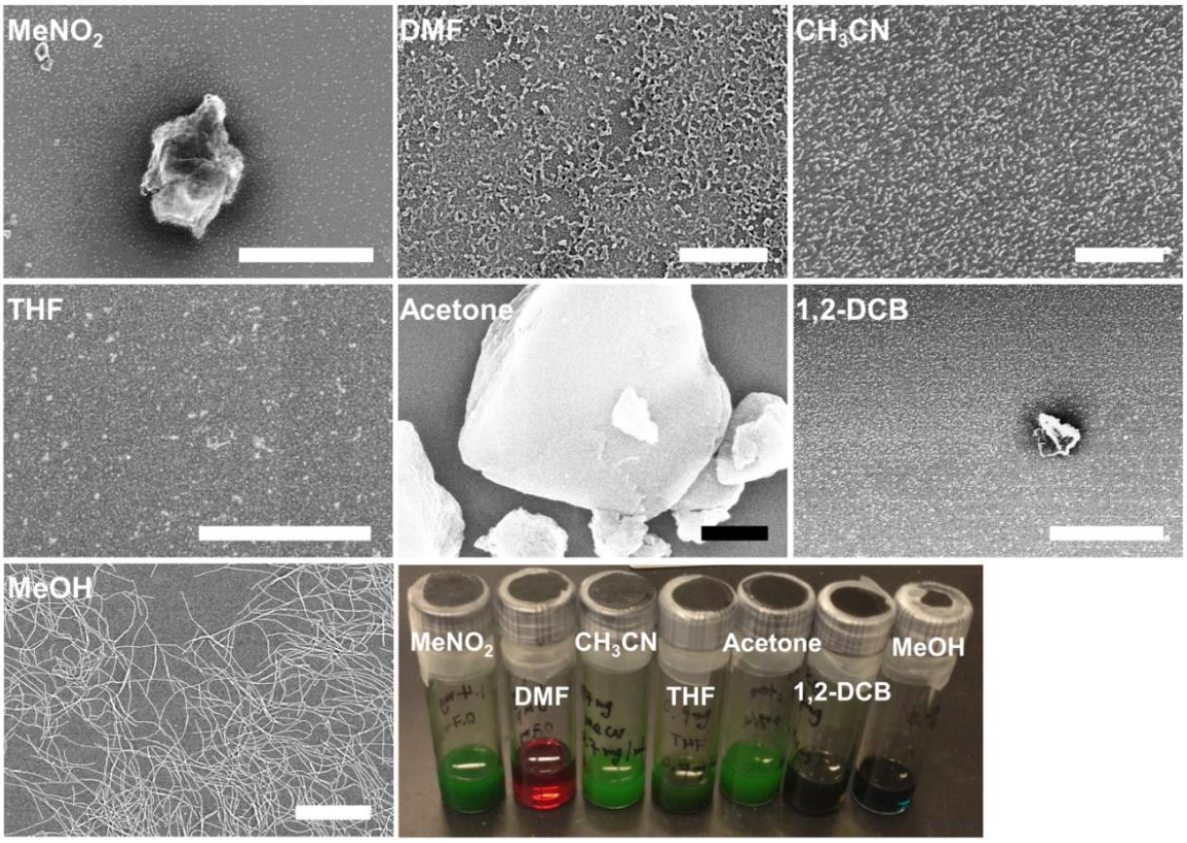

Figure 2.28. SEM images of **(G∧C)$_2$-Por 2** in different solvents. Concentration: 0.5 mM. Condition: sonication (30 s), heating at boiling points (1 min). Aging: 1 h. The last picture shows the colors of the solutions.

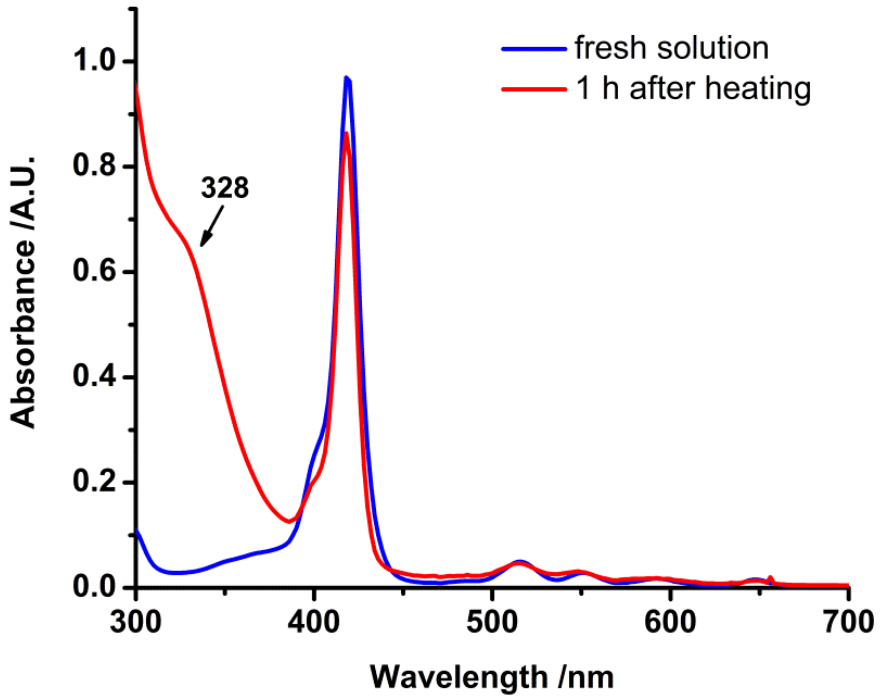

Figure 2.29. Absorption spectra of **(G∧C)$_2$-Por 2** in DMF (0.05 mM) before and after heating. Condition: sonication (30 s), heating (150 °C, 1 min). Path length: 1 mm.

In a fresh solution of **(G∧C)$_2$-Por 2** in MeOH, no RNTs were present (Figure 2.30A). When the solution was heated to the boiling point for 1 min and aged for 10 min until cooling to room temperature, long RNTs were found in SEM imaging, with the maximum length up to a few micrometers (Figure 2.30B). Upon the formation of RNTs, a new band at 402 nm appears in the absorption spectrum (Figure 2.30C), which indicates that the porphyrin groups on the surface of RNTs adopt the H-type arrangement. This is different from the spectroscopic changes observed in the self-assembly process of **G∧C-Por 1** in $MeNO_2$, where a red shift of the Soret band is observed. In addition, the peaks at 235 nm and 295 nm are the characteristic absorption bands of the G∧C motifs. The decrease in absorbance at 295 nm is indicative of the formation of RNTs, as similar changes are

observed in the cases of other self-assembled RNTs. This change is probably because the self-organized G∧C motifs via the complementary H-bonds are shielded by the outer functional groups and the resonance behaviors of the G∧C motifs are restricted by the H-bonds, as they face inside and consist of the inner core of RNTs.

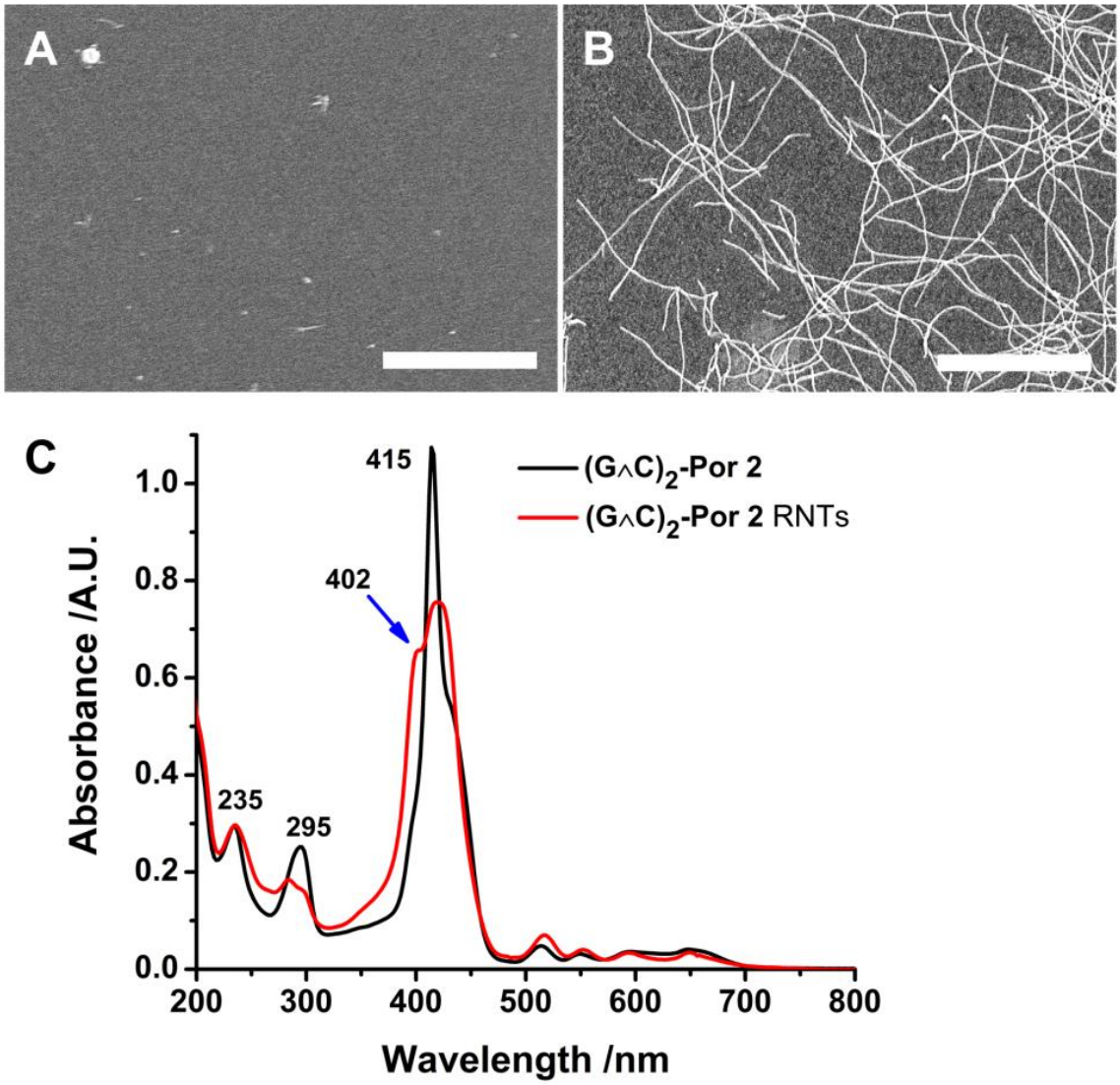

Figure 2.30. SEM images of **$(G\wedge C)_2$-Por 2** in MeOH (A) before and (B) after self-assembly; (C) absorption spectra. Concentration: 0.05 mM. Path length: 1 mm. Scale bars: 500 nm.

In fact, **(G∧C)$_2$-Por 2** can form RNTs in MeOH without heating, although heating can lead to instant self-assembly. The spontaneous self-assembly process of **(G∧C)$_2$-Por 2** in MeOH was tracked by SEM (Figure 2.31). MeOH was added to **(G∧C)$_2$-Por 2** and the solution was shaken by a vortex mixer. The SEM sample of this fresh solution shows some amorphous particles which are thought to be the undissolved compound. After 1 h the particles are gone and short RNTs are present, with the length of a few hundred nanometers. After 2 d, the length of some RNTs reaches over 10 μm.

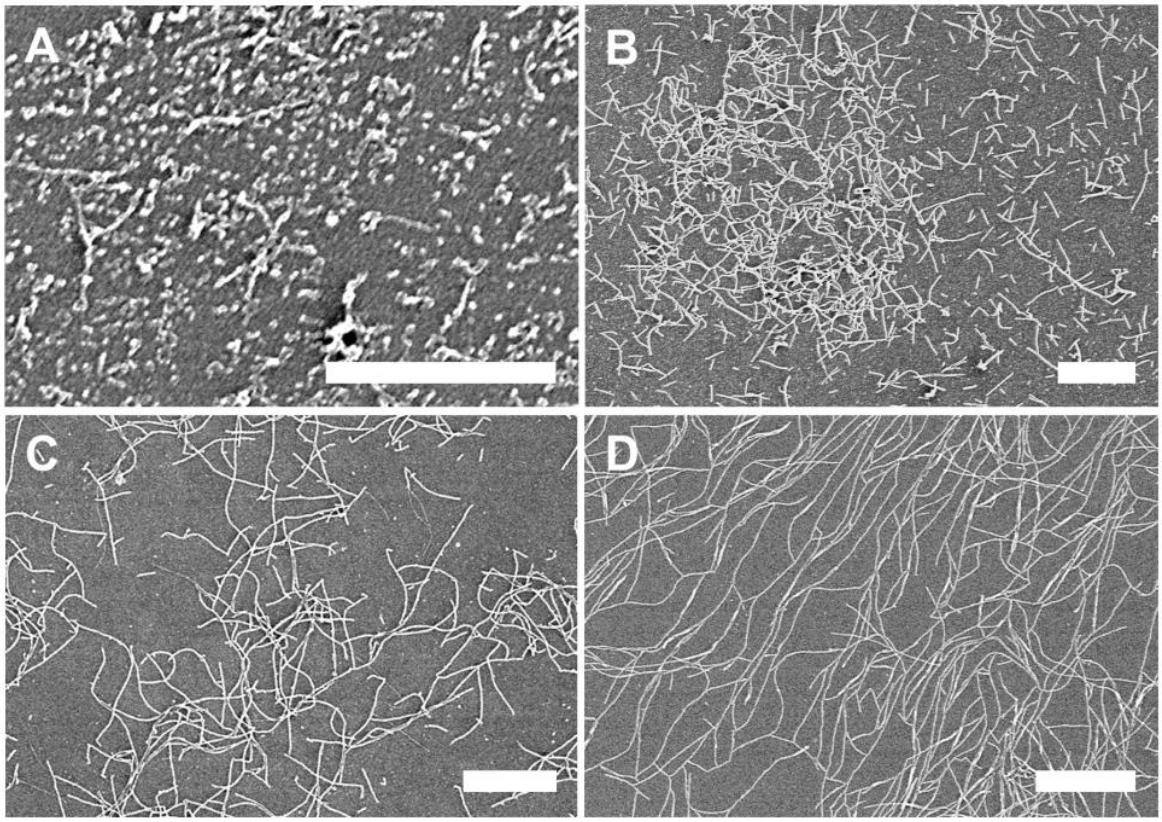

Figure 2.31. SEM images of spontaneous self-assembly of **(G∧C)$_2$-Por 2** in MeOH at different aging time. (A) 1 min; (B) 1 h; (C) 3 h; (D) 2 d. Concentration: 0.07 mM. Scale bars: 500 nm.

2.8.2 (G∧C)$_2$-Por 2 in a binary solvent system

Although MeOH is a good solvent to process self-assembled RNTs of **(G∧C)$_2$-Por 2**, it cannot be used in the wet process of an OPV device that has $PC_{61}BM$ as the component in the active layer, because $PC_{61}BM$ is insoluble in MeOH. On the other hand, $PC_{61}BM$ is very soluble in 1,2-DCB, with the solubility up to 42.1 mg/mL (46.2 mM). Most of polymer electron-donor materials are also highly soluble in 1,2-DCB. The compatibility makes 1,2-DCB the most used solvent in the active layer casting of $PC_{61}BM$-polymer blend.

Since MeOH and 1,2-DCB are miscible, a mixture of the two was used to improve the solubility of **(G∧C)$_2$-Por 2**. Indeed, **(G∧C)$_2$-Por 2** can be dissolved at a high concentration in the binary solvent system. The solubility increases as the proportion of MeOH increases. In a mixture of 1,2-DCB/MeOH (7:3, v/v), a solution can be prepared at a concentration of 20 mg/mL (14.0 mM). The optimized self-assembly condition is to add the binary solvent to a pre-weight amount of **(G∧C)$_2$-Por 2**, mix them well by a vortex mixer, heat the solution to boiling point for 2 min, and cool it to room temperature. The clear solution has a deep green color, and the formation of long RNTs is almost instant after this process (Figure 2.32A). In fact, the self-assembly process of **(G∧C)$_2$-Por 2** is spontaneous. With a moderate period of aging, long RNTs are also found in the solution even with no heating (Figure 2.32B). The good self-assembly capability of **(G∧C)$_2$-Por 2** is mainly due to the doubled hydrogen bonding sites in the twin G∧C motif, and a good solubility in the binary solvent.

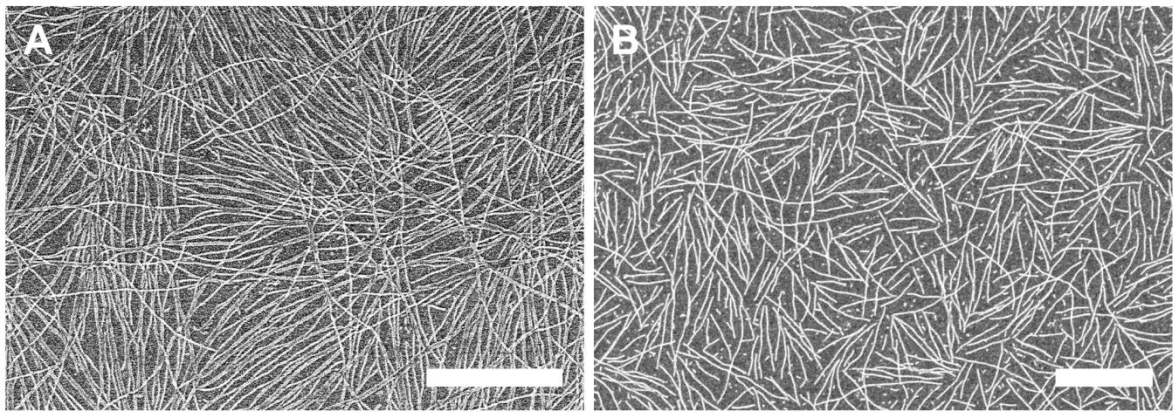

Figure 2.32. SEM images of **(G∧C)$_2$-Por 2** RNTs in 1,2-DCB/MeOH (7:3, v/v, 0.07 mM) under different processing conditions. (A) heating (70 °C, 2 min), aging (30 min); (B) sonication (30 s), aging (7 d). Scale bars: 500 nm.

2.8.3 Organogel of (G∧C)$_2$-Por 2

The solution of **(G∧C)$_2$-Por 2** in a mixture of 1,2-DCB/MeOH has a tendency to form a self-supporting organogel (defined as absence of flow upon inversion of the vial). A stock solution with a low concentration at 0.07 mM (1 mg/mL) formed an organogel after aging for 30 d at room temperature (Figure 2.33A–C). When the organogel was applied to vibration and sonication for a short period of time, it became a viscous liquid (Figure 2.33D). An interpenetrating network of long RNTs was found in the solution by SEM imaging (Figure 2.33E). Interestingly, the solution turned to an organogel again after aging for 1 d (Figure 2.33F), indicating that its formation is reversible. Heating also turns the organogel to the corresponding solution, and the solution forms an organogel again over time.

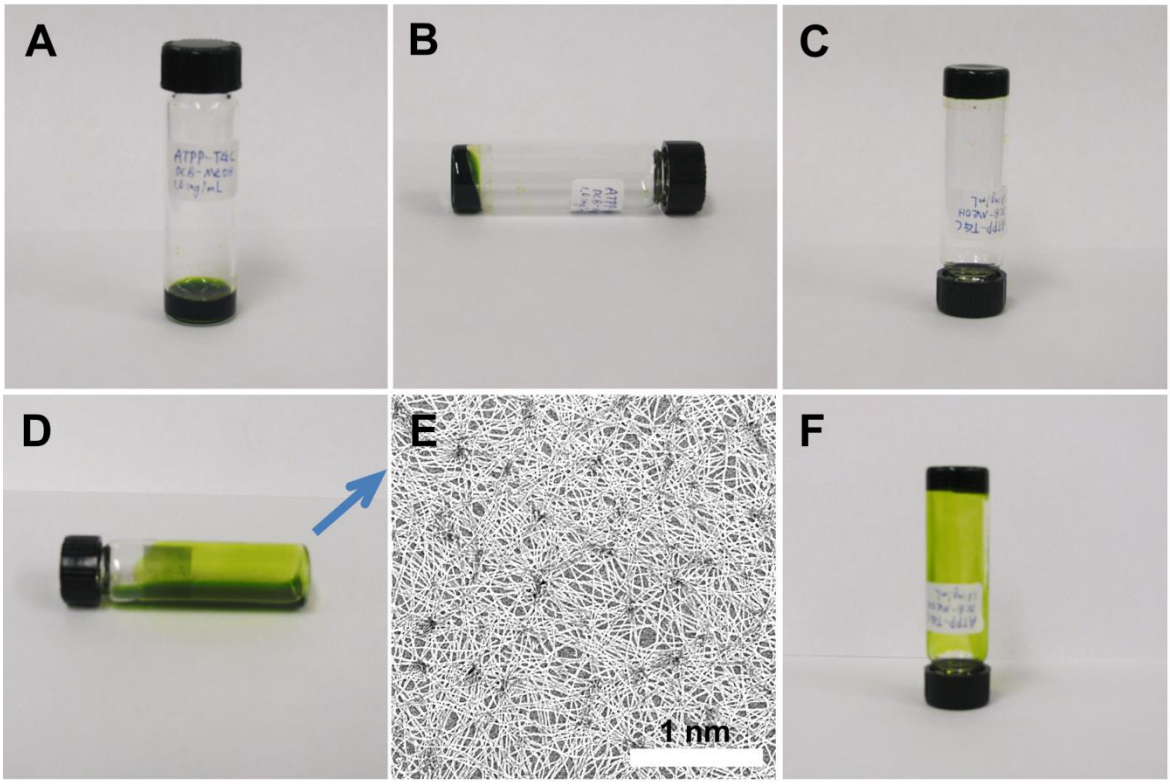

Figure 2.33. A vial sample of organogel of **(G∧C)$_2$-Por 2**. (A–C) a solution of **(G∧C)$_2$-Por 2** turns to an organogel in 1,2-DCB/MeOH (7:3, v/v, 0.07 mM), aging for 30 d; (D) organogel turns to liquid after vibration and sonication; (E) SEM image of solution (D), scale bar: 500 nm; (F) solution (D) turns to organogel again after 1 d aging.

The gelation of **(G∧C)$_2$-Por 2** in solution is likely due to strong intermolecular interactions between the self-assembled RNTs and the solvent molecules. Since the RNTs elongate and entangle over time, they form an interpenetrating network that retains and immobilizes the solvent. As the network grows, it exhibits gel-like physical properties. The RNTs-solvent interactions involve only weak forces including hydrogen bonding, π–π stacking and hydrophobic interaction, so the organogel breaks up when it is heated at a high temperature, or applied to vibration and sonication for a period of time. Interestingly, the

gelation of **(G∧C)$_2$-Por 2** is solvent-dependent. A MeOH solution became viscous but did not form an organogel even after aging for 1 year. For the binary solvent system, the greater the proportion of the 1,2-DCB in the solution, the shorter gelation time it takes. This is attributed to the hydrophobic interaction between the RNTs and 1,2-DCB as it is a non-polar aromatic solvent. The gelation of **(G∧C)$_2$-Por 2** is also concentration-dependent. At a high concentration, the gelation time of the solution is short, and the strength of the organogel is strong, as it needs a long period of time of heating to break it up. At a concentration low as 0.2 mM (0.3 mg/mL), the solution of **(G∧C)$_2$-Por 2** in the mixture of 1,2-DCB/MeOH (7:3, v/v) still forms an organogel.

The studies above indicate that **(G∧C)$_2$-Por 2** is a good small-molecule gelator via self-assembly. The reversibility of the organogel formation may imply new applications of this material. To achieve this goal, more gelation parameters need to be collected, such as the organogel network strength and viscoelasticity.

2.8.4 Thermodynamics of self-assembly

Since **(G∧C)$_2$-Por 2** has a good solubility in a mixture of 1,2-DCB/MeOH, the thermodynamics of the self-assembly process can be investigated by variable temperature (VT) UV-Vis spectroscopy and SEM imaging. Herein a fresh solution of **(G∧C)$_2$-Por 2** was gradually heated to 60 °C and then cooled to 20 °C. Only short stacks of rosettes were found in the SEM imaging when the compound was initially dissolved in the solution at 20 °C. As the temperature was elevated, the stacks grew longer to form RNTs. Upon cooling, the RNTs extended to several micrometers in length and entangled to form an intercrossing network (Figure 2.34).

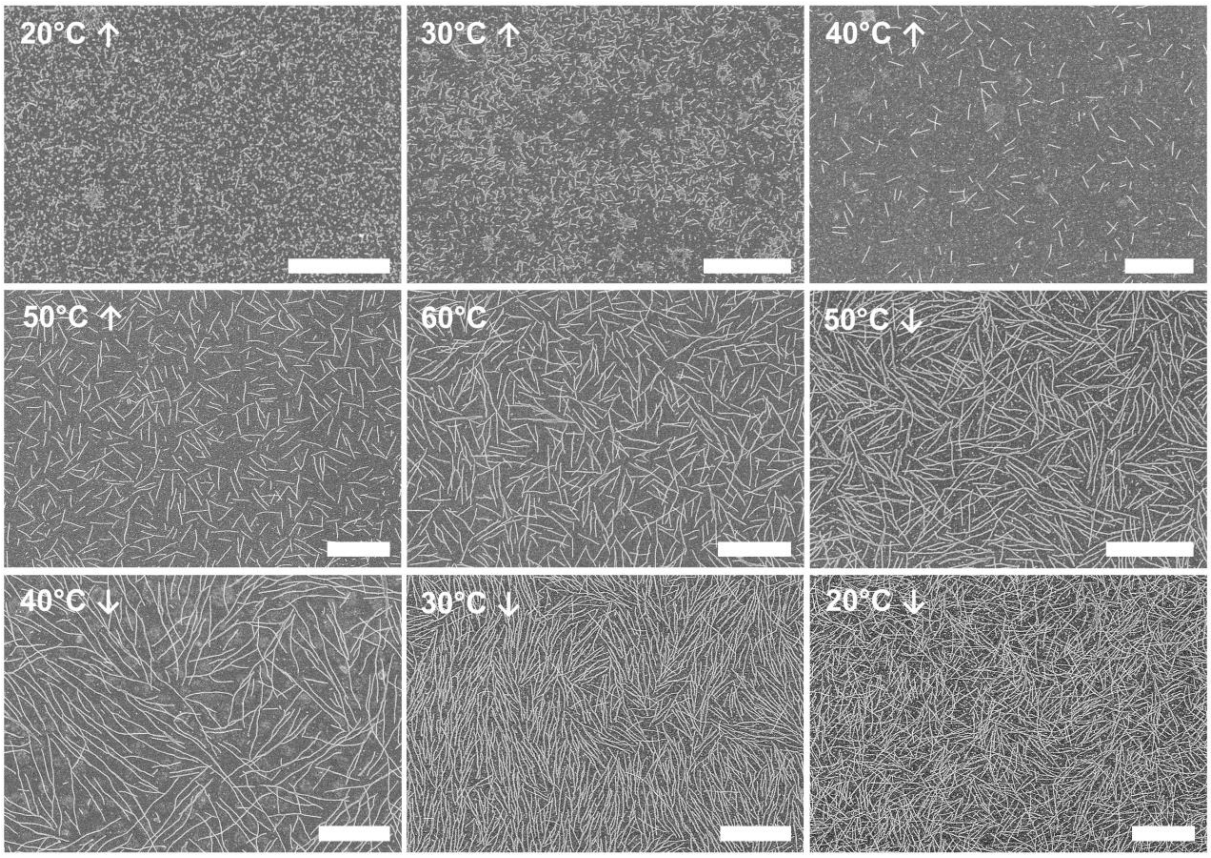

Figure 2.34. SEM images of **(G∧C)$_2$-Por 2** RNTs (0.07 mM in 1,2-DCB/MeOH, 7:3, v/v) at different temperatures. Condition: the temperature was controlled by a digital water bath system with a 2 min interval for every 5 °C change. Scale bars: 500 nm.

Red shifts and intensity changes in both Soret and Q bands were observed in the absorption spectra during the self-assembly process (Figure 2.35). In the Soret band region, the peak at 423 nm decreased, and the one at 447 nm decreased upon heating and then increased upon cooling. A new shoulder appeared at 466 nm. The plot of absorbance at 446 nm as a function to temperature fits a sigmoid function, revealing the isodesmic self-assembly mechanism of **$(G\wedge C)_2$-Por 2**.[45] On the other hand, the Q band shifted from 667 nm to 676 nm, accompanied with an increase in absorbance. These spectroscopic changes indicate that the peripheral porphyrin groups on RNTs also adopt a J-type arrangement. In addition, the absorbance at 299 nm also decreased, which is also indicative of the formation of RNTs, as this band is characteristic for G∧C motifs. Upon self-assembly, G∧C motifs are shielded in the channel of RNTs by the outside functional groups and their resonance behaviors are restricted by the H-bonds, which normally results a decrease in absorbance of the G∧C bands.

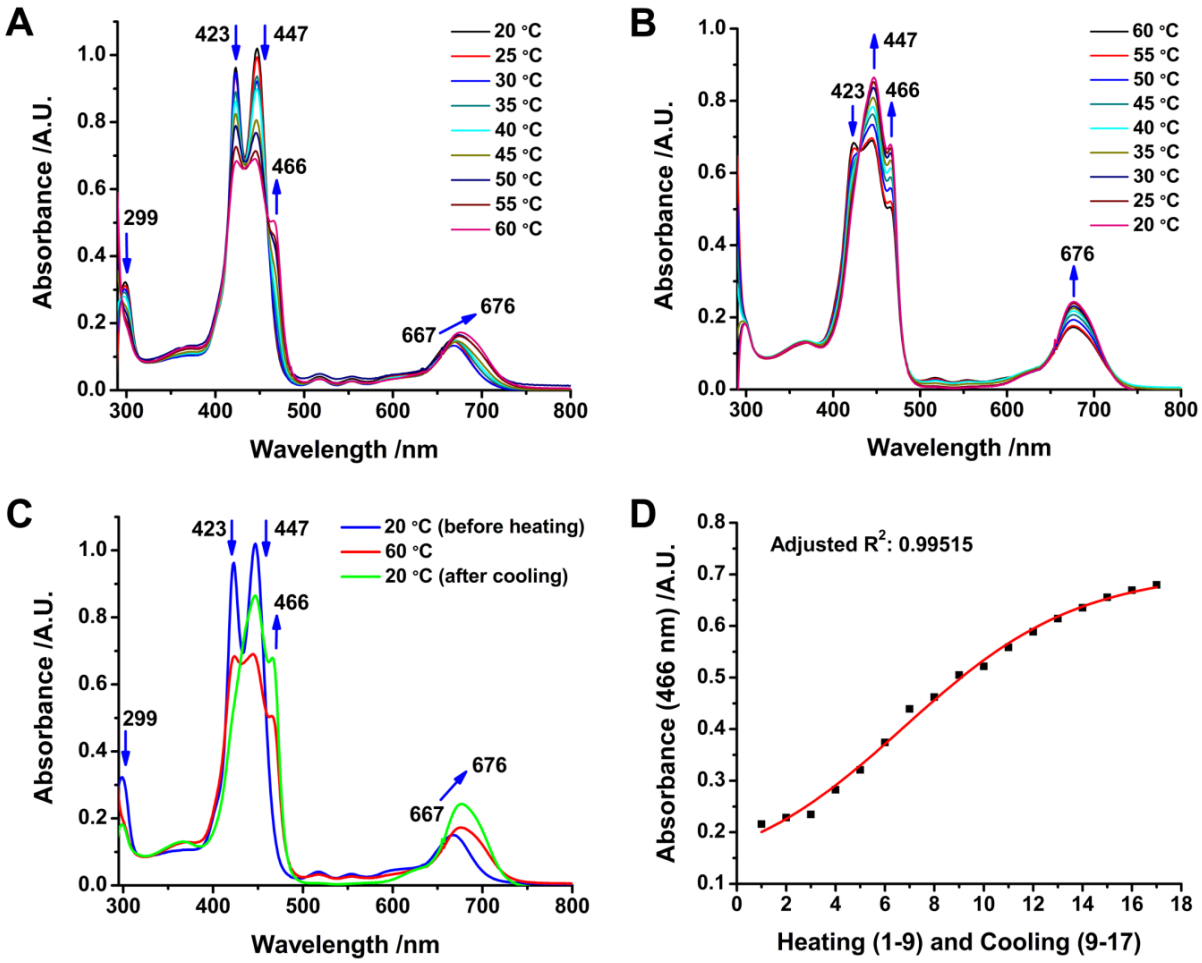

Figure 2.35. VT UV-Vis spectra of a solution of **(G∧C)$_2$-Por 2** (0.07 mM in 1,2-DCB/MeOH, 7:3, v/v). (A) Heating; (B) cooling; (C) comparison before heating and after cooling; (D) plot of absorbance at a fixed wavelength (466 nm) as a function of temperature. Condition: the temperature was controlled by a digital water bath system with a 2 min interval for every 5 °C change. Path length: 1 mm.

2.8.5 TEM, AFM and STM studies of $(G\wedge C)_2$-Por 2 RNTs

Uranyl acetate in different solvents were used to stain samples of **$(G\wedge C)_2$-Por 2** RNTs for TEM. Initially the stain was prepared in MeOH, since MeOH is a good solvent for processing self-assembled RNTs. However, it was unsuccessful, as a patterned layer was observed that covers the background in the SEM imaging and leads to poor contrast in the TEM imaging. The stains in H_2O, $MeNO_2$ or CH_3CN did not work either. The best stain for **$(G\wedge C)_2$-Por 2** RNTs was found to be 0.2% uranyl acetate in acetone. RNTs with a good contrast were found both in the SEM and TEM imaging (Figure 2.36). Unlike **G∧C-Por 1** RNTs, **$(G\wedge C)_2$-Por 2** RNTs have a low tendency to form bundles, as most RNTs observed by TEM are well dispersed. The cross-sectional diameter of a single RNT of **$(G\wedge C)_2$-Por 2** is 4.9 ± 0.4 nm from the TEM measurement.

Figure 2.37 depicts the tapping mode AFM images of **$(G\wedge C)_2$-Por 2** RNTs. Although single RNTs are dominant, some entangled bundles are also present, which is probably due to the solvent evaporation effect and air turbulence over the rotating substrate during spin-casting. The single RNTs display a height of 3.9 ± 0.3 nm.

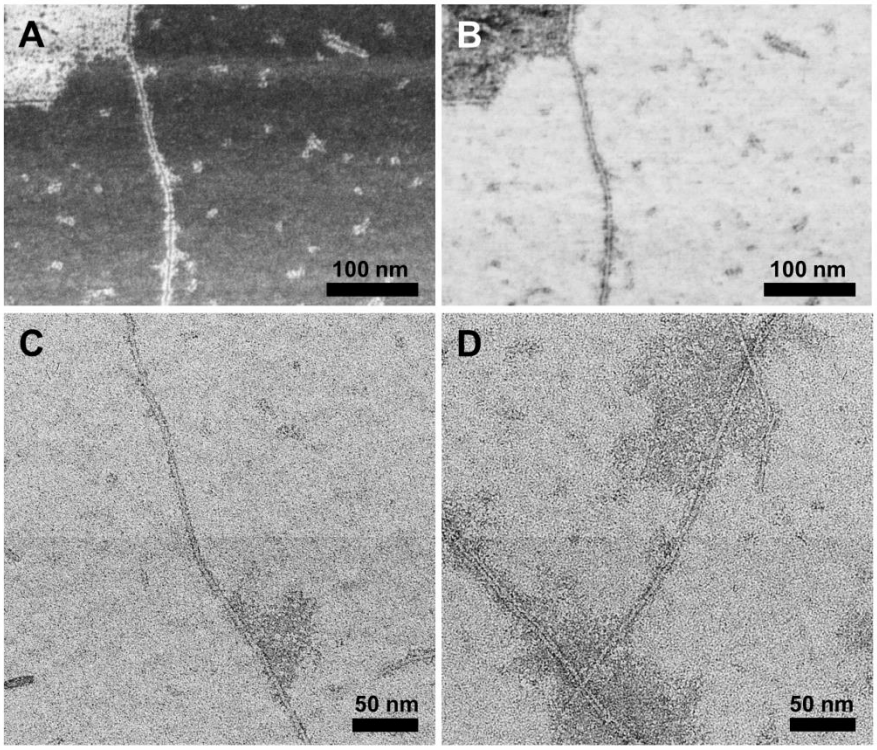

Figure 2.36. SEM and TEM images of well-stained **(G∧C)$_2$-Por 2** RNTs. SEM images taken under SE mode (A) and TE mode (B) show the same area. Concentration: 0.006 mM in 1,2-DCB/MeOH (7:3, v/v). Stain: 0.2% uranyl acetate in acetone.

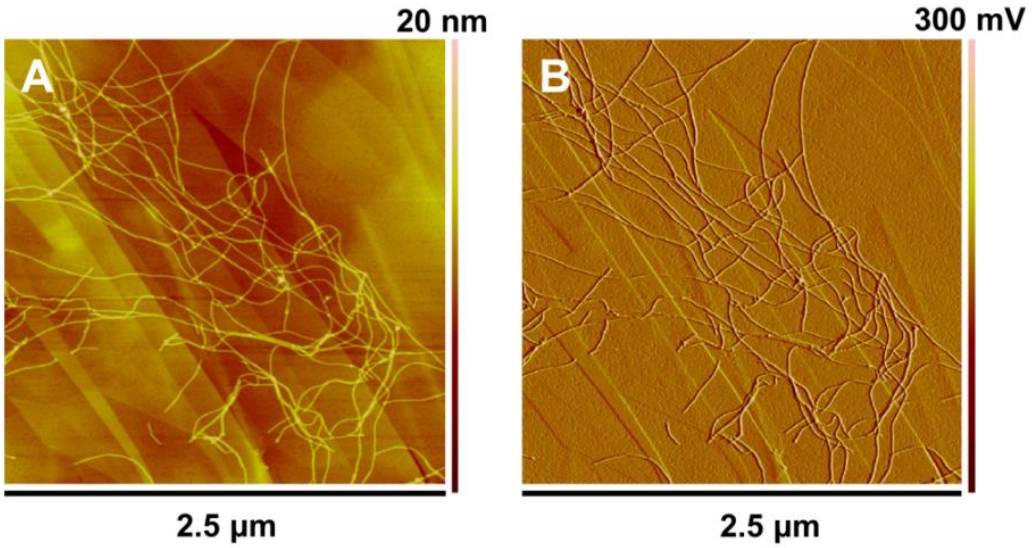

Figure 2.37. Tapping mode AFM images of **(G∧C)$_2$-Por 2** RNTs on HOPG. (A) height profile; (B) amplitude profile. Concentration: 0.03 mM in 1,2-DCB/MeOH (7:3, v/v).

Figure 2.38 depicts a STM image of a single **(G∧C)$_2$-Por 2** RNT and the current profile along a section of the RNT. The bright spots on the RNT surface are thought to be porphyrin groups, although we were unable to obtain an image with submolecular resolution. From the current profile the distance between four adjacent porphyrin groups was measured to be 4.98 nm, and the distance between two adjacent porphyrin groups was calculated to be 1.66 nm, which is almost a half to the value of 3.47 nm in the case of **G∧C-Por 1**. The shorter distance may cause more repulsion among porphyrin groups when two single RNTs are in close proximity to each other. In fact, no bundles were observed by STM.

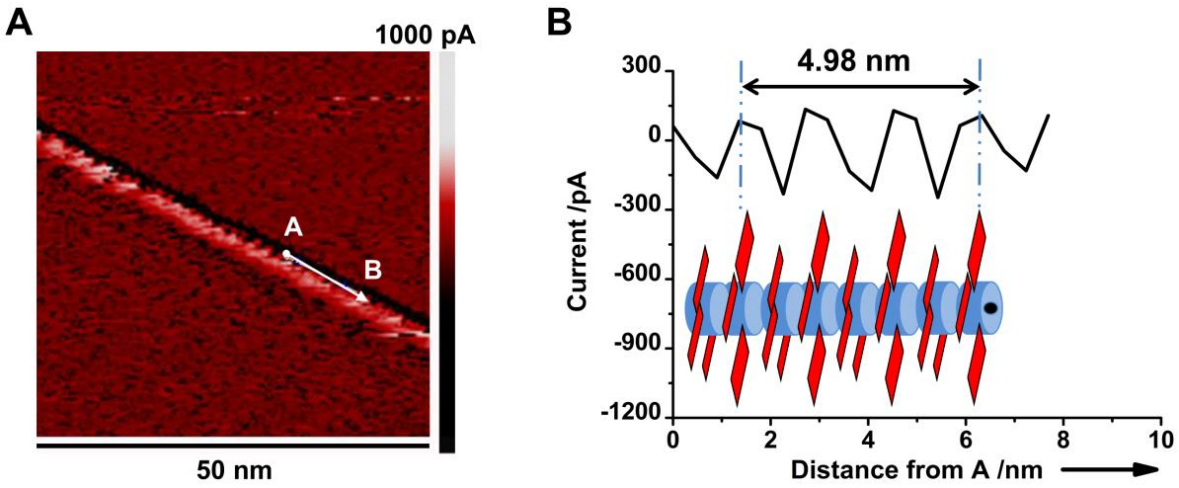

Figure 2.38. (A) STM image of a single **(G∧C)$_2$-Por 2** RNT; (B) current profile along the arrow in (A), inset is a schematic illustration of a section of the RNT, the two-headed arrow shows the distance between four adjacent porphyrin groups along the long axis. STM conditions: current setpoint: 400 pA; bias voltage: 800 mV.

2.9 Synthesis of $(G\wedge C)_2$-Por 3

The poor solubility of **$(G\wedge C)_2$-Por 2** in 1,2-DCB may be due to the highly hydrophilic amide bond, which can also form unwanted intermolecular hydrogen bonds. To improve the solubility of the porphyrin-functionalized twin G∧C building block, **$(G\wedge C)_2$-Por 3** was designed. It features an ether group that bridges porphyrin to the twin G∧C motif.

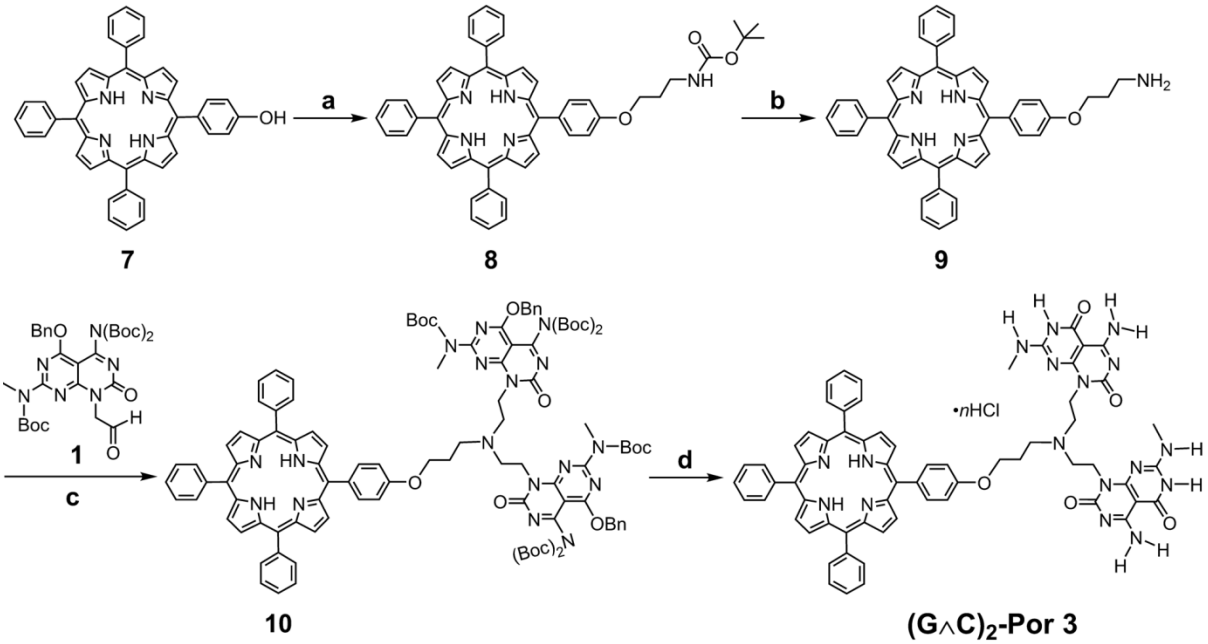

Figure 2.39. Synthesis Route of **$(G\wedge C)_2$-Por 3**. Reagents and conditions: (a) 3-(Boc-amino)propyl bromide, Cs_2CO_3, KI, DMF, 65 °C, 24 h, 97%; (b) DCM/TFA (1:1), 25 °C, 2 h, followed by work-up with $NaHCO_3$, 100%; (c) $NaBH(OAc)_3$, triethylamine, THF, 4 d, 28%; (d) HCl (4 M in dioxane), 80 °C, 4 h, quantitative yield.

Figure 2.39 shows the synthesis route of **$(G\wedge C)_2$-Por 3**. 5-(4-Hydroxylphenyl)-10,15,20-triphenylporphyrin (compound **7**) was chosen because phenol OH is a good nucleophilic group that eases modification of porphyrin with a spacer. In fact, the reaction between

compound **7** and 3-(Boc-amino)propyl bromide was smooth and quantitative. Compound **9** was obtained after deprotection of **8** and basification work-up. The reaction condition of reductive amination between **9** and G∧C aldehyde **1** was similar to that for the synthesis of **(G∧C)$_2$-Por 2**. **(G∧C)$_2$-Por 3** was obtained as a green solid after deprotection of **10** in HCl (4 M in 1,4-dioxane).

2.10 Self-Assembly of (G∧C)$_2$-Por 3

2.10.1 (G∧C)$_2$-Por 3 in 1,2-DCB

(G∧C)$_2$-Por 3 can be dissolved in 1,2-DCB at a concentration of 1.3 mM (2 mg/mL) with heating. The solution has a light brown color and did not form a precipitate even after 30 d. Although still low, the solubility is much greater than that of **(G∧C)$_2$-Por 2**. At the same concentration a **(G∧C)$_2$-Por 2** solution was turbid and quickly formed a precipitate. Figure 2.40 shows the self-assembly of **(G∧C)$_2$-Por 3** in 1,2-DCB. The solution was heated at 140 °C for 5 min. Very short stacks were found in the hot solution and long RNTs were found when the solution cooled to room temperature. This indicates that π–π stacking and hydrophobic interactions are unstable at high temperatures, but intermolecular hydrogen bonds are strong to maintain the intact hexameric rosettes. In the absorption spectra of **(G∧C)$_2$-Por 3** RNTs, a small shoulder appeared at 453 nm in the Soret band region, and the last Q band shifted from 650 nm to 678 nm. These changes are indications of porphyrin J-aggregates.

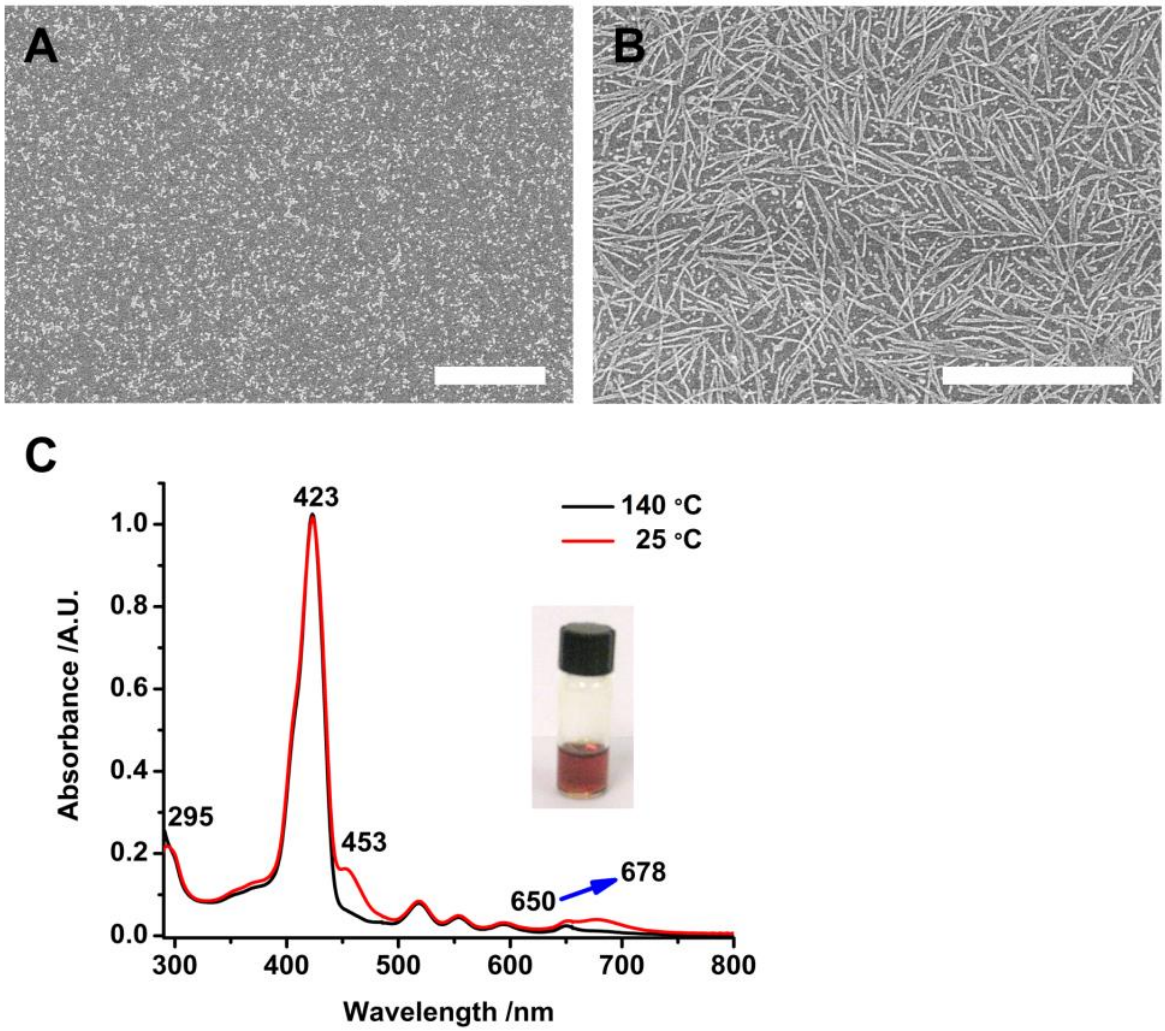

Figure 2.40. SEM images of **(G∧C)$_2$-Por 3** RNTs in 1,2-DCB at (A) 140 °C and (B) 25 °C; (C) absorption spectra, inset is a sample solution. Concentration: 0.05 mM. Path length: 1 mm. Scale bars: 500 nm.

2.10.2 $(G\wedge C)_2$-Por 3 in a binary solvent system

Similar to **$(G\wedge C)_2$-Por 2**, **$(G\wedge C)_2$-Por 3** can self-assemble in MeOH into RNTs spontaneously, and a short period of heating at boiling point leads to instant formation of assembly. When a small ratio of MeOH is added to 1,2-DCB, the solubility of **$(G\wedge C)_2$-Por 3** is largely improved in the binary solvent. In a mixture of 1,2-DCB/MeOH (9:1, v/v), it can be dissolved at a concentration of 6.6 mM (10 mg/mL). The self-assembly process is also spontaneous, and the RNTs solution becomes viscous and finally forms an organogel over time. Figure 2.41 shows a time-dependent SEM study of **$(G\wedge C)_2$-Por 3** in the binary solvent.

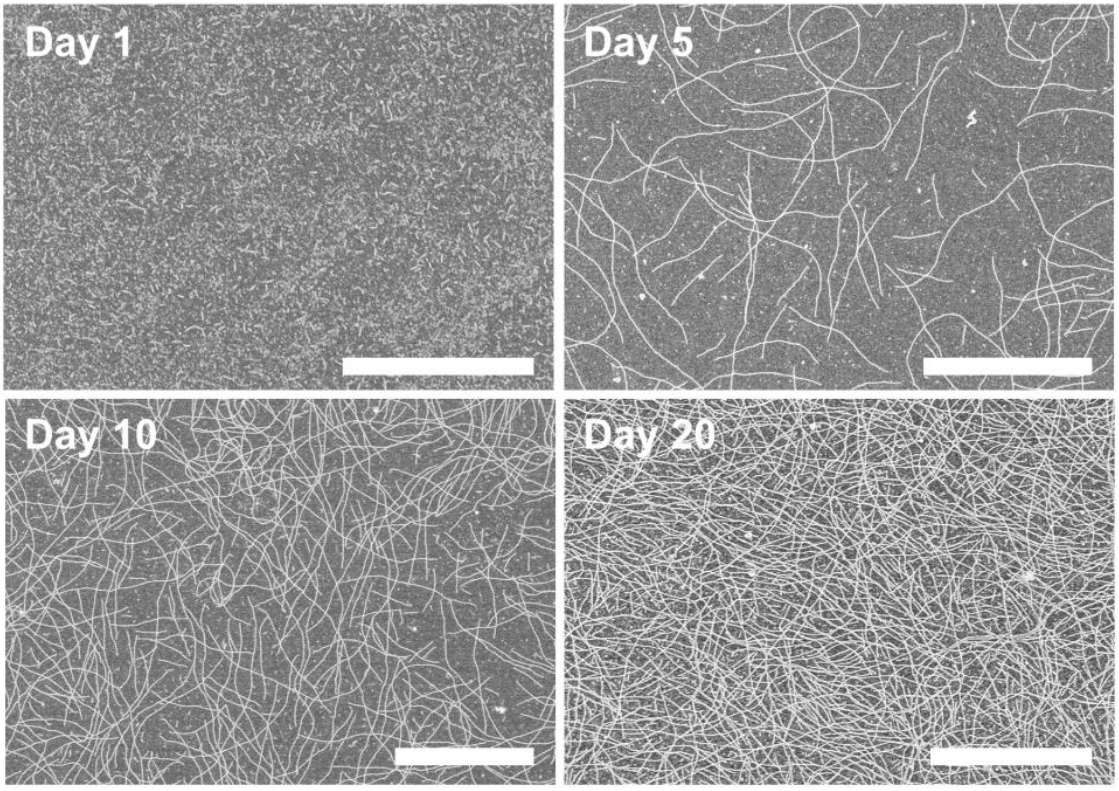

Figure 2.41. Time-dependent SEM study of **$(G\wedge C)_2$-Por 3** in 1,2-DCB/MeOH (9:1, v/v) at room temperature. Concentration: 0.07 mM. Scale bars: 1 μm.

A time-dependent UV-Vis study was also carried out to investigate the spectroscopic changes during the course of self-assembly (Figure 2.42). The absorbance of the Soret band at 422 nm does not change, and two new peaks appear at 451 nm and 465 nm, in conjunction with a red shift of the last Q band from 649 nm to 678 nm. All these changes clearly indicate that the porphyrin groups on the RNTs are J-aggregates.

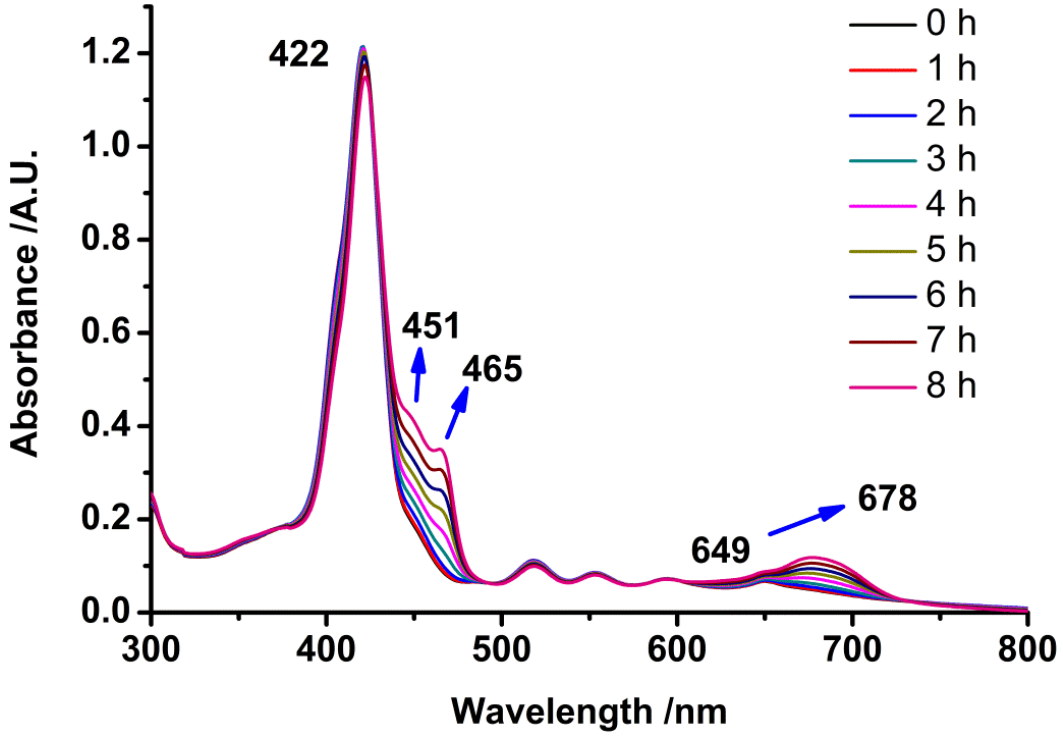

Figure 2.42. Time-dependent UV-Vis study of **(G∧C)$_2$-Por 3** in 1,2-DCB/MeOH (9:1, v/v) at room temperature. Concentration: 0.05 mM. Path length: 1 mm.

2.10.3 TEM and AFM studies of $(G\wedge C)_2$-Por 3 RNTs

The cross-sectional diameter of a single RNT of **$(G\wedge C)_2$-Por 3** was measured by tapping mode AFM and TEM (Figure 2.43). The value from height profile of AFM is 3.9 ± 0.4 nm, and the one from TEM is 5.0 ± 0.3 nm. The diameter is very close to that of a single RNT of **$(G\wedge C)_2$-Por 2**.

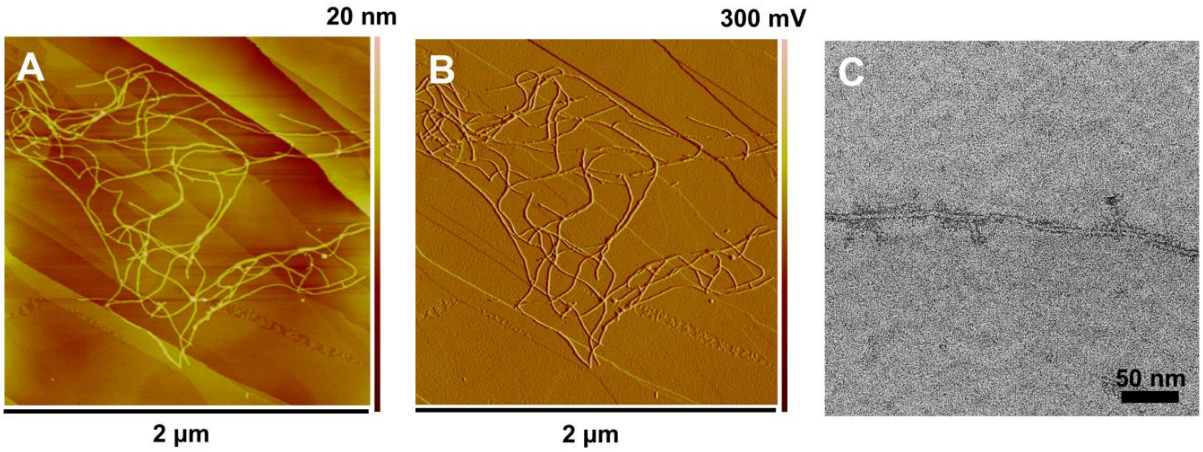

Figure 2.43. Tapping mode AFM and TEM images of **$(G\wedge C)_2$-Por 3** RNTs. (A) height profile; (B) amplitude profile. AFM sample concentration: 0.03 mM in 1,2-DCB/MeOH (7:3, v/v). TEM stain: 0.2% uranyl acetate in acetone.

2.11 Photoluminescence of RNTs

Porphyrins are well-known fluorescent dyes. A qualitative photoluminescence study was carried out for the three types of porphyrin-functionalized RNTs in solution. The normalized fluorescence spectra are presented in Figure 2.44. **G∧C-Por 1** has two emission peaks at 651 nm and 714 nm in $MeNO_2$. **$(G\wedge C)_2$-Por 2** has two emission peaks at 654 nm and 718 nm in a mixture of 1,2-DCB/MeOH (7:3, v/v). **$(G\wedge C)_2$-Por 3** has two emission peaks at 655 nm and 718 nm in 1,2-DCB.

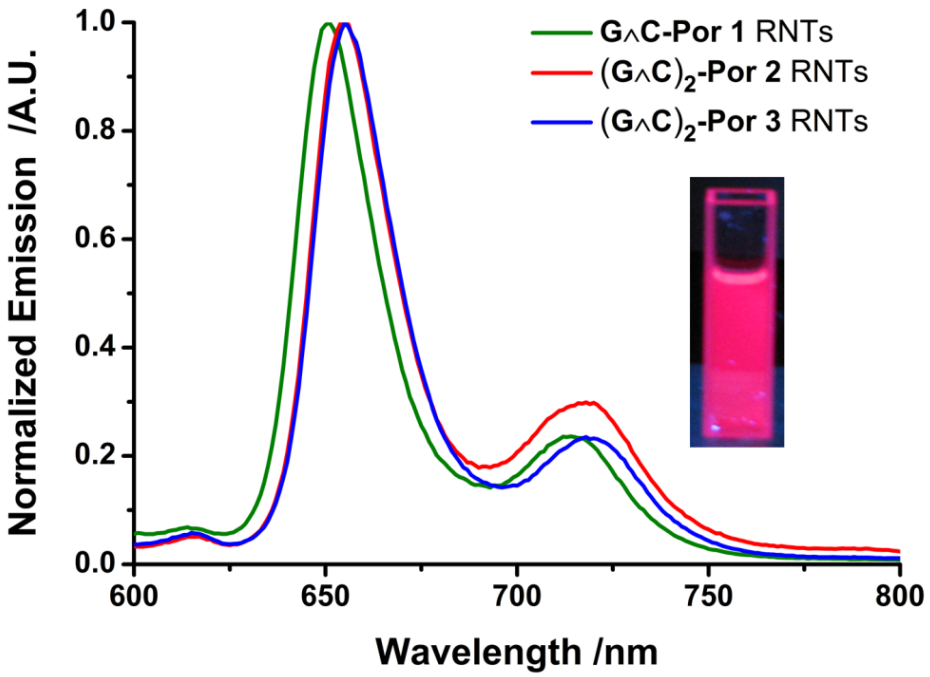

Figure 2.44. Normalized fluorescence spectra of solutions of porphyrin-functionalized G∧C RNTs excited at 518 nm. Inset shows a solution of **$(G\wedge C)_2$-Por 3** (1 μM in 1,2-DCB) under UV light (366 nm).

2.12 Conclusion

Three porphyrin-functionalized G∧C building blocks were synthesized. The desired solubility in a specific solvent was realized by tuning the functional groups on the molecules. **G∧C-Por 1** is a mono G∧C motif, whereas **$(G\wedge C)_2$-Por 2** and **$(G\wedge C)_2$-Por 3** are twin G∧C motifs. All of them can form RNTs in solution via hierarchical self-assembly, although they display different solubility and stability. Upon self-assembly, red shifts were observed both in porphyrin Soret and Q bands, indicating the porphyrin groups on the RNTs are J-aggregates.

These molecules are in the form of HCl salts. Protonation of the pyrrole N in the core of porphyin and chloride ions are essential to stabilize the tubular nanostructure. **G∧C-Por 1** can be dissolved in $MeNO_2$ at a maximum concentration of 0.5 mM. Sonication and gentle heating are required for the self-assembly process. Both **$(G\wedge C)_2$-Por 2** and **$(G\wedge C)_2$-Por 3** can spontaneously form RNTs in MeOH and mixtures of 1,2-DCB/MeOH. Instant self-assembly can be obtained by heating the solution to the boiling point. The solutions of **$(G\wedge C)_2$-Por 2** and **$(G\wedge C)_2$-Por 3** in the binary solvent can form an organogel after aging. TEM, AFM, STM and molecular modeling simulation were used to measure the diameters of the RNTs. VT UV-Vis spectroscopy and SEM were used to study the thermodynamics of self-assembly.

Optoelectronic properties of these 1D porphyrin nanotubes are discussed in Chapter 4.

2.13 Experimental section

2.13.1 Materials and methods

All of the commercially available reagents were purchased from Sigma-Aldrich or Acros Organics unless otherwise noted. NMR solvents were obtained from Cambridge Isotope Laboratories. Reagent grade solvents were purified using a MBraun (SP05-172) solvent purification system, and all other commercial reagents were used as received. All of the reactions were performed under N_2 atmosphere using oven-dried glassware equipped with a magnetic stirring bar and rubber septum unless otherwise noted. Reactions were monitored by thin layer chromatography (TLC) using either silica or alumina-coated TLC plates (Macherey-Nagel) and visualized under UV light (Entela, UVGL-58). LC-MS (Agilent 1100 series) was also used when it was necessary. Silica (Silicycle, SiliaFlash F60, 230-400 mesh) and alumina (basic, Sigma-Aldrich, Brockmann I or II) were used for flash column chromatography.

2.13.2 Characterization

2.13.2.1 Nuclear magnetic resonance spectroscopy

^{1}H, ^{13}C and 2D NMR spectra were recorded on a 600 MHz Varian VNMRS 600 spectrometer at 298 K in the specific deuterated solvents noted in the synthetic procedures section. The NMR data is presented as follows: chemical shift, multiplicity (s = singlet, d = doublet, t = triplet, m = multiplet, br s = broad singlet, br t = broad triplet), integration, coupling constant, peak assignment. ^{1}H and ^{13}C NMR spectra were referenced relative to $SiMe_4$ using the chemical shifts of the NMR solvent residual peaks.

2.13.2.2 UV-Vis spectroscopy

UV-Vis spectra were recorded on an Agilent 8453 UV-Vis spectrophotometer and a PerkinElmer Lambda 1050 UV-Vis-NIR spectrophotometer equipped with a temperature programmer system. Due to the strong absorption in the Soret band region of these molecules, in some cases an aliquot of a stock solution was diluted prior to spectra recording. To eliminate the possible disassembly effect of RNTs at a low concentration, a quartz cuvette with a path length of 1 mm was used unless otherwise noted.

2.13.2.3 Fluorescence spectroscopy

Fluorescence spectra of solutions were recorded on a PTI spectrofluorometer (QM40). Prior to spectra recording, an aliquot of a stock solution was diluted in gradient and UV-Vis spectra were recorded to ensure the emission intensity of the solution was not saturated. The solutions were excited at 518 nm, which is the wavelength of a Q band absorption maximum.

2.13.2.4 SEM imaging

SEM imaging was performed on a Hitachi S-4800 field emission high-resolution scanning electron microscope using 15–30 kV accelerating voltage and 15–20 μA current. SEM samples were prepared by casting a droplet (5 μL) of a specific sample solution on a carbon-coated 400-mesh copper grid (Electron Microscopy Sciences). After 10 s the grid was blotted by filter paper and secured in a sample box, dried in air and then placed under high vacuum for 1 day to remove any residual solvent before imaging. SEM images were taken under scanning electron (SE) mode unless otherwise noted.

2.13.2.5 TEM imaging

TEM imaging was performed on a JEOL 2200FS TEM (200 kV Schottky field emission) with an in-column omega filter and cryo pole piece. Bright field TEM images were acquired using energy filtered zero loss beam (slit width 8 eV). TEM samples were prepared by casting a droplet of a specific sample solution on a carbon-coated 400-mesh copper grid (Electron Microscopy Sciences). After 10 s the grid was blotted by filter paper and secured in a sample box, dried in air and then placed under high vacuum for 1 day to remove any residual solvent. The sample was then negatively stained by casting a droplet of uranyl acetate in a specific solvent. After 30 s the grid was blotted by filter paper and secured in a sample box, dried in air and then placed under high vacuum to remove any residual solvent. All of the stained TEM grids were examined and screened by TE mode SEM to confirm that the samples have high contrast for TEM imaging. The cross-sectional diameter of a single RNT was determined by randomly measuring individual assemblies using Digital Micrograph software (version 3.9.3 by Gatan). The data was presented in the form of average diameter ± standard deviation.

2.13.2.6 AFM imaging

AFM samples were prepared by spin-casting a droplet of a specific sample solution on a freshly cleaved HOPG or mica substrate (1 cm × 1 cm) at 2000 rpm for 40 s. Sample surface imaging was performed on a Digital Instruments/Veeco Instruments MultiMode Nanoscope IV AFM equipped with an E scanner. To get optimized height profile, silicon cantilevers (MikroMasch USA, Inc.) with a low spring constant of 4.5 N/m were used in tapping mode AFM (cantilever length 130 ± 5 μm, width 35 ± 3 μm, resonance frequency

135 kHz). To obtain a clean image from surface, low scan rate (0.5–1 Hz) and amplitude setpoint (1 V) were chosen during measurement.

2.13.2.7 STM imaging

Sample preparation for STM was the same as that for AFM, and only HOPG substrate was used as it is conductive. Prior to STM imaging, all samples were examined and screened by tapping mode AFM to confirm that it has a flat surface without any background layer and RNTs are evenly distributed on the surface. Well-defined Pt-Ir STM tips were fabricated mechanically from the alloy wire (80% Pt, 20% Ir, work function of 4.7 eV, NanoScience Instruments) which is resistant to oxidation in air. The STM images were acquired using ambient STM system, a MultiMode Nanoscope IV equipped with an A scanner. The sample sureface (500 nm × 500 nm) was scanned using a constant current mode with a low scan rate (1–2 Hz). The current setpoint and bias voltage vary in different samples.

2.13.3 Synthetic procedures of target molecules

5-(4-aminophenyl)-10,15,20-triphenylporphyrin (2)

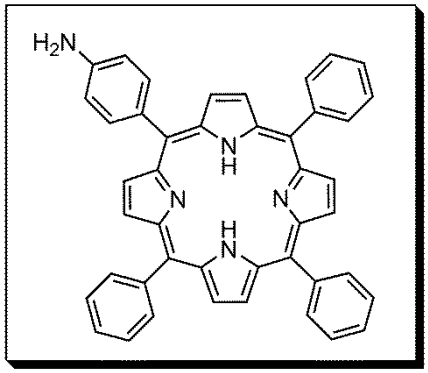

Compound **2** was synthesized following the reported methods[23] with some modification. Thus, $NaNO_2$ (123.5 mg, 1.79 mmol) was added to a solution of tetraphenylporphyrin (1.0

g, 1.63 mmol) in trifluoroacetic acid (TFA, 60 mL) at -10 °C. After stirring for 30 min, the reaction was quenched by pouring the mixture into ddH_2O (500 mL). DCM (3 × 200 mL) was used for extraction, and the organic layer was washed with aqueous $NaHCO_3$ (5%, 2 × 200 mL), ddH_2O (2 × 200 mL), dried over Na_2SO_4 and filtered. The filtrate was evaporated under reduced pressure to give a purple solid which was then dissolved in hydrochloric acid (38%, 80 mL). $SnCl_2$•2H_2O (2.64 g, 11.70 mmol) was added and the reaction mixture was heated to 68 °C for 12 h. The mixture was then poured into ice water (500 mL) and neutralized by adding ammonium hydroxide (4 M) until pH 8.0. The crude product was extracted with DCM (3 × 200 mL) and the organic layer was washed with ddH_2O (2 × 200 mL), dried over Na_2SO_4 and filtered. The filtrate was evaporated to dryness by a rotavapor. The product was purified via flash column chromatography (alumina basic, n-hexane, 30%–50% DCM) and dried under vacuum to give **2** as a purple solid (420.8 mg, 0.67 mmol, 41% over two steps).

^{1}H NMR (600 MHz, $CDCl_3$) δ (ppm): 8.96 (d, 2H, J = 4.2 Hz, β-pyrrole), 8.86 (s, 6H, β-pyrrole), 8.24 (d, 6H, J = 6.6 Hz, ortho triphenyl), 8.01 (d, 2H, J = 7.2 Hz, 4-aminophenyl), 7.75−7.80 (m, 9H, meta/para triphenyl), 7.05 (d, 2H, J = 7.2 Hz, 4-aminophenyl), 3.98 (s, 2H, NH_2), -2.71 (s, 2H, pyrrole NH).

^{13}C NMR (150 MHz, $CDCl_3$) δ (ppm): 146.2, 142.4, 142.4, 135.8, 134.7, 132.5, 131.2 (br), 127.8, 126.8, 121.0, 120.1, 119.9, 113.6. Note: The broad signal at 131.2 was assigned to the 8 β-pyrrole carbons. The signal for the 8 α-pyrrole carbons (expected around 146) did not show up in this case due to pyrrole NH tautomerism, which is common in many tetrasubstituted porphyrins.[46]

Positive LRMS (ESI): Expected mass for ($M+H^+$)/z, 630.3; Observed, 630.5 [$M+H^+$)/z].

UV-Vis (in $MeNO_2$): λ 417 nm (ε = 1.63×10^5 $cm^{-1}M^{-1}$), 515 nm (ε = 1.16×10^4 $cm^{-1}M^{-1}$), 551 nm (ε = 6.22×10^3 $cm^{-1}M^{-1}$), 591 nm (ε = 3.30×10^3 $cm^{-1}M^{-1}$), 646 nm (ε = 2.89×10^3 $cm^{-1}M^{-1}$).

Compound 3

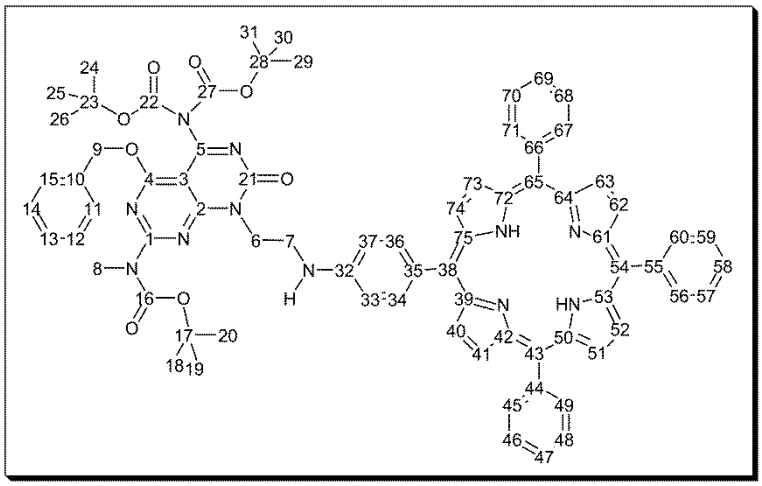

G∧C aldehyde **1**[22c] (524.5 mg, 0.82 mmol) and **2** (515.5 mg, 0.82 mmol) were dissolved in 1,2-dichloroethane (1,2-DCE, 40 mL). The mixture was stirred for 1 h at 25 °C under Ar before $NaBH(OAc)_3$ was added (175.0 mg, 0.83 mmol). Every other day, over a period of 7 days, $NaBH(OAc)_3$ (100 mg, 0.47 mmol) was added to the stirring mixture (4 × 100 mg in total). After 7 days *N*,*N*-Diisopropylethylamine (DIPEA, 0.6 mL, 3.46 mmol) was added before quenching the reaction with ddH_2O (10 mL). The organic layer was washed with ddH_2O (2 × 30 mL) and the solvent was then removed by under reduced pressure. The pure product (410 mg, 0.33 mmol, 40%) was obtained as a purple solid after purification via flash column chromatography (alumina basic, n-hexane, 10–30% EtOAc, 0.4% triethylamine).

^{1}H NMR (600 MHz, $CDCl_3$) δ (ppm): 8.96 (d, 2H, J = 4.2 Hz, β-pyrrole), 8.84−8.82 (m, 6H, β-pyrrole), 8.23 (d, 6H, J = 6.6 Hz, ortho triphenyl), 7.99 (d, 2H, J = 8.4 Hz, meta 4-aminophenyl), 7.78–7.76 (m, 9H, meta/para triphenyl), 7.48 (d, 2H, J = 7.2 Hz, ortho benzyl), 7.41–7.35 (m, 3H, meta and para benzyl), 7.02 (d, 2H, J = 8.4 Hz, ortho 4-aminophenyl), 5.63 (s, 2H, benzyl CH_2), 5.35 (br s, 1H, NH on 4-aminophenyl), 4.87 (br t, 2H, J = 5.4 Hz, β CH_2 on ethyl-NH-phenyl), 3.87 (br s, 2H, α CH_2 on ethyl-NH-phenyl), 3.57 (s, 3H, N-CH_3), 1.64 (s, 9H, Boc on guanine ring), 1.39 (s, 18H, Boc on cytosine ring), -2.70 (s, 2H, pyrrole NH).

^{13}C NMR (150 MHz, $CDCl_3$) δ (ppm): 166.1 (C_4), 161.8 (C_2), 161.2 (C_1), 160.8 (C_5), 156.3 (C_{21}), 152.5 (C_{16}), 149.6 (C_{22}, C_{27}), 148.2 (C_{32}), 142.5 (C_{44}, C_{66}), 142.4 (C_{55}), 136.0 (C_{34}, C_{36}), 135.0 (C_{10}), 134.7 (C_{45}, C_{49}, C_{56}, C_{60}, C_{67}, C_{71}), 131.2 (br, C_{40}, C_{41}, C_{51}, C_{52}, C_{62}, C_{63}, C_{73}, C_{74}), 130.8 (C_{35}), 128.79, 128.75, 128.71 (C_{12}, C_{13}, C_{14}), 128.4 (C_{11}, C_{15}), 127.8 (C_{47}, C_{58}, C_{69}), 126.80, 126.77 (C_{46}, C_{48}, C_{57}, C_{59}, C_{68}, C_{70}), 121.7 (C_{38}), 120.0 (C_{43}, C_{65}), 119.7 (C_{54}), 110.9 (C_{33}, C_{37}), 93.4 (C_3), 84.1 (C_{23}, C_{28}), 83.5 (C_{17}), 70.4 (C_9), 43.1 (C_6, C_7), 35.1 (C_8), 28.3 (C_{18}, C_{19}, C_{20}), 28.0 (C_{24}, C_{25}, C_{26}, C_{29}, C_{30}, C_{31}). Note: the signals for the 8 α-pyrrole carbons (expected around 146) did not show up in this case due to pyrrole NH tautomerism.

^{13}C ↔ ^{1}H HSQC (600 MHz, $CDCl_3$), significant correlations δ (ppm): 136.0 ↔ 7.99 (C_{34}H, C_{36}H), 134.7 ↔ 7.78–7.76 (C_{45}H, C_{49}H, C_{56}H, C_{60}H, C_{67}H, C_{71}H), 128.79, 128.75, 128.71 ↔ 7.41–7.35 (C_{12}H, C_{13}H, C_{14}H), 128.4 ↔ 7.48 (C_{11}H, C_{15}H), 127.8, 126.80, 126.77 ↔ 7.78–7.76 (C_{46}H, C_{47}H, C_{48}H, C_{57}H, C_{58}H, C_{59}H, C_{68}H, C_{69}H, C_{70}H), 110.9 ↔ 7.02 (C_{33}H, C_{37}H), 70.4 ↔ 5.63 (C_9H), 43.1 ↔ 4.87 (C_6H), 43.1 ↔ 3.87 (C_7H), 35.1 ↔

3.57 (C_8H), 28.3 ↔ 1.64 ($C_{18}H$, $C_{19}H$, $C_{20}H$), 28.0 ↔ 1.39 ($C_{24}H$, $C_{25}H$, $C_{26}H$, $C_{29}H$, $C_{30}H$, $C_{31}H$). Note: There was no signal for β-pyrrole $^{13}C \leftrightarrow {}^{1}H$ correlation.

Positive HRMS (ESI): Expected mass for $(M+H^+)/z$, 1254.5560; Observed, 1254.5557 $[M+H^+)/z]$.

Elemental Analysis: Calculated for $(C_{75}H_{71}N_{11}O_8)$•0.70(EtOAc), C: 71.00, H: 5.87, N: 11.71; Found: C: 71.04, H 5.79, N: 11.65.

UV-Vis (in $MeNO_2$): λ 417 nm ($\varepsilon = 1.70 \times 10^5$ $cm^{-1}M^{-1}$), 516 nm ($\varepsilon = 1.42 \times 10^4$ $cm^{-1}M^{-1}$), 554 nm ($\varepsilon = 8.83 \times 10^3$ $cm^{-1}M^{-1}$), 591 nm ($\varepsilon = 4.86 \times 10^3$ $cm^{-1}M^{-1}$), 648 nm ($\varepsilon = 4.70 \times 10^3$ $cm^{-1}M^{-1}$).

G∧C-Por 1

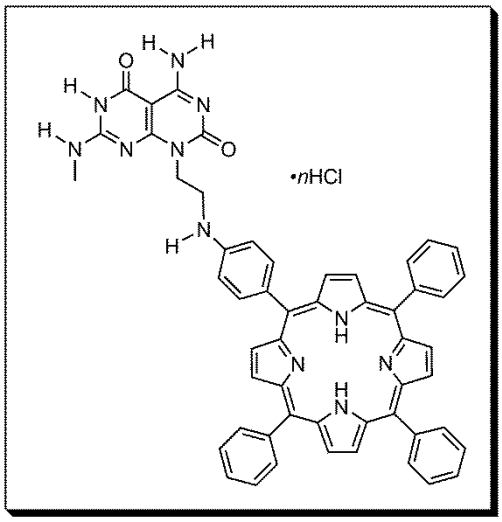

Compound **3** (260 mg, 0.21 mmol) and HCl (4 M in 1,4-dioxane, 20 mL) were added to a round bottom flask. The reaction mixture was heated at 80 °C for 4 h, cooled to room temperature and then suspended in diethyl ether (50 mL). The slurry was applied to a centrifuge and the supernatant liquid was disposed of. The precipitate was again washed with diethyl ether (6 × 20 mL) and the contents were centrifuged to remove residual solvent

and excess HCl. The precipitate was dried in the fume hood and then placed under high vacuum to provide **G∧C-Por 1** as a fine green solid (210 mg, 0.21 mmol, quantitative yield).

^{1}H NMR (600 MHz, $CDCl_3$: F_3CCOOD = 7: 1) δ (ppm): 9.31 (br s, minor) and 9.24 (br s, major) (1H, NH), 8.78 (br s, 6H, β-pyrrole), 8.74 (br t, 2H, J = 8.4 Hz, meta 4-aminophenyl), 8.66 (br s, 2H, β-pyrrole), 8.56 (br s, 2H, ortho triphenyl), 8.53 (br s, 4H, ortho triphenyl), 8.17 (br t, 2H, J = 8.4 Hz, ortho 4-aminophenyl), 8.35 (br s,1H, NH), 8.05 (br s, 9H, meta/para triphenyl), 7.91 (br s, 1H, NH), 7.68 (br s, 1H, NH), 7.59-7.45 (dd, 1H, NH), 7.31 (br s, 1H, NH), 4.96 (br s, minor) and 4.88 (br s, major) (2H, β CH_2 on ethyl-NH-phenyl), 4.33 (br s, minor) and 4.28 (br s, major) (2H, α CH_2 on ethyl-NH-phenyl), 3.22-3.12 (m, 3H, N-CH_3), -1.52 (d, 2H, J = 4.8 Hz, pyrrole-NH).

^{13}C NMR (150 MHz, $CDCl_3$: F_3CCOOD = 7: 1) δ (ppm): 164.1, 159.7, 156.0, 155.8, 146.3, 145.8, 145.6, 144.6, 141.2, 139.5, 139.4, 138.8, 138.7, 138.4, 138.3, 136.2, 131.7, 131.1, 131.0, 130.1, 129.6, 129.3, 128.7, 128.6, 128.4, 127.4, 124.9, 124.2, 124.1, 122.5, 122.4, 118.9, 81.9, 52.5, 39.8, 28.6, 28.3.

Positive HRMS (ESI): Expected mass for $(M+H^+)/z$, 864.3517, $(M+2H^+)/z$, 432.6795; Observed, 864.3515 [$(M+H^+)/z$], 432.6798 [$(M+2H^+)/z$].

Elemental Analysis: Calculated for $(C_{53}H_{41}N_{11}O_2)$•4.2(HCl), C: 62.59, H: 4.48, N: 15.15; Found: C: 62.28, H: 4.53, N: 15.47. For **G∧C-Por 1** (TFA), calculated for $(C_{53}H_{41}N_{11}O_2)$•2.62(F_3CCOOH)•2.45(H_2O), C: 57.96, H: 4.05, N: 12.77; Found: C: 57.57, H: 3.67, N: 13.17.

5-[4-(*N*-Boc-*β*-alanylamino)phenyl]-10,15,20-triphenylporphyrin (4)

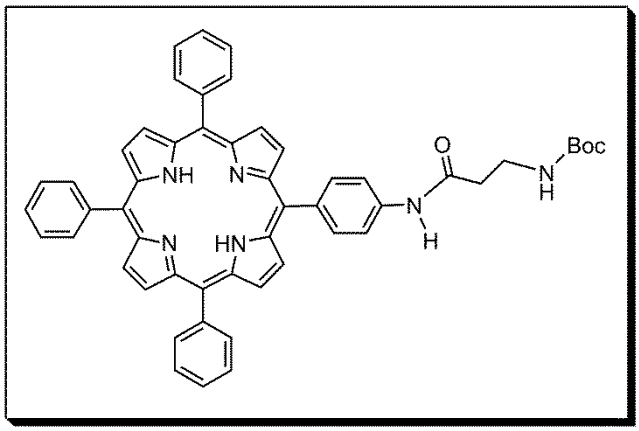

Boc-*β*-alanine (109 mg, 0.58 mmol), 1-Ethyl-3-(3-dimethylaminopropyl)carbodiimide (EDC) (110 mg, 0.58 mmol) and DIPEA (0.21 mL, 1.2 mmol) were dissolved in DCM (50 mL) in a round bottom flask. After stirring for 30 min, Compound **2** (300 mg, 0.48 mmol) was added. The reaction was allowed to run at 25 °C for 24 h. The reaction mixture was then poured to ddH_2O (100 mL) for extraction. The organic layer was continuously washed with ddH_2O (3 × 100 mL) to completely remove the byproduct urea, excess EDC and Boc-*β*-alanine. The solvent was removed by a rotavapor, and the crude product was purified via flash column chromatography (alumina basic, n-hexane, 70-100% EtOAc). The pure product **4** was obtained as a purple solid (350 mg, 0.44 mmol, 92%).

^{1}H NMR (600 MHz, $CDCl_3$) δ (ppm): 8.84-8.87 (m, 8H, *β*-pyrrole), 8.22 (d, 6H, J = 6.6 Hz, ortho triphenyl), 8.18 (d, 2H, J = 8.4 Hz, ortho anilide), 8.05 (br s, 1H, anilide NH), 7.94 (d, 2H, J = 8.4 Hz, meta anilide), 7.73−7.80 (m, 9H, meta/para triphenyl), 5.26 (br s, 1H, amide NH), 3.65 (q, 2H, J=6.0 Hz, β CH_2), 2.80 (t, 2H, J = 6.6 Hz, α CH_2), 1.52 (s, 9H, Boc), -2.77 (s, 2H, pyrrole NH).

^{13}C NMR (150 MHz, $CDCl_3$) δ (ppm): 170.0, 156.6, 142.2, 138.3, 137.6, 135.2, 134.6, 131.0, 127.8, 126.7, 120.2, 119.5, 118.1, 79.9, 38.1, 36.7, 28.5.

Positive LRMS (ESI): Expected mass for ($M+H^+$)/z, 801.4; Observed, 801.6 [$M+H^+$)/z].

5-[4-(*β*-alanylamino)phenyl]-10,15,20- triphenylporphyrin (5)

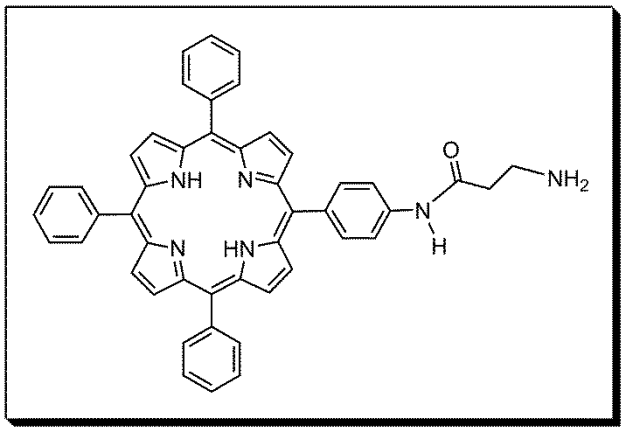

To a round bottom flask, Compound **4** (600 mg, 0.75 mmol), DCM (20 mL) and TFA (20 mL) were added. The reaction mixture was stirred at 25 °C for 2 h. The reaction was quenched by ddH_2O (150 mL). The mixture was extracted with DCM (3 × 100 mL). The organic layer was washed with aqueous $NaHCO_3$ (5%, 2 × 100 mL), ddH_2O (100 mL), brine (saturated, 50 mL) and dried over Na_2SO_4. The solvent was removed under reduced pressure to give the pure product 5 in the form of a purple solid (505 mg, 0.72 mmol, 96%).

^{1}H NMR (600 MHz, $CDCl_3$) δ (ppm): 10.33 (s, 1H, analide NH), 8.90 (d, 2H, J = 4.8 Hz, *β*-pyrrole), 8.84 (s, 6H, *β*-pyrrole), 8.22 (d, 6H, J = 6.6 Hz, ortho triphenyl), 8.16 (d, 2H, J = 8.4 Hz, ortho anilide), 7.94 (d, 2H, J = 8.4 Hz, meta anilide), 7.74−7.79 (m, 9H, meta/para triphenyl), 3.67 (br s, 2H, α CH_2), 2.84 (tt, 2H, J = 6.0 Hz, 1.8 Hz, β CH_2), 1.61 (br s, 2H, NH_2), -2.76 (s, 2H, pyrrole NH).

^{13}C NMR (150 MHz, $CDCl_3$) δ (ppm): 171.6, 142.2, 138.4, 137.3, 135.1, 134.5, 131.0, 127.7, 126.7, 120.1, 120.0, 119.9, 119.8, 118.0, 117.8, 47.3, 38.3.

Positive LRMS (ESI): Expected mass for ($M+H^+$)/z, 701.3; Observed, 701.5 [$M+H^+$)/z].

Compound 6

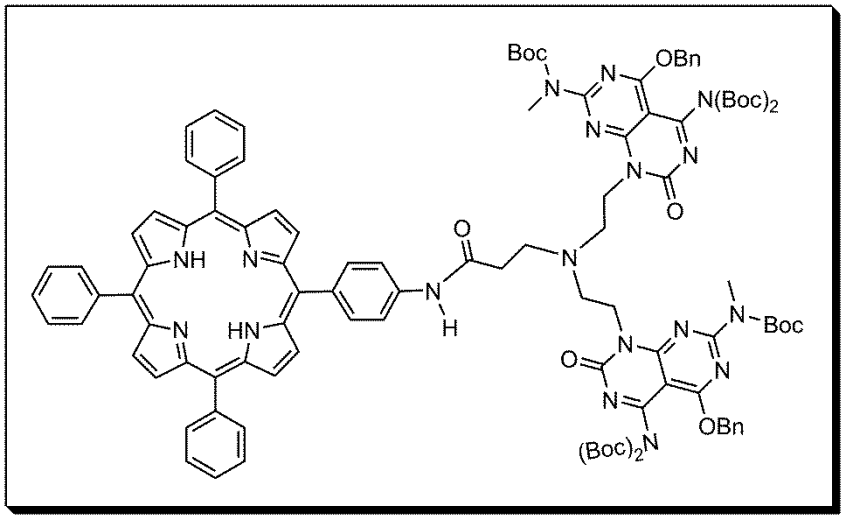

Compound **5** (505 mg, 0.72 mmol) and G∧C aldehyde **1** (692.5 mg, 1.08 mmol) were dissolved in dry THF (50 mL) in a round bottom flask. Triethylamine (0.2 mL, 1.44 mmol) was added. The reaction mixture was stirred at 25 °C under N_2 for 24 h before $NaBH(OAc)_3$ (305 mg, 1.44 mmol) was added. After 24 h, triethylamine (0.4 mL, 2.88 mmol) and aqueous $NaHCO_3$ (5%, 15 mL) were added, and the mixture was stirred for 10 min to quench the reaction. The mixture was then extracted with DCM (150 mL). The organic layer was washed by ddH_2O (100 mL), brine (saturated, 100 mL) and dried over Na_2SO_4. The solvent was removed under reduced pressure and the residue was placed under high vacuum for 12 h. The reaction procedure was repeated and new starting materials were added to push this reductive amination proceed forward. Herein the dry residue was redissolved in fresh THF (50 mL). Compound **1** (462 mg, 0.72 mmol) and triethylamine (0.2 mL, 1.44 mmol) were added. The reaction mixture was stirred at 25 °C under N_2 for 24 h, and then $NaBH(OAc)_3$ (305 mg, 1.44 mmol) was added. After 24 h, the reaction was quenched by the same procedure above and followed by the work-up. The crude product after two reaction cycles was purified via flash column chromatography

(alumina basic, n-hexane, 50-70% EtOAc). The pure product **6** was obtained as a purple solid (590 mg, 0.30 mmol, 42%).

^{1}H NMR (600 MHz, $CDCl_3$) δ (ppm): 9.66 (s, 1H, anilide NH), 8.90 (d, 2H, J = 4.2 Hz, β-pyrrole), 8.83 (s, 6H, β-pyrrole), 8.20-8.22 (m, 6H, ortho triphenyl), 8.14 (d, 2H, J =8.4 Hz, ortho anilide), 8.04 (d, 2H, J = 8.4 Hz, meta anilide), 7.73-7.79 (m, 9H, meta/para triphenyl), 7.43 (d, 4H, J =7.2 Hz, ortho benzyl), 7.30-7.34 (m, 6H, meta/para benzyl), 5.58 (s, 4H, benzyl CH_2), 4.62 (s, 4H, J =7.2 Hz, CH_2 one atom away from G∧C), 3.56 (s, 6H, N-CH_3), 3.29 (t, J =6.6 Hz, β-alanine β CH_2), 3.13 (d, 4H, J =7.2 Hz, CH_2 two atoms away from G∧C), 2.72 (6.6 Hz, β-alanine α CH_2), 1.57 (s, 18H, Boc on guanine ring), 1.33 (s, 36H, Boc on cytosine ring), -2.78 (s, 2H, pyrrole NH).

^{13}C NMR (150 MHz, $CDCl_3$) δ (ppm): 171.0, 165.9, 161.5, 161.1, 160.7, 156.0, 152.5, 149.5, 142.4, 138.1, 137.5, 135.3, 135.0, 134.7, 131.2 (br), 128.7, 128.6, 127.8, 126.8, 120.2, 120.1, 118.1, 93.2, 84.0, 83.2, 70.3, 51.1, 51.0, 41.6, 36.3, 35.3, 28.2, 28.0.

Positive HRMS (ESI): Expected mass for $(M+2H^+)/z$, 975.4456; Observed, 975.4439 $[M+2H^+)/z]$.

UV-Vis (in MeOH): Porphyrin moiety λ 415 nm ($\varepsilon = 2.64 \times 10^5$ $cm^{-1}M^{-1}$), 512 nm ($\varepsilon = 1.13 \times 10^4$ $cm^{-1}M^{-1}$), 548 nm ($\varepsilon = 5.89 \times 10^3$ $cm^{-1}M^{-1}$), 588 nm ($\varepsilon = 3.86 \times 10^3$ $cm^{-1}M^{-1}$), 645 nm ($\varepsilon = 2.67 \times 10^3$ $cm^{-1}M^{-1}$); $(G\wedge C)_2$ moiety 220 nm ($\varepsilon = 4.86 \times 10^4$ $cm^{-1}M^{-1}$), 239 nm (4.47×10^4 $cm^{-1}M^{-1}$), 324 nm (2.93×10^4 $cm^{-1}M^{-1}$), 337 nm (2.73×10^4 $cm^{-1}M^{-1}$).

(G∧C)$_2$-Por 2

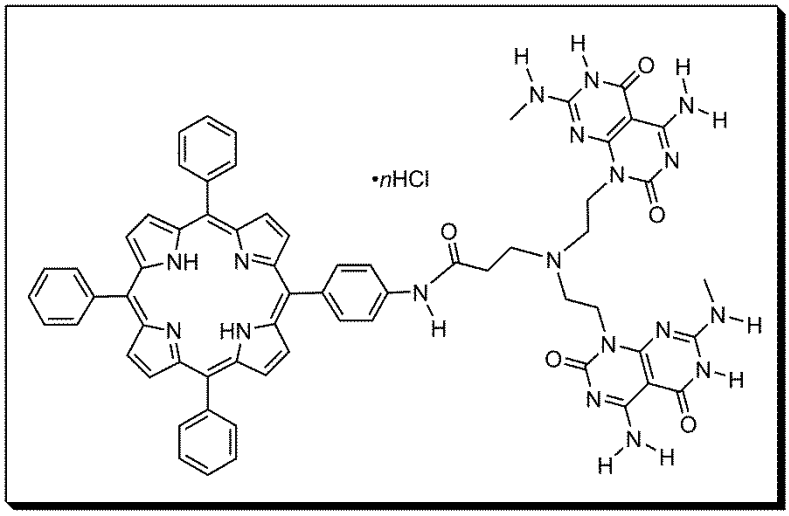

Compound **6** (500 mg, 0.26 mmol) was dissolved in HCl (4 M in 1,4-dioxane, 25 mL). The reaction mixture was stirred at 80 °C for 4 h. After the mixture cooled down, diethyl ether (100 mL) was added to form a suspension. The mixture was then applied to a centrifuge and the supernatant was disposed of. The precipitate was again washed with diethyl ether (6 × 20 mL) and the contents were centrifuged to remove residual solvent and excess HCl. The precipitate was dried in the fume hood and then placed under high vacuum to provide **(G∧C)$_2$-Por 2** as a fine green solid (365 mg, 0.25 mmol, quantitative yield).

^{1}H NMR (600 MHz, F$_3$CCOOD) δ (ppm): 9.15 (br s, 6H, β-pyrrole), 9.12 (br s, 2H, β-pyrrole), 9.05 (br s, 2H, ortho anilide) 8.94 (br s, 6H, ortho triphenyl), 8.53 (br s, 2H, meta anilide), 8.37 (dd, 9H, meta/para triphenyl), 5.35-5.09 (br m, 4H, CH_2 one atom away from G∧C), 4.58-4.32 (br m, 6H, $N(CH_2)_3$), 3.83 (br s, 2H, β-alanine α CH_2), 3.55 (br s, 6H, N-CH_3).

^{13}C NMR (150 MHz, F$_3$CCOOD) δ (ppm): 171.0, 164.3, 163.4, 160.6, 159.9, 156.5, 156.1, 155.4, 146.2, 146.1, 145.8, 139.3, 138.8, 138.4, 131.1, 129.8, 129.6, 129.1, 128.7, 124.5, 122.0, 121.4, 83.2, 82.6, 51.2, 38.1, 37.7, 28.3, 27.8.

Positive LRMS (ESI): Expected mass for $(M+H^+)/z$, 1169.4754, $(M+2H^+)/z$, 585.2413, $(M+3H^+)/z$, 390.4966; Observed, 1169.4749 [$(M+H^+)/z$], 585.2413 [$(M+2H^+)/z$], 390.4966 [$(M+3H^+)/z$].

Elemental Analysis: Calculated for $(C_{65}H_{56}N_{18}O_5)$• 6(HCl)•2.5(H_2O), C: 54.48, H: 4.71, N: 17.59; Found: C: 54.51, H 4.96, N: 17.43.

5-[4-(3-(Boc-amino)propoxy)phenyl]-10,15,20-triphenylporphyrin (**8**)

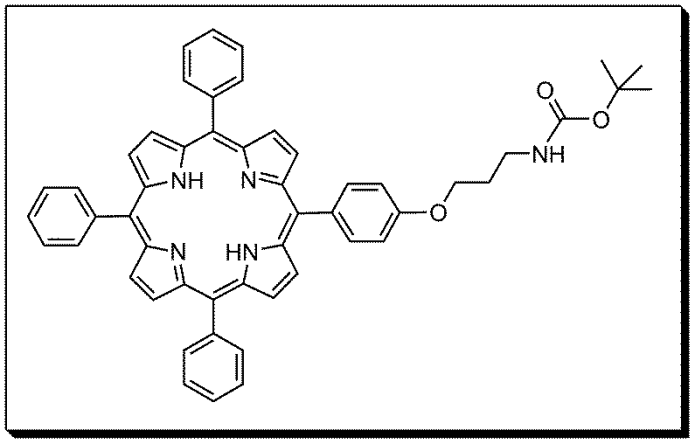

5-(4-Hydroxylphenyl)-10,15,20-triphenylporphyrin (compound **7**, 250 mg, 0.40 mmol, Frontier Scientific), 3-(Boc-amino)propyl bromide (124 mg, 0.52 mmol), Cs_2CO_3 (195 mg, 0.60 mmol), KI (20 mg, 0.12 mmol) and DMF (10 mL) were added into a round bottom flask. The reaction mixture was stirred at 65 °C for 24 h. The solvent was then removed under reduced pressure and the residue was dispersed in DCM (50 mL) and then filtered. The DCM in the filtrate was removed under reduced pressure, and the crude product was purified by flash column chromatography (alumina basic, n-hexane, 30% EtOAc) to provide **8** as a purple solid (305 mg, 0.39 mmol, 97%).

^{1}H NMR (600 MHz, $CDCl_3$) δ (ppm): 8.88 (d, 2H, J = 4.2 Hz, β-pyrrole), 8.84 (s, 6H, β-pyrrole), 8.22-8.23 (m, 6H, ortho tripheyl), 8.13 (dd, 2H, J = 6.0 Hz, 1.8 Hz, meta phenol

ether), 7.74-7.80 (m, 9H, meta/para triphenyl), 7.28 (dd, 2H, J = 6.0 Hz, 1.8 Hz, ortho phenol ether), 4.92 (br s, 1H, Boc-NH), 4.32 (t, 2H, J = 6.0 Hz, O-CH_2-), 3.51 (q, 2H, J = 6.0 Hz, 6.0 Hz, CH_2), 2.18 (t, 2H, J = 6.0 Hz, N-CH_2-), 1.51 (s, 9H, Boc), -2.76 (s, 2H, pyrrole NH).

^{13}C NMR (150 MHz, $CDCl_3$) δ (ppm): 158.8, 156.3, 142.4, 142.38, 142.35, 135.8, 134.9, 134.7, 134.6, 127.8, 126.8, 120.2, 120.1, 112.9, 79.5, 29.9, 28.6, 28.5.

Positive LRMS (ESI): Expected mass for ($M+H^+$)/z, 788.4; Observed, 788.5 [$M+H^+$)/z].

5-[4-(3-aminopropoxy)phenyl]-10,15,20-triphenylporphyrin (9)

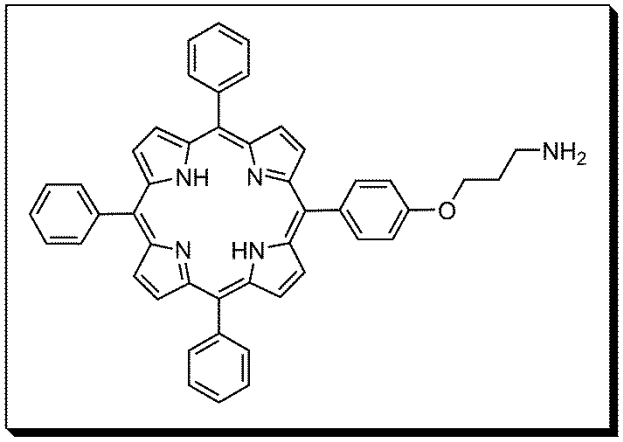

Compound **8** (305 mg, 0.39 mmol) was dissolved in DCM (10 mL) in a round bottom flask and then TFA (10 mL) was added. The reaction mixture was stirred at 25 °C for 2 h. The reaction was quenched by adding ddH_2O (50 mL), followed by extraction with DCM (3 × 50 mL). The organic layer was neutralized by aqueous $NaHCO_3$ (5%, 2 × 50 mL), washed with ddH_2O (50 mL), and brine (50 mL). The solvent was removed under reduced pressure to provide the pure product **9** as a purple solid (265 mg, 0.39 mmol, 100%).

^{1}H NMR (600 MHz, $CDCl_3$) δ (ppm): 8.89 (d, 2H, J = 4.8 Hz, β-pyrrole), 8.85 (s, 6H, β-pyrrole), 8.22 (d, 6H, J = 7.8 Hz, ortho tripheyl), 8.12 (dd, 2H, J = 6.0 Hz, 2.4 Hz, meta

phenol ether), 7.74-7.80 (m, 9H, meta/para triphenyl), 7.28 (dd, 2H, J = 6.0 Hz, 1.8 Hz, ortho phenol ether), 4.35 (t, 1H, J = 6.0 Hz, O-CH_2-), 3.10 (br s, 2H, N-CH_2-), 2.13 (p, 2H, J = 6.6 Hz, CH_2), 1.44 (br s, 2 H, NH_2), -2.75 (s, 2H, pyrrole NH).

^{13}C NMR (150 MHz, $CDCl_3$) δ (ppm): 159.0, 142.4, 142.3, 135.8, 134.7, 131.2 (br), 127.8, 126.8, 120.25, 120.22, 120.1, 112.9, 66.3, 39.6, 33.5.

Positive LRMS (ESI): Expected mass for ($M+H^+$)/z, 688.3; Observed, 688.5 [$M+H^+$)/z].

Compound 10

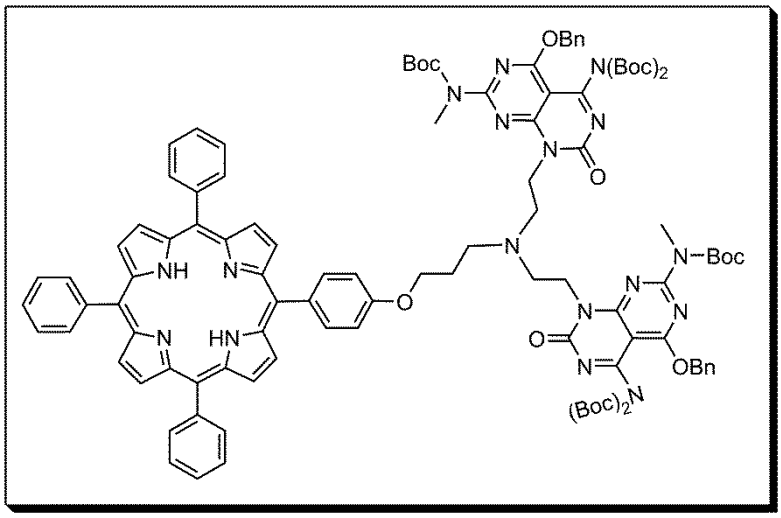

To a round bottom flask, Compound **9** (200 mg, 0.29 mmol), compound **1** (280 mg, 0.44 mmol), triethylamine (0.08 mL, 0.58 mmol) and THF (15 mL) were added. The reaction mixture was stirred at 25 °C under N_2 for 24 h before $NaBH(OAc)_3$ (123 mg, 0.58 mmol) was added. The reaction was quenched by adding aqueous $NaHCO_3$ (5%, 20 mL), and the mixture was extracted by DCM (3 × 50 mL). The organic layer was washed by ddH_2O (50 mL), brine (50 mL) and dried over Na_2SO_4. The solvent was removed under reduced pressure and the residue was placed under high vacuum for 12 h. The procedure was repeated to move the reaction forward. Herein the residue was redissolved in THF (15 mL),

and compound **1** (280 mg, 0.44 mmol) and triethyl amine (0.08 mL, 0.58 mmol) were added. After 24 h, $NaBH(AcO)_3$ (123 mg, 0.58 mmol) was added. The reaction mixture was stirred at 25 °C under N_2 for 24 h, followed by quenching and extraction in the same way above. The crude product was purified using flash column chromatography (alumina basic, n-hexane, 30-50% EtOAc) to provide **10** as a purple solid (157 mg, 0.08 mmol, 28%).

^{1}H NMR (600 MHz, $CDCl_3$) δ (ppm): 8.89 (d, 2H, J = 4.8 Hz, β-pyrrole), 8.84 (s, 6H, β-pyrrole), 8.21-8.23 (m, 6H, ortho tripheyl), 8.10 (dd, 2H, J = 8.4 Hz, meta phenol ether), 7.73-7.79 (m, 9H, meta/para triphenyl), 7.45 (d, 4H, J = 6.6 Hz, ortho benzyl), 7.28-7.35 (m, 6H, meta/para benzyl),7.27 (d, 2H, J = 7.8 Hz, ortho phenol ether), 5.59(s, 4H, benzyl CH_2), 4.53 (t, 4H, J =8.4 Hz, CH_2 one atom away from G∧C), 4.29 (t, 2H, J = 6.0 Hz, O-CH_2), 3.57 (s, 6H, N-CH_3), 3.05-3.09 (m, 6H, $N(CH_2)_3$), 2.14 (q, 2H, J = 6.6 Hz, CH_2), 1.58 (s, 18H, Boc on guanine ring), 1.32 (s, 36H, Boc on cytosine ring), -2.76 (s, 2H, pyrrole NH).

^{13}C NMR (150 MHz, $CDCl_3$) δ (ppm): 165.8, 161.4, 161.3, 160.5, 155.8, 152.7, 149.4, 142.4, 135.7, 135.1, 134.7, 128.68, 128.66, 127.8, 126.8, 120.2, 112.9, 93.1, 83.8, 83.0, 70.2, 66.3, 51.3, 51.1, 41.6, 35.2, 28.3, 28.1, 28.0.

Positive HRMS (ESI): Expected mass for $(M+2H^+)/z$, 968.9479; Observed, 968.9484 $[(M+2H^+)/z]$.

(G∧C)$_2$-Por 3

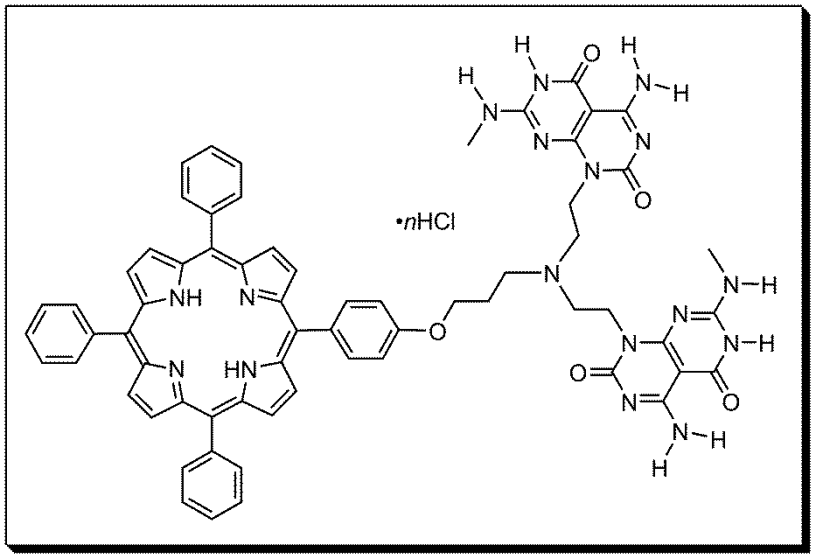

Compound **10** (140 mg, 0.07 mmol) was dissolved in HCl (4 M in 1,4-dioxane, 10 mL). The reaction mixture was stirred at 80 °C for 4 h. After cooling to room temperature, the mixture was poured into diethyl ether (100 mL) to form a suspension. The mixture was centrifuged and the supernatant was disposed of. The precipitate was again washed with diethyl ether (6 × 20 mL) and then centrifuged to remove residual solvent and excess HCl. The precipitate was dried in the fume hood and then placed under high vacuum to provide **(G∧C)$_2$-Por 3** as a fine green solid (102 mg, 0.07 mmol, quantitative yield).

^{1}H NMR (600 MHz, F$_3$CCOOD) δ (ppm): 9.14 (m, 4 H, β-pyrrole), 9.10 (br s, 4H, β-pyrrole), 8.98 (br s, 2H, meta phenol ether), 8.94-8.91 (m, 6 H, ortho triphenyl), 8.37-8.34 (m, 9H, meta/para triphenyl), 7.99 (br s, 2H, ortho phenol ether), 5.37-5.18 (br m, 4H, N-CH_2 one atom away from G∧C), 4.91 (br s, 2H, O-CH_2), 4.49 (br m, 6H, N(CH_2)$_3$), 3.59-3.51 (br d, 6H, N-CH_3), 2.97 (br s, 2H, CH_2).

^{13}C NMR (150 MHz, F_3CCOOD) δ (ppm): 164.3, 163.4, 160.7, 159.9, 156.5, 156.1, 155.4, 146.5, 146.2, 146.1, 145.7, 140.4, 138.8, 138.3, 138.1, 131.1, 129.8, 129.6, 129.4, 129.1, 128.7, 124.3, 123.6, 83.2, 82.5, 66.5, 65.2, 38.0, 37.8, 28.2, 27.7.

Positive HRMS (ESI): Expected mass for $(M+2H^+)/z$, 578.7437; Observed, 578.7440 $[(M+2H^+)/z]$.

Elemental Analysis: Calculated for $(C_{65}H_{57}N_{17}O_5)$•7(HCl)•6.1(H_2O), C: 51.31, H: 5.05, N: 15.65; Found: C: 51.30, H 5.02, N: 15.69.

2.14 References

(1) Fuhrhop, J.-H. *Langmuir* **2014**, *30*, 1–12.

(2) Caughey, W. S.; Ibers, J. A. *J. Am. Chem. Soc.* **1977**, *99*, 6639−6645.

(3) Silvers, S. J.; Tulinsky, A. *J. Am. Chem. Soc.* **1967**, *89*, 3331–3337.

(4) (a) O'Shea, D. F.; Miller, M. A.; Matsueda, H.; Lindsey, J. S. *Inorg. Chem.* **1996**, *35*, 7325–7338. (b) Conant, J. B.; Chow, B. F.; Dietz, E. M. *J. Am. Chem. Soc.* **1934**, *56*, 2185–2189. (c) Aronoff, S. *J. Phys. Chem.* **1958**, *62*, 428–431.

(5) (a) De Luca, G.; Romeo, A.; Scolaro, L. M.; Ricciardi, G.; Rosa, A. Inorg. Chem. 2007, 46, 5979–5988. (b) Rudine, A. B.; DelFatti, B. D.; Wamser, C. C. J. Org. Chem. 2013, 78, 6040–6049. (c) Honda, T.;Kojima, T.; Fukuzumi, S.; *Chem. Common.***2009**, 4994–4996.

(6) (a) Hasobe, T.; Fukuzumi, S.; Kamat, P. V. *J. Am. Chem. Soc.* **2005**, *127*, 11884–11885. (b) Walter, R. I.; Ojadi, E. C. A.; Linschitz, H. *J. Phys. Chem.* **1993**, *97*, 13308–13312.

(7) (a) Stone, A.; Fisher, E. B. *J. Am. Chem. Soc.***, 1968**, *90*, 2735–2748. (b) Ma, Y.-P.; He, S.-G.; Ding, X.-L.; Wang, Z.-C.; Xue, W.; Shi, Q. *Phys. Chem. Chem. Phys*. **2009**, *11*, 2543–2552.

(8) (a) Gouterman, M. *J. Mol. Spectrosc.* **1961**, *6*, 138–163. (b) Gouterman, M.; Wagniere, G.; Snyder, L. R. *J. Mol. Spectrosc.* **1963**, *11*, 108–127.

(9) (a) Gouterman, M. *J. Chem. Phys.* **1959**, *30*, 1139–161. (b) Rosa, A.; Ricciardi, G.; Baerends, E. J.; Romeo, A.; Monsù Scolaro, L. *J. Phys. Chem. A* **2003**, *107*, 11468–11482. (c) Taniguchi, M.; Cramer, D. L.; Bhise, A. D.; Kee, H. L.; Bocian, D. F.; Holten, D.; Lindsey, J. S. *New J. Chem.* **2008**, *32*, 947–958.

(10) (a) Drain, C. M.; Varotto, A.; Radivojevic, I. *Chem. Rev.* **2009**, *109,* 1630–1658. (b) Elemans, J. A. A. W.; van Hameren, R.; Nolte, R. J. M.; Rowan, A. E. *Adv. Mater.* **2006**,

18, 1251–1266. (c) Maiti, N. C.; Mazumdar, S.; Periasamy, N. *J. Phys. Chem. B* **1998**, 102, 1528 –1538. (d) Ohno, O.; Kaizu, Y.; Kobayashi, H.; J. Chem. Phys.**1993**, *99*, 4128–4139.

(11) (a) Jelley, E. E. *Nature* **1936**, 1009–1010. (b) Eisfeld, A.; Briggs, J. S. *Chem. Phys.* **2006**, *324*, 376–384. (c) McHale, J. L. *J. Phys. Chem. Lett.* **2012**, *3*, 587–597.

(12) (a) Sternberg, E. D.; Dolphin, D, Brückner, C. *Tetrahedron* **1998**, *54*, 4151–4202. (b) Lovell, J. F.; Jin, C. S.; Huynh, E.; Jin, H.; Kim, C.; Rubinstein, J. L.; Chan, W. C. W.; Cao, W.; Wang, L. V.; Zheng, G. *Nat. Mater.* **2011**, *10*, 324–332. (c) Ng, K. K.; Lovell, J. F.; Vedadi, A.; Hajian, T.; Zheng, G. *ACS NANO*, **2013**, *7*, 3484–3490.

(13) (a) Lu, H.; Zhang, X. P. *Chem. Soc. Rev.* **2011**, *40*, 1899–1909. (b) Rose, E.; Andrioletti, B.; Zrig, S.; Quelquejeu-Etheve, M. *Chem. Soc. Rev.* **2005**, *34*, 573–583. (c) Chen, G.-Q.; Xu, Z.-J.; Zhou, C.-Y.; Che, C.-M. *Chem. Commun.* **2011**, *47*, 10963–10965. (d) Ma, C.; Xing, D.; Zhai, C.; Che, J.; Liu, S.; Wang, J.; Hu, W. *Org. Lett.* **2013**, *15*, 6140–6143.

(14) (a) Jurow, M.; Schuckman, A. E.; Batteas, J. D.; Drain, C. M. *Coord. Chem. Rev.* **2010**, 254, 2297–2310. (b) Imaoka, T.; Ueda, H.; Yamamoto, K. *J. Am. Chem. Soc.* **2012**, 134, 8412–8415. (c) Auwärter, W.; Seufert, K.; Bischoff, F.; Ecija, D.; Vijayaraghavan, S.; Joshi, S.; Klappenberger, F.; Samudrala, N.; Barth, J. V. *Nat. Nanotechnol.* **2012**, *7*, 41–46.

(15) (a) Li, L.-L.; Diau, E. W.-G. *Chem. Soc. Rev.* **2013**, *42*, 291–304. (b) Imahori, H.; Fukuzumi, S. *Adv. Funct. Mater.* **2004**, *14*, 525–536. (c) Yamamoto, T.; Hatano, J.; Nakagawa, T.; Yamaguchi, S.; Mastsuo, Y. *Appl. Phys. Lett.* **2013**, *102*, 013305. (d) Hatano, J.; Obata, N.; Yamaguchi, S.; Yasuda, T.; Matsuo, Y. *J. Mater. Chem.* **2012**, *22*, 19258–19263. (e) Huang, Y.; Li, L.; Peng, X.; Peng, J.; Cao, Y. *J. Mater. Chem.* **2012**, *22*, 21841–21844.

(16) (a) Collman, J. P.; McDevitt, J. T.; Yee, G. T.; Leitner, C. R.; McCullough, L. G.; Little, W. A.; Torrance, J. B. *Proc. Natl. Acad. Sci. U.S.A.* **1986**, *83*, 4581–4585. (b) Ogawa, K.; Kobuke, Y. *Angew. Chem., Int. Ed.* **2000**, *39*, 4070–4073. (c) Lu, G.; Zhang, X.; Cai, X.; Jiang, J. *J. Mater. Chem.* **2009**, *19*, 2417–2424.

(17) (a) Wang, Z.; Medforth, C. J.; Shelnutt, J. A. *J. Am. Chem. Soc.* **2004**, *126*, 15954–15955. (b) Rich, C. C.; McHale, J. L. *Phys. Chem. Chem. Phys.* **2012**, *14*, 2362–2373. (c) Lauer, M. E.; Fuhrhop, J.-H. *Langmuir* **2004**, *20*, 8321–8328.

(18) (a) Hasobe, T.; Saito, K.; Kamat, P. V.; Troiani, V.; Qiu, H.; Solladié, N.; Kim, K. S.; Park, J. K.; Kim, D.; D'Souza, F.; Fukuzumi, S. *J. Mater. Chem.* **2007**, *17*, 4160–4170. (b) Wang, Q.; Chen, Y.; Ma, P.; Lu, J.; Zhang, X.; Jiang, J. *J. Mater. Chem.* **2011**, *21*, 8057–8065. (c) Li, H. P.; Martin, R. B.; Harruff, B. A.; Carino, R. A.; Allard, L. F.; Sun, Y. P. *Adv. Mater.* **2004**, *16*, 896–900. (d) Fendt, L.; Bouamaied, I.; Thoni, S.; Amiot, N.; Stulz, E. *J. Am. Chem. Soc.* **2007**, *129*, 15319–15329. (e) Lee, S. J.; Hupp, J. T.; Nguyen, S. T. *J. Am. Chem. Soc.* **2008**, *130*, 9632–9633. (f) van Hameren, R.; Schön, P.; Van Buul, A. M.; Hoogboom, J.; Lazarenko, S. V.; Gerritsen, J. W.; Engelkamp, H.; Christianen, P. C. M.; Heus, H. A.; Maan, J. C.; Rasing, T.; Speller, S.; Rowan, A. E.; Elemans, J. A. A. W.; Nolte, R. J. M. *Science* **2006**, *314*, 1433–1436. (g) Sengupta, S.; Ebeling, D.; Patwardhan, S.; Zhang, X.; von Berlepsch, H.; Böttcher, C.; Stepanenko, V.; Uemura, S.; Hentschel, C.; Fuchs, H.; Grozema, F. C.; Siebbeles, L. D. A.; Holzwarth, A. R.; Chi, L.; Würthner, F. *Angew. Chem., Int. Ed.* **2012**, *51*, 6378–6382. (h) Charvet, R.; Yamamoto, Y.; Sasaki, T.; Kim, J.; Kato, K.; Takata, M.; Saeki, A.; Seki, S.; Aida, T. *J. Am. Chem. Soc.* **2012**, *134*, 2524–2527. (i) Tu, S.; Kim, S. H.; Joseph, J.; Modarelli, D. A.; Parquette, J. R. *J. Am.*

Chem. Soc. **2011**, *133*, 19125–19130. (j) Fathalla, M.; Neuberger, A.; Li, S. C.; Schmehl, R.; Diebold, U.; Jayawickramarajah, J. *J. Am. Chem. Soc.* **2010**, *132*, 9966–9967.

(19) Fenniri, H.; Deng, B.-L.; Ribbe, A. E.; Hallenga, K.; Jacob, J.; Thiyagarajan, O. *Proc. Natl. Acad. Sci. U.S.A.* **2002**, *99*, 6487–6492.

(20) (a) Luguya, R.; Jaquinod, L.; Fronczek, F. R.; Vicente, M. G. H.; Smith, K. M. *Tetrahedron* **2004**, *60*, 2757–2763. (b) Kruper, W.J.; Chamberlin, T.A.; Kochanny, M. *J. Org. Chem.* **1989**, *54*, 2753–2756.

(21) Abdel-Magid, A. F.; Carson K. G.; Harris, B. D.; Maryanoff, C. A.; Shah, R. D. *J. Org. Chem.* **1996,** *61,* 3849–3862.

(22) (a) Okada, S.; Segawa, H. *J. Am. Chem. Soc.* **2003**, *125*, 2792–2796. (b) Sakata, A.; Kobuke, Y. *Org. Biomol. Chem.* **2007**, *5*, 1679–1691.

(23) (a) Nagayama K. *Eur. Biophys. J.* **2008**, *37*, 345–358. (b) Nagayama, K. *J. Electron Microsc.* **2011**, *60*, S43–S62.

(24) Eaton, P. and West, P. *Atomic Force Microscopy* 1st ed.; Oxford University Press: Oxford, 2010.

(25) (a) Kasumov, A. Y.; Klinov, D. V.; Roche, P.-E.; Guéron, S.; Bouchiat, H. *Appl. Phys. Lett.* **2004**, *84*, 1007−1009. (b) DeRose, J. A.; Revel, J.-P. *Thin Solid Films* **1998**, *331*, 194−202.

(26) Chen, C. J. *Introduction to Scanning Tunneling Microscopy* 2nd ed.; Oxford University Press: Oxford, 2007.

(27) Otsuki, J. *Coord. Chem. Rev.* **2010**, *254*, 2311–2341.

(28) Nishino, T.; Ito, T.; Umezawa, Y. *Proc. Natl. Acad. Sci. U.S.A.* **2005**, *102*, 5659–5662.

(29) Almarsson, O.; Blasko, A.; Bruice, T. C. *Tetrahedron* **1993**, *49*, 10239–10252.

(30) (a) Hasobe, T.; Fukuzumi, S.; Kamat, P. V. *J. Am. Chem. Soc.* **2005**, *127*, 11884–11885. (b) Tu, S.; Kim, S.-H.; Joseph, J.; Modarelli, D. A.; Parquette, J. R. *ChemPhysChem* **2013**, *14*, 1609–1617.

(31) Humphrey, W.; Dalke, A.; Schulten, K. *J. Molec. Graphics* **1996**, *14*, 33–38.

(32) Moralez, J. G.; Raez, J.; Yamazaki, T.; Motkur, K.; Kovalenko, A.; Fenniri, H. *J. Am. Chem. Soc.* **2005**, *127*, 8307–8309.

(33) Wang, J.; Wolf, R. M.; Caldwell, J. W.; Kollman, P. A.; Case, D. A. *J. Comput. Chem.* **2004**, *25*, 1157–1174.

(34) MacroModel, version 9.9. Schrödinge , LLC: New York, NY, USA, 2011.

(35) Bayly, C. I.; Cieplak, P.; Cornell, W.; Kollman, P. A. *J. Phys. Chem.* **1993**, *97*, 10269–10280.

(36) Gaussian 09, Revision D.01, Frisch, M. J.; Trucks, G. W.; Schlegel, H. B.; Scuseria, G. E.; Robb, M. A.; Cheeseman, J. R.; Scalmani, G.; Barone, V.; Mennucci, B.; Petersson, G. A.; Nakatsuji, H.; Caricato, M.; Li, X.; Hratchian, H. P.; Izmaylov, A. F.; Bloino, J.; Zheng, G.; Sonnenberg, J. L.; Hada, M.; Ehara, M.; Toyota, K.; Fukuda, R.; Hasegawa, J.; Ishida, M.; Nakajima, T.; Honda, Y.; Kitao, O.; Nakai, H.; Vreven, T.; Montgomery, J. A., Jr.; Peralta, J. E.; Ogliaro, F.; Bearpark, M.; Heyd, J. J.; Brothers, E.; Kudin, K. N.; Staroverov, V. N.; Kobayashi, R.; Normand, J.; Raghavachari, K.; Rendell, A.; Burant, J. C.; Iyengar, S. S.; Tomasi, J.; Cossi, M.; Rega, N.; Millam, N. J.; Klene, M.; Knox, J. E.; Cross, J. B.; Bakken, V.; Adamo, C.; Jaramillo, J.; Gomperts, R.; Stratmann, R. E.; Yazyev, O.; Austin, A. J.; Cammi, R.; Pomelli, C.; Ochterski, J. W.; Martin, R. L.; Morokuma, K.; Zakrzewski, V. G.; Voth, G. A.; Salvador, P.; Dannenberg, J. J.; Dapprich, S.; Daniels, A. D.; Farkas, Ö.;

Foresman, J. B.; Ortiz, J. V.; Cioslowski, J.; Fox, D. J. Gaussian, Inc., Wallingford CT, 2009.

(37) Case, D. A.; Darden, T. A.; Cheatham, T. E., III; Simmerling, C. L.; Wang, J.; Duke, R. E.; Luo, R.; Walker, R. C.; Zhang, W.; Merz, K. M.; Roberts, B.; Hayik, S.; Roitberg, A.; Seabra, G.; Swails, J.; Goetz, A. W.; Kolossváry, I.; Wong, K. F.; Paesani, F.; Vanicek, J.; Wolf, R. M.; Liu, J.; Wu, X.; Brozell, S. R.; Steinbrecher, T.; Gohlke, H.; Cai, Q.; Ye, X.; Wang, J.; Hsieh, M. J.; Cui, G.; Roe, D. R.; Mathews, D. H.; Seetin, M. G.; Salomon-Ferrer, R.; Sagui, C.; Babin, V.; Luchko, T.; Gusarov, S.; Kovalenko, A.; Kollman, P. A. AMBER 12. University of California, San Francisco, 2012.

(38) Ryckaert, J. P.; Ciccotti, G.; Berendsen, H. J. C. *J. Comput. Phys.* **1977**, *23*, 327–341.

(39) Darden, T.; York, D.; Pedersen, L. *J. Chem. Phys.* **1993**, *98*, 10089–10092.

(40) Yu, G.; Gao, J.; Hummelen, J. C.; Wudl, F.; Heeger, A. J. *Science* **1995**, *270*, 1789–1791.

(41) (a) Xin, H.; Kim, F. S.; Jenekhe, S. A. *J. Am. Chem. Soc.* **2008**, *130*, 5424–5425. (b) Li, F.; Yager, K. G.; Dawson, N. M.; Jiang, Y.-B.; Malloy, K. J.; Qin, Y. *Chem. Mater.* **2014**, *26*, 3747–3756. (c) Sun, Y.; Welch, G. C.; Leong, W. L.; Takacs, C. T.; Bazan, G. C.; Heeger, A. J. *Nat. Mater.* **2012**, *11*, 44–48.

(42) (a) Li, C.-Z.; Yip, H.-L.; Jen, A. K. Y. *J. Mater. Chem.* **2012**, *22*, 4161–4177. (b) He, Y.; Li, Y. *Phys. Chem. Chem. Phys.* **2011**, *13*, 1970–1983.

(43) Ruoff, R. S.; Tse, D. S.; Malhotra, R.; Lorents, D. C. *J. Phys. Chem.* **1993**, *97*, 3379–3383.

(44) Iranpoor, N.; Firouzabadi, H.; Nowrouzi, N.; Khalili, D. *Tetrahedron* **2009**, *65*, 3893–3899.

(45) (a) Smulders, M. M. J.; Nieuwenhuizen, M. M. L.; de Greef, T. F. A.; van der Schoot, P.; Schenning, A. P. H. J.; Meijer, E. W. *Chem.—Eur. J.* **2010**, *16*, 362–367. (b) De Greef, T. F. A.; Smulders, M. M. J.; Wolffs, M.; Schenning, A. P. H. J.; Sijbesma, R. P.; Meijer, E. W. *Chem. Rev.* **2009**, *109*, 5687–5754.

(46) (a) Abraham, R. J.; Hawkes, G. E.; Smith, K. M. *Tetrahedron Lett.* **1974**, *16*, 1483–1486. (b) Abraham, R. J.; Hawkes, G. E.; Hudson, M. F.; Smith, K. M. *J. Chem. Soc., Perkin Trans. 2* **1975**, *3*, 204–211. (c) Shaw, S. J.; Shanmugathasan, S.; Clarke, O. J.; Boyle, R. W.; Osborne, A. G.; Edwards, C. *J. Porphyrins Phthalocyanines* **2001**, *5*, 575–581.

Chapter 3

Optoelectronic Characterization of Porphyrin-Functionalized Guanine–Cytosine Rosette Nanotubes

3.1 Introduction

An important aspect to developing novel organic optoelectronic materials is to characterize and tune their chemical and physical properties via chemical modification at the molecular level using synthetic chemistry or via external physical stimulation and mechanical modulation. For example, in the field of OPVs, the goal is to develop suitable electron donor and acceptor materials for the active layer in the device. A few critical issues regarding the materials properties should be kept in mind when selecting the electron donor and acceptor pairs.[1] Are they well matched in terms of HOMO and LUMO energy levels for photoinduced charge transfer? What is the conductivity and charge mobility for each of them? Are they capable of generating efficient bulk heterojunction interfaces by large-area solution-processing techniques? Are their chemical and physical properties stable under heating, aging and exposure to light and oxygen? Two more critical concerns that are usually overlooked by research chemists are the safety of these materials and the potential effects in the environment.[2] To solve these issues, multidisciplinary expertise is required, including chemistry, physics, electrical and mechanical engineering. From the perspective of an organic and materials chemist, some of the properties can be solely characterized, while others can be obtained via collaboration.

To explore the potential applications of the self-assembled RNTs of porphyrin-functionalized guanine-cytosine (G∧C) molecules in the field of OPVs, the properties

discussed above should be characterized. Since a comprehensive discussion about the self-assembly and spectroscopic properties of **G∧C-Por 1**, **$(G\wedge C)_2$-Por 2** and **$(G\wedge C)_2$-Por 3** are presented in Chapter 2, this chapter focuses on the characterization of some important optoelectronic properties of these materials, including HOMO and LUMO energy levels, optical band gaps, conductivity of thin films, microscopic morphology and solid state photoluminescence quenching phenomena of the blends of RNTs and $PC_{61}BM$.

3.2 HOMO–LUMO determination

3.2.1 Overview on techniques

In the view of molecular orbital (MO) theory, for an organic molecule subjected to the excitation by electromagnetic radiation, the highest occupied molecular orbital (HOMO) is the orbital that loses an electron, and the lowest unoccupied molecular orbital (LUMO) is the orbital that receives an electron escaped from the HOMO.[3] When the molecule is at the ground electronic state, the LUMO is empty of electrons, while the HOMO is filled with electrons and the molecule adopts a closed-shell configuration if all electrons pair and two electrons count per orbital. The HOMO and LUMO energy levels are normally set as negative values (absolute energy levels) relative to the vacuum level (E_{vac}), whose energy level is zero. The energy difference between the HOMO and LUMO of a molecule is called the HOMO–LUMO gap.

The HOMO and LUMO energy levels of a molecule can be approximated by different MO calculation methods including the most widely used *ab initio*[4] and density functional theory (DFT)[5]. In general, the uniform goal of applying all these calculation methods is to solve the Schrödinger equation for complex systems. For small molecules, the HOMO and

LUMO energy levels obtained from computational chemistry may be in good agreement with those values from experimental techniques. However, for more complex systems such as polymers and other macromolecules, the discrepancy between the computational and experimental results is usually substantial. Here the focus is given to the two most widely used experimental techniques to ascertain the HOMO and LUMO energy levels — cyclic voltammetry and photoelectron spectroscopy.

3.2.1.1 Cyclic voltammetry

Cyclic voltammetry (CV) is an electrochemical technique widely used by OPV researchers to determine the HOMO and LUMO energy levels, mainly due to its comparatively simple setup and low cost. Basically, CV investigates a process that involves electron transfer of a redox couple (analyte). A redox couple that exhibits fast electron transfer is called an electrochemically reversible couple.[6] A standard CV apparatus is composed of a working electrode (glassy carbon), an auxiliary electrode (platinum), and a reference electrode (usually Ag/AgCl). In a potential-controlled CV experiment, the three electrodes are immersed in a deoxygenated solution containing the redox couple and a supporting electrolyte such as tetrabutylammonium hexafluorophosphate (Bu_4NPF_6). During a reversible CV scan, the electrical potential (voltage) is linearly applied to the stationary working electrode from zero to the preset maximum, and then it turns to the reverse direction and finally reaches zero. Accordingly, the electrical current that runs through the system changes as the electrical potential changes. Hence, a curve of current and voltage called a voltammogram can be represented from the data.[7]

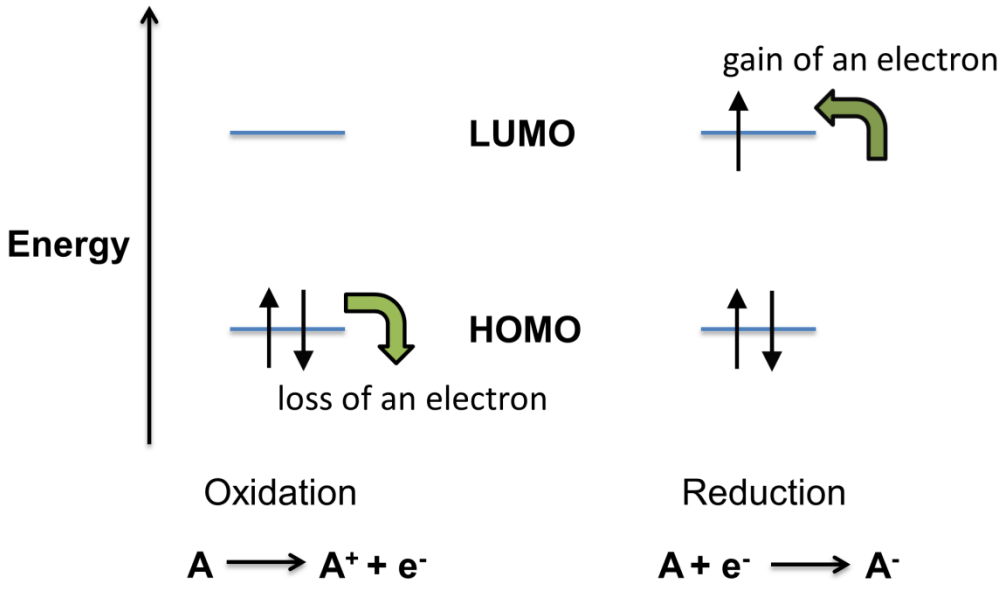

Figure 3.1. Schematic illustration of HOMO and LUMO electron transfer in the processes of the first oxidation and reduction during an electrochemical scan.

During the positive forward scan in the oxidation process of an analyte, the electrons lying in the HOMO of the analyte molecules have the lowest oxidation potential and can be removed first and collected at the surface of the working eletrode to form the anodic current (Figure 3.1).[8] In contrast, during the backward scan, the cations of the analyte molecules are reduced to the ground state by abstracting electrons from the surface of the working electrode and form the cathodic current. The peaks of the anodic current and the cathodic current are called peak currents i_{pa} and i_{pc}, respectively.[9] Accordingly, the electrical potential at which the currents reach the maxima are called peak potentials E_{pa} and E_{pc}, respectively. The average of the sum of E_{pa} and E_{pc} is called the half-wave potential ($E_{1/2,ox}$), which is generally taken as a good approximation of the oxidation formal potential ($E^{\circ\prime}$) of the analyte, given that diffusion coefficients of the oxidized and reduced species are approximately equal.[9,10] An analyte may have several oxidation states, especially in the

cases of inorganic compounds, but only the formal potential of the first oxidation is taken as a measurement correlated to the HOMO energy level.

Similarly, during the negative forward scan in the reduction process, the LUMO of the analyte molecules having the lowest electron affinity can be filled with electrons that escape from the surface of the working electrode to form the anions (Figure 3.2). During the backward scan from the preset negative maximum voltage to zero, the anions lose electrons at the surface of the working electrode to reach the ground state. The first half-wave potential ($E_{1/2,red}$) obtained from the negative scan is approximately equal to the formal potential of the first reduction, which is correlated to the LUMO energy level of the analyte.

Unfortunately, not all molecules are a reversible redox couple. The peak potentials of the materials having slow electron transfer properties largely depend on the scan rate, which makes the determination of formal potentials more complicated. On the other hand, the processes of addition or removal of electrons from macromolecules such as conjugated polymers are not equal, since the molecular conformational reorganization and variations of the energy levels could happen during the processes.[11] In these cases, it is impossible to measure the formal potential. Therefore, the onset potentials ($E_{ox,onset}$ and $E_{red,onset}$) are widely used to estimate the oxidation and reduction potentials,[12] since theoretically the onsets represent the initial injection states of holes to the HOMO (oxidation) and electrons to the LUMO (reduction). The onset is obtained by drawing two tangents for each peak, and the intersection is taken where the onset lies.[11] Figure 3.2 shows an example of using CV to measure the $E_{ox,onset}$ and $E_{red,onset}$ of a copolymer (PTICThBT).[13] The $E_{ox,onset}$ and $E_{red,onset}$ were measured to be 1.00 eV and −1.10 eV, respectively.

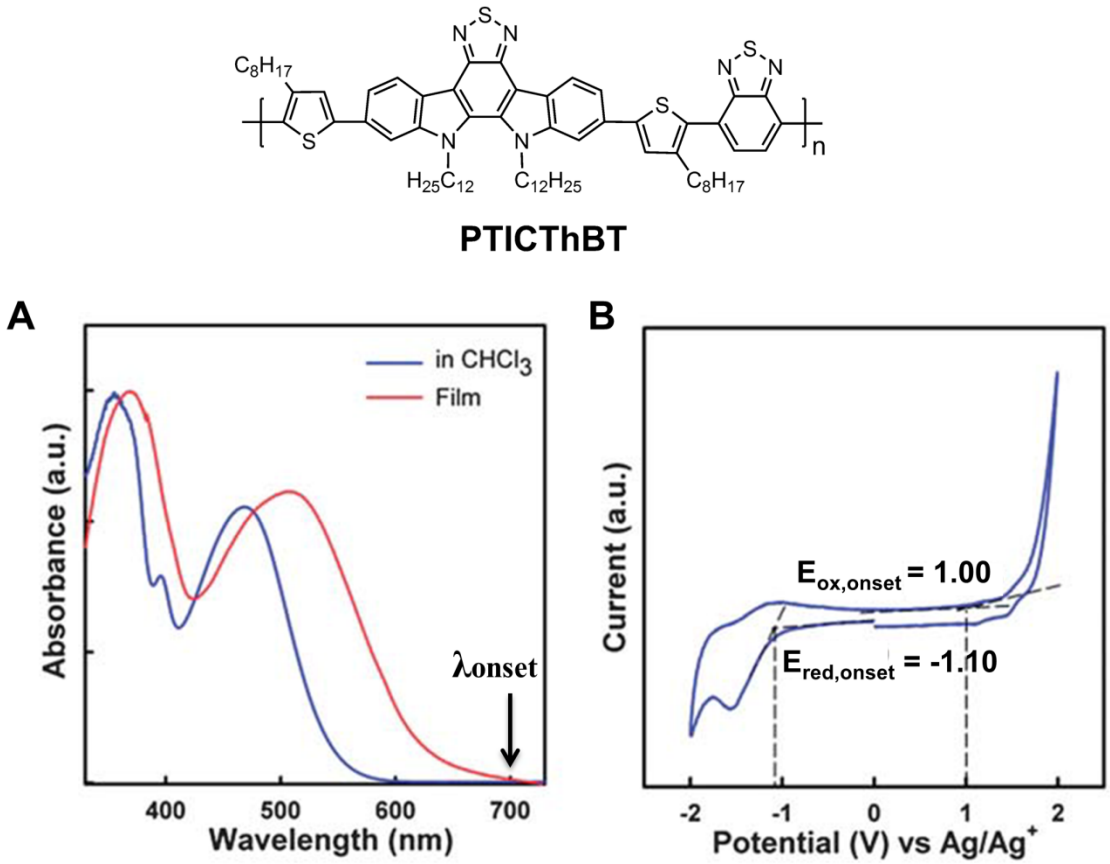

Figure 3.2. Molecular structure and (A) UV-Vis absorption spectra and (B) cyclic voltammogram of a conjugated polymer. Figure adapted with permission from Ref. 13 © 2012 Royal Society of Chemistry.

The difference between the oxidation and reduction formal potentials (or the onsets in most cases) of a material is called the electrochemical band gap (E_g^{ec}). This is differentiated from the optical band gap (E_g^{opt}) that is obtained from the UV-Vis absorption spectrum onset (λ_{onset}) of the material. The calculation of E_g^{opt} is given in **E1**.[14]

$$E_g^{opt} = \frac{1243.125}{\lambda_{onset}} \text{ eV} \qquad \textbf{(E1)}$$

Theoretically, the band gaps measured by CV and absorption spectroscopy should be the same as both of them represent the HOMO–LUMO energy gap. However, in most cases E_g^{ec} and E_g^{opt} are not equal.[12,15] For example, the E_g^{ec} of the copolymer PTICThBT was measured to be 2.1 eV (Figure 3.2B), while the E_g^{opt} was measured to be 1.78 eV (Figure 3.2A). The discrepancy is ascribed to the fundamental differences of the two techniques.[11] The value measured by CV is obtained on the premise that the charge transfer is fast (in the range below 1 ns) and the solvation and supporting electrolyte effects are neglected, although the creation of free ions is always involved in CV experiments. In UV-Vis absorption spectroscopy, the formation of free charge carriers in the sample is not revealed, and the neutral excited state is viewed as a bound exciton. The optical band gap seems to be more popular in the OPV community, not only because it is obtained from a thin-film sample that resembles the real OPV devices, but also because the $E_{ox,onset}$ and $E_{red,onset}$ are not always measurable due to the constraint of solvent and supporting electrolyte potential windows (the solvent or the supporting electrolyte may be oxidized or reduced prior to the analyte).

It is important to note that the oxidation or reduction formal potentials of a material are not its absolute HOMO or LUMO energy levels directly relative to the vacuum level, since the formal potential values from CV are indirectly related to the ionization energy. Instead, they are recorded relative to the reference electrode such as Ag/AgCl[12,16] or saturate calomel electrode (SCE)[17]. On the other hand, ferrocene/ferrocenium (Fc^+/Fc) is often used as an internal reference in non-aqueous solvents, due to its excellent electrochemical reversibility, little variation and low sensitivity to the environmental effects.[18] In fact, many researchers like to report the formal potential values relative to Fc^+/Fc.[19] Hence, the formal

potentials can be converted to the absolute HOMO and LUMO energy levels by using different electrochemical scales. Unfortunately, there is little consensus on how the measured formal potential values relate to the vacuum level, since there are at least four sets of conversion equations for the calculation.[10] One set of the conversion equations based on the Fc^+/Fc reference is given in **E2** and **E3** as below.[10]

$$E_{HOMO} = -(E_{[ox(onset)\ vs.\ Fc+/Fc]} + 5.1)\ (eV) \quad \textbf{(E2)}$$

$$E_{LUMO} = -(E_{[red(onset)\ vs.\ Fc+/Fc]} + 5.1)\ (eV) \quad \textbf{(E3)}$$

In summary, CV is a useful tool for researchers to determine the HOMO and LUMO energy levels of a material. However, the environmental effects such as concentration, solvent, scan rate, supporting electrolyte, reversibility of the redox couple are generally neglected. In addition, there is lack of a uniform electrochemical scale for the conversion of redox potentials to the absolute HOMO and LUMO energy levels. Hence, care should be taken when reporting the energy-level values obtained by CV or using the values from other studies.

3.2.1.2 Ultraviolet photoelectron spectroscopy

Ultraviolet photoelectron spectroscopy (UPS) is a member of the family of photoemission spectroscopy (PES). Other well-known techniques include X-ray photoelectron spectroscopy (XPS) and inverse photoemission spectroscopy (IPES). All these techniques are important tools for surface chemical analysis. The fundamental principle of UPS and XPS is the "photoelectric effect" which was quantitatively described by Albert Einstein in

one of his four revolutionary publications in 1905.[20] The photoelectric effect describes the phenomenon that shining a light onto a metal surface could lead to the emission of electrons, if the energy of the photon absorbed by the electrons in the metal is large enough for the electrons to overcome the ionization energy and escape from the surface of the metal.[21] The maximum kinetic energy (E_k^{max}) of the photoelectron (also called as secondary electron) upon the absorption of a photon with adequate energy is given by **E4**.

$$E_k^{max} = h\nu - W \qquad \textbf{(E4)}$$

Where h is the Planck constant, ν is the frequency of the incident photon, and W is the work function (also denoted as Φ) of the material. The work function is defined as the minimum thermodynamic work that is needed to remove an electron from a solid surface to a point that is just outside the surface (atomic scale) and lies at the vacuum level where the kinetic energy of the electron is zero.[22] Obviously the energy of the absorbed photon needs to be greater than the work function of the material to allow for the emission of the photoelectron.

XPS was the first photoelectron spectroscopy technique used for surface chemical analysis, which was initially developed by the Nobel Laureate Kai Siegbahn in 1956.[23] A few years later, William Spicer and David Turner developed UPS.[20] XPS and UPS are similar in the instrument setup, but different in the incident light source. High energy X-ray is used in XPS, while ultraviolet light is used in UPS.[23b, 24] In XPS, the common monochromatic incident photon light sources are anodes of aluminium (Al-K_α $h\nu$ = 1486.6 eV) or magnesium (Mg-K_α $h\nu$ = 1253.6 eV). In UPS, the photon energy of the light source is much lower. Discharge lamps of rare gases like helium I_α ($h\nu$ = 21.23 eV, λ = 58.4 nm)

and helium II_α ($h\nu$ = 40.82 eV, λ = 30.4 nm) are the monochromatic light sources widely used in UPS. Hence, XPS is more useful in obtaining the information of core-level states at higher binding energies of the sample material, and UPS is excellent in providing the fine structure of the valence band.

Figure 3.4 is a schematic illustration of the setup of a modern UPS spectrometer.[20] It is important to note that both the XPS and UPS setups should be evacuated to ultrahigh vacuum (UHV) for sample analysis (typically $\leqslant 10^{-13}$ bar or 10^{-10} Torr). The kinetic energy (E_k) of the photoelectron is a function of a series of experimental parameters, such as emission angle, electron spin orientation and polarization. There are several types of analyzers, such as plane mirror analyzer (PMA), cylindrical mirror analyzer (CMA), cylindrical deflection analyzer (CDA) and spherical deflection analyzer (SDA).[25] Among them, SDA is the most common analyzer, as the one shown in Figure 3.3. Typically, the detector of photoelectrons contains an electron multiplier to amplify the signals. In some cases a series of electron multipliers are used and the signal can be amplified up to 10^7 times. The common energy resolution of UPS is about 0.15 eV, compared to 1 eV for XPS.[20, 26] The energy resolutions of UPS and XPS largely depend on the line width of the incident photon source, which is a few meV for the discharge lamp of UPS and ~1.0 eV for the X-ray anodes of XPS. Using synchrotron radiation sources can effectively improve the resolution of UPS to 0.02 eV, although the maintenance cost is huge.

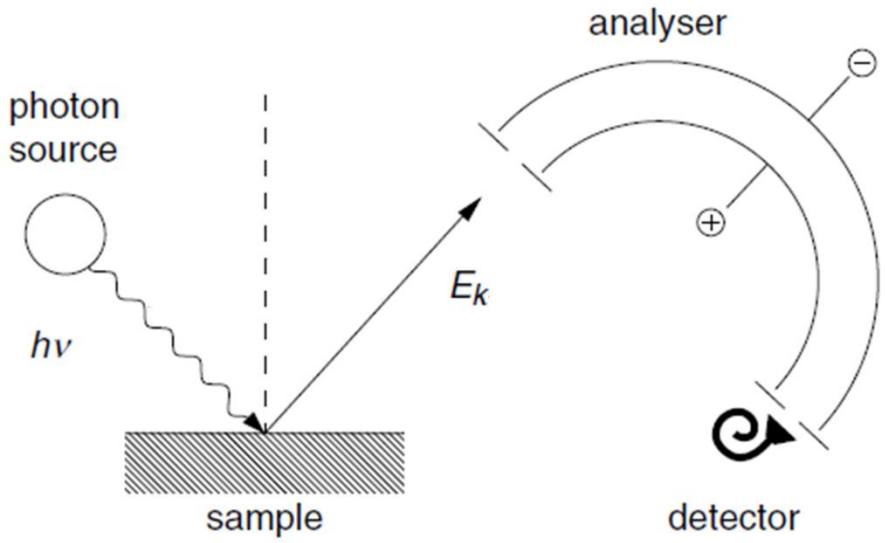

Figure 3.3. Schematic illustration of the principle of a modern ultraviolet photoelectron spectrometer. Figure adapted with permission from Ref. 20 © 2005 Institute of Physics.

UPS is a surface sensitive technique. The penetration depth of the photons on the sample surface is up to around 10 nm.[25b] Nevertheless, the capability of mapping the fine structure of the valence band makes it a primary tool in surface chemical analysis. For definition purposes, in the band theory for solids, the valence band refers to the HOMO, and the conducting band refers to the LUMO. The energy difference between the HOMO and LUMO is called the band gap (E_g).[3] The energy difference between the HOMO and the vacuum level is equal to the ionization energy (IE). Similarly, the energy difference between the LUMO and the vacuum level is equal to the electron affinity (EA).[17b,27] According to the theory of statistical mechanics, at thermodynamic equilibrium the electrons occupying a specific density of states (DOS) follow the Fermi-Dirac distribution. The Fermi level (E_F) is the top of the valence band, at which there is a 50% probability for the hypothetical energy level being occupied by the HOMO electrons at any given time.[3,22]

In metals, the E_F lies inside at least one band since the valence band and the conducting band of a metal overlap and there is no band gap. In semiconductors and insulators, E_F resides in the band gap. The energy needed to elevate an electron from the Fermi level to the vacuum level is the work function (Φ) of a material. The energy difference between the Fermi level and the HOMO energy level is the binding energy (E_B) relative to E_F, which corresponds to the hole injection barrier (E_h) at the metal/solid sample interface.[28]

The relations among these common terms are depicted in Figure 3.4,[28] which is a schematic illustration of the electronic structure of a sample (thin film on the metal substrate) probed by UPS. Once a valence electron is excited upon the absorption of a photon from the light source, it is able to overcome the ionization energy barrier (the sum of E_B and Φ) and escape from the sample surface as a photoelectron (secondary electron) carrying the kinetic energy (E_k). The vacuum level (E_{vac}), at which $E_k = 0$, is identified by the cutoff position of the binding energy of the photoelectron in the UPS spectrum. The onset of the binding energy from the lowest value end correlates to the edge of Fermi level. Hence, the photoelectrons collected at this point have the maximum kinetic energy (E_k^{max}).

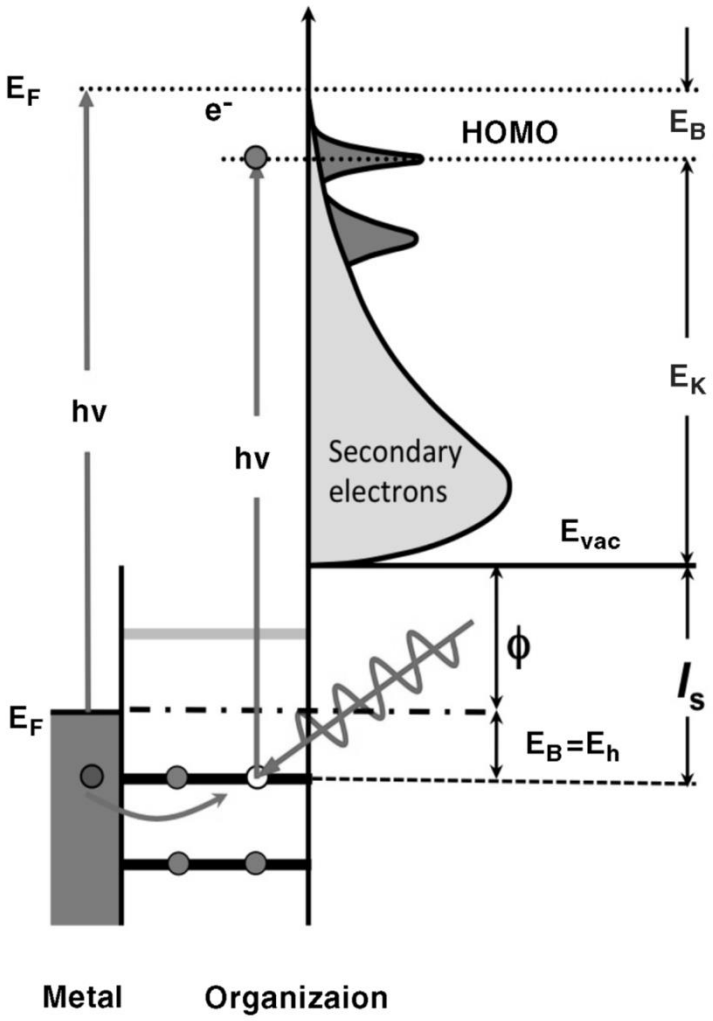

Figure 3.4. Schematic illustration of the electronic structure of a sample (thin film on the metal substrate) probed by UPS. Parameters in the figure are: binding energy from E_F (E_B); hole injection barrier (E_h); Fermi level (E_F); kinetic energy (E_k); work function (Φ); vacuum level (E_{vac}); ionization energy (I_s). Figure adapted with permission from Ref. 28 © 2012 Wiley-VCH.

Because of experimental convenience, the UPS spectrum is normally collected as a graph of the emission intensity as a function of the binding energy (E_B) relative to the Fermi level,[25b, 29] which is converted from the kinetic energy using **E5** by the data processing unit in the UPS instrument.[25b,28]

$$E_k = h\nu - E_B - \Phi \quad \textbf{(E5)}$$

The ionization energy (IE) of a valence electron is expressed by **E6**.

$$IE = (\Phi + E_B) \quad \textbf{(E6)}$$

Substituting **E5** into **E6** gives **E7**, which directly correlates the binding energy of the valence electron with the kinetic energy of the photoelectron and the incident photon energy.[29]

$$IE = h\nu - E_k \quad \textbf{(E7)}$$

Since the electron lying in the HOMO has the lowest ionization energy, the HOMO energy level (E_{HOMO}) relative to the vacuum level can be calculated by subtracting the maximum kinetic energy of the photoelectron from the incident photon energy, which is expressed in **E8**.[26]

$$E_{HOMO} = -(h\nu - E_k^{max}) \quad \textbf{(E8)}$$

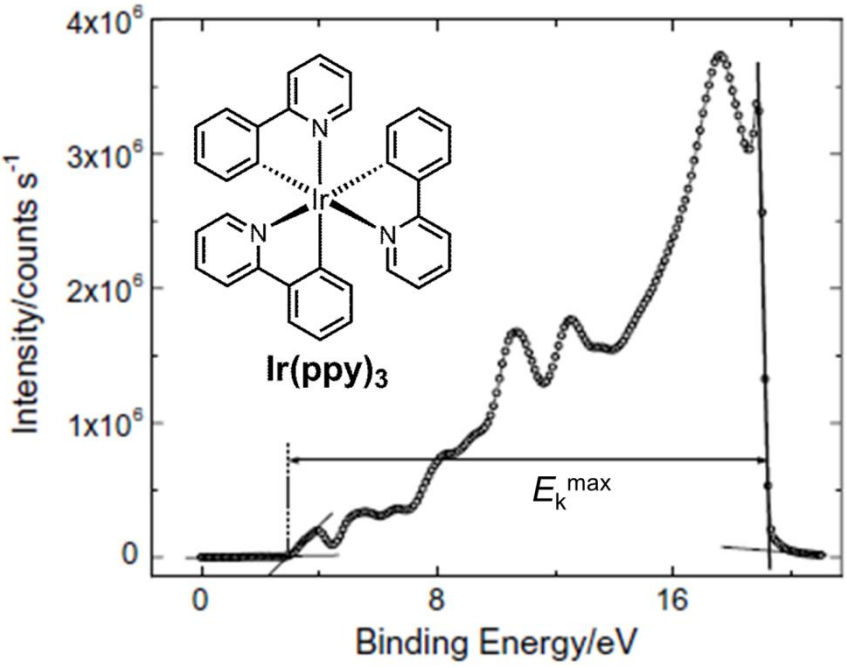

Figure 3.5. Molecular structure and UPS spectrum of an $Ir(ppy)_3$ thin film grown on Ag and biased at −3 V. Figure adapted with permission from Ref. 26 © 2005 Elsevier.

From the UPS spectrum of a sample material, the work function (Φ), binding energy (E_B) relative to the Fermi level (E_F) and the maximum kinetic energy of the photoelectron (E_k^{max}) can all be obtained. For example, Figure 3.5 shows the UPS spectrum of an $Ir(ppy)_3$ thin film on the Ag substrate.[26] By linearly extrapolating the high binding energy slope to the intersection of the baseline, the cutoff position that indicates the vacuum level was identified. The work function was calculated by subtracting the binding energy at the cutoff position (E_{cutoff}) from the incident photon energy ($h\nu$). The onset of the spectrum that indicates the binding energy relative to the Fermi level was identified by linearly extrapolating the low energy slope to the intersection of the baseline. The energy difference between the onset of the low energy slope and the cutoff of the high energy slope reflects E_k^{max}. By using **E8**, the HOMO energy level of $Ir(ppy)_3$ was determined to be –5.10 eV.

Although the information of the LUMO energy level of a sample material is not directly revealed by UPS, it can be conveniently deduced from **E9** if the optical band gap (E_g^{opt}) is available from the UV-Vis spectrum.[14,19b]

$$E_{LUMO} = E_{HOMO} + E_g^{opt} \quad \textbf{(E9)}$$

A more sophisticated and less common technique to directly determine the LUMO energy level of a material is inverse photoemission spectroscopy (IPES), which is a complementary technique to UPS.[25a] Instead of a photon source, a beam of electrons of a well-defined kinetic energy is directed at the sample surface in IPES. These incident electrons initially occupy the high-lying unoccupied orbitals that correspond to low electron affinities, and decay to the low-lying unoccupied orbitals. During the decay process, the energy loss of the electrons is released in the form of emitted photons, whose energy and counts can be detected. From the IPES spectrum, the HOMO energy level of a sample material can be obtained since the energy of the incident electrons is a constant. Although the measurements of the LUMO energy levels by IPES have been reported,[30] the technique is still less common, especially in the OPV community, mainly due to the complexity of the instrument setup and high cost of the maintenance.

In summary, UPS is a well-established surface chemical analysis technique to directly map the valence band fine structure and determine the absolute HOMO energy level of a material relative to the vacuum level. The LUMO energy level can be calculated by adding the optical band gap to the HOMO energy level. Alternatively, the LUMO energy level can be directly determined by IPES.

3.2.2 HOMO–LUMO energy levels of G∧C-porphyrin RNTs

The HOMO energy level of **G∧C-Por 1** RNTs was determined by UPS. To prepare the UPS sample, a drop of the stock solution of **G∧C-Por 1** RNTs (0.5 mM in $MeNO_2$) was deposited on a clean Si (100) wafer (18 mm × 13 mm, 10-20 Ω•cm, etched by 5% HF) by a glass pipette (see experimental section for details). The wafer was then placed in a vacuum chamber. After 30 min, the solvent was removed and a thin film of the material formed on the wafer surface. The wafer was then immediately loaded into the ultrahigh vacuum ($< 5 \times 10^{-10}$ Torr) chamber of the UPS instrument and allowed to stay for 30 min to remove the residual solvent before analysis. During the analysis, monochromatized helium I ($h\nu$ = 21.23 eV, λ = 58.4 nm) was used as the light source. An example of the UPS spectrum of **G∧C-Por 1** RNTs is shown in Figure 3.6. The cutoff position was obtained by extrapolating the high energy slope of the spectrum to the intersection of the baseline,[27,31] which was identified as 16.25 eV (Figure 3.6A). Hence, the work function of the material on the Si (100) interface was calculated as 4.98 eV (21.23 eV – 16.25 eV). On the other hand, the binding energy relative to the Fermi level was obtained in the Fermi-edge region by extrapolating the low energy slope of the spectrum to the intersection of the baseline, and it was determined as 0.48 eV (Figure 3.6B). By adding up the work function and the binding energy relative to the Fermi level, the HOMO energy level of **G∧C-Por 1** RNTs was calculated to be –5.46 eV [−(4.98 eV + 0.48 eV)].

To validate the value of the HOMO energy level measured by UPS, three samples of **G∧C-Por 1** RNTs on three Si (100) wafers were prepared in the same way as described above, and the average value along with the standard deviation was calculated based on the

measurements of all three samples. Hence, the HOMO energy level of **G∧C-Por 1** RNTs was determined to be –5.46 ± 0.04 eV.

The optical band gap (E_g^{opt}) of **G∧C-Por 1** RNTs was measured from the UV-Vis spectra of a drop-cast thin film on quartz. As shown in Figure 3.7, the absorption onset was estimated at 784 nm, and E_g^{opt} was calculated to be 1.59 eV. Hence, the LUMO energy level of **G∧C-Por 1** RNTs was calculated to be –3.87 eV.

To investigate the effect of the self-assembled supramolecular nanostructures on the HOMO and LUMO energy levels of **G∧C-Por 1**, the UPS and UV-Vis samples prepared from unassembled **G∧C-Por 1** (0.5 mM in $MeNO_2$) were also characterized. The HOMO energy level of the unassembled **G∧C-Por 1** was determined to be –5.50 ± 0.04 eV based on the measurements of three samples. Figure 3.8 shows the UPS spectra of one sample. E_g^{opt} was calculated to be 1.65 eV from the UV-Vis spectrum of a thin film on quartz (Figure 3.9). Hence, the LUMO energy level of unassembled **G∧C-Por 1** was calculated to be –3.85 eV.

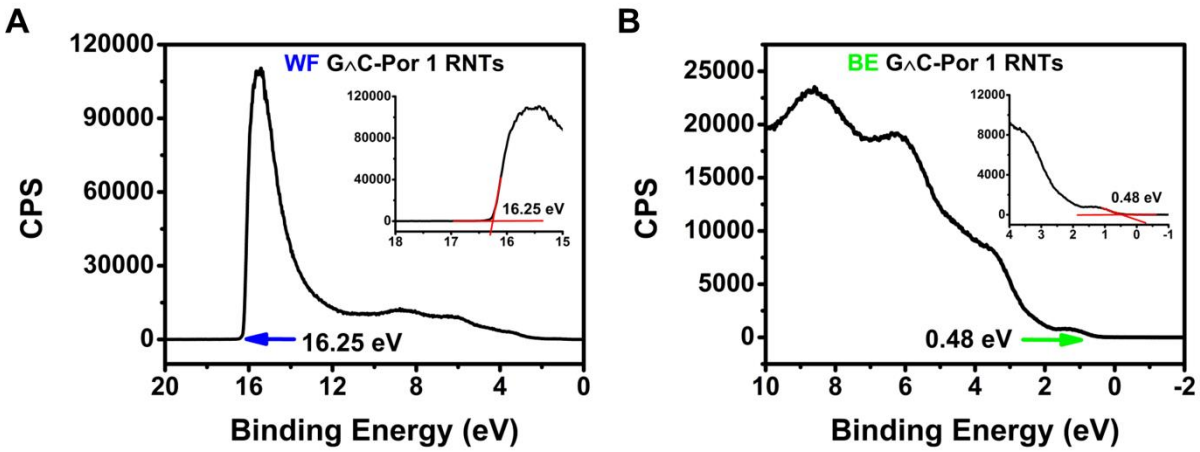

Figure 3.6. UPS spectra of **G∧C-Por 1** RNTs on Si (100). (A) Work function determination; the inset shows the highest binding energy cutoff; (B) Binding energy (relative to Fermi level) determination; the inset shows the spectrum onset.

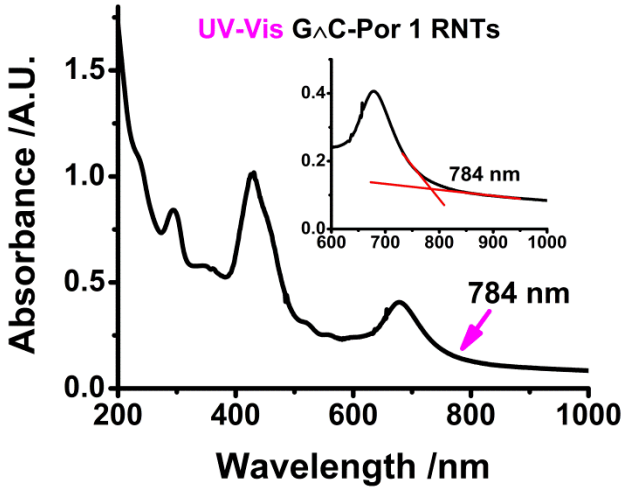

Figure 3.7. UV-Vis spectrum of a thin film of **G∧C-Por 1** RNTs on quartz; the inset shows the absorption onset.

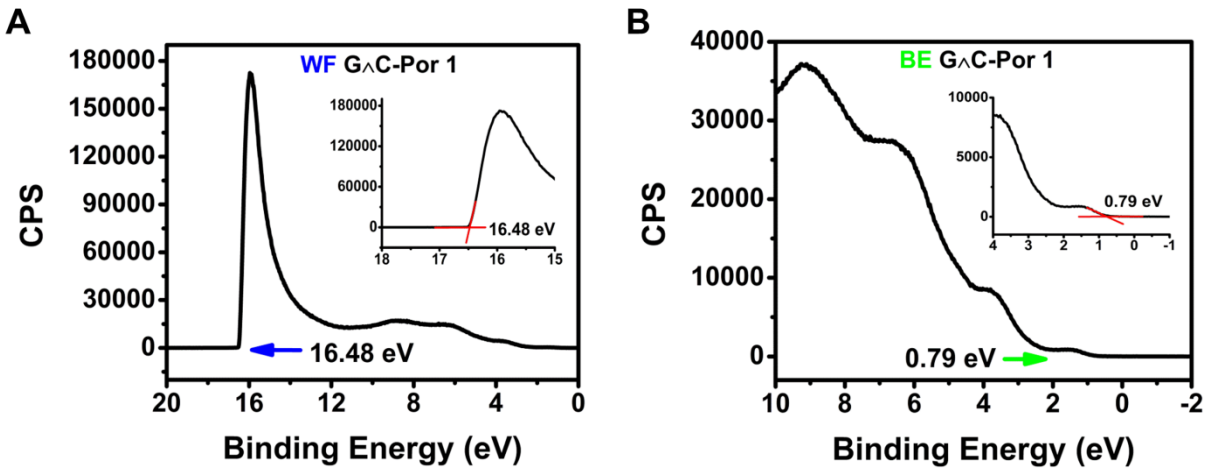

Figure 3.8. UPS spectra of unassembled **G∧C-Por 1** on Si (100). (A) Work function determination; the inset shows the highest binding energy cutoff; (B) Binding energy (relative to Fermi level) determination; the inset shows the spectrum onset.

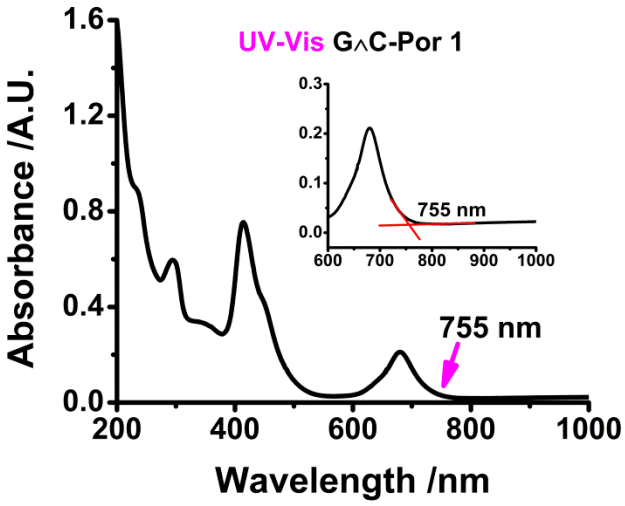

Figure 3.9. UV-Vis spectrum of a thin film of unassembled **G∧C-Por 1** on quartz; the inset shows the absorption onset.

Similarly, the HOMO and LUMO energy levels and band gaps of **(G∧C)$_2$-Por 2** and **(G∧C)$_2$-Por 3** and the unassembled controls were also determined by UPS and UV-Vis spectroscopy.

The UPS and UV-Vis samples of the assembled and unassembled **(G∧C)$_2$-Por 2** were prepared from the respective solutions at the same concentration (1.0 mM in 1,2-DCB/MeOH, 7:3, v/v). Figure 3.10 and Figure 3.12 show the UPS spectra of **(G∧C)$_2$-Por 2** RNTs and unassembled **G∧C)$_2$-Por 2**, respectively. Figure 3.11 and Figure 3.13 show the UV-Vis spectra of thin films of **(G∧C)$_2$-Por 2** RNTs and unassembled **(G∧C)$_2$-Por 2** on quartz, respectively. The HOMO energy level, the optical band gap and the LUMO energy level of **(G∧C)$_2$-Por 2** RNTs were determined to be –5.61 ± 0.03 eV, 1.59 eV, –4.02 eV, respectively. In contrast, the HOMO energy level, the optical band gap and the LUMO energy level of unassembled **(G∧C)$_2$-Por 2** were determined to be –5.59 ± 0.02 eV, 1.65 eV and –3.94 eV, respectively.

The UPS and UV-Vis samples of the assembled and unassembled **(G∧C)$_2$-Por 3** were prepared from the respective solutions at the same concentration (1.0 mM in 1,2-DCB). Figure 3.14 and Figure 3.16 show the UPS spectra of **(G∧C)$_2$-Por 3** RNTs and unassembled **G∧C)$_2$-Por 3**, respectively. The UV-Vis spectra of thin films of **(G∧C)$_2$-Por 3** RNTs and unassembled **(G∧C)$_2$-Por 3** on quartz are shown in Figure 3.15 and Figure 3.17, respectively. The HOMO energy level, the optical band gap and the LUMO energy level of **(G∧C)$_2$-Por 3** RNTs were determined to be –5.62 ± 0.05 eV, 1.62 eV and –4.00 eV, respectively. In contrast, the HOMO energy level, the optical band gap and the LUMO

energy level of unassembled **(G∧C)$_2$-Por 3** were determined to be –5.63 ± 0.05 eV, 1.66 eV and –3.97 eV, respectively.

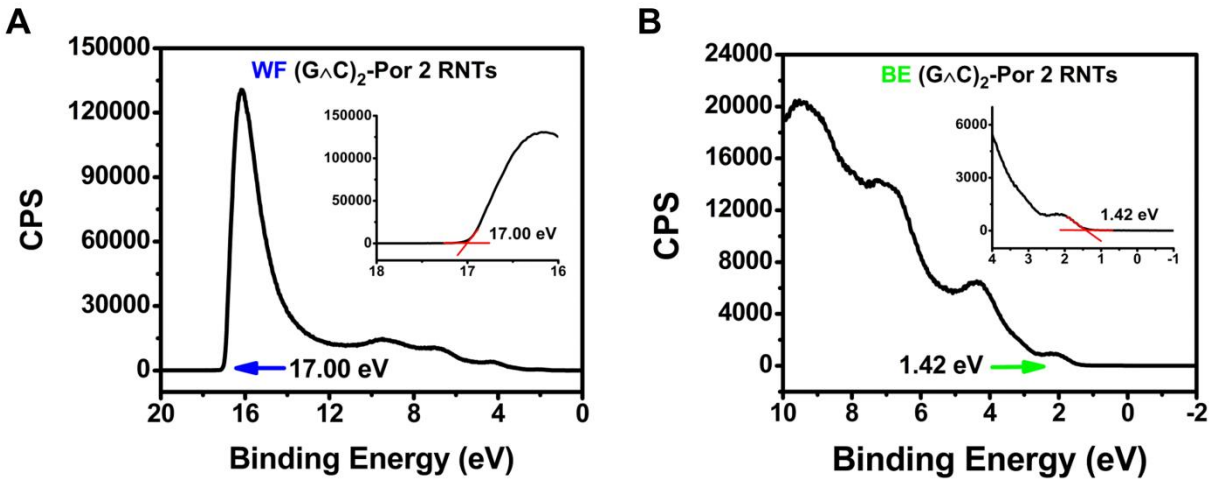

Figure 3.10. UPS spectra of **(G∧C)$_2$-Por 2** RNTs on Si (100). (A) Work function determination; the inset shows the highest binding energy cutoff; (B) Binding energy (relative to Fermi level) determination; the inset shows the spectrum onset.

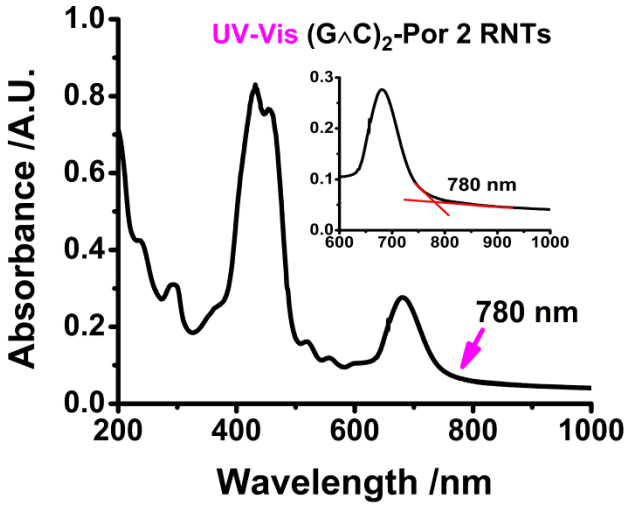

Figure 3.11. UV-Vis spectrum of a thin film of **(G∧C)$_2$-Por 2** RNTs on quartz; the inset shows the absorption onset.

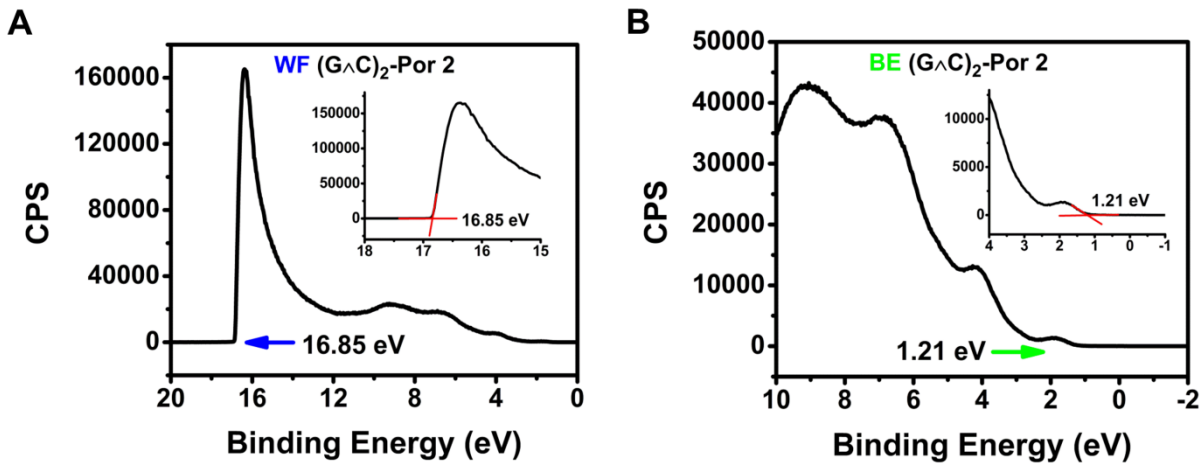

Figure 3.12. UPS spectra of unassembled **$(G\wedge C)_2$-Por 2** on Si (100). (A) Work function determination; the inset shows the highest binding energy cutoff; (B) Binding energy (relative to Fermi level) determination; the inset shows the spectrum onset.

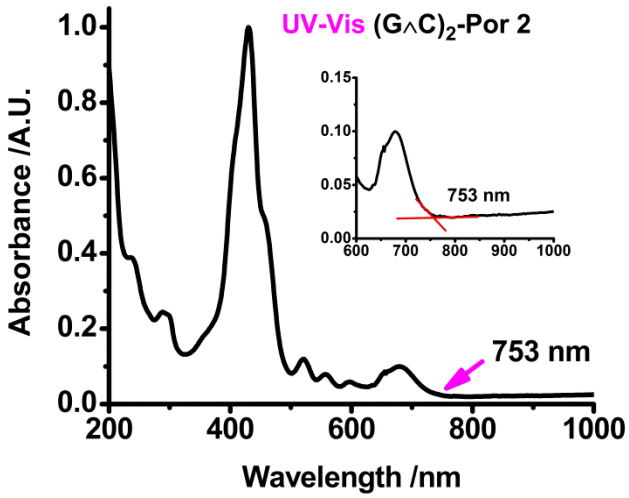

Figure 3.13. UV-Vis spectrum of a thin film of unassembled **$(G\wedge C)_2$-Por 2** on quartz; the inset shows the absorption onset.

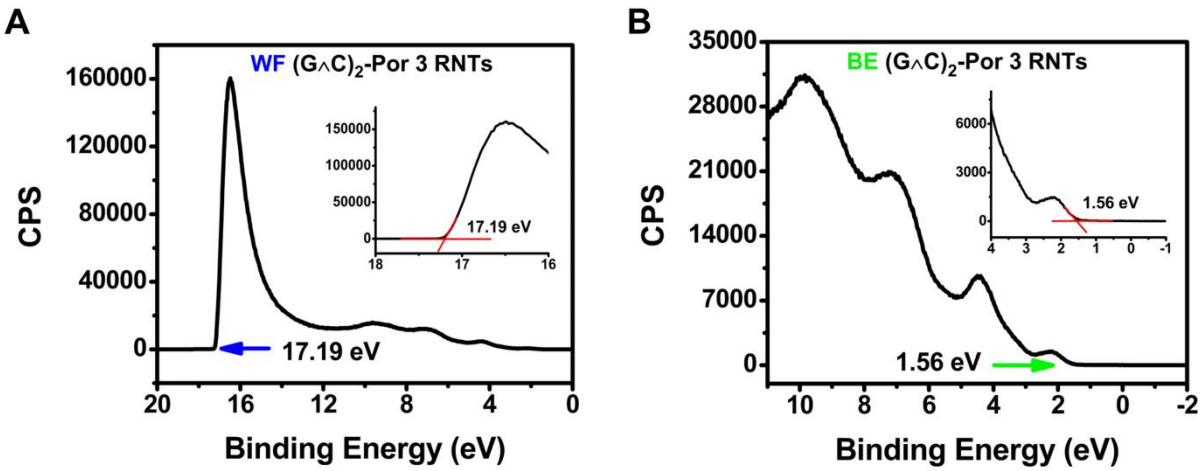

Figure 3.14. UPS spectra of **(G∧C)$_2$-Por 3** RNTs on Si (100). (A) Work function determination; the inset shows the highest binding energy cutoff; (B) Binding energy (relative to Fermi level) determination; the inset shows the spectrum onset.

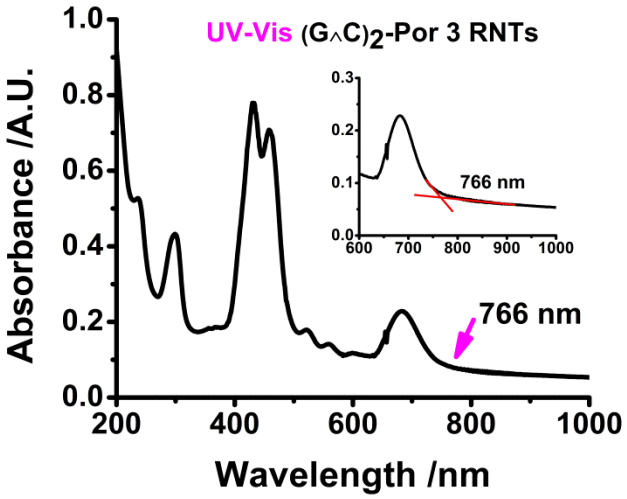

Figure 3.15. UV-Vis spectrum of a thin film of **(G∧C)$_2$-Por 3** RNTs on quartz; the inset shows the absorption onset.

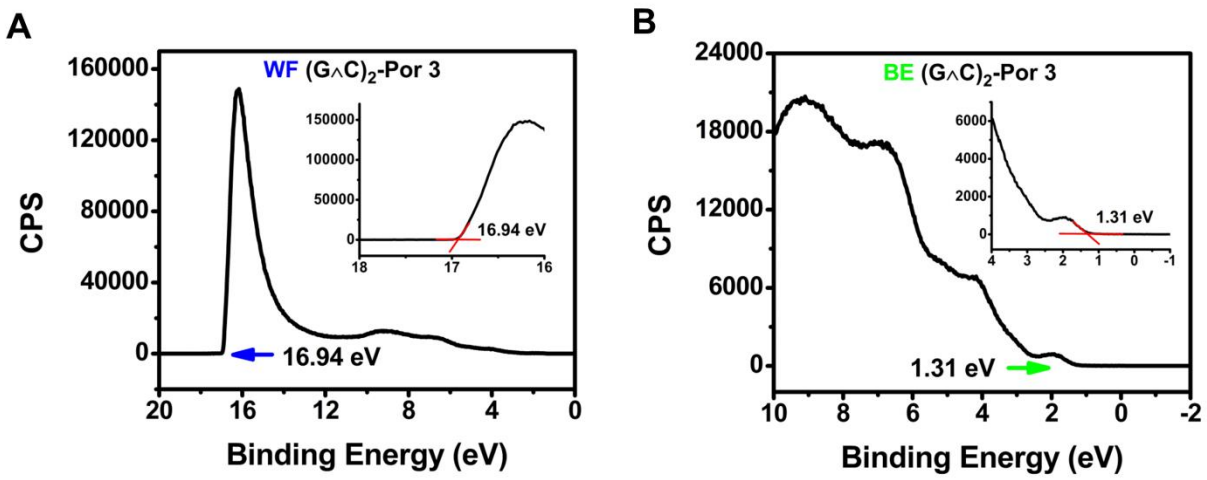

Figure 3.16. UPS spectra of unassembled **(G∧C)$_2$-Por 3** on Si (100). (A) Work function determination; the inset shows the highest binding energy cutoff; (B) Binding energy (relative to Fermi level) determination; the inset shows the spectrum onset.

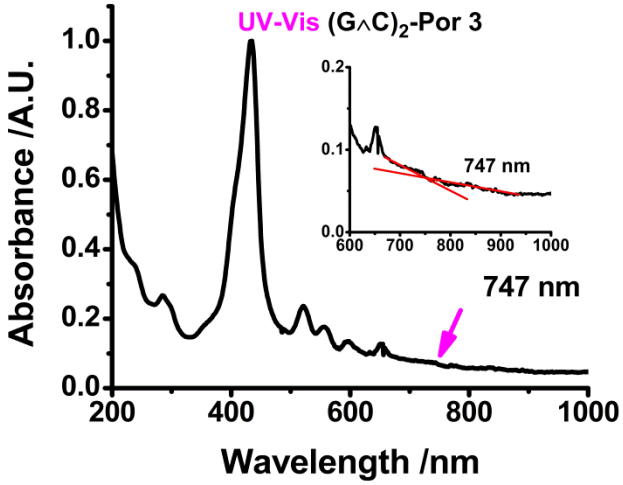

Figure 3.17. UV-Vis spectrum of a thin film of unassembled **(G∧C)$_2$-Por 3** on quartz; the inset shows the absorption onset.

The HOMO–LUMO energy levels and the optical band gaps of the assembled and unassembled **G∧C-Por 1**, **(G∧C)$_2$-Por 2** and **(G∧C)$_2$-Por 3** are summarized in Table 3.1. The self-assembled supramolecular nanostructures did not change the HOMO energy levels of these materials significantly. However, the optical band gaps of the RNTs were slightly smaller than their unassembled counterparts, which is due to the red-shifted absorption onsets of the thin films that were also observed in the UV-Vis spectra in solution. Consequently, the LUMO energy levels of the RNTs were slightly lower than their unassembled counterparts. It is interesting to note that the HOMO and LUMO energy levels of both **(G∧C)$_2$-Por 2** RNTs and **(G∧C)$_2$-Por 3** RNTs were ~0.15 eV lower than those of **G∧C-Por 1** RNTs. Similar results were also observed in the unassembled counterparts. These variations are likely related to the self-assembly cores, since both **(G∧C)$_2$-Por 2** and **(G∧C)$_2$-Por 3** have a twin G∧C motif while **G∧C-Por 1** has a single G∧C motif.

Table 3.1. HOMO–LUMO energy levels and optical band gaps of assembled and unassembled **G∧C-Por 1**, **(G∧C)$_2$-Por 2** and **(G∧C)$_2$-Por 3**.

Compounds	E_{HOMO} (eV) [a]	E_{LUMO} (eV)	E_g^{opt} (eV)
G∧C-Por 1 RNTs	–5.46 ± 0.04	–3.87	1.59
G∧C-Por 1	–5.50 ± 0.04	–3.85	1.65
(G∧C)$_2$-Por 2 RNTs	–5.61 ± 0.03	–4.02	1.59
(G∧C)$_2$-Por 2	–5.59 ± 0.02	–3.94	1.65
(G∧C)$_2$-Por 3 RNTs	–5.62 ± 0.05	–4.00	1.62
(G∧C)$_2$-Por 3	–5.63 ± 0.05	–3.97	1.66

[a] The standard deviation was calculated based on UPS measurements on 3 samples of each compound.

The UPS and UV-Vis spectra of $PC_{61}BM$, a widely used electron acceptor material in OPV devices, were also collected. These spectra are shown in Figure 3.18 and Figure 3.19, respectively. The HOMO and LUMO energy levels and the optical band gap of $PC_{61}BM$ were calculated to be –6.10 eV, –4.26 eV and 1.84 eV, respectively, which are very close to the reported values in the literature.[32] It is important to note that although the reported values of the HOMO energy level of $PC_{61}BM$ were similar in the literature (between –5.9 eV and –6.1 eV), the reported values of the LUMO energy level are varied in the range of –3.7 eV to –4.3 eV. This is mainly due to the different electrochemical standards and conversion equations to estimate the values (see the discussion in CV technique).[33] In addition, the estimated values of the absorption onsets of $PC_{61}BM$ are also varied in the spectra of the thin films and solutions, especially in different solvents. Consequently, the values of the optical band gap are also varied in the literature, which accounts for the uncertainty of the LUMO energy level of this material.

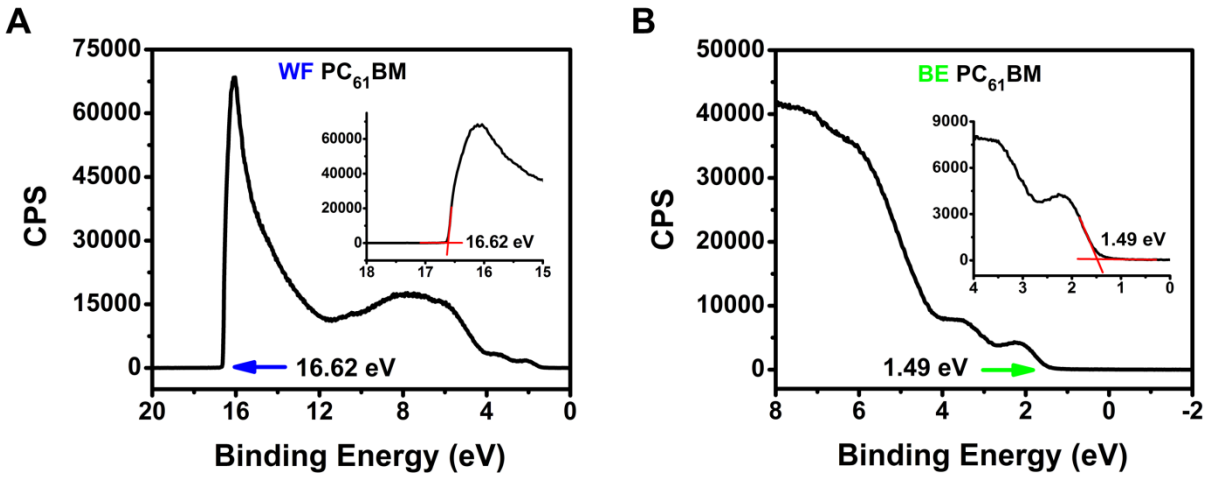

Figure 3.18. UPS spectra of $PC_{61}BM$ on Si (100). (A) Work function determination; the inset shows the highest binding energy cutoff; (B) Binding energy (relative to Fermi level) determination; the inset shows the spectrum onset.

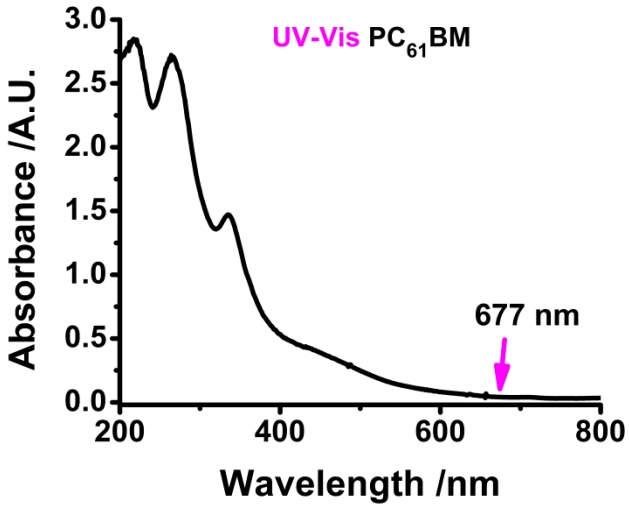

Figure 3.19. UV-Vis spectrum of a thin film of $PC_{61}BM$ on quartz; the inset shows the absorption onset.

3.3 Energy level diagram

Since the LUMO energy level of $PC_{61}BM$ is aligned between the HOMO and LUMO energy levels of the RNTs of **G∧C-Por 1**, **$(G\wedge C)_2$-Por 2** and **$(G\wedge C)_2$-Por 3**, these G∧C-porphyrin RNTs can be used as potential electron donor materials in the $PC_{61}BM$ based OPV devices. Figure 3.20 shows the energy level diagram of the components used in the conceived OPV devices. Photoinduced electron transfer is expected to happen at the interfaces of the elector donor and acceptor materials in the active layer. The transfer of electrons from the LUMO of the donor to the LUMO of the acceptor is driven by the energy difference between the two orbitals. The work functions of ITO (anode), Al (cathode) and PEDOT:PSS (hole transporting layer) are adapted from the literature.[34] The insertion of the PEDOT:PSS layer is to block the electrons, since the direct contact of the active layer with the anode is known to lead to current leakage and the recombination of charge carriers, which are detrimental to the device performance.[35]

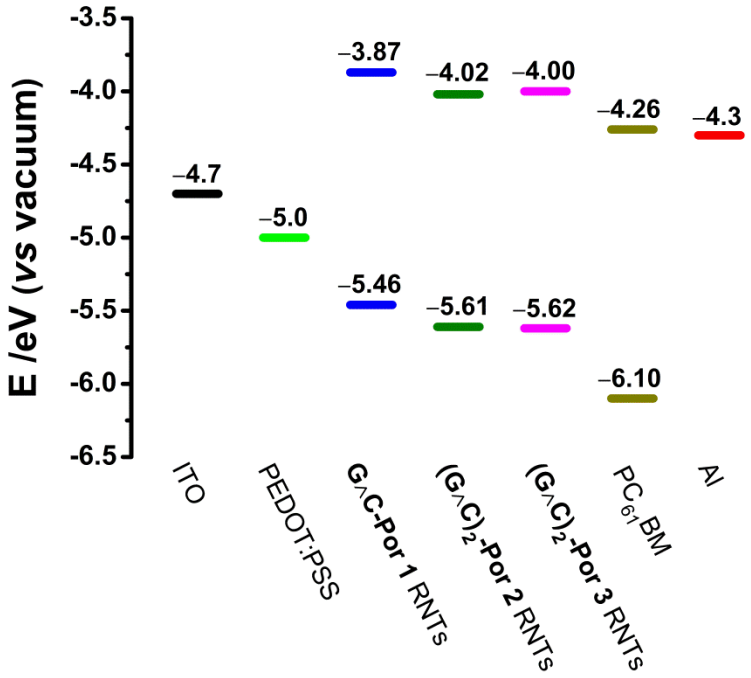

Figure 3.20. Energy level diagram of components used in the conceived OPV devices with the active layers based on three types of G∧C-porphyrin RNTs and $PC_{61}BM$. The work functions of ITO, PEDOT:PSS and Al are adapted from Ref. 34.

3.4 Fluorescence quenching in the blended films of G∧C-porphyrin RNTs:$PC_{61}BM$

Fullerene and its derivatives have been demonstrated to have a high binding affinity to porphyrin,[36] and the well matched alignment of their HOMO and LUMO energy levels results in quenching of porphyrin fluorescence by photoinduced electron transfer.[37] To investigate the efficiency of photoinduced electron transfer between the G∧C-porphyrin RNTs and $PC_{61}BM$ in the blended films, the photoluminescence (PL) spectra of the spin-cast thin films on quartz were collected and compared to those of the thin films comprising the RNTs only. Strong and broad emission bands in the Vis-NIR region were observed in the PL spectra of the RNTs in the solid state (Figure 3.21), which are the characteristic

porphyrin emission bands (see Chapter 2 for the PL spectra in solution). In contrast, the emission bands fell off in all the blended films, indicating the fluorescence quenching by photoinduced electron transfer from the RNTs to $PC_{61}BM$. A nearly complete quenching was observed in the film of **G∧C-Por 1** RNTs:$PC_{61}BM$ (Figure 3.21A). This is probably due to the larger energy difference (0.39 eV) between the LUMO of **G∧C-Por 1** RNTs and the LUMO of $PC_{61}BM$.

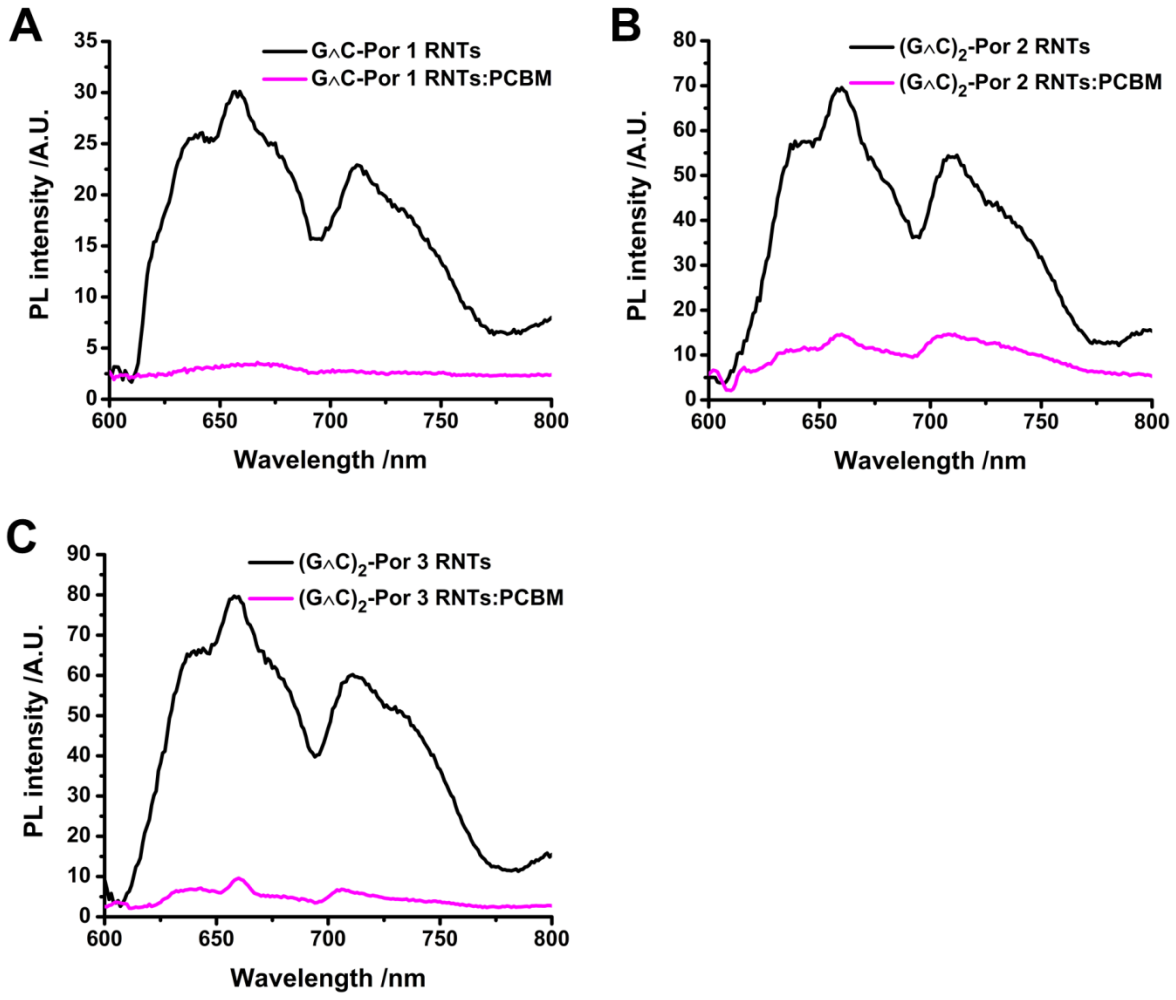

Figure 3.21. Photoluminescence spectra of spin-cast thin films of G∧C-porphyrin RNTs and blended films with $PC_{61}BM$ (molar ratio 1:1) on quartz. (A) **G∧C-Por 1** RNTs; (B) **$(G∧C)_2$-Por 2** RNTs; (C) **$(G∧C)_2$-Por 3** RNTs. Excitation wavelength: 446 nm.

3.5 Microscopic morphology of the blended films of G∧C-porphyrin RNTs:$PC_{61}BM$

A prerequisite to create the solution-processed bulk heterojunction (BHJ) morphology of the active layer in OPV devices is that the solutions of the electron donor and acceptor materials should be miscible. The mixed solution with a high concentration and moderate viscosity is suitable for the spin-casting process to create the bicontinous phases of the electron donor and acceptor materials. For example, in the fabrication of the famous P3HT:$PC_{61}BM$ based BHJ OPV device,[38] the polymer P3HT was usually prepared at a high concentration (>10 mg/mL in 1,2-DCB or chlorobenzene) and the solution was applied to heating and slow cooling to allow for the formation of crystalline nanofibers. The solution was then mixed with a concentrated solution of $PC_{61}BM$ (>10 mg/mL in 1,2-DCB or chlorobenzene), and subsequently spin-cast onto a PEDOT:PSS coated ITO glass. After that, a thin film of the cathode metal was deposited on the top of the active layer to complete the device fabrication. Compared to the phase-separate bilayer morphology of the planar heterojunction,[39] the morphology of the BHJ has a larger donor/acceptor interfacial area, which allows for efficient exciton dissociation and improves the device performance.[35a,40]

To investigate whether the intact tubular nanostructures of the G∧C-porphyrin RNTs can be conserved in the mixed solutions, the stock solutions of **G∧C-Por 1** RNTs, **$(G\wedge C)_2$-Por 2** RNTs and **$(G\wedge C)_2$-Por 3** RNTs were mixed with a solution of $PC_{61}BM$, respectively. Since the solution of **G∧C-Por 1** RNTs was in $MeNO_2$ (0.5 mg/mL), a solvent that could not dissolve $PC_{61}BM$, the $PC_{61}BM$ was first dissolved in 1,2-DCB at a concentration of 0.5 mg/mL, and then the $PC_{61}BM$ solution was added to the $MeNO_2$ solution of **G∧C-Por 1** RNTs with a 1:1 ratio (v/v). The mixed solution (a total concentration of 0.5 mg/mL in

$MeNO_2$/1,2-DCB, 1:1, v/v) was clear and did not form a precipitate over time. However, the SEM image of a sample prepared from this mixed solution after aging for 3 d showed large amorphous particles dispersing in the network of long RNTs (Figure 3.22B). These were probably the aggregates of $PC_{61}BM$, since adding 1,2-DCB to a stock solution of **G∧C-Por 1** RNTs in $MeNO_2$ did not lead to aggregation or disassembly of the RNTs in the mixed solvent (1:1, v/v). The stock solution of **$(G\wedge C)_2$-Por 2** RNTs was in a mixed solvent (10.0 mg/mL in 1,2-DCB/MeOH, 7:3, v/v), and $PC_{61}BM$ was also prepared in the mixed solvent at the same concentration. The two solutions were then mixed together at a 1:1 ratio (v/v). The mixed solution was aged for 3 d and diluted to 1.0 mg/mL (total concentration), and the SEM sample was immediately prepared from the dilute solution. As shown in Figure 3.22C, many long RNTs were found by SEM imaging and no aggregates were observed. The $PC_{61}BM$ molecules probably stick on or surrounded the RNTs, although no direct observation was attempted due to the resolution limits of the SEM. Since **$(G\wedge C)_2$-Por 3** was soluble in 1,2-DCB upon heating, the RNTs solution was then prepared in 1,2-DCB at a concentration of 2.0 mg/mL. The stock solution was then mixed with a $PC_{61}BM$ solution (2.0 mg/mL in 1,2-DCB), and the mixed solution was aged for 3 d and diluted to 1.0 mg/mL (total concentration) for the SEM sample preparation. As shown in the SEM image (Figure 3.22D), the tubular nanostructures of the RNTs were conserved, and many tiny dots were also observed, which were thought to be the $PC_{61}BM$ molecules.

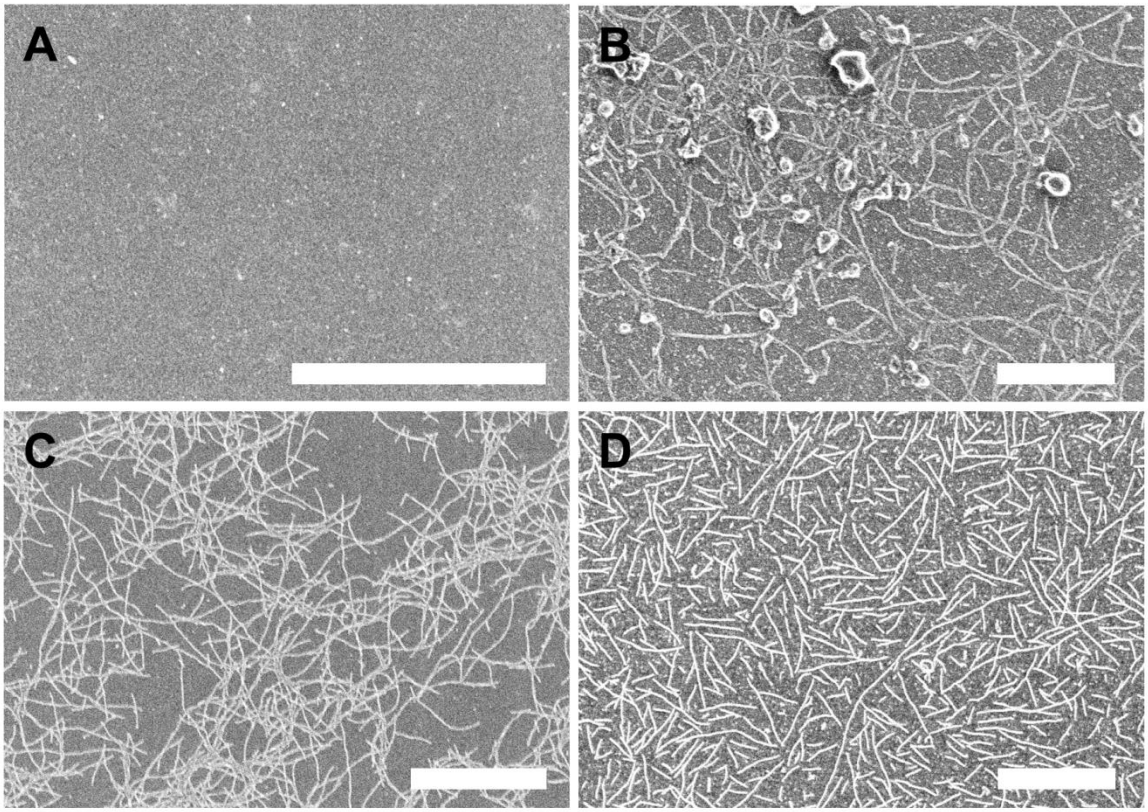

Figure 3.22. SEM images of (A) $PC_{61}BM$ (0.5 mg/mL in 1,2-DCB); (B) blend of **G∧C-Por 1** RNTs:$PC_{61}BM$ (1:1, w/w, total concentration 0.5 mg/mL in $MeNO_2$/1,2-DCB, 1:1, v/v); (C) blend of **(G∧C)$_2$-Por 2** RNTs:$PC_{61}BM$ (1:1, w/w, total concentration 1.0 mg/mL in 1,2-DCB/MeOH, 7:3, v/v); (D) blend of **(G∧C)$_2$-Por 3** RNTs:$PC_{61}BM$ (1:1, w/w, total concentration 1.0 mg/mL in 1,2-DCB). All mixed solutions were aged for 3 d before the SEM sample preparation. Scale bars: 500 nm.

In summary, we found the intact tubular nanostructures of the RNTs of **(G∧C)$_2$-Por 2** and **(G∧C)$_2$-Por 3** were conserved in the mixed solution with $PC_{61}BM$. These observations suggest that the mixture of these RNTs and $PC_{61}BM$ are suitable for the spin-casting process to create the BHJ morphology in the thin film of the electron donor/acceptor layer.

The charge separation and transport are expected to be improved by the bicontinuous network of the RNTs. Unfortunately, at this point we are unable to fabricate the OPV device to validate our expectations. On the other hand, although the tubular nanostructures of **G∧C-Por 1** RNTs were not significantly changed in the mixed solution with $PC_{61}BM$, the amorphous aggregates observed by SEM imaging might lead to the formation of large islands in the spin-cast film, which is detrimental to efficient charge separation and transport. Nevertheless, **G∧C-Por 1** RNTs is still suitable for the construction of the planar heterojunction in the bilayer films with $PC_{61}BM$, since the films of the electron donor and acceptor materials are not deposited simultaneously. The biggest challenge that impedes the application of **G∧C-Por 1** RNTs in the field of solution-processed OPVs is the low solubility, since 0.5 mg/mL in $MeNO_2$ is still too low for the spin-casting process.

3.6 Conductivity of G∧C-porphyrin RNTs

It was reported that 1D porphyrin-functionalized supramolecular assemblies can be highly conductive, which are even comparable to the well-known conductive polymers.[41] Herein we investigated the conductivity of the thin films of **G∧C-Por 1**, **$(G∧C)_2$-Por 2** and **$(G∧C)_2$-Por 3**.

3.6.1 Device and method

Two electrode devices were fabricated for the measurement (see details in the experimental section).[41a,c,42] The micrographs of the two-electrode device under an optical microscope and a schematic illustration of the device structure are shown in Figure 3.23. The two electrodes had 600 unbridged interlacing teeth with a gap of 10 μm (Figure 3.23B). The

electrodes were composed of a 5 nm thick chromium (Cr) layer and a 50 nm thick gold (Au) layer (Figure 3.23C). The nonconductive SiO_2 layer acted as a global back-gate. The thin films of both G∧C-Porphyrin RNTs and unassembled controls were cast on the devices by the drop-casting technique (Figure 3.23D).

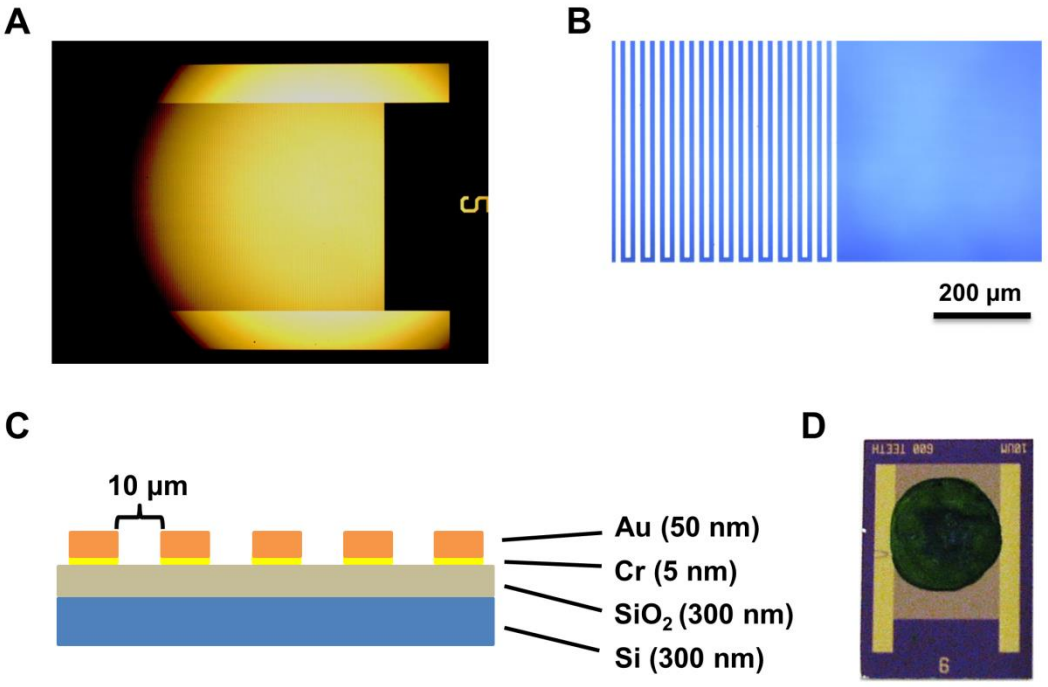

Figure 3.23. (A–B) Micrographs of the two-electrode device under an optical microscope; (C) schematic illustration of a cross-sectional view of the device; (D) a sample thin film cast on a two-electrode device.

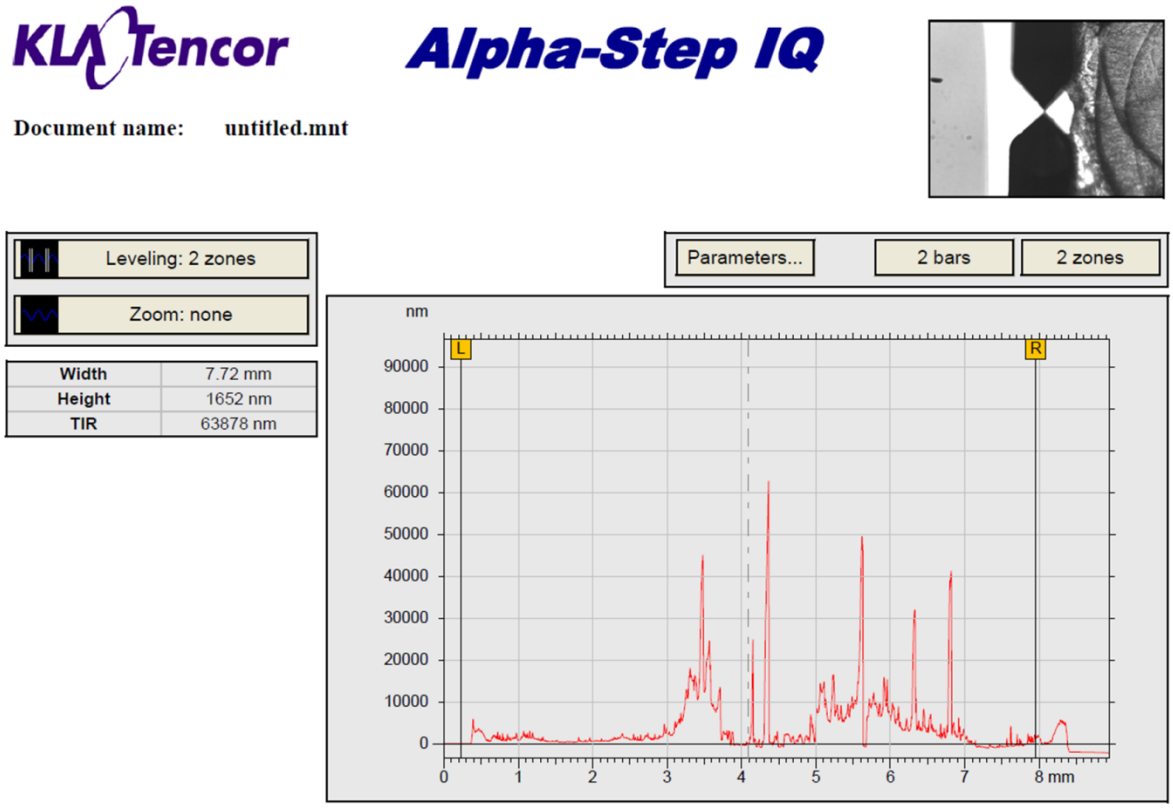

Figure 3.24. Average thickness measurement of a sample film by a digital profilometer. The image at the top right corner shows the probe touching the bare electrode surface (setpoint) beside the sample film. The image in the middle reflects the height profile when the probe scanned across the film between the two electrodes. The height value (thickness) in the table on the left is the average value of the data points between the two cursors in the height profile.

Before casting the sample film, the two-electrode device was checked by an optical microscope and tested on an integrated electronic characterization setup (see details in the experimental section) to ensure that the teeth were well separated and defect-free. The average thickness (D) of the sample film was estimated from its surface topographic profile using a digital profilometer (Figure 3.24). The effective junction area (A, film-filled gaps) is

given in **E10**, where l is the electrode teeth length (0.8 cm), and N is the number of the teeth covered by the sample film.

$$A = l \bullet D \bullet (N-1) \quad \textbf{(E10)}$$

The device was tested on the same I–V setup to depict the current–voltage curves with the maximum bias voltage up to 3 V. The resistance (R) of the sample film was calculated from the I–V curve using Ohm's law (**E11**).

$$R = \frac{V}{I} \quad \textbf{(E11)}$$

The resistivity (ρ) of the sample film was calculated by **E12**, where d is the gap width between two adjacent electrode teeth (10 μm).

$$\rho = \frac{RA}{d} \quad \textbf{(E12)}$$

The conductivity (σ) of the sample film ρ 1 was calculated by **E13**.

$$\sigma = \frac{1}{\rho} \quad \textbf{(E13)}$$

3.6.2 Results and discussion

Thin films of the RNTs and unassembled controls of **G∧C-Por 1, (G∧C)$_2$-Por 2** and **(G∧C)$_2$-Por 3** were cast on the two-electrode devices to measure the current–voltage (*I–V*) curves (Figure 3.25). Under the bias voltage from –3 V to 3 V, *I–V* curves of both the RNTs and controls displayed quasilinear characteristics. Under the same condition, the currents of all the RNTs were detected around the magnitude of μA, while the currents of all the unassembled controls were around or below the magnitude of nA.

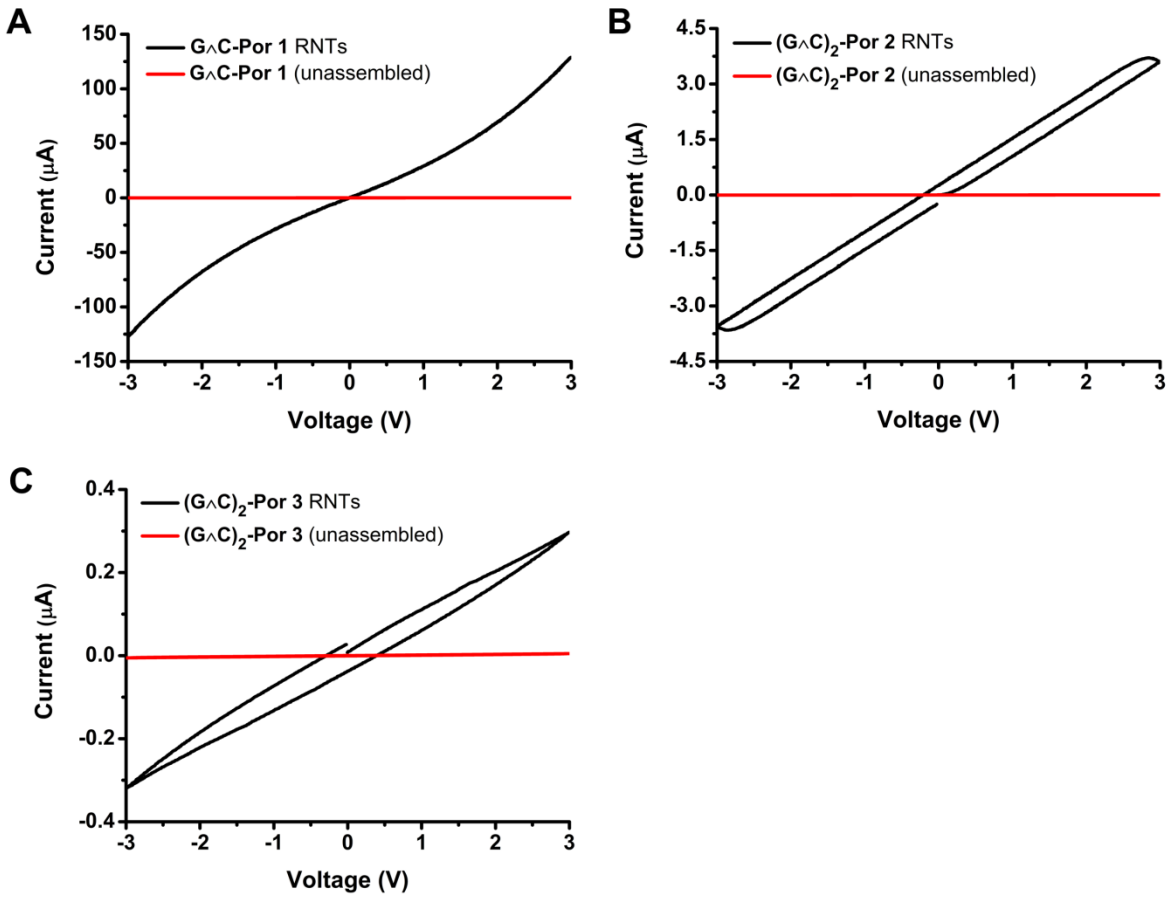

Figure 3.25. *I-V* curves measured on thin films of G∧C-porphyrin RNTs and non-assembled controls. (A) **G∧C-Por 1**; (B) **(G∧C)$_2$-Por 2**; (C) **(G∧C)$_2$-Por 3**.

Table 3.2. Conductivity of the thin films of G∧C-porphyrin RNTs and the unassembled counterparts.

Compounds	Conductivity σ (S/m)
G∧C-Por 1 RNTs	8.1×10^{-5}
G∧C-Por 1	3.3×10^{-10}
$(G \wedge C)_2$-Por 2 RNTs	4.5×10^{-6}
$(G \wedge C)_2$-Por 2	1.9×10^{-9}
$(G \wedge C)_2$-Por 3 RNTs	1.75×10^{-7}
$(G \wedge C)_2$-Por 3	2.5×10^{-9}

Based on the resistance calculated from the *I–V* curves at 3 V, and the film thickness measured by a profilometer, the conductivity of the sample films were calculated (Table 3.2). In general, the films of G∧C-porphyrin RNTs were much more conductive than those of the unassembled controls. The film of **G∧C-Por 1** RNTs showed the highest conductivity (8.1×10^{-5} S/m), which is 2.5×10^5 times higher than that of the unassembled control film. On the other hand, the conductivity of the films of **$(G \wedge C)_2$-Por 2** RNTs and **$(G \wedge C)_2$-Por 3** RNTs are also several orders of magnitude higher than those measured for their unassembled counterparts. In addition, the conductivity of the sample films were very stable. No obvious current decay was observed when the films were retested after being stored under ambient conditions for one year. The significant improvement in conductivity is presumably due to the highly ordered arrangement of the porphyrin arrays on the RNT scaffold, which may favor the unidirectional movement of the electrons and reduce random charge diffusion.[41,43] Furthermore, it is interesting to credit the high conductivity of the film of **G∧C-Por 1** RNTs to the binary-bundle nanostructures observed by STM (see chapter 2

for images), as the closely packed porphyrin arrays are nearly continuous at the interface of two single RNTs in the bundle.

3.7 Conclusion

In this chapter, some important optoelectronic properties of the assembled and unassembled **G∧C-Por 1**, **$(G\wedge C)_2$-Por 2** and **$(G\wedge C)_2$-Por 3** were presented. The HOMO–LUMO energy levels and optical band gaps of these materials were characterized by UPS and UV-Vis spectroscopy. No significant changes of the HOMO–LUMO energy levels were observed in the self-assembled RNTs and the unassembled counterparts. However, the RNTs showed smaller optical band gaps, which are due to the red-shifted absorption onsets in the UV-Vis spectra of the thin films. The well matched energy level alignments of the G∧C-Porphyrin RNTs and $PC_{61}BM$ indicates that they are potential electron donor-acceptor pairs for novel OPV devices. The RNT solutions of **$(G\wedge C)_2$-Por 2** and **$(G\wedge C)_2$-Por 3** were mixed with $PC_{61}BM$ solutions at high concentrations, and the intact tubular nanostructures were conserved, indicating that the mixed solutions are suitable for constructing the BHJ morphology using wet-processing techniques. Thin films of the RNTs displayed high conductivity, which are comparable in magnitude to those of semiconducting polymers. These self-assembled G∧C-porphyrin RNTs are anticipated to contribute to the repertoire of electron donor materials in solution-processed OPVs and nanoscale organic electronics.

3.8 Experimental section

3.8.1 Materials and methods

All the spectrophotometric grade solvents were purchased from Sigma-Aldrich or Acros Organics. $PC_{61}BM$ (99.5%) was purchased from Solaris Chem, Inc., Canada. All the reagents and solvents were used as received. Quartz cuvettes for the UV-Vis and photoluminescence study were purchased from Starna Cells, Inc., USA. The p-type Si (100) wafers for UPS sample analysis (diameter: 100 mm; thickness: 525 ± 20 μm; dopant: Boron; resistivity: 10-20 Ω•cm) were purchased from Silicon Materials, Inc., USA. The wafers were diced into small rectangular chips (18 mm × 13 mm) using a dicing saw (Disco DAD 321) to be used as the substrates for the UPS sample preparation. Si/SiO_2 wafers (diameter: 100 mm, 300 nm thick layer of thermally grown of SiO_2) were purchased from Silicon Materials Inc., USA, and were diced into small rectangular chips (18 mm × 15 mm) using a dicing saw (Disco DAD 321) to be used as the substrates for the two-electrode device fabrication.

3.8.2 Characterization

3.8.2.1 UV-Vis spectroscopy

UV-Vis spectra of the thin films were recorded on an Agilent 8453 UV-Vis spectrophotometer. The sample films were cast on clean quartz plates using the drop-casting technique. More specifically, a drop of a specific sample solution was deposited on a quartz plate by a glass pipette. The plate was placed in a vacuum chamber over night to remove the solvent. If the film was too thin for recording the spectrum, the drop-casting process was repeated on the same plate until a neat spectrum could be collected from the cast film.

3.8.2.2 Solid state photoluminescence spectroscopy

Solid state photoluminescence spectra of the thin films were collected on a Varian fluorescence spectrophotometer (CARY Eclipse). The sample thin films on quartz were prepared in the same way as mentioned above in the UV-Vis section. To cast a blended film, a mixed solution of the RNTs and $PC_{61}BM$ (molar ratio 1:1 in all cases) were used. The sample films were excited at 446 nm and the emission spectra were collected from 600 nm to 800 nm.

3.8.2.3 Ultraviolet photoelectron spectroscopy

Room-temperature UPS experiments were performed at the Alberta Center for Surface and Engineering Science (ACSES) using a Kratos Axis spectrometer with monochromatized Helium I radiation ($h\nu$ = 21.23 eV) and a hemispherical electron energy analyzer (Kratos Ultra Spectrometer). The system was maintained under ultrahigh vacuum ($< 5 \times 10^{-10}$ Torr), and the power for UPS was 3 kV × 20 mA (60 W). All of the samples were biased at −10 V during the measurements to observe the peak edge of the secondary electron.

The drop-casting technique was used in the UPS sample preparation. Hence, to a diced p-type Si (100) wafer (13 mm × 18 mm, freshly etched with 5% HF for 2 minutes, rinsed with ddH_2O water and dried with purified N_2 gas), a drop of the sample solution (0.5 mM in $MeNO_2$ for **G∧C-Por 1**; 1.0 mM in 1,2-DCB/MeOH, 7:3, v/v for **$(G\wedge C)_2$-Por 2**; 1.0 mM in 1.2-DCB for **$(G\wedge C)_2$-Por 3**, 2.0 mM in 1,2-DCB for $PC_{61}BM$) was cast using a glass pipette. The wafer was dried under a vacuum chamber for 30 min, and then transferred into the ultrahigh vacuum chamber ($< 5 \times 10^{-10}$ Torr) of the UPS instrument and allowed to stay for 30 min to remove residual solvent before analysis. For each material, three samples

were prepared on three separate Si wafers, and the average value was reported based on measurements on all three samples.

3.8.2.4 Conductivity of thin films

Commercially available Si/SiO_2 wafers (size 18 mm × 15 mm, 300 nm thick layer of thermally grown of SiO_2) were used as substrates for the two-electrode device. The substrates were cleaned with piranha solution, and then dried using a stream of filtered N_2. With a chromium mask (600 teeth, 10 μm gap width), the substrates were treated by a standard photolithography method to coat a patterned photoresist layer. A 5 nm thick adhesion layer of Cr was then deposited on the substrates using e-beam evaporation, followed by a 50 nm thick Au layer. To prepare the patterned two-electrode devices, the lift-off method was used.[42] More specifically, the chips were ultrasonically cleaned in acetone, 2-propanol and ultrapure water for 5 min each, and dried using a stream of filtered N_2. Prior to sample deposition, the two-electrode devices were checked by an optical microscope for any fabrication defects, and also tested for blank *I–V* curves to preclude the possibility of bridged electrode teeth that may arise from the photolithography process.

To cast a thin film on the two-electrode device, a drop of a specific sample solution (0.5 mg/mL in $MeNO_2$ for **G∧C-Por 1**; 2.0 mg/mL in 1,2-DCB/MeOH, 7:3, v/v for **$(G\wedge C)_2$-Por 2**; 2.0 mg/mL in 1.2-DCB for **$(G\wedge C)_2$-Por 3**) was deposited on the device using a glass pipette. The device was first placed in a low-vacuum chamber overnight to form a thin film, and then transferred to a high-vacuum heater and heated at 80 °C for 30 min and allowed to cool to room temperature in vacuum to remove the residual solvent.

The *I–V* curves of the two-electrode devices were recorded on an integrated electronic characterization setup.[44] The data acquisition (DAQ) board was manufactured by National Instruments (USA) with the model PCI-6110 and the operation software LabVIEW (LV3). The low noise current preamplifier SR570 was manufactured by Stanford Research Systems (USA), and capable of current gains as large as 1 pA/V. The maximum bias voltage was 3.0 V, and the scan rate was set as 1 V/s. The sensitivity varied from 100 pA/V to 1 mA/V, depending on the conductivity of a specific sample.

3.8.2.5 Profilometer

The thickness of the thin film on a two-electrode device was measured by a digital profilometer (KLA Tencor, Alpha Step IQ) featuring automatic leveling and multi-scan mode. The bare edge of the electrode was used as the setpoint. During each scan, the probe was allowed to scan across the approximate diameter of the sample spot, and the average thickness was obtained. For each thin film sample, three scans were performed and the thickness value for conductivity calculation was averaged based on all three scans.

3.9 References

(1) (a) Scharber, M. C.; Mühlbacher, D.; Koppe, M.; Denk, P.; Waldauf, C.; Heeger A. J.; Brabec, C. J. *Adv. Mater.* **2006**, *18*, 789–794. (b) Brabec, C. J.; Scherf, U.; Dyakonov, V. *Organic Photovoltaics: Materials, Device Physics, and Manufacturing Technologies* 2nd ed.; Wiley-VCH: Weinheim, 2014.

(2) Zimmermann, Y.-S.; Schaffer, A.; Hugi, C.; Fent, K.; Corvini, P. F.-X.; Lenz, M. *Environ. Int.* **2012**, *49*, 128–140.

(3) Anslyn, E. V.; Dougherty, D. A. *Modern Physical Organic Chemistry* 1st ed.; University Science Books: Sausalito, 2006.

(4) (a) Brocks, G.; Tol, A. *J. Phys. Chem.* **1996**, *100*, 1838−1846. (b) Naito, K.; Sakurai, M.; Egusa, S. *J. Phys. Chem. A* **1997**, *101*, 2350−2357. (c) Acebal, P.; Blaya, S.; Carretero, L. *Chem. Phys. Lett.* **2003**, *374*, 206−214.

(5) (a) Mete, E.; Uner, D.; Çakmak, M.; Gülseren, O.; Ellialtıoğlu, Ş. *J. Phys. Chem. C* **2007**, *111*, 7539–7547. (b) Zhang, G.; Musgrave, C. B. *J. Phys. Chem. A* **2007**, *111*, 1554–1561. (c) Ra, C. S.; Yim, S.; Park, G. *Bull. Korean Chem. Soc*. **2008**, *29*, 891–893. (d) Zhang, Y.; Basel, T. P.; Gautam, B. R.; Yang, X. M.; Mascaro, D. J.; Liu, F.; Vardeny, Z. V. *Nat. Commun.* **2012**, *3*, 1043.

(6) (a) Bard, A. J.; Faulkner, L. R. *Electrochemical Methods: Fundamentals and Applications* 2nd ed.; Wiley: New York, 2001. (b) Compton, R. G.; Banks, C. E. *Understanding Voltammetry* 2nd ed.; Imperial College Press: London, 2011.

(7) Kissinger, P. T.; Heineman, W. R. *J. Chem. Educ.* **1983**, *60*, 702–706.

(8) Gosser, D. K. Cyclic Voltammetry: Simulation and Analysis of Reaction Mechanisms 1st ed.; Wiley-VCH: New York, 1993.

(9) Evans, D. H.; O'Connell, K. M.; Petersen, R. A.; Kelly, M. J. *J. Chem. Educ.* **1983**, *60*, 290–293.

(10) Cardona, C. M.; Li, W.; Kaifer, A. E.; Stockdale, D.; Bazan, G. C. *Adv. Mater.* **2011**, *23*, 2367–2371.

(11) (a) Johansson, T.; Mammo, W.; Svensson, M.; Andersson, M. R.; Inganäs, O. *J. Mater. Chem.* **2003**, *13*, 1316–1323.

(12) Brédas, J. L.; Silbey, R.; Boudreaux, D. S.; Chance, R. R. *J. Am. Chem. Soc.* **1983**, *105*, 6555–1323.

(13) Park, H. H.; Lee, Y.; Jo, J. W.; Jo, W. H. *Polym. Chem.* **2012**, *3*, 2928–2932.

(14) Mercier, L. G.; Mishra, A.; Ishigaki, Y.; Henne, F.; Schulz, G.; Bäuerle, P. *Org. Lett.* **2014**, *16*, 2642–2645.

(15) (a) Baran, D.; Balan, A.; Celebi, S.; Esteban, B. M.; Neugebauer, H.; Sariciftci, N. S.; Toppare, L. *Chem. Mater.* **2010**, *22*, 2978–2987. (b) Zheng, M.; Sarker, A. M.; Gurel, E. E.; Lahti, P. M.; Karaz, F. E. *Macromolecules* **2000**, *33*, 7426–7430. (c) Ma, C. Q.; Fonrodona, M.; Schikora, M. C.; Wienk, M. M.; Janssen, R. A. J.; Bauerle, P. *Adv. Funct. Mater.* **2008**, *18*, 3323–3331.

(16) (a) Chen, X.; Zhang, G.; Luo, H.; Li, Y.; Liu, Z.; Zhang, D. *J. Mater. Chem. C* **2014**, *2*, 2869–2876. (b) Shen, S.; Jiang, P.; He, C.; Zhang, J.; Shen, P.; Zhang, Y.; Yi, Y.; Zhang, Z.; Li, Z.; Li, Y. *Chem. Mater.* **2013**, *25*, 2274–2281.

(17) (a) Meng, H.; Wudl, F. *Macromolecules* **2001**, *34*, 1810–1816. (b) Yang, C.-J.; Jenekhe, S. A.; *Macromolecules* **1995**, *28*, 1180–1196.

(18) (a) Gritzner, G.; Kuta, J. *Pure Appl. Chem.* **1984**, *56*, 461–466. (b) Bard, A. J.; Stratmann, M.; Schäfer, H. J. *Encyclopedia of Electrochemistry, Volume 8: Organic Electrochemistry*; Wiley-VCH: Weinheim, 2004.

(19) (a) Charvet, R.; Yamamoto, Y.; Sasaki, T.; Kim, J.; Kato, K.; Takata, M.; Saeki, A.; Seki, S.; Aida, T. *J. Am. Chem. Soc.* **2012**, *134*, 2524–2527. (b) Kumar, R. J.; MacDonald, J. M.; Singh, T. B.; Waddington, L. J.; Holmes, A. B. *J. Am. Chem. Soc.* **2011**, *133*, 8564–8573. (c) Schulz, G. L.; Urdanpilleta, M.; Fitzner, R.; Brier, E.; Mena-Osteritz, E.; Reinold, E.; Bäuerle, P. *Beilstein J. Nanotechnol.* **2013**, *4*, 680–689.

(20) Reinert, F.; Hüfner, S. *New J. Phys.* **2005**, *7*, 97.

(21) Wilson, J. D.; Buffa, A. J.; Lou, B. *College Physics* 7th ed.; Addison-Wesley: San Francisco, 2010.

(22) Kittel, C. *Introduction to Solid State Physics* 8th ed.; Wiley: Hoboken, 2005.

(23) (a) Van der Heide, P. *X-ray Photoelectron Spectroscopy: An Introduction to Principles and Practices* 1st ed.; Wiley: Hoboken, 2012. (b) Hüfner, S. *Photoelectron Spectroscopy: Principles and Applications* 3rd ed.; Springer: Bridgewater, 2003.

(24) Ellis, A. M.; Feher, M.; Wright, T. G. *Electronic and Photoelectron Spectroscopy: Fundamentals and Case Studies* 1st ed.; Cambridge University Press: London, 2005.

(25) (a) Suga, S.; Sekiyama, A. "*Photoelectron Spectroscopy: Bulk and Surface Electronic Structures*" in *Springer Series Optical Sciences Volume 176*; Springer: Heidelberg, 2014. (b) University of California, Davis ChemWiki: The Dynamic Chemistry E-textbook. http://chemwiki.ucdavis.edu/Physical_Chemistry/Spectroscopy/Photoelectron_Spectroscopy/Photoelectron_Spectroscopy%3A_Application (Accessed Sept. 25, 2014).

(26) D'Andrade, B. W.; Datta, S.; Forrest, S. R.; Djurovich, P.; Polikarpov, E.; Thompson, M. E. *Org. Electron.* **2005**, *6*, 11–20.

(27) (a) Seo, J. H.; Nguyen, T.-Q. *J. Am. Chem. Soc.* **2008**, *130*, 10042–10043.

(28) Brütting, W.; Adachi, C.; Holmes, R. J. *Physics of Organic Semiconductors* Wiley-VCH: Weinheim, 2012.

(29) Scudiero, L.; Barlow, D. E.; Mazur, U.; Hipps, K. W. *J. Am. Chem. Soc.* **2001**, *123*, 4073–4080.

(30) (a) Djurovich, P. I.; Mayo, E. I.; Forrest, S. R.; Thompson, M. E. *Org. Electron.* **2009**, *10*, 515–520. (b) Yaffe, O.; Qi, Y.; Scheres, L.; Puniredd, S. R.; Segev, L.; Ely, T.; Haick, H.; Zuilhof, H.; Vilan, A.; Kronik, L.; Kahn, A.; Cahen, D. *Phys. Rev. B* **2012**, *85*, 045433. (c) Yan, L.; Watkins, N. J.; Zorba, S.; Gao, Y. L.; Tang, C. W. *Appl. Phys. Lett.* **2001**, *79*, 4148−4150.

(31) (a) Koo, J.; Cho, J.-J.; Yang, J. H.; Yoo, P. J.; Ph, K. W.; Park, J. *Bull. Korean Chem. Soc.* **2012**, *33*, 636–640. (b) Tada, A.; Geng, Y.; Wei, Q.; Hashimoto, K.; Tajima, K. *Nat. Mater.* **2011**, *10*, 450–455. (c) Sayed, S. Y.; Fereiro, J. A.; Yan, H.; McCreery, R. L.; Bergren, A. J. *Proc. Natl. Acad. Sci. U.S.A.* **2012**, *109*, 11498–11503.

(32) (a) Kim, J. Y.; Lee, K.; Coates, N. E.; Moses, D.; Nguyen, T.-Q.; Dante, M.; Heeger, A. J. *Science* **2007**, *317*, 222–225. (b) Xu, Z.; Chen, L.-M.; Chen, M.-H.; Li, G.; Yang, Y. *Appl. Phys. Lett.* **2009**, *95*, 013301. (c) Maibach, J.; Mankel, E.; Mayer, T.; Jaegermann, W. *J. Mater. Chem. C* **2013**, *1*, 7635–7642.

(33) (a) Li, C.-Z.; Yip, H.-L.; Jen, A. K.-Y. *J. Mater. Chem.* **2012**, *22*, 4161–4177. (b) He, Y.; Li, Y. *Phys. Chem. Chem. Phys*. **2011**, *13*, 1970–1983.

(34) (a) Umeyama, T.; Watanabe, Y.; Oodoi, M.; Evgenia, D.; Shishido, T.; Imahori, H. *J. Mater. Chem.* **2012**, *22*, 24394–24402. (b) Sun, Y. M.; Welch, G. C.; Leong, W. L.; Takacs, C. J.; Bazan, G. C.; Heeger, A. J. *Nat. Mater.* **2012**, *11*, 44–48. (c) Li, G.; Zhu, R.; Yang, Y. *Nat. Photonics* **2012**, *6*, 153–161.

(35) (a) Choi, J. K.; Jin, M. L.; An, C. J.; Kim, D. W.; Jung, H.-T. *ACS Appl. Mater. Interfaces* **2014**, *6*, 11047–11053. (b) Cao, Y.; Yu, G.; Zhang, C.; Menon, R.; Heeger, A. J. *Synth. Met.* **1997**, *87*, 171–174.

(36) (a) Sun, D.; Tham, F. S.; Reed, C. A.; Boyd, P. D. W. *Proc. Natl. Acad. Sci. U.S.A.* **2002**, *99*, 5088−5092. (b) Jurow, M.; Farley, C.; Pabon, C.; Hageman, B.; Dolor, A.; Drain, C. M. *Chem. Commun.* **2012**, *48*, 4731–4733.

(37) (a) Walter, M. G.; Rudine, A. B.; Wamser, C. C. *J. Porphyrins Phthalocyanines* **2010**, *14*, 759–792. (b) Luechai, A.; Gasiorowski, J.; Petsom, A.; Neugebaurer, H.; Sariciftci, N. S.; Thamyongkit, P. *J. Mater. Chem.* **2012**, *22*, 23030–23037. (c) Kengthanomma, T.; Thamyongkit, P.; Gasiorowski, J.; Ramil, A. M.; Sariciftci, N. S. *J. Mater. Chem. A* **2013**, *1*, 10524–10531. (d) Calderon, R. M. K.; Valero, J.; Grimm, B.; de Mendoza, J.; Guldi, D. M. *J. Am. Chem. Soc.* **2014**, *136*, 11436−11443.

(38) (a) Berson, S.; De Bettignies, R.; Bailly, S.; Guillerez, S. *Adv. Funct. Mater.* **2007**, *17*, 1377–1384. (b) Xin, H.; Kim, F. S.; Jenekhe, S. A. *J. Am. Chem. Soc.* **2008**, *130*, 5424–5425.

(39) (a) Sariciftci, N. D.; Braun, D.; Zhang, C.; Srdanov, V. I.; Heeger, A. J.; Stucky, G.; Wudl, F. *Appl. Phys. Lett.* **1993**, *62*, 585–587. (b) McGehee, M. D.; Topinka, M. A. *Nat. Mater.* **2006**, *5*, 675–676.

(40) (a) Yu, G.; Gao, J.; Hummelen, J. C.; Wudl, F.; Heeger, A. J. *Science* **1995**, *270*, 1789–1791. (b) Thompson, B. C.; Fréchet, J. M. J. *Angew. Chem., Int. Ed.* **2008**, *47*, 58–77.

(41) (a) Wang, Q.; Chen, Y.; Ma, P.; Lu, J.; Zhang, X.; Jiang, J. *J. Mater. Chem.* **2011**, *21*, 8057–8065. (b) Sengupta, S.; Ebeling, D.; Patwardhan, S.; Zhang, X.; von Berlepsch, H.; Böttcher, C.; Stepanenko, V.; Uemura, S.; Hentschel, C.; Fuchs, H.; Grozema, F. C.; Siebbeles, L. D. A.; Holzwarth, A. R.; Chi, L.; Würthner, F. *Angew. Chem., Int. Ed.* **2012**, *51*, 6378–6382. (c) Liu, C.-Y.; Pan, H.-L.; Tang, H. J.; Fox, M. A.; Bard, A. J. *J. Phys. Chem.* **1995**, *99*, 7632–7636. (d) Zhao, Q.; Wang, Y.; Qiao, Y.; Wang, X.; Guo, X.; Yan Y.; Huang J. *Chem. Commun.* **2014**, *50*, 13537–13539.

(42) Mahmoud, A. M.; Bergren, A. J.; Pekas, N.; McCreery, R. L. *Adv. Funct. Mater.* **2011**, *21*, 2273–2281.

(43) (a) Ozawa, H.; Tanaka, H.; Kawao, M.; Unoa, S.; Nakazato, K. *Chem. Commun.* **2009**, *47*, 7411–7413. (b) Yoon, D.; Lee, S.; Yoo, K.; Kim, J.; Lim, J.; Aratani, N.; Tsuda, A.; Osuka, A.; Kim, D. *J. Am. Chem. Soc.* **2003**, *125*, 11062–11064.

(44) Shoute, L. C. T.; Wu, Y.; McCreery, R. L. *Electrochim. Acta* **2013**, *110*, 437–445.

Chapter 4

Self-Assembly and Characterization of Oligothiophene-Functionalized Guanine–Cytosine Building Blocks

4.1 Introduction

Organic photoactive and electroactive molecular materials have attracted substantial attention due to their application in various fields including OLEDs[1], OFETs[2] and OPVs[3]. Devices fabricated from these materials are light weight, low-cost and flexible, which makes them commercially appealing and superior to the inorganic counterparts. Conducting polymers and small molecules are two major types of organic optoelectronic materials. Among the class of π-conjugated conducting polymers, polythiophenes have emerged from extensive studies on account of their low band gaps, high charge mobility and feasibility to various functionalization. [4] For example, a polymer mixture of poly-(3,4-ethylenedioxythiophene) and polystyrene sulfonate (PEDOT:PSS) has been commercialized as a leading conducting polymer product and an antistatic agent with different trade names. In polythiophenes, charge conduction occurs by an interchain hopping mechanism via spatial overlap of π-orbitals between adjacent conjugates that are in close proximity.[5] High charge mobility is attributed to high regioregularity and effective conjugation length at the molecular level, and high crystallinity and ordering in solid-state nanoscale morphology.[6] However, long-range molecular order is often lost in polymers due to defects arising during polymerization.[7] Small amounts of impurities in the polymer backbone can lead to a strong negative effect on the physical properties of the material and device performance.[8] Moreover, spin-casting of the polymer solutions produces amorphous

films, in which the microstructure feature of high crystallinity is absent.[6e,9] On the other hand, small molecules including π-conjugated oligomers have well-defined chemical structures and can be purified relatively easily. Many studies have been focused on the synthesis and characterization of π-conjugated oligomers with long axis dimensions up to 10 nm.[10] In some cases, vacuum sublimation deposition of these molecules on specific substrates can generate highly ordered layers that display superior charge mobility than those solution-processed films.[11] However, thermal evaporation is more expensive and not ideal for large area depositions.

In this respect, supramolecular nanoscale self-assembly of small conjugated molecules and oligomers provides an attractive approach to bring solution-processability and high ordering together to generate well-organized nanomaterials for application in organic optoelectronics.[8] In the bottom-up design strategy, the building block consists of a conjugated molecule with a self-assembly design. In solution, the building blocks hierarchically self-assemble into highly order architectures, driven by intra and intermolecular non-covalent interactions. These architectures are uniform and error-free, since the programmed self-assembly process is self-correcting and the precise arrangement of building blocks is pre-encoded at a molecular level. In addition, these assemblies adopt the most thermodynamically stable structure.[12] Although it is appealing, rational design of the building blocks is required, because nanoscopic ordering of the supramolecular architecture entirely depends on their precise chemical structure. Moreover, the optoelectronic properties of the conjugated molecules are not automatically transferred into the assemblies.[13] Hence an ordered nanostructure that promotes overlap of π-orbitals is needed to improve the physical properties and device performance.

Various functionalization and self-assembly scaffolds have been explored to incorporate oligothiophene and construct supramolecular assemblies,[14] such as sulfur-alkyl,[13] ethylene oxide,[15] diketopyrrolopyrrole (DPP),[16] 3,5-dihydroxyl-benzoic ester dendritic segments,[17] amide-rich segments,[18] nucleobases,[19] carbohydrates,[20] steroids,[21] and peptides[22]. The non-covalent interactions within the nanoarchitectures include hydrogen bonding, π–π stacking and van der Waals forces. However, most of the assemblies form large aggregates and fibers with the width falling in the range from several hundred nanometers to a few micrometers. The lost control over uniform morphology is mainly due to π–π stacking of the thiophenes and van der waals interactions of alkyl side sides, which drive the materials to form lamellae, rods, superhelices and other superstructures. For many applications in the field of organic optoelectronics, well-defined and uniform nanostructures of the material is highly demanded, as they can improve the charge mobility by orders of magnitudes.[8,23]

This chapter focuses on the self-assembly studies of three oligothiophene-functionalized guanine–cytosine (G∧C) molecules. **$(G\wedge C)_2$-3T** is an alkyl-flanked terthiophene covalently bonded to a twin G∧C motif. **$(G\wedge C)_2$-6T** is a butyl-functionalized sexithiophene linked to a twin G∧C motif via an benzylamine spacer. Mono **G∧C-6T** is a butyl-functionalized sexithiophene covalently bonded to a single G∧C motif via an aniline spacer. Figure 4.1 shows the molecular structures and models of the three molecules. The models were generated using VMD.[24] Optoelectronic properties of the self-assembled RNTs of **$(G\wedge C)_2$-6T** are also presented. This project was done via collaboration with my previous colleague Dr. Venkatakrishnan Parthasarathy, who synthesized the three molecules. I assisted in the spectrometric identification of the chemical structures, systematically investigated the self-assembly, and carried out the optical and electronic characterization.

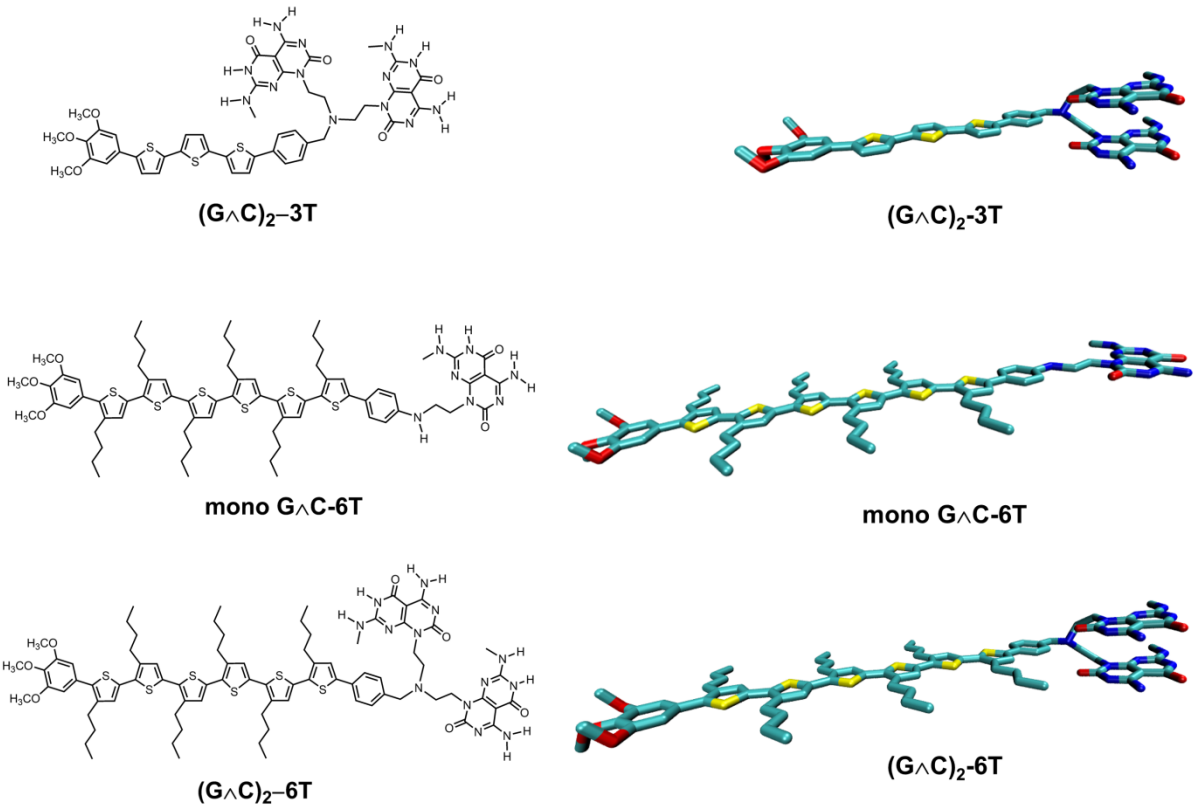

Figure 4.1. Molecular structures and models of **(G∧C)$_2$-3T**, mono **G∧C-6T** and **(G∧C)$_2$-6T**. Atom colors: cyan, C; blue, N; red, O; yellow, S. Hydrogen atoms are removed for clarity.

4.2 Synthesis of (G∧C)$_2$-3T

The synthesis route of **(G∧C)$_2$-3T** is shown in Figure 4.2. The starting material 2-bromothiophene was treated in a standard procedure to form the corresponding Grignard reagent, which was then converted to thiophene-2-boronate ester (**1**) by adding 2-isopropoxy-4,4,5,5-tetramethyl-1,3,2-dioxaborolane. Meanwhile, the Suzuki cross-coupling partner 2-bromo-5-iodothiophene (**2**) was prepared from iodination to 2-bromothiophene. The cross-coupling product bromobithiophene (**3**) was converted to bithiophene-2-boronate

ester (**4**), which was then coupled with 2-bromo-5-iodothiophene to produce bromoterthiophene (**5**). The product was again converted to the corresponding Grignard reagent and then boronate ester (**6**). The cross-coupling reaction between 3,4,5-trimethoxyiodobenzene and compound **6** produced compound **7**. It is important to note that the aryl group was incorporated in order to improve the solubility of **(G∧C)$_2$-3T** in non-polar solvents, as unsubstituted oligothiophene is known to have poor solubility. In fact, spectroscopic characterization for unsubstituted oligothiophenes containing seven or more units is virtually impossible since these compounds are insoluble.[25] The bromination product (**8**) of compound **7** was coupled with 4-(*N*-boc-aminomethyl)phenylboronic acid pinacol ester followed by deprotection to produce compound **9**. The benzylamine group serves as a short spacer between terthiophene and the twin G∧C motif. Reductive amination between G∧C aldehyde and compound **9** followed by HCl deprotection produced the final compound **(G∧C)$_2$-3T**, which is a bright yellow solid.

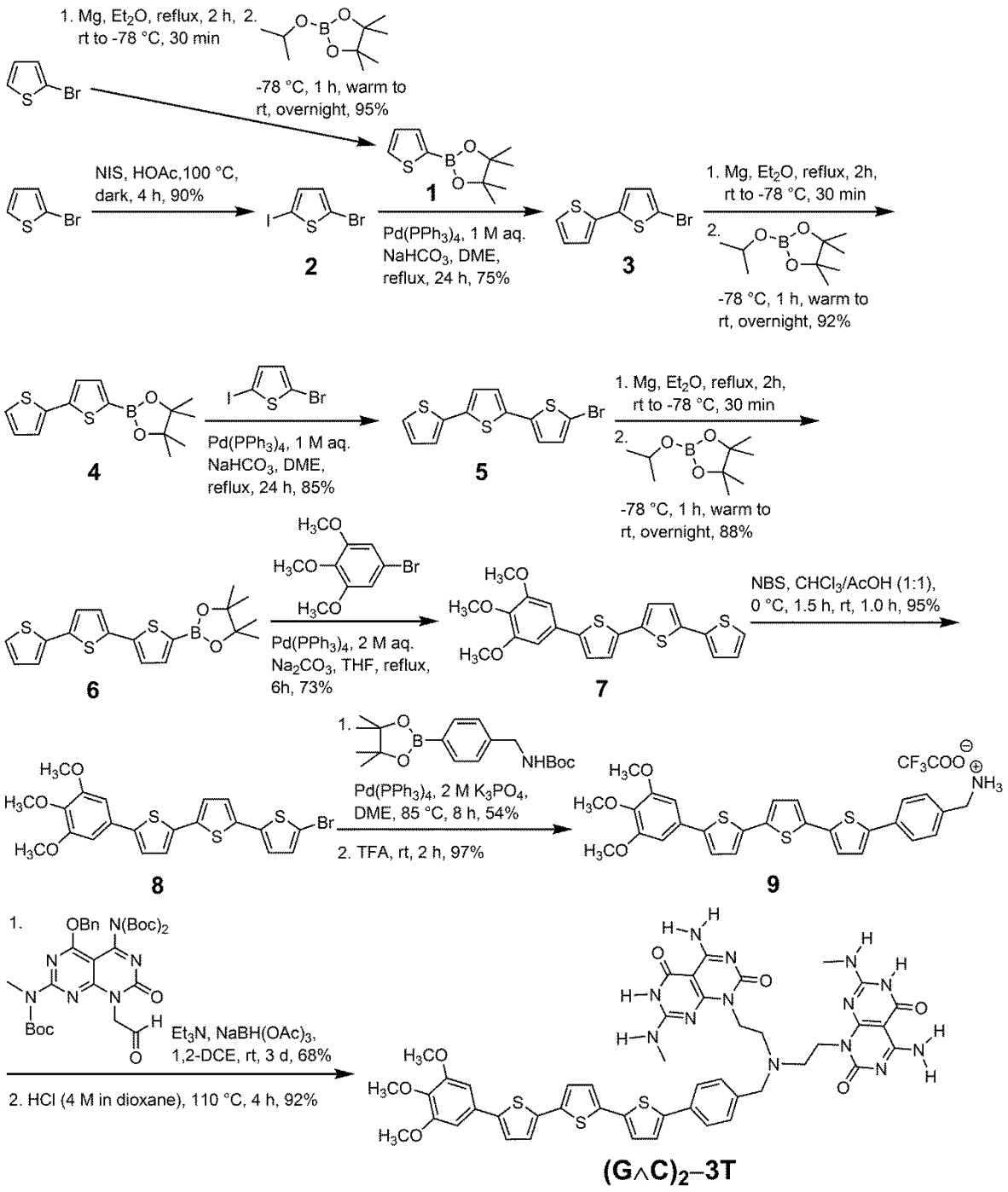

Figure 4.2. Synthesis route of **(G∧C)$_2$-3T**.

4.3 Self-assembly of $(G\wedge C)_2$-3T

$(G\wedge C)_2$-3T has poor solubility in common solvents such as DCM, chloroform, DMF or toluene. Figure 4.3 shows the SEM images of **$(G\wedge C)_2$-3T** in four different solvents. The solution in DMSO at a concentration of 0.1 mg/mL became clear after heating. However, no tubular nanostructures were observed, rather large amorphous aggregates were found in the SEM image (Figure 4.3A). A DCM solution at the same concentration was turbid even after gentle heating and sonication. The SEM image of this sample shows a thin layer consisting of many tiny dots of a similar size (Figure 4.3B). These dots are considered to be single rosettes or short stacks. Similar morphology was observed in a stock solution after aging for 7 d. A 1,2-DCB solution was prepared after heating at 120 °C for 3 min. The solution became clear upon heating and the color changed from yellow to pale yellow. However, the solution became turbid after cooling to room temperature. Although many tiny dots were observed in the SEM image, large fibers were also present (Figure 4.3C). The poor solubility of **$(G\wedge C)_2$-3T** in 1,2-DCB and DCM is likely due to the G∧C module which is very polar. In fact, unfunctionalized and unprotected G∧C aldehyde is insoluble in DCM or 1,2-DCB, but very soluble in MeOH, DMF and DMSO. Hence, a small portion of MeOH was mixed with 1,2-DCB to see whether it can improve the solubility of **$(G\wedge C)_2$-3T** and promote self-assembly. Unfortunately, the solubility was not improved, and large aggregates were found in the SEM image along with the tiny dots (Figure 4.3D).

Due to the solubility constraint, the application of **$(G\wedge C)_2$-3T** in the field of organic nanoelectronics is restricted. My focus was shifted to **$(G\wedge C)_2$-6T**, which not only has a good solubility in the ideal solvents for OPV device fabrication such as 1,2-DCB and chlorobenzene, but also has a long effective conjugation length.

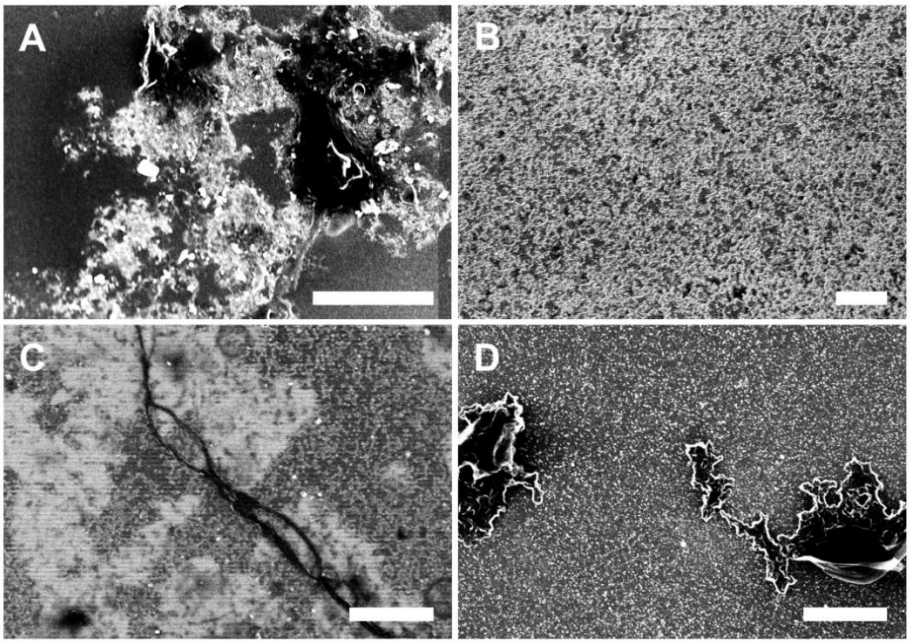

Figure 4.3. SEM images of **(G∧C)$_2$-3T** assemblies in different solvents. (A) DMSO; (B) DCM; (C) 1,2-DCB; (D) 1,2-DCB/MeOH (9:1, v/v). Concentration: 0.05 mg/mL. Aging: 1 d. Scale bars: 500 nm.

4.4 Synthesis of (G∧C)$_2$-6T

The synthesis of **(G∧C)$_2$-6T** (Figure 4.4) is quite similar to that of **(G∧C)$_2$-3T**. The compound has an orange color as compared to the bright yellow color of **(G∧C)$_2$-3T**, indicating the extended conjugation length. Unlike the unsubstituted thiophene unit in **(G∧C)$_2$-3T**, **(G∧C)$_2$-6T** comprises six units of 3-butylthiophene which was prepared via Kumada cross coupling. The butyl groups were introduced in order to further improve the solubility of this material in nonpolar solvents. However, they also give rise to more steric hindrance and may reduce the ability of self-assembly due to intermolecular repulsion. Indeed, this is what we observed in mono **G∧C-6T**, which has a single G∧C module instead of two.

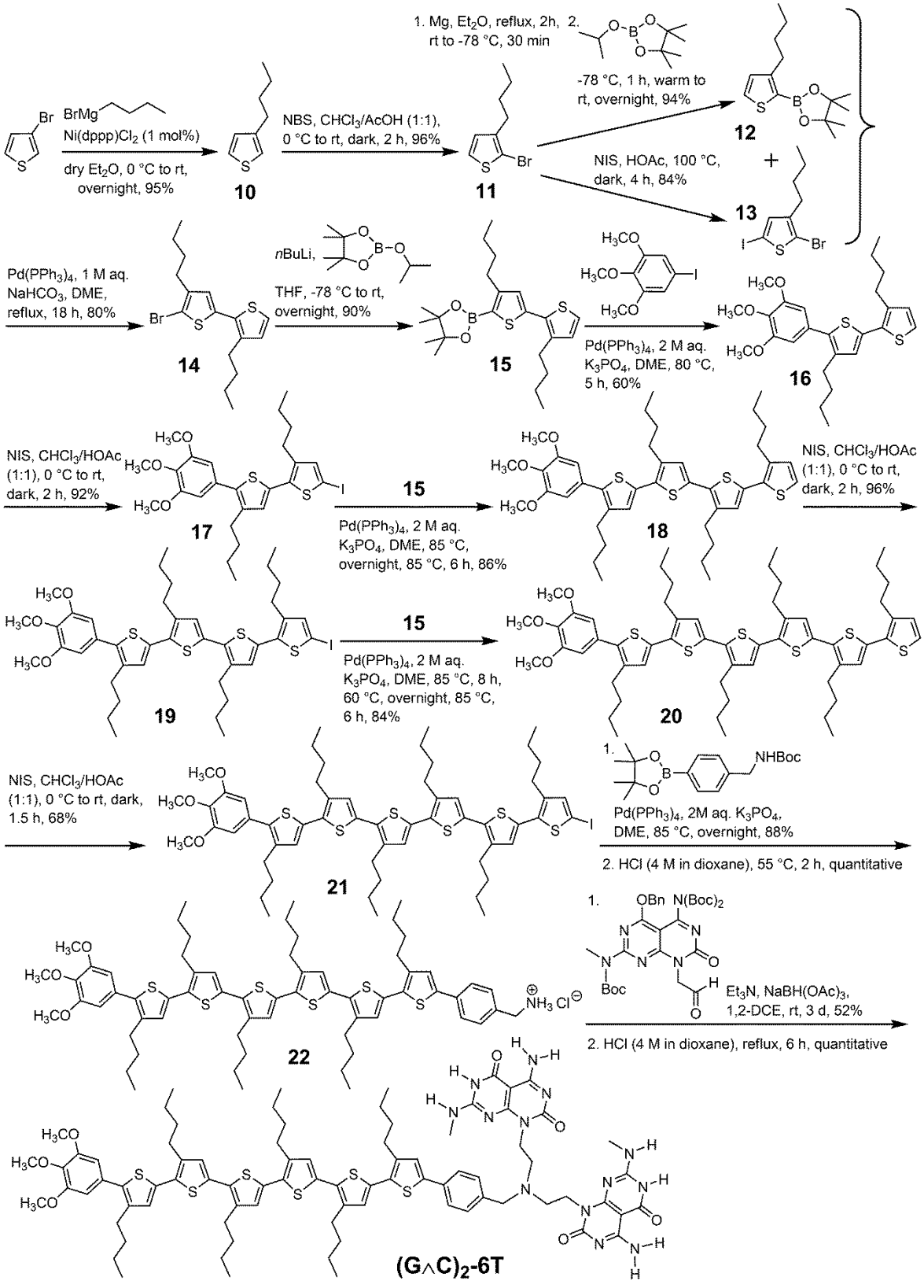

Figure 4.4. Synthesis route of **(G∧C)$_2$-6T**.

4.5 Self-assembly of mono G∧C-6T

As mentioned above, sexithiophene unit is anchored to a single G∧C via the aniline spacer in mono **G∧C-6T** (Figure 4.5). The low nucleophilicity of aniline exclusively produced the mono-N-alkylation[26] product in the reductive amination reaction with G∧C aldehyde. On the contrary, the benzylamine spacer in **$(G\wedge C)_2$-6T** only produced the dialkylation product even when G∧C aldehyde was added in half of the stoichiometrically equivalent molar quantity.

Mono **G∧C-6T** is very soluble in DCM, toluene, and 1,2-DCB. In DMSO it can also be dissolved at a concentration of 0.5 mg/mL after heating. Small particles and islands of thin layers were observed in the SEM image of the DMSO sample (Figure 4.5A). The formation of islands is presumably due to intermolecular π–π stacking of the sexithiophene units and van der Waals interactions between the substituted butyl chains. Holey films were observed in the low-magnification SEM image of the DCM sample (Figure 4.5B), while amorphous aggregates were present in the high-magnification image (Figure 4.5C). The SEM image of the toluene sample also displayed islands of thin layers (Figure 4.5D). In 1,2-DCB, tiny dots and short tubular structures were observed, which might be single rosettes or short stacks (Figure 4.5E). However, the short tubes did not elongate even after an aging period of 10 d. Different conditions were tested for the toluene and 1,2-DCB solutions, but no long tubular nanostructures were found by SEM imaging. Heating, sonication or aging did not promote assembly of this molecule.

The inability of **G∧C-6T** to form long self-assembled RNTs is likely due to the steric hindrance caused by the substituted butyl chains, as π–π stacking interaction attenuates when the distance between the G∧C modules increases.

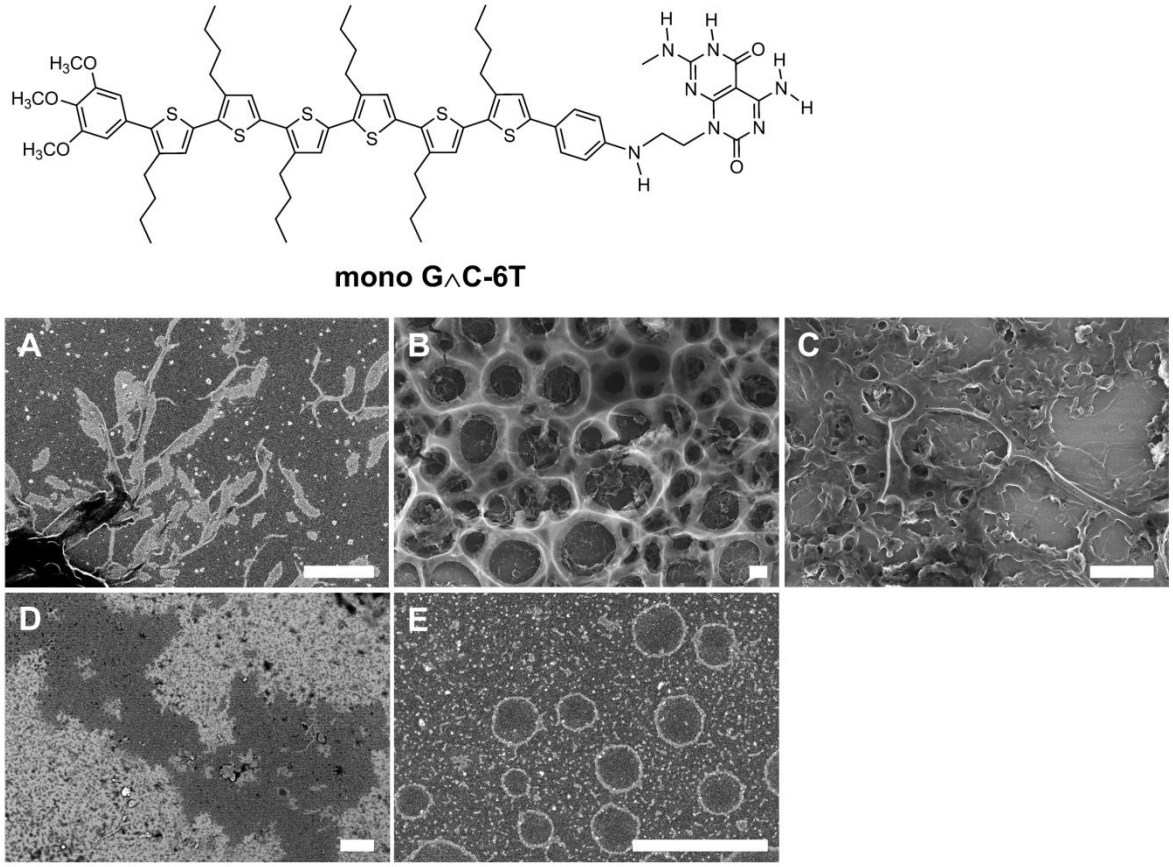

Figure 4.5. Molecular structure of mono **G∧C-6T** and SEM images of its assemblies in different solvents. (A) DMSO; (B–C) DCM; (D) toluene; (E) 1,2-DCB. Concentration: 0.1 mg/mL. Aging: 1d. Scale bars: 500 nm.

4.5 Self-assembly of $(G\wedge C)_2$-6T

4.5.1 Solvent effect

$(G\wedge C)_2$-6T can be easily dissolved in DCM, chlorobenzene and 1,2-DCB. In DMSO and DMF, the solution became clear upon heating. The time-dependent SEM images of **$(G\wedge C)_2$-6T** in the four solvents are shown in Figure 4.6. All of the solutions were prepared at a concentration of 0.2 mg/mL and heated for 3 min to promote self-assembly. Three batches of SEM samples were prepared with the respective aging time of 4 h, 1 d and 10 d.

In DMSO, small particles and islands of thin layers were found initially. Over time, less particles but more tiny dots were observed. However, no tubular nanostructures were present even after 10 d. In DMF, large amorphous aggregates were found in all of the SEM samples. In DCM, holey films and tiny dots were found after 4 h of aging. Although the films disappeared and tiny dots became dominant over time, RNTs were still not observed. In chlorobenzene, which is one of the ideal solvents for fabrication of solution-processed OPV devices, tiny dots and short RNTs that are just a few tens of nanometers long were observed after 4 h of aging. After 1 d, the SEM image still showed a similar morphology. Interestingly, after 10 d the tiny dots and short RNTs almost disappeared and small islands of thin layers were found in the SEM image. These thin-layer nanostructures are likely driven by intermolecular π–π stacking and van der Waals interactions between the sexithiophene units and the butyl chains, which are competing against hydrogen bonding and π–π stacking interactions between the G∧C modules. To promote the formation of RNTs and suppress other unwanted nanostructures, an appropriate solvent and processing condition are needed.

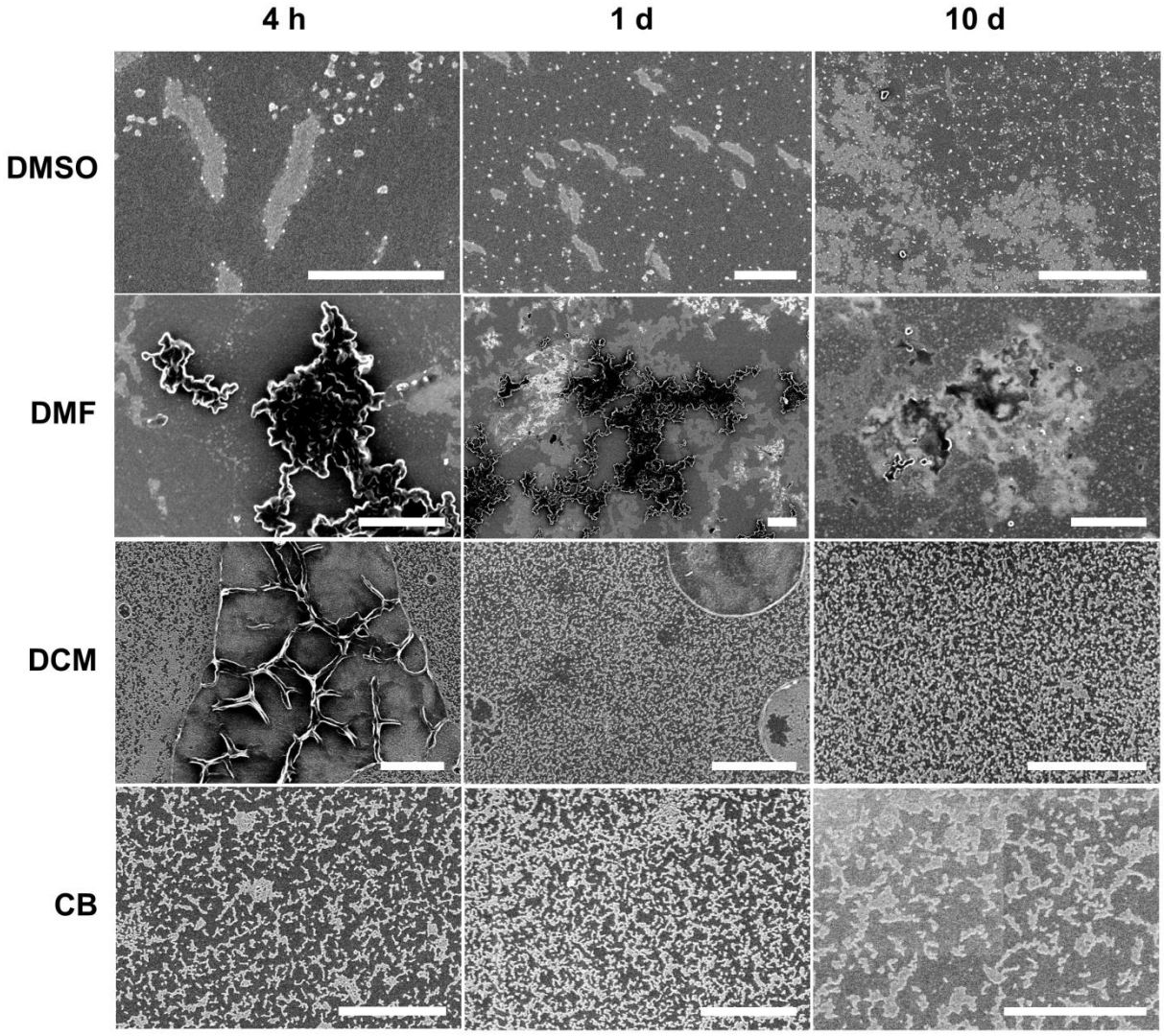

Figure 4.6. SEM images of **(G∧C)$_2$-6T** assemblies in DMSO, DMF, DCM and chlorobenzene (CB) with different aging times. Concentration: 0.2 mg/mL. Conditions: DMSO (100 °C, 3 min); DMF (100 °C, 3 min); DCM (35 °C, 3 min); chlorobenzene (90 °C, 3 min). Scale bars: 500 nm.

4.5.2 Optimization of the self-assembly conditions in 1,2-DCB

(G∧C)$_2$-6T is very soluble in 1,2-DCB. A clear solution at a concentration of 10 mg/mL can be obtained by just dissolving the compound in the solvent without the assistance of sonication or heating. Different processing conditions were tested to optimize the self-assembly of **(G∧C)$_2$-6T** in 1,2-DCB. Hence three solutions were prepared at the same concentration of 1.0 mg/mL but under three different conditions, and were labeled as **S1**, **S2** and **S3**. **S2** was applied to sonication for 5 min, while **S3** was heated at 120 °C for 5 min and then taken out from the heating block to cool to room temperature. In comparison, **S2** was prepared by dissolving the compound in the solvent without any special treatment. After aging for 30 min and 7 d respectively, SEM samples were prepared from these solutions. Figure 4.7 shows the SEM images. After 30 min of aging, a few short tubes with many tiny dots were found in the SEM sample from **S1** (Figure 4.7A). After 7 d of aging, many short tubes with the length of about 100 nm were found (Figure 4.7B). This clearly indicates that the spontaneous self-assembly of **(G∧C)$_2$-6T** is a slow process. Interestingly, some nanotubes seem to stick to each other to form bundles, which might be due to the interaction between the butyl chains. In the SEM images of the samples from **S2**, similar results were observed (Figure 4.7C and D), indicating that sonication does not promote self-assembly, or to a very little extent. In contrast, nanotubes with the length in the range from several hundred nanometers to micrometers were present in the SEM image of the sample from **S3** after 30 min of aging (Figure 4.7E). The nanotubes grew over time in solution, as after 7 d of aging the length of the nanotubes was generally more than 1 μm (Figure 4.7F). Figure 4.8 shows an schematic illustration of the hierarchical self-assembly process of **(G∧C)$_2$-6T** to form an interconnected network of RNTs. It is worth noting that

few bundles were present in the SEM samples prepared from **S3**. We conclude that heating can promote the self-assembly of **(G∧C)$_2$-6T** in 1,2-DCB, and may also supress van der Waals interactions between the butyl chains.

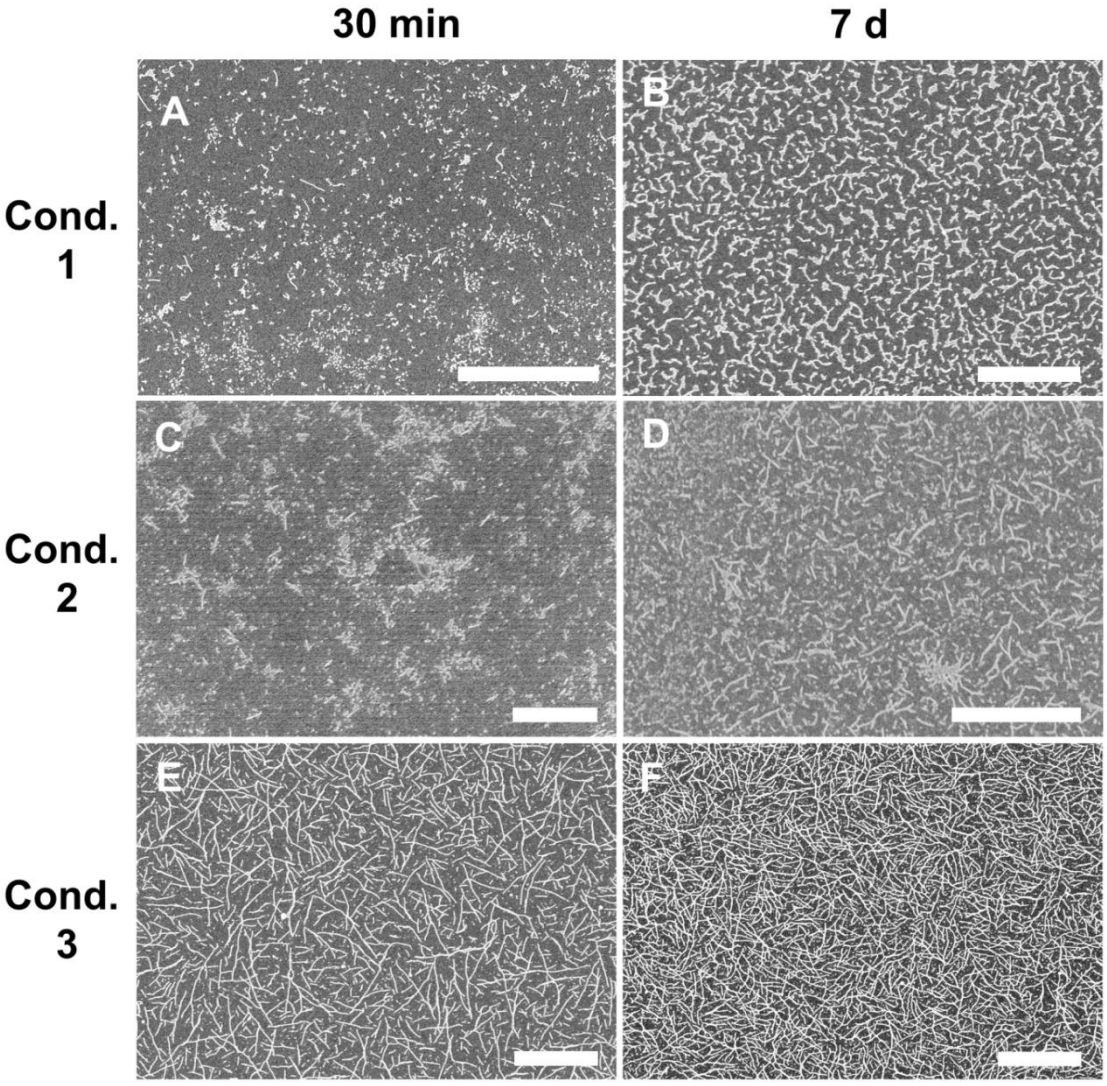

Figure 4.7. SEM images of **(G∧C)$_2$-6T** RNTs in 1,2-DCB under different processing conditions. Concentration: 1.0 mg/mL, all solutions were diluted to 0.5 mg/mL right before SEM sample preparation. Condition 1: spontaneous self-assembly, no heating or sonication; condition 2: sonication for 5 min; condition 3: heating at 120 °C for 5 min. All solutions were aged for 30 min and 7 d respectively. Scale bars: 500 nm.

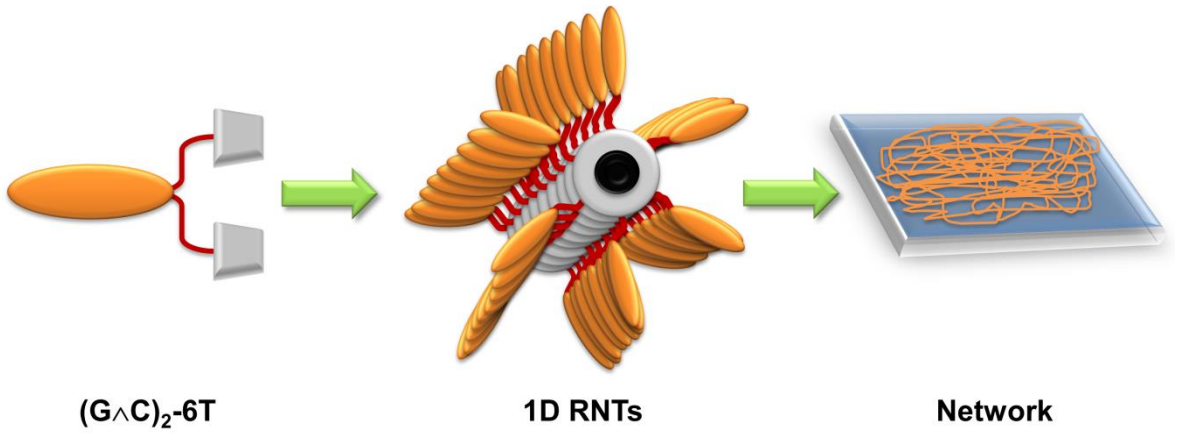

Figure 4.8. Schematic illustration of hierarchical self-assembly of **(G∧C)$_2$-6T**.

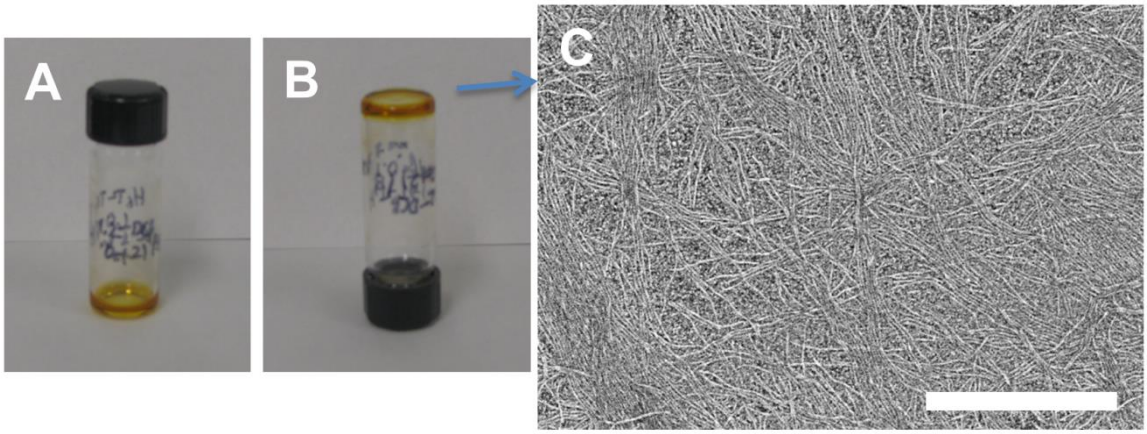

Figure 4.9. (A–B) Pictures of organogel of **(G∧C)$_2$-6T** RNTs in 1,2-DCB (1.0 mg/mL) after 240 d; (C) SEM image of a sample from the break-up solution of the organogel. Scale bar: 500 nm.

Interestingly, the solution of **(G∧C)$_2$-6T** RNTs in 1,2-DCB (1.0 mg/mL) can form an organogel after a long aging time. The organogel could be broken up easily by heating or sonication. SEM imaging revealed an interconnected network structure composed of long

RNTs (Figure 4.9). The formation of an organogel is likely due to the strong non-covalent interaction between the solvent molecules and the sexithiophene units.

4.5.3 Effect of MeOH

The self-assembly ability of **(G∧C)$_2$-6T** in 1,2-DCB can be greatly improved by adding a small portion of MeOH to the solvent. However, the volume percentage of MeOH is crucial for the morphology of RNTs. Four **(G∧C)$_2$-6T** solutions at the concentration of 1.0 mg/mL but with different volume percentage of MeOH were heated to boil for 1 min and slowly cooled down to room temperature. The SEM images of the samples prepared from these solutions are shown in Figure 4.9. When 5% MeOH was present in the binary solvent system, RNTs with the length of about 1 μm were observed along with some tiny dots (Figure 4.10A). In the solution that contained 10% MeOH, RNTs with the lengths of several micrometers were observed (Figure 4.10B). When 30% MeOH was present in the mixed solvent, the RNTs were even longer, but they also entangled to form aggregates (Figure 4.10C). When the ratio of 1,2-DCB/MeOH was 1:1, the solution was turbid and did not become clear even at the boiling point (Figure 4.10D). Accordingly, large aggregates of short nanotubes were found in the SEM image. In conclusion, a small amount of MeOH can promote the self-assembly of **(G∧C)$_2$-6T** in 1,2-DCB, while a large amount of MeOH in the mixed solvent causes the compound to form large bundles and precipitate.

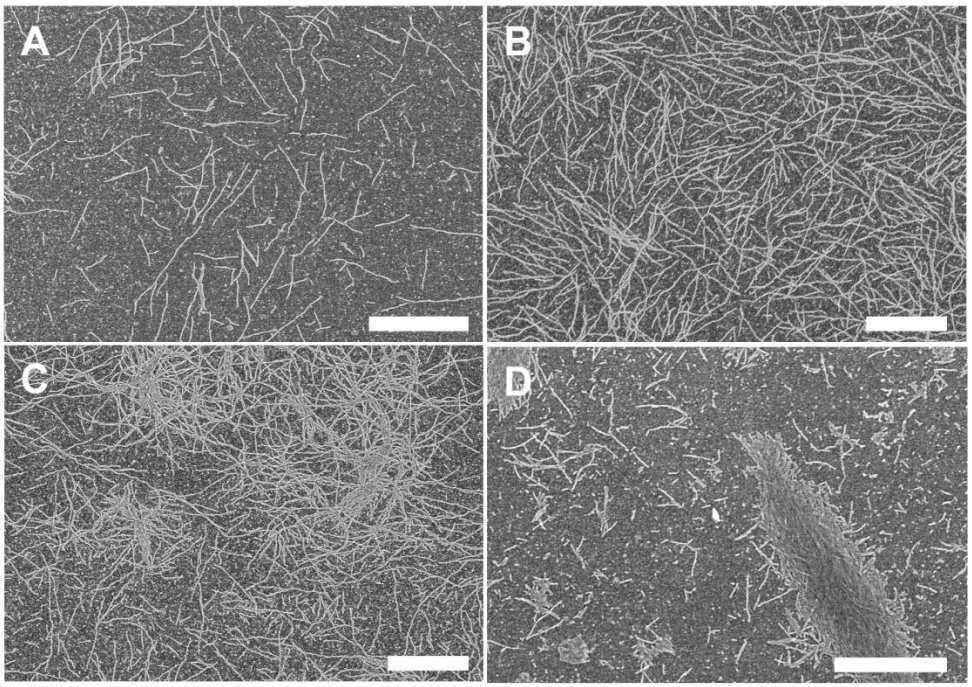

Figure 4.10. SEM images of **(G∧C)$_2$-6T** RNTs in a mixture of 1,2-DCB/MeOH with different volume percentages of MeOH. (A) 5%; (B) 10%; (C) 30%; (D) 50%. Concentration: 1.0 mg/mL. All solutions were heated to boil for 1 min. Scale bars: 500 nm.

4.6 Identification of (G∧C)$_2$-6T RNTs

To prove that the observed tubular nanostructures were due to the hierarchical self-assembly of the twin G∧C modules instead of the π–π stacking and van de Waals interaction between the sexithiophene units, two control solutions of compound **20** in chlorobenzene and 1,2-DCB were also processed under the same conditions as that of **(G∧C)$_2$-6T**. Compound **20** is the trimethoxyphenyl- and butyl-substituted sexithiophene unit which is not anchored to the twin (G∧C)$_2$ module. No tubular nanostructures were found in the SEM samples from either the chlorobenzene or the 1,2-DCB solutions (Figure

4.11). This clearly shows the inability of sexithiophene to form self-assembled nanostructure.

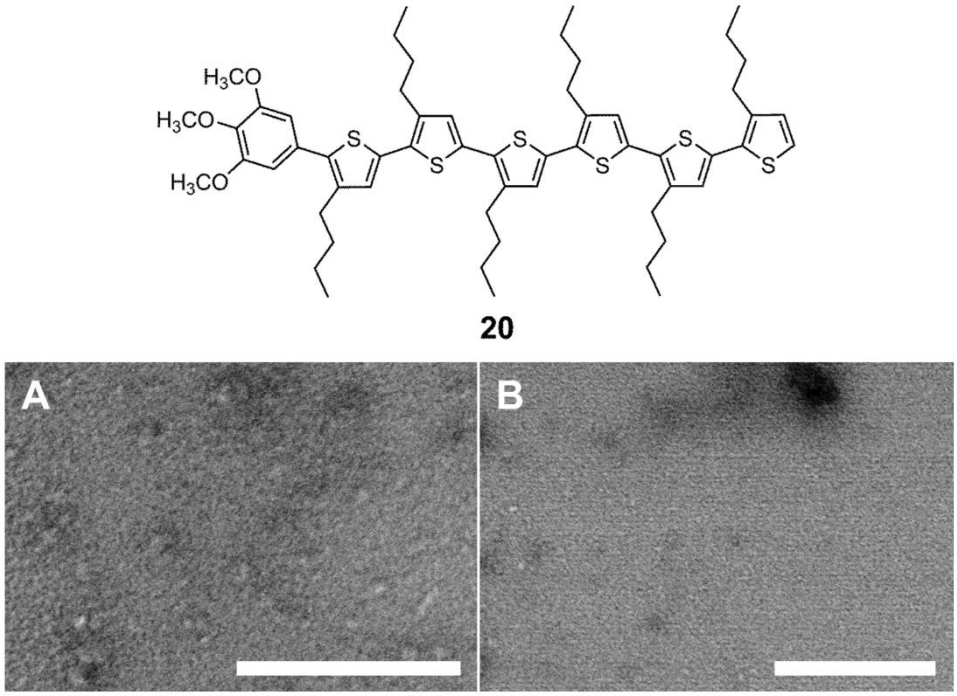

Figure 4.11. Molecular structure of compound **20** and SEM images of the samples prepared from its solutions in (A) chlorobenzene and (B) 1,2-DCB. Concentration: 1.0 mg/mL. Conditions: chlorobenzene, 90 °C, 3 min; 1,2-DCB, 120 °C, 5 min; aging for 1 d. Scale bars: 500 nm.

4.7 UV-Vis absorption spectra of $(G\wedge C)_2$-6T RNTs

To investigate the changes in the UV-Vis absorption spectrum upon the self-assembly of **$(G\wedge C)_2$-6T** in 1,2-DCB, a solution of **$(G\wedge C)_2$-6T** with a concentration of 2.0 mg/mL was heated at 120 °C for 5 min and then allowed to cool to room temperature. SEM samples were prepared from the diluted aliquots (0.5 mg/mL) of the solution before heating and after cooling. As expected, the SEM image of the sample prepared from the initially

dissolved solution before heating process showed many tiny dots and a few short RNTs (Figure 4.12A), while the SEM image of the sample from the solution after heating and aging for 1 h displayed a few tiny dots and many well dispersed RNTs with a length of several hundred nanometers (Figure 4.12B). Meanwhile, the UV-Vis spectra of the diluted solution (0.5 mg/mL) before and after heating were also collected. Figure 4.12C shows the spectral changes. After the treatment of heating and aging for 1 h, a blue shift was observed for the broad π–π* absorption band of the sexithiophene unit.[22b] More specifically, the absorption maximum of this band shifted from 419 nm to 382 nm upon self-assembly, indicating that the peripheral sexithiophene units on the RNTs are typical head-to-head H-type aggregates.[18b,21] This arrangement may improve the charge transport in the OPV device. In addition, no significant color change of the solution was observed upon self-assembly. By contrast, the blue shift of the sexithiophene absorption band was not observed in the solution of **(G∧C)$_2$-6T** in DCM (Figure 4.13), which is a solvent that does not promote self-assembly (see Figure 4.6 for SEM images). It is worth noting that the peak at 292 nm is one of the characteristic peaks for the G∧C motif.

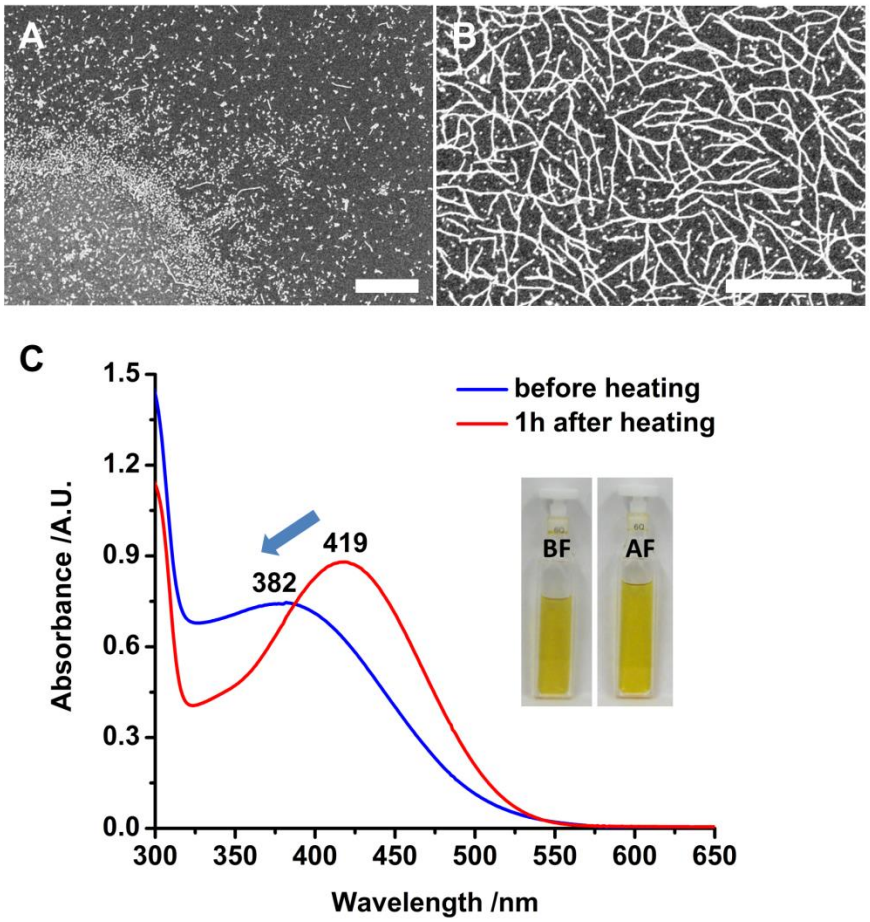

Figure 4.12. SEM images of **$(G\wedge C)_2$-6T** (A) before and (B) after self-assembly in 1,2-DCB (0.5 mg/mL); (C) absorption spectra (0.5 mg/mL), insets show the solution (0.5 mg/mL) before and after heating. Path length: 1 mm. Scale bars: 500 nm.

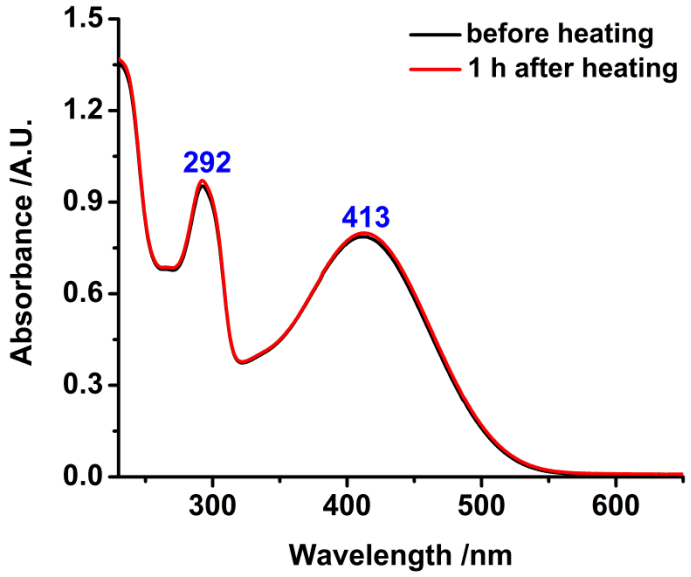

Figure 4.13. Absorption spectra of **(G∧C)$_2$-6T** (A) before and (B) after heating in DCM (0.5 mg/mL). Heating condition: 35 °C, 3 min. Path length: 1 mm.

The absorption spectra of the drop-cast thin films on quartz were also collected for **(G∧C)$_2$-6T** RNTs and the unassembled control (Figure 4.14). Two characteristic absorption bands of the G∧C motif were present in both spectra, with the maxima at 235 nm and 293 nm in the film of unassembled **(G∧C)$_2$-6T**, and 234 nm and 288 nm in the film of **(G∧C)$_2$-6T** RNTs. In terms of the sexithiophene unit, the absorption maximum of the thin film did not have a significant change compared to that of the solution in the case of unassembled **(G∧C)$_2$-6T**. However, in the case of **(G∧C)$_2$-6T** RNTs, the absorption maximum was seen at 393 nm, which had a 11 nm red shift compared to that of the solution. The red shift is likely due to the restricted molecular motions and increased planarization of the sexithiophene units in the solid state.[27] In addition, the absorption onsets were observed at 563 nm in the case of the unassembled **(G∧C)$_2$-6T**, and 551 nm in the case of **(G∧C)$_2$-6T**

RNTs. The absorption onsets can be used to calculate the optical band gaps between the HOMO and LUMO energy levels.

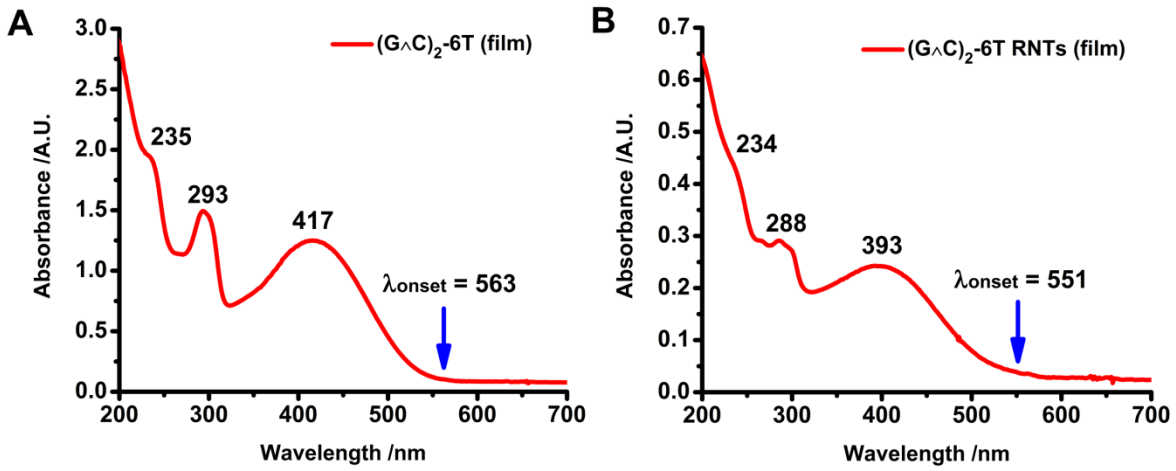

Figure 4.14. Absorption spectra of thin films of (A) **(G∧C)$_2$-6T** and (B) **(G∧C)$_2$-6T** RNTs on quartz.

4.8 Photoluminescence of (G∧C)$_2$-6T RNTs

The fluorescence spectrum of a solution of **(G∧C)$_2$-6T** RNTs (4 μg/mL in 1,2-DCB) is shown in Figure 4.15. Under the excitation wavelength of 384 nm, a broad emission band from 400 nm to 750 nm was observed, which was assigned to the emission band of the sexithiophene unit. The emission maximum wavelength of the spectrum at 510 nm is in close agreement with the onset wavelength of the absorption spectrum of the compound in solution. When the solution was exposed to UV light irradiation in a dark environment (λ = 366 nm), it emitted a pale yellow luminescence. Unfortunately, we were unable to collect the fluorescence spectrum of a drop-cast thin film of **(G∧C)$_2$-6T** RNTs on quartz as the fluorescence signals were too weak.[28]

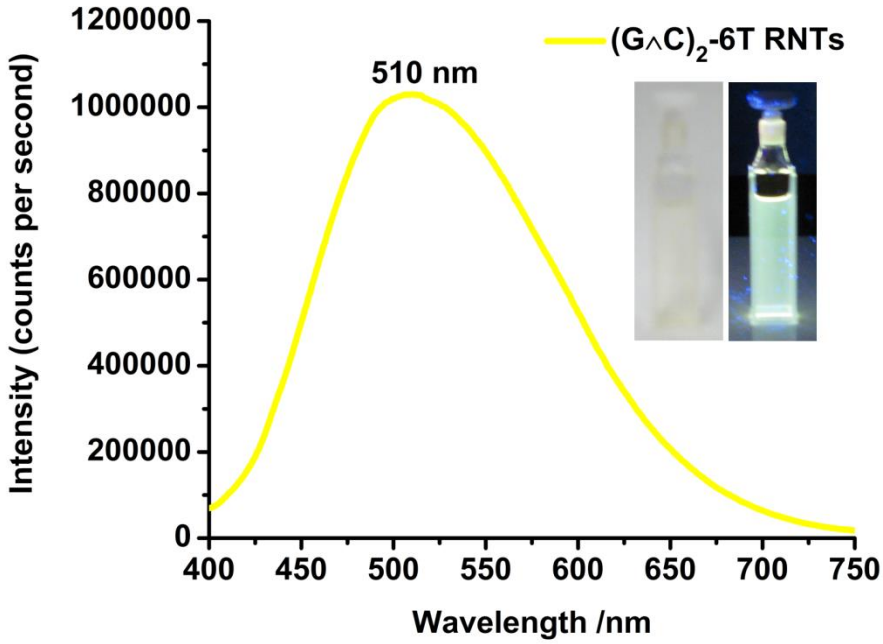

Figure 4.15. Fluorescence spectrum of a 1,2-DCB solution of **(G∧C)$_2$-6T** RNTs (4 μg/mL) excited at 384 nm. The inset shows the solution under fluorescence lighting (left) and UV light (366 nm).

4.9 TEM and AFM characterization of (G∧C)$_2$-6T RNTs

TEM and AFM techniques were used to characterize the RNTs of **(G∧C)$_2$-6T**. In order to stain the RNTs, uranyl acetate solutions in H_2O, CH_3CN, MeOH and acetone were tested. When the H_2O or CH_3CN solutions were used, the RNTs were not stained since the surface boundaries were not clear (Figure 4.16A and B). When the MeOH solution was used, the boundaries of the RNTs were improved. However, a patterned unknown layer was also found in the background, which makes the measurement of the cross-sectional diameter of the RNTs inaccurate (Figure 4.16C).

The best stained TEM samples were found when 0.2% uranyl acetate in acetone was used. Under the SE-mode SEM imaging, the RNTs were dark and covered by the bright stain particles (Figure 4.17A). When the imaging was switched to the TE mode for the same sample area, the RNTs became bright while the boundaries became dark, indicating that the RNTs were well-stained (Figure 4.17B). The solvent-dependent staining properties are likely due to the hydrophobic nature of the surface of the RNTs. High-resolution TEM images revealed that the cross-sectional diameter of a single RNT is 8.2 ± 0.5 nm (Figuer 4.17C and D).

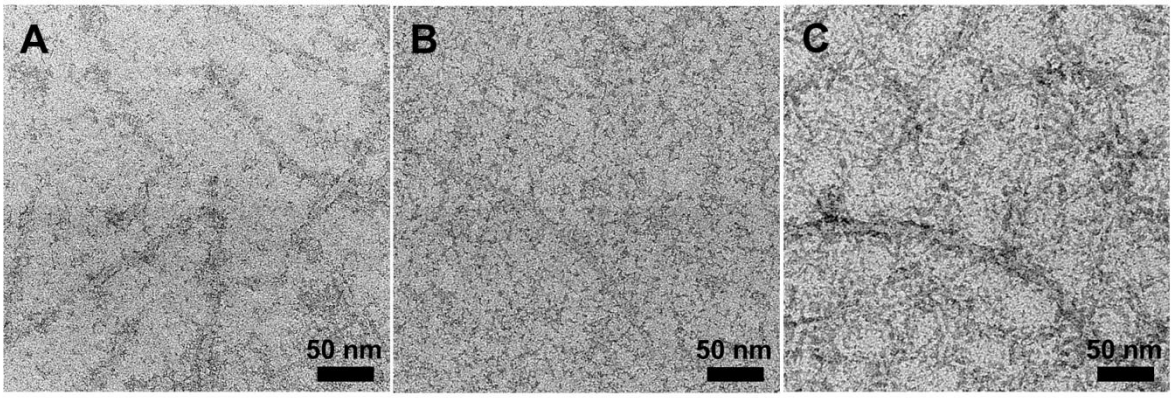

Figure 4.16. TEM images of poorly-stained **(G∧C)$_2$-6T** RNTs. Concentration: 0.01 mg/mL in 1,2-DCB. Stains: (A) 1% uranyl acetate in H_2O; (B) 0.2% uranyl acetate in CH_3CN; (C) 0.25 uranyl acetate in MeOH.

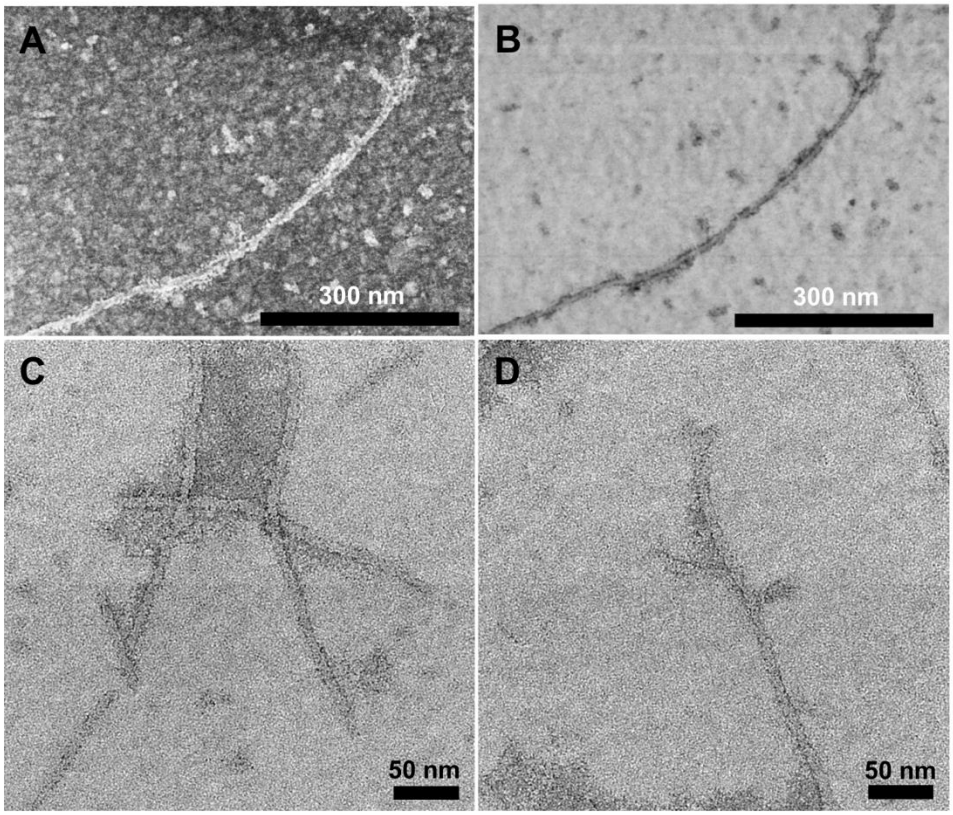

Figure 4.17. SE-mode (A) and TE-mode (B) SEM and TEM (C–D) images of well-stained **(G∧C)$_2$-6T** RNTs. Concentration: 0.01 mg/mL in 1,2-DCB. Stain: 0.2% uranyl acetate in acetone.

Figure 4.18 shows the tapping mode AFM images of **(G∧C)$_2$-6T** RNTs on HOPG. Some tiny dots were found stuck to the surface of a single nanotube, which are thought to be the unassembled single rosette rings, or their short stacks. The height of a single RNT was measured to be 5.6 ± 0.8 nm from the AFM images (Figure 4.19), which is ~ 2.6 nm smaller than the cross-sectional diameter from the TEM measurements. This is likely due to the deformation caused by AFM tip during scanning, as the RNTs are soft materials.[29]

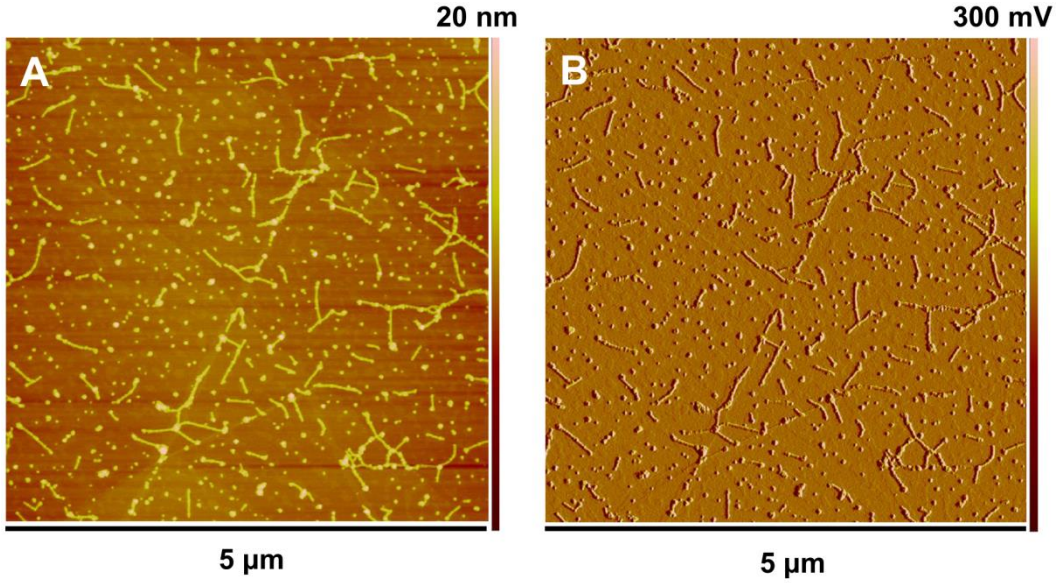

Figure 4.18. Tapping mode AFM images of **(G∧C)$_2$-6T** RNTs on HOPG. (A) Height profile; (B) amplitude profile. Concentration: 0.05 mg/mL in 1,2-DCB.

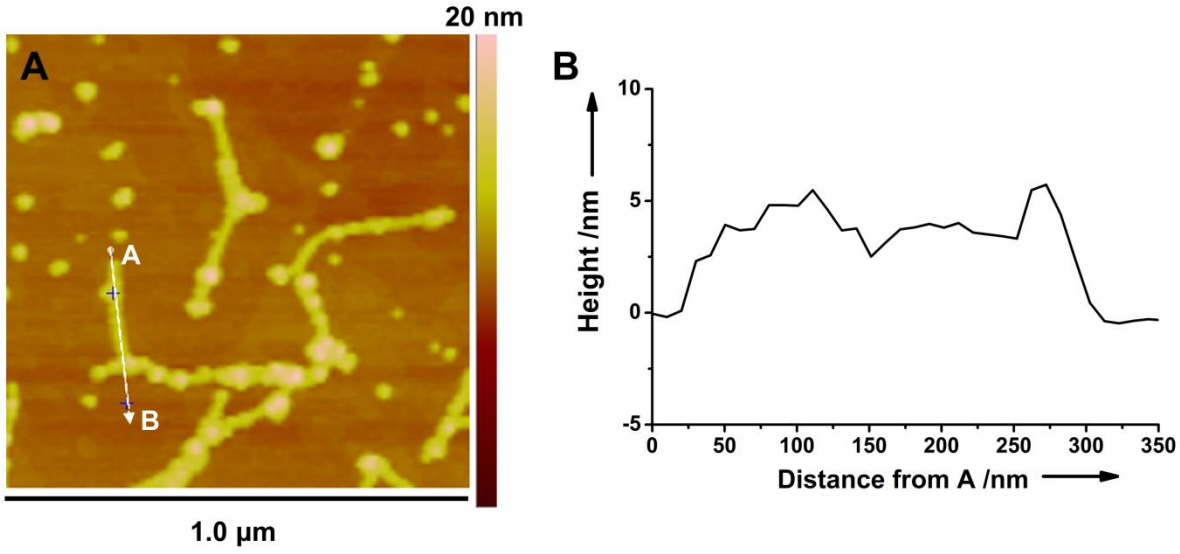

Figure 4.19. Height measurement of a single **(G∧C)$_2$-6T** RNT by tapping mode AFM. (A) AFM image; (B) height profile along the arrow in (A). Concentration: 0.05 mg/mL in 1,2-DCB.

4.10 HOMO–LUMO determination of (G∧C)$_2$-6T RNTs

The HOMO energy level of **(G∧C)$_2$-6T** RNTs was determined by UPS analysis of the thin films from a stock RNTs solution (1.0 mg/mL in 1,2-DCB, checked by SEM before casting) on Si (100) wafers (see Chapter 3 for the fundamentals about UPS, and experimental sections for the sample preparation). Figure 4.20 shows the UPS spectra of a sample film. The work function (Φ) of the RNTs was determined to be 4.16 eV, which was calculated by subtracting the highest binding energy cutoff (17.07 eV) from the incident photon energy ($h\nu$ = 21.23 eV, λ = 58.4 nm) of the monochromatized Helium I light source (Figure 4.20A).[30] The binding energy (E_B) relative to the Fermi level (E_F) of the RNTs is 1.29 eV, which was obtained by extrapolating the edge of the spectrum onset to the intersection of the baseline in the Fermi-edge region (Figure 4.20B). Hence, the HOMO energy level of the RNTs of **(G∧C)$_2$-6T** from this sample film was calculated to be −5.45 eV relative to the vacuum level [−(4.16 eV + 1.29 eV)]. From the measurements of three films on three Si wafers, the HOMO energy level of **(G∧C)$_2$-6T** RNTs was calculated to be −5.40 ± 0.05 eV.

Meanwhile, thin films of unassembled **(G∧C)$_2$-6T** were also prepared as a control. The UPS spectra were also collected in the same manner. Figure 4.21 shows the UPS spectra of a sample film. The HOMO energy level of unassembled **(G∧C)$_2$-6T** was calculated to be −5.18 ± 0.08 eV from the measurements of three films on three Si (100) wafers.

The optical band gaps (E_g^{opt}) of **(G∧C)$_2$-6T** RNTs and unassembled **(G∧C)$_2$-6T** are 2.26 eV and 2.21 eV respectively, which were calculated from the onsets of the corresponding UV-Vis spectra of the thin films on quartz (see Figure 4.14). The LUMO energy level was calculated by adding the optical band gap to the corresponding HOMO energy level. Hence,

for **(G∧C)$_2$-6T** RNTs and unassembled **(G∧C)$_2$-6T** the LUMOs were calculated to be −3.14 eV and −2.97 eV, respectively.

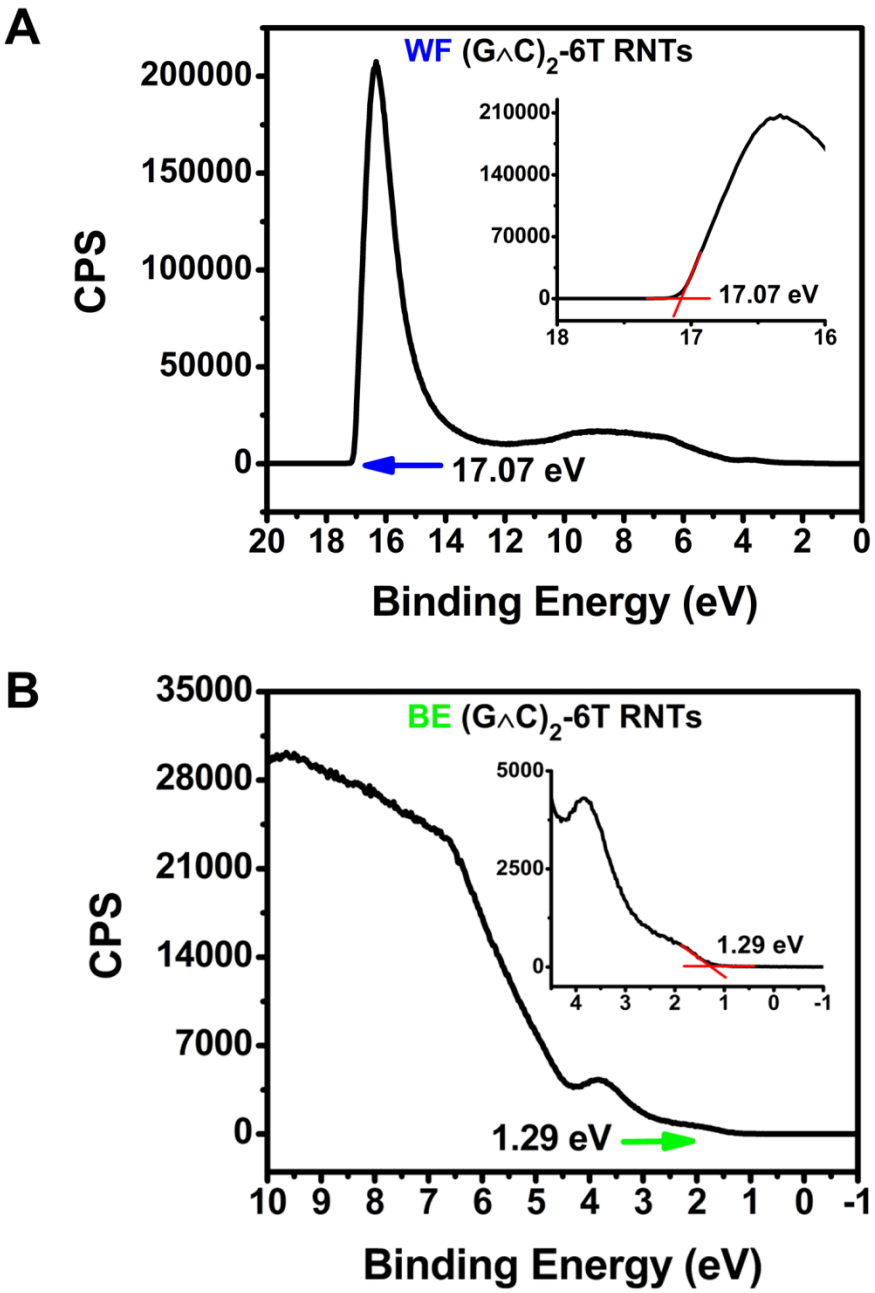

Figure 4.20. UPS spectra of **(G∧C)$_2$-6T** RNTs on Si (100). (A) Work function determination; the inset shows the highest binding energy cutoff; (B) Binding energy (relative to Fermi level) determination; the inset shows the spectrum onset.

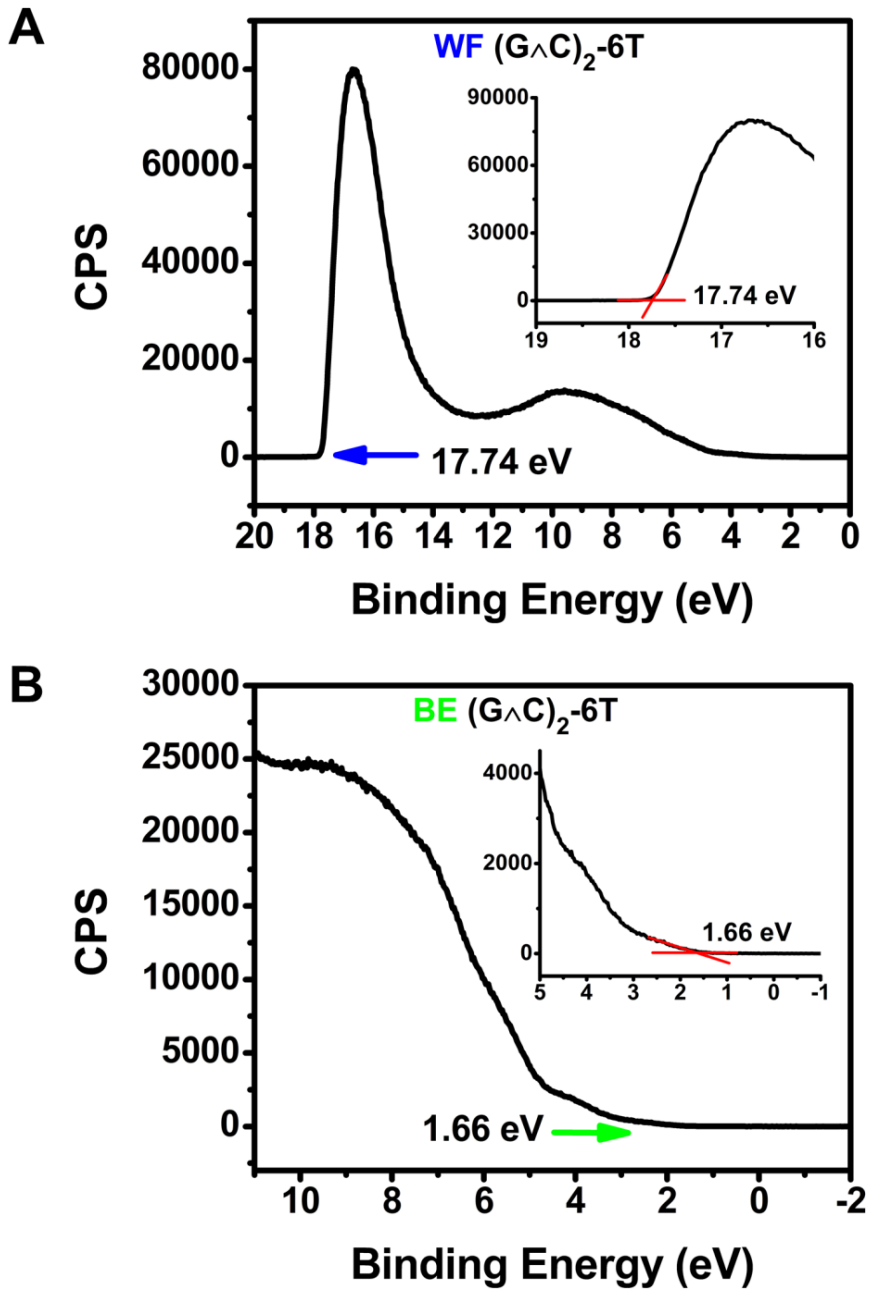

Figure 4.21. UPS spectra of unassembled **$(G\wedge C)_2$-6T** on Si (100). (A) Work function determination; the inset shows the highest binding energy cutoff; (B) Binding energy (relative to Fermi level) determination; the inset shows the spectrum onset.

The HOMO–LUMO energy levels of the well-established electron acceptor $PC_{61}BM$ were also determined in the same manner as described above. The HOMO and LUMO were determined to be −6.15 eV and −4.26 eV, respectively. Since the HOMO–LUMO energy levels of **(G∧C)$_2$-6T** RNTs and **(G∧C)$_2$-6T** match well with those of $PC_{61}BM$, these two materials can be used as promising electron donors in solution-processed OPV devices using $PC_{61}BM$ as the acceptor. Figure 4.22 shows the energy level diagram of the conceived OPV devices in where **(G∧C)$_2$-6T** RNTs:$PC_{61}BM$ and **(G∧C)$_2$-6T**:$PC_{61}BM$ are used as the electron donor-acceptor pairs. In these devices, indium tin oxide (ITO) is the anode and Al is the cathode, PEDOT:PSS is the hole-transporting material. Although the HOMO–LUMO energy gaps of **(G∧C)$_2$-6T** RNTs and **(G∧C)$_2$-6T** are very close, the HOMO of **(G∧C)$_2$-6T** RNTs is 0.22 eV lower than that of **(G∧C)$_2$-6T**. Similarly, the LUMO of **(G∧C)$_2$-6T** RNTs is 0.17 eV lower than that of **(G∧C)$_2$-6T**. The changes in energy levels are attributed to the highly ordered nanostructures in the self-assembled RNTs of **(G∧C)$_2$-6T**.

The energy difference between the donor's HOMO and the acceptor's LUMO determines the open-circuit voltage (V_{OC}) of an OPV device. Many reports have shown that V_{OC} is linearly related to this energy difference.[31] The larger the energy difference between the donor's HOMO and the acceptor's LUMO, the larger the V_{OC} is. A large V_{OC} can improve the power conversion efficiency (PCE) of the OPV device, as PCE is proportional to V_{OC}. The energy difference between the donor's HOMO and acceptor's LUMO is 0.92 eV in the pair of **(G∧C)$_2$-6T**:$PC_{61}BM$, and 1.14 eV in the pair of **(G∧C)$_2$-6T** RNTs:$PC_{61}BM$. Hence, the OPV device using **(G∧C)$_2$-6T** RNTs as the donor material is expected to have a larger V_{OC} and a larger PCE compared to the device using unassembled

(G∧C)$_2$-6T. Unfortunately at this stage we are not able to fabricate the OPV devices and validate our expectations.

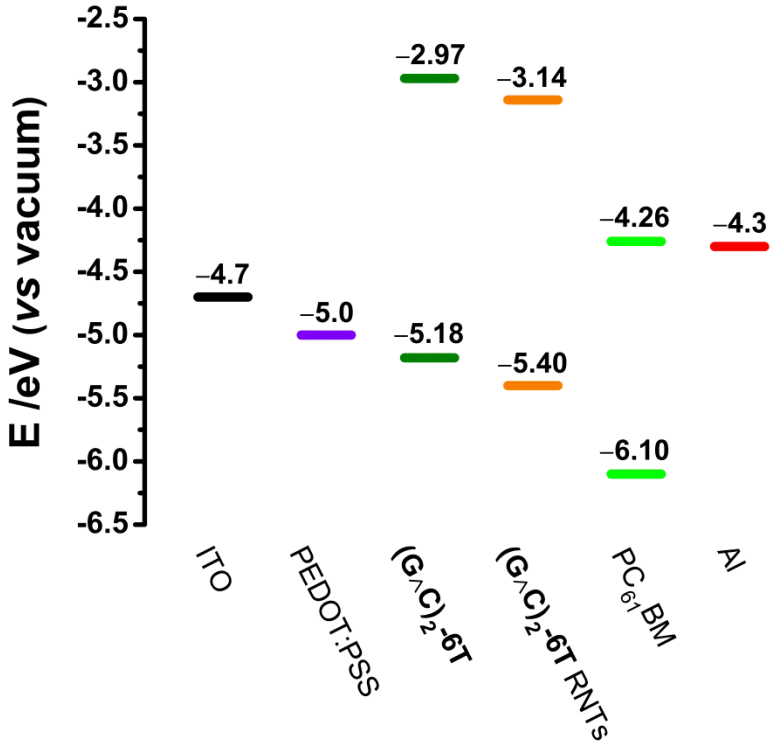

Figure 4.22. Energy level diagram of components used in the conceived OPV devices including ITO and Al electrodes, hole-transporting PEDOT:PSS, and the electron donor-acceptor pairs of **(G∧C)$_2$-6T** RNTs:$PC_{61}BM$ and **(G∧C)$_2$-6T**:$PC_{61}BM$.

4.11 Blend of (G∧C)$_2$-6T RNTs and $PC_{61}BM$

4.11.1 SEM imaging

To create efficient bulk-heterojunction (BHJ) interfaces in the active layer of an OPV device, the electron donor and acceptor materials need to be mixed and solution-processed. For example, to fabricate the active layer of a BHJ OPV device based on

P3HT:$PC_{61}BM$,[23,32] the donor material P3HT is commonly dissolved in chlorobenzene or 1,2-DCB at a high concentration (>10 mg/mL) by heating. The polymer forms crystalline nanofibers during the process of slow-cooling to room temperature. Then the solution is mixed with a concentrated solution of $PC_{61}BM$ in the same solvent at a specific weight ratio. The mixed solution is then spin-cast on the pretreated substrate to form a homogenous thin film, where the pristine nanostructure of P3HT is conserved. The uniform and well dispersed nanostructures are critical to the high PCE of the OPV devices, as it has been reported that they can enhance the hole mobility of the material and the short-circuit current density (J_{SC}) in the OPV device.[23,33]

For using the pair of **(G∧C)$_2$-6T** RNTs:$PC_{61}BM$ as the active layer components in the OPV device, a practical issue is whether the pristine self-assembled tubular structures can be conserved intact when the RNTs solution is mixed with the $PC_{61}BM$ solution. To prove this, 0.5 mL of a stock solution of **(G∧C)$_2$-6T** RNTs (3.0 mg/mL in 1,2-DCB) was mixed with 0.5 mL of a $PC_{61}BM$ solution (3.0 mg/mL in 1,2-DCB). Hence, in the mixed solution whose total concentration was 6 mg/mL, the weight ratio of **(G∧C)$_2$-6T** RNTs:$PC_{61}BM$ was 1:1. The mixed solution was aged for 3 d. SEM samples were then prepared from an aliquot that was immediately diluted (total concentration 1.0 mg/mL) from the mixed solution by adding 1,2-DCB. Meanwhile, a solution of **(G∧C)$_2$-6T** RNTs only (0.5 mg/mL in 1,2-DCB) and a solution of $PC_{61}BM$ only (0.5 mL in 1,2-DCB) were used as controls. For comparison, a solution of commercial grade P3HT (5 mg/mL in 1,2-DCB) was heated at 120 °C for 5 min and allowed to cool to room temperature, which was the same procedure used to process the RNTs of **(G∧C)$_2$-6T**. The P3HT solution was then mixed

with a $PC_{61}BM$ solution (1:1, w/w). For the SEM sample preparation, the mixed solution of P3HT:$PC_{61}BM$ was also diluted to a total concentration 0.5 mg/mL by adding 1,2-DCB.

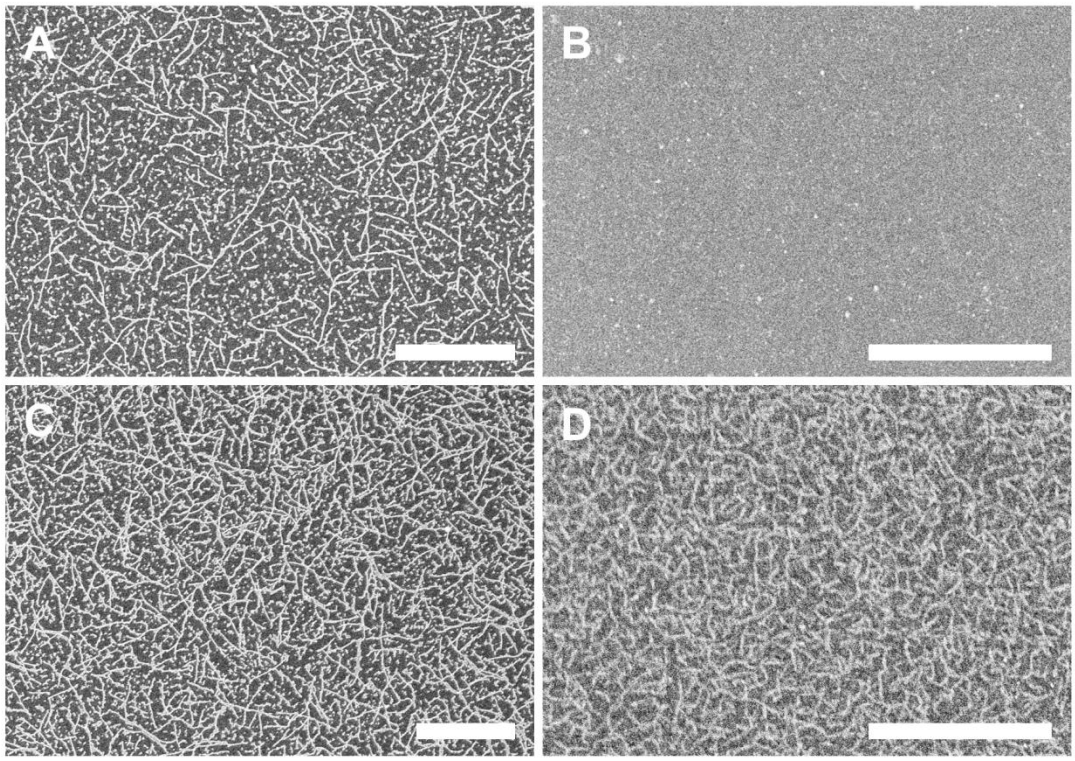

Figure 4.23. SEM images of (A) **$(G\wedge C)_2$-6T** RNTs (0.5 mg/mL in 1,2-DCB); (B) $PC_{61}BM$ (0.5 mg/mL in 1,2-DCB); (C) blend of **$(G\wedge C)_2$-6T** RNTs:$PC_{61}BM$ (1:1, w/w, total concentration 1.0 mg/mL in 1,2-DCB); (D) P3HT:$PC_{61}BM$ (0.5 mg/mL in 1,2-DCB). Scale bars: 500 nm.

The SEM images of the donor-acceptor blends and controls are present in Figure 4.23. As expected, the RNTs and short stacks of rosettes were found in the sample of **$(G\wedge C)_2$-6T** RNTs only (Figure 4.23A). A few shiny dots were found in the sample of $PC_{61}BM$ only (Figure 4.23B), which might be the small aggregates of $PC_{61}BM$ formed during the drying process when the sample grid was placed under high vacuum before imaging. In the SEM

image of the blend of **(G∧C)$_2$-6T** RNTs:$PC_{61}BM$ (1:1, w/w), both the RNTs and tiny dots were present (Figure 4.23C), and they formed an interconnected network. No large bundles or aggregates were observed by SEM imaging, indicating $PC_{61}BM$ molecules were well-dispersed in the network of **(G∧C)$_2$-6T** RNTs. Hence, it was clear that the intact tubular nanostructure of the RNTs was conserved in the mixed solution. On the other hand, the SEM image of the blend of P3HT:$PC_{61}BM$ also showed the uniform nanofibers with the length of about 100 nm (Figure 4.23D).

From the similarity in micromorphology in the SEM images of the blend of **(G∧C)$_2$-6T** RNTs:$PC_{61}BM$ and the blend of P3HT:$PC_{61}BM$, and the well-matched energy levels shown in Figure 4.22, we conclude that **(G∧C)$_2$-6T** RNTs can be a promising electron donor material, and can be mixed with the fullerene-type acceptors including $PC_{61}BM$ for BHJ OPV devices. The uniform tubular nanostructure may improve the PCE of the device compared to the unassembled **(G∧C)$_2$-6T**.

4.11.2 UV-Vis absorption spectra

Figure 4.24 shows the absorption spectra of $PC_{61}BM$ (solution and film) and the blend of **(G∧C)$_2$-6T** RNTs:$PC_{61}BM$ (1:1, w/w) (solution and film). Three characteristic peaks of $PC_{61}BM$ at 330 nm, 433 nm and 696 nm are present in the spectrum of $PC_{61}BM$ in 1,2-DCB (Figure 4.24A). In the spectrum of the thin film of $PC_{61}BM$ on quartz, two more characteristic peaks at 219 nm and 273 nm are found. A broad absorption slope covers the range from 400 nm to 800 nm (Figure 4.24B). In the spectrum of the mixed solution of **(G∧C)$_2$-6T** RNTs:$PC_{61}BM$ (1:1, w/w), two bumps around 330 nm and 400 nm are present, but no obvious peaks can be identified (Figure 4.24C). In the spectrum of the blended thin

film of **(G∧C)$_2$-6T** RNTs:$PC_{61}BM$ (1:1, w/w), the characteristic peaks of $PC_{61}BM$ are present while the absorption of **(G∧C)$_2$-6T** RNTs is underneath the broad absorption tail from 400 nm to around 700 nm (Figure 4.24D).

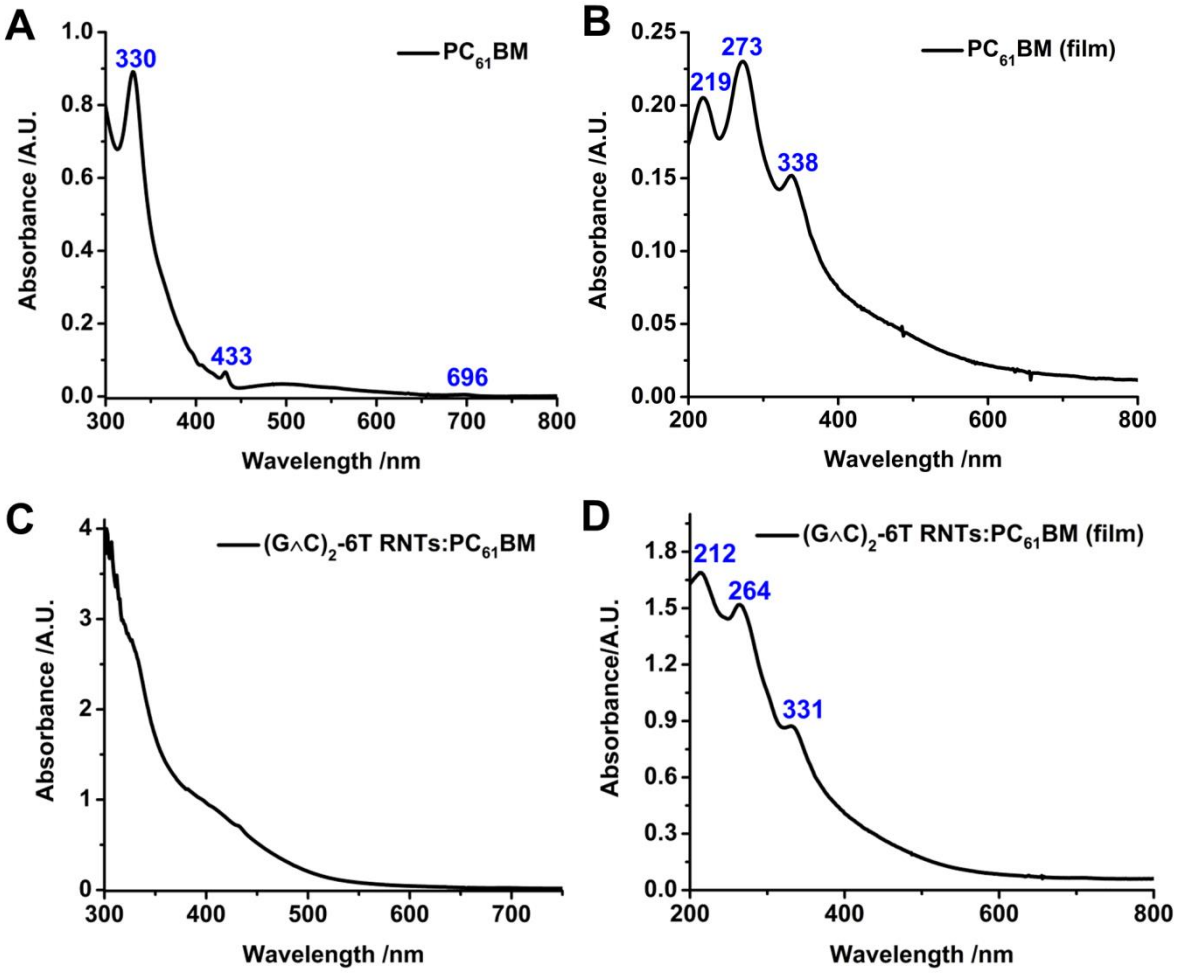

Figure 4.24. Absorption spectra of (A) $PC_{61}BM$ (0.15 mg/mL in 1,2-DCB); (B) $PC_{61}BM$ thin film on quartz; (C) mixed solution of **(G∧C)$_2$-6T** RNTs:$PC_{61}BM$ (total concentration 1 mg/mL in 1,2-DCB, 1:1, w/w); (D) drop-cast thin film of **(G∧C)$_2$-6T** RNTs:$PC_{61}BM$ (1:1, w/w) on quartz.

4.12 Conductivity of $(G\wedge C)_2$-6T RNTs

To measure the conductivity of the thin films of **$(G\wedge C)_2$-6T** RNTs, a two-electrode device was fabricated on fused quartz substrate. The device features 600 teeth and a 2.5 μm gap between the teeth. The details about the device fabrication and sample preparation can be found in the experimental section. Figure 4.25A shows a sample device with a thin film of **$(G\wedge C)_2$-6T** RNTs on the top. Meanwhile, the thin films of unassembled **$(G\wedge C)_2$-6T** and commercial grade P3HT were also cast on separate devices as controls. Figure 4.25 B–D show the current–voltage (*I–V*) curves of the respective films, which were measured on an integrated electronic characterization setup (see details in the experimental section). In all cases, the *I–V* curve fits a linear function. The average thickness of a thin film was obtained from its surface topographic profile which was depicted by a digital profilometer. From the *I–V* curve and film thickness, the conductivity of the thin film of **$(G\wedge C)_2$-6T** RNTs was calculated to be 1.7×10^{-4} S/m (see chapter 3 for the calculation method), which is about 3 times of the value of the P3HT (6.1×10^{-5} S/m). In contrast, the conductivity of the thin film of unassembled **$(G\wedge C)_2$-6T** was several orders of magnitude lower (3.2×10^{-10} S/m). The spectacular improvement of conductivity in the RNTs of **$(G\wedge C)_2$-6T** is attributed to the highly ordered sexithiophene units on the surface of RNTs and the interconnected network of the tubular nanostructures in the solid state. Similar observations in a different electronically conductive oligothiophene self-assembly system was reported by Stupp.[18a] In addition, all of the two-electrode devices were stored at ambient conditions and retested after 10 months, and similar *I–V* curves and conductivity values were observed, indicating that the materials were stable and resistant to oxidation over the period.

Unfortunately, we were unable to measure the charge mobility of **(G∧C)$_2$-6T** RNTs due to the lack of corresponding facilities. Nevertheless, this important parameter should be collected in the future for the material to be used in the application of OPVs.

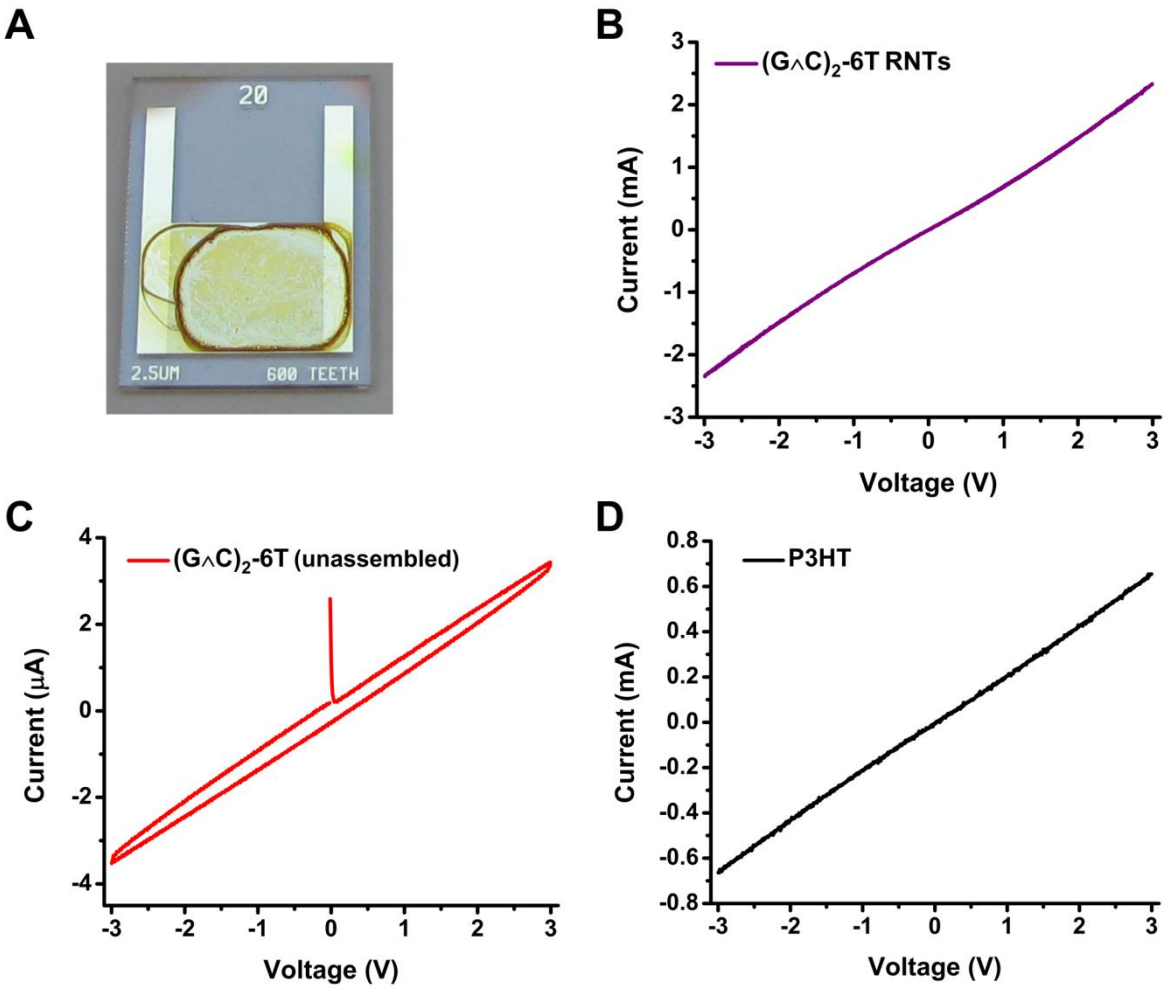

Figure 4.25. Two-electrode device (A) and *I*–*V* curves measured on the thin films of (B) **G∧C)$_2$-6T** RNTs, (C) unassembled **G∧C)$_2$-6T** and (D) P3HT.

4.13 Conclusion

In this chapter, the self-assembly of three oligothiophene functionalized G∧C molecules **(G∧C)$_2$-3T**, mono **G∧C-6T** and **(G∧C)$_2$-6T** were discussed, with the focus on **(G∧C)$_2$-6T** as it is a promising material to generate well dispersed RNTs. The self-assembly condition of **(G∧C)$_2$-6T** was optimized. The solvent, heating and aging effects on the assembly were also studied. The 1,2-DCB solution of **(G∧C)$_2$-6** RNTs can form an organogel over time. The assemblies of **(G∧C)$_2$-6T** were fully characterized by SEM, TEM and AFM. The cross-sectional diameter of a single RNT was measured to be 8.2 ± 0.5 nm by TEM, and 5.6 ± 0.8 nm by AFM. SEM images showed that the intact tubular nanostructures were conserved in the blend of **(G∧C)$_2$-6T** RNTs:$PC_{61}BM$.

The UV-Vis absorption spectrum of the **(G∧C)$_2$-6T** RNTs solution showed a significant blue shift compared to that of the unassembled **(G∧C)$_2$-6T** solution, revealing that the sexithiophene units on the RNTs are H-type aggregates. The photoluminescence spectrum of the **(G∧C)$_2$-6T** RNTs in solution was also presented. UPS spectra were used to determine the HOMO energy levels of the materials. The HOMO of **(G∧C)$_2$-6T** RNTs is 0.22 eV lower than that of unassembled **(G∧C)$_2$-6T**. A comprehensive energy level diagram indicates that both the assembled and unassembled **(G∧C)$_2$-6T** can be used as electron-donor materials in the OPV devices using $PC_{61}BM$ as the electron acceptor, although the tubular nanostructures of RNTs may improve the charge transport and the device performances.

The conductivity of the thin film of **(G∧C)$_2$-6T** RNTs was measured to be 1.7×10^{-4} S/m, which is comparable to that of P3HT (6.1×10^{-5} S/m), and is several orders of magnitude

higher than that of unassembled **(G∧C)$_2$-6T** (3.2×10^{-10} S/m). The improvement in conductivity is likely due to the highly ordered aggregation patterns of the sexithiophene units on the surface of RNTs and the interconnected network in the thin film.

In conclusion, highly ordered oligothiophene aggregates can be constructed via the hierarchical self-assembly of the covalently bonded G∧C building blocks. The optoelectronic properties of **(G∧C)$_2$-6T** RNTs indicates its potential application in OPVs and organic semiconductors.

4.14 Experimental section

4.14.1 Materials and methods

All the spectrophotometric grade solvents for self-assembly study were purchased from Sigma-Aldrich or Acros Organics. P3HT (approximate regioregularity = 96% or above) was purchased from Rieke Metals, Inc., USA. $PC_{61}BM$ (99.5%) was purchased from Solaris Chem, Inc., Canada. All the reagents and solvents were used as received. Quartz cuvettes for UV-Vis and photoluminescence study were purchased from Starna Cells, Inc., USA. Fused quartz wafers (diameter 100 mm, thickness 500 μm) were purchased from University Wafer, USA. The wafers were diced into small rectangular chips (18 mm × 15 mm) using a dicing saw (Diamond Touch) to be used as the substrates for the two-electrode device fabrication. The p-type Si (100) wafers for UPS sample analysis (diameter: 100 mm; thickness: 525 ± 20 μm; dopant: Boron; resistivity: 10-20 Ω•cm) were purchased from Silicon Materials, Inc., USA. The wafers were diced into small rectangular chips (18 mm × 13 mm) using a dicing saw (Disco DAD 321) to be used as the substrates for UPS sample preparation.

4.14.2 Characterization

4.14.2.1 Ultraviolet photoelectron spectroscopy

Room-temperature UPS experiments were performed at the Alberta Center for Surface and Engineering Science (ACSES) using a Kratos Axis spectrometer with monochromatized Helium I radiation ($h\nu$ = 21.23 eV) and a hemispherical electron energy analyzer (Kratos Ultra Spectrometer). The system was maintained under ultrahigh vacuum (< 5×10^{-10} Torr), and the power for UPS was 3 kV × 20 mA (60 W). All of the samples were biased at −10 V during the measurements to observe the peak edge of the secondary electron.

The drop-casting technique was used in the UPS sample preparation. Hence, to a diced p-type Si (100) wafer (13 mm × 18 mm, freshly etched with 5% HF for 2 minutes, rinsed with ddH_2O water and dried with purified N_2 gas), a drop of the sample solution (1.0 mg in 1,2-DCB as a uniform concentration for all the solutions) was cast using a glass pipette. The wafer was dried under a vacuum chamber for 30 min, and then transferred into the ultrahigh vacuum chamber (< 5×10^{-10} Torr) of the UPS instrument and allowed to stay for 30 min to remove residual solvent before analysis. For each material, three samples were prepared on three separate Si wafers, and the average value was reported based on measurements on all three samples.

4.14.2.2 Conductivity of thin films

Commercially available polished quartz wafers (size 18 mm × 15 mm, thickness 500 μm) were used as substrates for the two-electrode device. The substrates were cleaned with piranha solution, and then dried using a stream of filtered N_2. With a chromium mask (600 teeth, 2.5 μm gap width), the substrates were treated by a standard photolithography

method to coat a patterned photoresist layer. A 5 nm thick adhesion layer of Cr was then deposited on the substrates using e-beam evaporation, followed by a 50 nm thick Au layer. To prepare the patterned two-electrode devices, the lift-off method was used.[34] More specifically, the chips were ultrasonically cleaned in acetone, 2-propanol and ultrapure water for 5 min each, and dried using a stream of filtered N_2. Prior to sample deposition, the two-electrode devices were checked by an optical microscope for any fabrication defects, and also tested for blank *I–V* curves to preclude the possibility of bridged electrode teeth that may arise from the photolithography process.

To cast a thin film on the two-electrode device, a drop of a specific sample solution (3.0 mg/mL in 1,2-DCB as a uniform concentration for all the solutions) was deposited on the device using a glass pipette and evenly spread over the whole electrode area. The device was first placed in a low-vacuum chamber overnight to form a thin film, and then transferred to a high-vacuum heater and heated at 80 °C for 30 min and allowed to cool to room temperature in vacuum to remove the residual solvent.

The *I–V* curves of the two-electrode devices were recorded on an integrated electronic characterization setup.[35] The data acquisition (DAQ) board was manufactured by National Instruments (USA) with the model PCI-6110 and the operation software LabVIEW (LV3). The low noise current preamplifier SR570 was manufactured by Stanford Research Systems (USA), and capable of current gains as large as 1 pA/V. The maximum bias voltage was 3.0 V, and the scan rate was set as 1 V/s. The sensitivity varied from 100 pA/V to 1 mA/V, depending on the conductivity of a specific sample.

4.14.2.3 Profilometer

The thickness of the thin film on a two-electrode device was measured by a digital profilometer (KLA Tencor, Alpha Step IQ) featuring automatic leveling and multi-scan mode. The bare edge of the electrode or the quartz substrate was used as the setpoint. During each scan, the probe was allowed to scan across the approximate diameter of the sample spot, and the average thickness was obtained. For each thin film sample, three scans were performed and the thickness value for conductivity calculation was averaged based on all three scans.

4.15 References

(1) (a) Tang, C. W.; Vanslyker, S. A. *Appl. Phys. Lett*. **1987**, *51*, 913–915. (b) Burroughes, J. H.; Bradley, D. D. C.; Brown, A. R.; Marks, R. N.; Mackay, K.; Friend, R. H.; Burns, P. L.; Holmes, A. B. *Nature* **1990**, *347*, 539–541. (c) Buckley, A. *Organic Light-Emitting Diodes (OLEDs): Materials, Devices and Applications* 1st ed.; Woodhead Publishing Limited: Cambridge, UK, 2013.

(2) (a) Tsumura, A.; Koezuka, H.; Ando, T. *Appl. Phys. Lett.* **1986**, *49*, 1210–1212. (b) Sirringhaus, H.; Tessler, N.; Friend, R. H. *Science* **1998**, *280*, 1741–1744. (c) Dimitrakopoulos, C. D.; Malenfant, P. R. L. *Adv. Mater.* **2002**, *14*, 99–117. (d) Wang, C.; Dong, H.; Hu, W.; Liu, Y.; Zhu, D. *Chem. Rev.* **2011**, *112*, 2208–2267. (e) Mei, J.; Diao, Y.; Appleton, A. L.; Fang, L.; Bao, Z. *J. Am. Chem. Soc.* **2013**, *135*, 6724–6746.

(3) (a) Sariciftci, N. S.; Smilowitz, L.; Heeger, A. J.; Wudl, F. *Science* **1992**, *258*, 1474–1476. (b) Hoppe, H.; Sariciftci, N. S. *J. Mater. Res*. **2004**, *19*, 1924–1945. (c) Zhao, G.; He, Y.; Li, Y. *Adv. Mater.* **2010**, *22*, 4355–4358. (d) Price, S. C.; Stuart, A. C.; Yang, L.; Zhou, H.; You, W. *J. Am. Chem. Soc.* **2011**, *133*, 4625–4631. (e) Sun, Y.; Welch, G. C.; Leong, W. L.; Takacs, C. T.; Bazan, G. C.; Heeger, A. J. *Nat. Mater.* **2012**, *11*, 44–48. (f) You, J.; Dou, L.; Yoshimura, K.; Kato, T.; Ohya, K.; Moriarty, T.; Emery, K.; Chen, C.; Gao, J.; Li, G.; Yang, Y. *Nat. Commun.* **2013**, *4*, 1446.

(4) (a) McCullough, R. D. *Adv. Mater.* **1998**, *10*, 93–116. (b) Ong, B. S.; Wu, Y.; Liu, P.; Gardner, S. *J. Am. Chem. Soc.* **2004**, *126*, 3378–3379. (c) Perepichka, I. F.; Perepichka, D. F.; Meng, H.; Wudl, F. *Adv. Mater.* **2005**, *17*, 2281−2305.

(5) (a) Horowitz, G. *Adv. Mater.* **1999**, *10*, 365−377. (b) Tevis, I. D.; Palmer, L. C.; Herman, D. J.; Murray, I. P.; Stone, D. A.; Stupp, S. I. *J. Am. Chem. Soc.* **2011**, *133*, 16486–16494.

(6) (a) Bao, Z.; Dodabalapur, A.; Lovinger, A. J. *Appl. Phys. Lett*. **1996**, *69*, 4108–4110. (b) Coropceanu, V.; Cornil, J.; da Silva Filho, D. A.; Olivier, Y.; Silbey, R.; Brédas, J. L. *Chem. Rev.* **2007**, *107*, 926–952. (c) Halik, M.; Klauk, H.; Zschieschang, U.; Schmid, G.; Ponomarenko, S.; Kirchmeyer, S.; Weber, W. *Adv. Mater.* **2003**, *15*, 917−922. (d) Kobashi, M.; Takeuchi, H. *Macromolecules* **1998,** *31*, 7273−7278. (e) Sirringhaus, H.; Brown, P. J.; Friend, R. H.; Nielsen, M. M.; Bechgaard, K.; Langeveld-Voss, B. M. W.; Spiering, A. J. H.; Janssen, R. A. J.; Meijer, E. W.; Herwig, P.; de Leeuw, D. M. *Nature* **1999**, *401*, 685−688.

(7) Bao, Z. N.; Rogers, J. A.; Katz, H. E. *J. Mater. Chem.* **1999**, *9*, 1895−1904.

(8) Hoeben, F. J. M.; Jonkheijm, P.; Meijer, E. W.; Schenning, A. P. H. J. *Chem. Rev.* **2005**, *105*, 1491–1546.

(9) Samuelsen, E. J.; Mårdalen, J. The Structure of Polythiophenes. In *Handbook of Organic Conductive Molecules and Polymers*; Nalwa, H. S., Ed.; Wiley: Chichester, UK, 1997; Vol. 3, pp 87–120.

(10) (a) Tour, J. M. *Chem. Rev.* **1996**, *96*, 537–554. (b) Fichou, D. *J. Mater. Chem.* **2000**, *10*, 571–588.

(11) (a) Martin, R. E.; Diederich, F. *Angew. Chem., Int. Ed.* **1999**, *38*, 1350–1377. (b) Melucci, M.; Gazzano, M.; Barbarella, G.; Cavallini, M.; Biscarini, F.; Maccagnani, P.; Ostoja, P. *J. Am. Chem. Soc.* **2003**, *125*, 10266–10274.

(12) Elemans, J. A. A. W.; van Hameren, R.; Nolte, R. J. M.; Rowan, A. E. *Adv. Mater.* **2006**, *18*, 1251–1266.

(13) Di Maria, F.; Olivelli, P.; Gazzano, M.; Zanelli, A.; Biasiucci, M.; Gigli, G.; Gentili, D.; D'Angelo, P.; Cavallini, M.; Barbarella, G. *J. Am. Chem. Soc.* **2011**, *133*, 8654–8661.

(14) Mishra, A.; Ma, C.-Q.; Bäuerle, P. *Chem. Rev.* **2009**, *109*, 1141–1276.

(15) Leclere, P.; Surin, M.; Viville, P.; Lazzaroni, R.; Kilbinger, A. F. M.; Henze, O.; Feast, W. J.; Cavallini, M.; Biscarini, F.; Schenning, A. P. H. J.; Meijer, E. W. *Chem. Mater.* **2004**, *16*, 4452–4466.

(16) (a) Tamayo, A. B.; Tantiwiwat, M.; Walker, B.; Nguyen, T.-Q. *J. Phys. Chem. C* **2008**, *112*, 15543–15552. (b) Mei, J. G.; Graham, K. R.; Stalder, R.; Tiwari, S. P.; Cheun, H.; Shim, J.; Yoshio, M.; Nuckolls, C.; Kippelen, B.; Castellano, R. K.; Reynolds, J. R. *Chem. Mater.* **2011**, 23, 2285–2288.

(17) Messmore, B. W.; Hulvat, J. F.; Sone, E. D.; Stupp, S. I. *J. Am. Chem. Soc.* **2006**, *126*, 14452–14458.

(18) (a) Stone, D. A.; Tayi, A. S.; Goldberger, J. E.; Palmer, L. C.; Stupp, S. I. *Chem. Commun.* **2011**, *47*, 5702–5704. (b) Pratihar, P.; Ghosh, S.; Stepanenko, V.; Patwardhan, S.; Grozema, F. C.; Siebbeles, L. D. A.; Wurthner, F. *Beilstein J. Org. Chem.* **2010**, *6*, 1070–1078.

(19) (a) Alesi, S.; Brancolini, G.; Melucci, M.; Capobianco, M. L.; Venturini, A.; Camaioni, N.; Barbarella, G. *Chem.—Eur. J.* **2008**, *14*, 513–521. (b) Spada, G. P.; Lena, S.; Masiero, S.; Pieraccini, S.; Surin, M.; Samorì, P. *Adv. Mater.* **2008**, *20*, 2433–2438.

(20) Schmid, S.; Mena-Osteritz, E.; Kopyshev, A.; Bäuerle, P. *Org. Lett.* **2009**, *11*, 5098–5101.

(21) Kawano, S.-I.; Fujita, N.; Shinkai, S. *Chem.—Eur. J.* **2005**, *11*, 4735–4742.

(22) (a) Schillinger, E.-K.; Mena-Osteritz, E.; Hentschel, J.; Börner, H. G.; Bäuerle, P. *Adv. Mater.* **2009**, *21*, 1562–1567. (b) Kumar, R. J.; MacDonald, J. M.; Singh, T. B.; Waddington, L. J.; Holmes, A. B. *J. Am. Chem. Soc.* **2011**, *133*, 8564–8573.

(23) Xin, H.; Kim, F. S.; Jenekhe, S. A. *J. Am. Chem. Soc.* **2008**, *130*, 5424–5425.

(24) Humphrey, W.; Dalke, A.; Schulten, K. *J. Molec. Graphics* **1996**, *14*, 33–38.

(25) (a) Nakayama, J.; Konishi, T.; Hoshino, M. *Heterocycles* **1988**, *27*, 1731–1754. (b) ten Hoeve, W.; Wynberg, H. *J. Am. Chem. Soc.* **1991**, *113*, 5887–5889.

(26) Byun, E.; Hong, B.; De Castro, K. A.; Lim, M.; Rhee, H. *J. Org. Chem.* **2007**, *72*, 9815–9817.

(27) McCullough, R. D.; Lowe, R. D.; Jayaraman, M.; Anderson, D. L. *J. Org. Chem.* **1993**, *58*, 904–912.

(28) Yassar, A.; Horowitz, G.; Valat, P.; Wintgens, V.; Hmyene, M.; Deloffre, F.; Srivastava, P.; Lang, P.; Garnier, F. *J. Phys. Chem.* **1995**, 99, 9155–9159.

(29) (a) Kasumov, A. Y.; Klinov, D. V.; Roche, P.-E.; Guéron, S.; Bouchiat, H. *Appl. Phys. Lett.* **2004**, *84*, 1007−1009. (b) DeRose, J. A.; Revel, J.-P. *Thin Solid Films* **1998**, *331*, 194−202.

(30) (a) Koo, J.; Cho, J.-J.; Yang, J. H.; Yoo, P. J.; Ph, K. W.; Park, J. *Bull. Korean Chem. Soc.* **2012**, *33*, 636–640. (b) Seo, J. H.; Nguyen, T.-Q. *J. Am. Chem. Soc.* **2008**, *130*, 10042–10043. (c) Tada, A.; Geng, Y.; Wei, Q.; Hashimoto, K.; Tajima, K. *Nat. Mater.* **2011**, *10*, 450–455.

(31) (a) Brabec, C. J.; Cravino, A.; Meissner, D.; Sariciftci, N. S.; Fromherz, T.; Rispens, M. T.; Sanchez, L.; Hummelen, J. C. *Adv. Funct. Mater.* **2001**, *11*, 374–380. (b) Scharber,

M. C.; Mühlbacher, D.; Koppe, M.; Denk, P.; Waldauf, C.; Heeger A. J.; Brabec, C. J. *Adv. Mater.* **2006**, *18*, 789–794. (c) Qi, B.; Wang, J. *J. Mater. Chem.* **2012**, *22*, 24315–24325.

(32) (a) Berson, S.; De Bettignies, R.; Bailly, S.; Guillerez, S. *Adv. Funct. Mater.* **2007**, *17*, 1377–1384.

(33) (a) Yang, X.; Loos, J.; Veenstra, S. C.; Verhees, W. J. H.; Wienk, M. M.; Kroon, J. M.; Michels, M. A. J.; Janssen, R. A. J. *Nano Lett.* **2005**, *5*, 579–583. (b) Lu, G., Tang, H., Qu, Y., Li, L.; Yang, X. *Macromolecules* **2007**, *40*, 6579–6584.

(34) Mahmoud, A. M.; Bergren, A. J.; Pekas, N.; McCreery, R. L. *Adv. Funct. Mater.* **2011**, *21*, 2273–2281.

(35) Shoute, L. C. T.; Wu, Y.; McCreery, R. L. *Electrochim. Acta* **2013**, *110*, 437–445.

Chapter 5

Summary of This Thesis Work and Outlook

5.1 Summary of this thesis work

This thesis work focuses on the development of G∧C RNTs for potential applications in the field of organic optoelectronics. Two classes of functional groups, the porphyrins and oligothiophenes, were covalently linked to the mono and twin G∧C motifs to form the self-assembly building blocks. The self-assembly ability and some important optoelectronic properties of these materials were investigated.

A comprehensive review on the supramolecular assemblies for organic optoelectronics is presented in Chapter 1. The fundamentals of OPVs and various electron donor and acceptor materials were described. Although conducting polymers such as P3HT have been extensively studied as the leading electron donors, conducting oligomers and small molecules have also demonstrated potential. In general, the high PCEs of solution-processed OPVs are mainly ascribed to the highly ordered nanostructures and bulk-heterojunction morphology in the active layer, as the later favors the charge separation and the former improves the charge transport. As shown in many examples, supramolecular self-assembly represents a convenient pathway to introduce nanoscale ordering at all dimensions to the electron donor and acceptor materials in the active layer. More specifically, the electron carrier mobility and conductivity have been found to be significantly improved in the highly ordered supramolecular assemblies of organic semiconducting materials, indicating that these materials may be able to compete with well-

known conducting polymers. Although yet rare, a few examples of using supramolecular assemblies as the functional materials in OLEDs and OFETs have also been demonstrated.

In Chapter 2, the synthesis and self-assembly study of three porphyrin-functionalized G∧C building blocks are presented. In $MeNO_2$, **G∧C-Por 1** formed long RNTs with a moderate solubility. **$(G\wedge C)_2$-Por 2** and **$(G\wedge C)_2$-Por 3** were designed to solve the solubility constraint and improve the solubility in nonpolar solvents. Indeed, both of them could be dissolved in the mixture of 1,2-DCB and MeOH at a high concentration of >10 mg/mL. More importantly, **$(G\wedge C)_2$-Por 3** could be dissolved in pure 1,2-DCB and form well-dispersed RNTs. All of these porphyrin-functionalized RNTs displayed red shifts in the porphyrin absorption bands, indicating the porphyrin groups are J-type aggregates. The diameters of individual RNTs from the TEM measurements were in the range of 4.9–5.4 nm, which are in good agreement with the values from the molecular modeling simulations, and are slightly larger than the height values from tapping mode AFM.

Some important optoelectronic properties of these porphyrin-functionalized RNTs are presented in Chapter 3. The HOMO and LUMO energy levels were measured by UPS and UV-Vis spectra. Compared to the energy-level values of unassembled counterparts, the RNTs of **G∧C-Por 1**, **$(G\wedge C)_2$-Por 2** and **$(G\wedge C)_2$-Por 3** did not show significant changes in the HOMO energy levels, while the LUMO energy levels were slightly lower, mainly due to their smaller optical band gaps. The energy-level alignments of these RNTs and PC61BM indicate they are potential electron donor-acceptor pairs in OPVs. The blended thin films of these RNTs and $PC_{61}BM$ showed significant quenching in the porphyrin fluorescence emissions, indicating the efficient photoinduced electron transfer from the RNTs to $PC_{61}BM$. The nanoscale morphologies of the blends of porphyrin-functionalized

RNTs:$PC_{61}BM$ were also studied. The tubular nanostructures were conserved and interconnected networks were found in the blends, indicating these electron donor-acceptor pairs are suitable for solution-processed OPVs. The conductivity of the thin films of these RNTs is much larger than those of the unassembled counterparts. The conductivity of the thin film of **G∧C-Por 1** RNTs was measured to be 8.1×10^{-5} S/m, which is several orders of magnitude larger the unassembled control (3.3×10^{-10} S/m).

In Chapter 4, three oligothiophene-functionalized G∧C building blocks were presented. **$(G\wedge C)_2$-3T** displayed poor solubility in most organic solvents and did not form well-dispersed nanostructures, which limits its application in solution-processed OPVs. Although **G∧C-6T** is very soluble in DCM and 1,2-DCB, it did not form long RNTs in these solvents, probably due to the steric repulsion between the alkyl substituents. In contrast, **$(G\wedge C)_2$-6T** is very soluble in 1,2-DCB and formed well-dispersed RNTs. Upon the formation of RNTs, the absorption band of the sexithiophene unit showed a significant blue shift, indicating the sexithiophene units on the RNTs are H-type aggregates. Both the HOMO and LUMO energy levels of **$(G\wedge C)_2$-6T** RNTs were found to be ~0.2 eV lower than those of the unassembled counterpart, although their optical band gaps are almost identical. **$(G\wedge C)_2$-6T** RNTs and $PC_{61}BM$ could be mixed in solution at a high concentration and the tubular nanostructures were intact in the blends, indicating **$(G\wedge C)_2$-6T** RNTs can be used as the electron donor materials in solution-processed OPV. The conductivity of the thin film of **$(G\wedge C)_2$-6T** RNTs (1.7×10^{-4} S/m) is comparable to those of conducting polymers such as P3HT.

In conclusion, G∧C modules with π-conjugated functional groups were successfully synthesized. More importantly, self-assembled RNTs can be obtained from these building

blocks in low-polarity solvents. This thesis work demonstrates that RNTs can be powerful supramolecular scaffolds for the application in organic optoelectronics.

5.2 Future work

It would be interesting to explore the self-assembly ability of G∧C modules bearing more challenging and complex photo- and electroactive groups, such as fullerene derivatives and rubrene. In fact, 1D supramolecular assemblies of fullerene derivatives using the bottom-up strategy is always a tough but appealing task for chemists as it requires delicate designs of the building blocks to balance the solubility, steric demand and feasibility in synthesis. Inspired by the one-component strategy of D-A dyad, a C_{60}-porphyrin dyad functionalized G∧C module (**C_{60}-TPP-G∧C**) was designed and the starting materials 5,15-bis(4-aminophenyl)-10,20- biphenylporphyrin [**$(NH_2)_2$TPP**] and phenyl-C_{61}-butyric acid (PCBA) were both prepared (Figure 5.1). A synthesis trial of the dyad was attempted using the EDC coupling between the mono(N-Boc)protected **$(NH_2)_2$TPP** and PCBA but no product was observed, probably due to the poor solubility of PCBA in chlorobenzene. In the future trials, PCBA should be converted to the more soluble and active carbonyl chloride.[1] In principle, the charge separation and transport should be further promoted in the RNTs of **C_{60}-TPP-G∧C**.

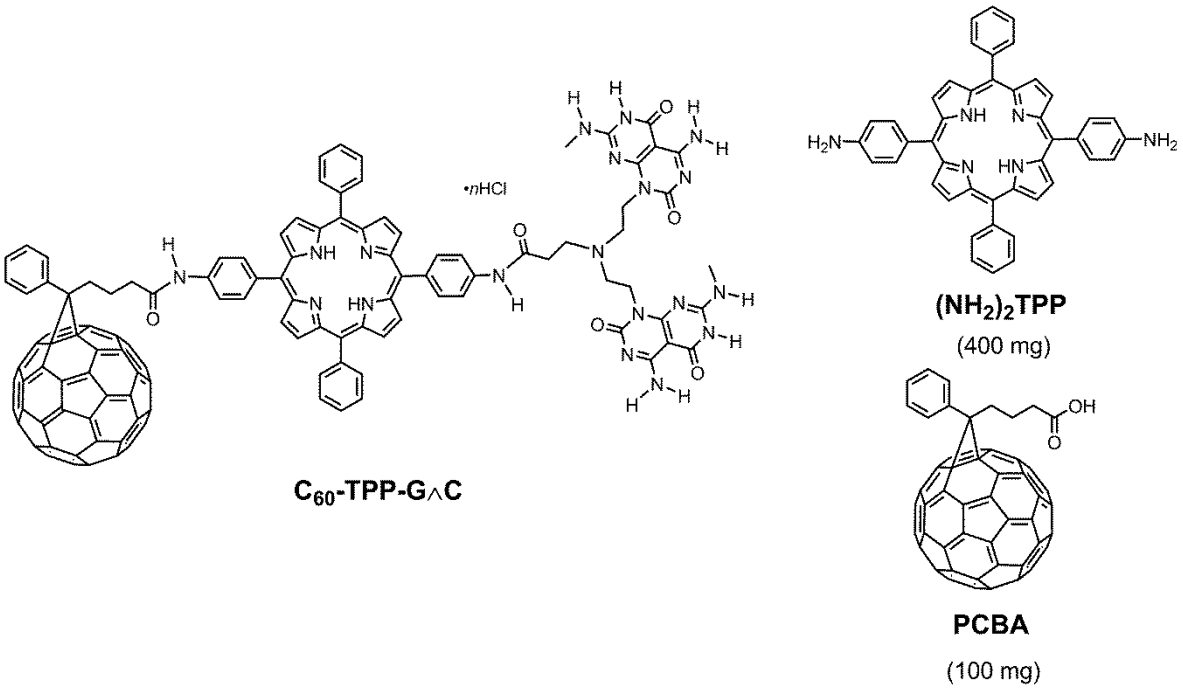

Figure 5.1. Molecular structures of **C_{60}-TPP-G∧C**, **$(NH_2)_2$TPP** and PCBA.

More importantly, the OPV devices based on the functionalized RNTs described in this thesis work and fullerene derivatives should be fabricated in the near future. Due to the limited time period in my PhD program and the lack of access to the facilities, the OPV device fabrication and characterization have not yet been realized. Nevertheless, all the essential materials including ITO-coated glass substrates (8–12 Ω/sq, Delta Technologies), highly conductive PEDOT:PSS suspensions (0.02–0.2 S/m, Clevios P VP AI 4083 Heraeus) and pure Al (99.999%, Kurt J. Lesker) have been purchased and the ITO-coated glass substrates have been diced into proper sizes for the device fabrication. The fabrication work for my successors should be straightforward if the facilities are available. However, a more significant challenge is the device optimization. Although the highly ordered nanostructures and bulk-heterojunction morphology have been successfully achieved in the blends of the

RNTs and $PC_{61}BM$, other important parameters such as the thickness of the layers, interface contacts and weight ratio of the electron donor and acceptor all affect the overall performance of the OPV device. Besides $PC_{61}BM$, other acceptor materials such as C_{60}, bis-$PC_{62}BM$ and $PC_{71}BM$ should also be examined as their HOMO–LUMO energy levels and solubility are different from those of $PC_{61}BM$. The reproducibility and stability of the OPV device should also be tested as they are also important from an industrial point of view.

5.3 Outlook

The world's energy requirement is increasing rapidly while the fossil fuel reserves are decreasing. To solve this problem, advanced technologies in clean energy, especially solar energy, are highly needed. Although the current crystalline Si-based photovoltaic technology is mature and contributing to the clean energy supply, the fabrication and installation cost is still high. With regard to the development of OPVs, there is a long way to go as the current device performance is still uncompetitive even though a PCE over 10% has been reported in a few studies.[2] On the other hand, supramolecular assemblies have been demonstrated as an attractive way to impose nanoscale ordering to the materials in active layers. Ideally, the configuration of the nanostructures of donor and acceptor materials should be vertically aligned between the electrodes. However, the macroscopic alignment of supramolecular assemblies remains a big challenge for chemists.[3] In the fields of organic semiconductors, OLED and OFET, the development of supramolecular assemblies is still at the very early stage. Nevertheless, challenges are the incubator of new

solutions. As an emerging field, supramolecular self-assembly is in progress to find its position in organic optoelectronics.

5.4 References

(1) Hummelen, J. C.; Knight, B. W.; LePeq, F.; Wudl, F.; Yao, J.; Wilkins, C. L. *J. Org. Chem.* **1995**, *60*, 532–538.

(2) (a) Liu, Y.; Chen, C. C.; Hong, Z.; Gao, J.; Yang, Y. M.; Zhou, H.; Dou, L.; Li, G.; Yang, Y. *Sci. Rep.* **2013**, *3*, 1616. (b) Yella, A.; Lee, H.-W.; Tsao, H. N.; Yi, C.; Chandiran, A. K.; Nazeeruddin, M. K.; Diau, E. W.-G.; Y, C.-Y.; Zakeeruddin, S. M.; Grätzel, M. *Science* **2011**, *334*, 629–634. (c) Heo, J. H.; Im, S. H.; Noh, J. H.; Mandal, T. N.; Lim, C. S.; Chang, J. A.; Lee, Y. H.; Kim, H. J.; Sarkar, A.; Nazeeruddin, M. K. *Nat. Photonics* **2013**, *7*, 487–492.

(3) Nakanishi, T. *Supramolecular Soft Matter: Applications in Materials and Organic Electronics* 1st ed.; Wiley: Hoboken, USA, 2011.

Bibliography

1. "The Nobel Prize in Chemistry 2000". *Nobelprize.org.* Nobel Media AB 2014. http://www.nobelprize.org/nobel_prizes/chemistry/laureates/2000/ (Accessed Oct 10, 2014).
2. Abbel, R.; Grenier, C.; Pouderoijen, M. J.; Stouwdam, J. W.; Leclère, P. E. L. G.; Sijbesma, R. P.; Meijer, E. W.; Schenning, A. P. H. J. *J. Am. Chem. Soc.* **2009**, *131*, 833–843.
3. Abdel-Magid, A. F.; Carson K. G.; Harris, B. D.; Maryanoff, C. A.; Shah, R. D. *J. Org. Chem.* **1996,** *61,* 3849–3862.
4. Abraham, R. J.; Hawkes, G. E.; Hudson, M. F.; Smith, K. M. *J. Chem. Soc., Perkin Trans. 2* **1975**, *3*, 204–211.
5. Abraham, R. J.; Hawkes, G. E.; Smith, K. M. *Tetrahedron Lett.* **1974**, *16*, 1483–1486.
6. Acebal, P.; Blaya, S.; Carretero, L. *Chem. Phys. Lett.* **2003**, *374*, 206−214.
7. Aguas, H.; Ram, S. K.; Araujo, A.; Gaspar, D.; Vicente, A.; Filonovich, S. A.; Fortunato, E.; Martins, R.; Ferreira, I.; *Energy Environ. Sci.* **2011**, *4*, 4620–4632.
8. Ahlswede, E.; Hanisch, J.; Powalla, M. *Appl. Phys. Lett.* **2007**, *90*, 163504.
9. Alesi, S.; Brancolini, G.; Melucci, M.; Capobianco, M. L.; Venturini, A.; Camaioni, N.; Barbarella, G. *Chem.—Eur. J.* **2008**, *14*, 513–521.
10. Almarsson, O.; Blasko, A.; Bruice, T. C. *Tetrahedron* **1993**, *49*, 10239–10252.
11. Anslyn, E. V.; Dougherty, D. A. *Modern Physical Organic Chemistry* 1st ed.; University Science Books: Sausalito, 2006.

12. Arias, A. C.; MacKenzie, J. D.; McCulloch, I.; Rivnay, J.; Salleo, A. *Chem. Rev.* **2010**, *110*, 3–24.

13. Aronoff, S. *J. Phys. Chem.* **1958**, *62*, 428–431.

14. Auwärter, W.; Seufert, K.; Bischoff, F.; Ecija, D.; Vijayaraghavan, S.; Joshi, S.; Klappenberger, F.; Samudrala, N.; Barth, J. V. *Nat. Nanotechnol.* **2012**, *7*, 41–46.

15. Babel, A.; Jenekhe, S. A. *Synth. Met.* **2005**, *148*, 169–173.

16. Bao, Z. N.; Rogers, J. A.; Katz, H. E. *J. Mater. Chem.* **1999**, *9*, 1895−1904.

17. Bao, Z.; Dodabalapur, A.; Lovinger, A. J. *Appl. Phys. Lett*. **1996**, *69*, 4108–4110.

18. Baran, D.; Balan, A.; Celebi, S.; Esteban, B. M.; Neugebauer, H.; Sariciftci, N. S.; Toppare, L. *Chem. Mater.* **2010**, *22*, 2978–2987.

19. Bard, A. J.; Faulkner, L. R. *Electrochemical Methods: Fundamentals and Applications* 2nd ed.; Wiley: New York, 2001.

20. Bard, A. J.; Stratmann, M.; Schäfer, H. J. *Encyclopedia of Electrochemistry, Volume 8: Organic Electrochemistry*; Wiley-VCH: Weinheim, 2004.

21. Bayly, C. I.; Cieplak, P.; Cornell, W.; Kollman, P. A. *J. Phys. Chem.* **1993**, *97*, 10269–10280.

22. Beaujuge, P. M.; Frechet, J. M. *J. Am. Chem. Soc.* **2011**, *133*, 20009–20029.

23. Beingessner, R. L.; Deng, B.-L.; Fanwick, P. E.; Fenniri, H. *J. Org. Chem.* **2008**, *73*, 931–939.

24. Berson, S.; De Bettignies, R.; Bailly, S.; Guillerez, S. *Adv. Funct. Mater.* **2007**, *17*, 1377–1384.

25. Blouin, N.; Michaud, A.; Leclerc, M. *Adv. Mater.* **2007**, *19*, 2295–2300.

26. Borzsonyi, G.; Alsbaiee, A.; Beingessner, R. L.; Fenniri, H. *J. Org. Chem.* **2010**, *75*, 7233–7239.

27. Borzsonyi, G.; Johnson, R. S.; Myles, A. J.; Cho, J. Y.; Yamazaki, T.; Beingessner, R. L.; Kovalenko, A.; Fenniri, H. *Chem. Commun*. **2010**, *46*, 6527–6529.

28. Boylestad, R. L.; Nashelsky, L. *Electronic Devices and Circuit Theory* 10th ed.; Upper Saddle River, USA, 2009.

29. Brabec, C. J.; Cravino, A.; Meissner, D.; Sariciftci, N. S.; Fromherz, T.; Rispens, M. T.; Sanchez, L.; Hummelen, J. C. *Adv. Funct. Mater.* **2001**, *11*, 374–380.

30. Brabec, C. J.; Dyakonov, V.; Parisi, J.; Sariciftci, N. S. *Organic Photovoltaics: Concepts and Realization* 1st ed.; Springer-Verlag: Berlin, 2003.

31. Brabec, C. J.; Sariciftci, N. S.; Hummelen, J. C. *Adv. Funct. Mater.* **2001**, *11*, 15−26.

32. Brabec, C. J.; Scherf, U.; Dyakonov, V. *Organic Photovoltaics: Materials, Device Physics, and Manufacturing Technologies* 2nd ed.; Wiley-VCH: Weinheim, 2014.

33. Brabec, C. J.; Shaheen, S. E.; Winder, C.; Sariciftci, N. S.; Denk, P. *Appl. Phys. Lett.* **2002**, *80*, 1288–1290.

34. Brabec, C. J.; Winder, C.; Sariciftci, N. S. Hummelen, J. C.; Dhanabalan, A.; van Hal, P. A.; Janssen, R. A. J. *Adv. Funct. Mater.* **2002**, *12*, 709−712.

35. Brédas, J. L.; Silbey, R.; Boudreaux, D. S.; Chance, R. R. *J. Am. Chem. Soc.* **1983**, *105*, 6555–1323.

36. Brédas, J.-L.; Norton, J. E.; Cornil, J.; Coropceanu, V. *Acc. Chem. Res.* **2009**, *42*, 1691–1699.

37. Brocks, G.; Tol, A. *J. Phys. Chem.* **1996**, *100*, 1838−1846.

38. Brunetti, F. G.; Gong, X.; Tong, M.; Heeger, A. J.; Fred, W. *Angew. Chem., Int. Ed.* **2010**, *49*, 532–536.

39. Brunsveld, L.; Folmer, B. J. B.; Meijer, E. W.; Sijbesma, R. P. *Chem. Rev.* **2001**, *101*, 4071–4097.

40. Brütting, W.; Adachi, C.; Holmes, R. J. *Physics of Organic Semiconductors* Wiley-VCH: Weinheim, 2012.

41. Bu, L.; Guo, X.; Yu, B.; Qu, Y.; Xie, Z.; Yan, D.; Geng, Y.; Wang, F. *J. Am. Chem. Soc.* **2009**, *131*, 13242–13243.

42. Buckley, A. *Organic Light-Emitting Diodes (OLEDs): Materials, Devices and Applications* 1st ed.; Woodhead Publishing Limited: Cambridge, UK, 2013.

43. Burroughes, J. H.; Bradley, D. D. C.; Brown, A. R.; Marks, R. N.; Mackay, K.; Friend, R. H.; Burns, P. L.; Holmes, A. B. *Nature* **1990**, *347*, 539–541.

44. Busseron, E.; Ruff, Y.; Moulin, E.; Giuseppone, N. *Nanoscale* **2013**, 5, 7098–7140.

45. Byun, E.; Hong, B.; De Castro, K. A.; Lim, M.; Rhee, H. *J. Org. Chem.* **2007**, *72*, 9815–9817.

46. Calderon, R. M. K.; Valero, J.; Grimm, B.; de Mendoza, J.; Guldi, D. M. *J. Am. Chem. Soc.* **2014**, *136*, 11436−11443.

47. Camaioni, N.; Ridolfi, G.; Fattori, V.; Favaretto, L.; Barbarella, G. *Appl. Phys. Lett.* **2004**, *84*, 1901–1903.

48. Cao, Y.; Yu, G.; Zhang, C.; Menon, R.; Heeger, A. J. *Synth. Met.* **1997**, *87*, 171–174.

49. Cardona, C. M.; Li, W.; Kaifer, A. E.; Stockdale, D.; Bazan, G. C. *Adv. Mater.* **2011**, *23*, 2367–2371.

50. Case, D. A.; Darden, T. A.; Cheatham, T. E., III; Simmerling, C. L.; Wang, J.; Duke, R. E.; Luo, R.; Walker, R. C.; Zhang, W.; Merz, K. M.; Roberts, B.; Hayik, S.; Roitberg, A.; Seabra, G.; Swails, J.; Goetz, A. W.; Kolossváry, I.; Wong, K. F.; Paesani, F.; Vanicek, J.; Wolf, R. M.; Liu, J.; Wu, X.; Brozell, S. R.; Steinbrecher, T.; Gohlke, H.; Cai, Q.; Ye, X.; Wang, J.; Hsieh, M. J.; Cui, G.; Roe, D. R.; Mathews, D. H.; Seetin, M. G.; Salomon-Ferrer, R.; Sagui, C.; Babin, V.; Luchko, T.; Gusarov, S.; Kovalenko, A.; Kollman, P. A. AMBER 12. University of California, San Francisco, 2012.

51. Charvet, R.; Yamamoto, Y.; Sasaki, T.; Kim, J.; Kato, K.; Takata, M.; Saeki, A.; Seki, S.; Aida, T. *J. Am. Chem. Soc.* **2012**, *134*, 2524–2527.

52. Chen, C. J. *Introduction to Scanning Tunneling Microscopy* 2nd ed.; Oxford University Press: Oxford, 2007.

53. Chen, D.; Nakahara, A.; Wei, D.; Nordlund, D.; Russell, T. P. *Nano Lett.* **2011**, *11*, 561–567.

54. Chen, G.-Q.; Xu, Z.-J.; Zhou, C.-Y.; Che, C.-M. *Chem. Commun.* **2011**, *47*, 10963–10965.

55. Chen, H.-Y.; Hou, J.; Zhang, S.; Liang, Y.; Yang, G.; Yang, Y.; Yu, L.; Wu, Y.; Li, G. *Nat. Photonics* **2009**, *3*, 649–653.

56. Chen, Li.-M.; Hong, Z.; Li, G.; Yang, Y. *Adv. Mater.* **2009**, *21*, 1434–1449.

57. Chen, X.; Zhang, G.; Luo, H.; Li, Y.; Liu, Z.; Zhang, D. *J. Mater. Chem. C* **2014**, *2*, 2869–2876.

58. Chen, Y. P.; Song, S.; Yan, Z. M.; Fenniri, H.; Webster, T. J. *Int. J. Nanomedicine* 2011, *6*, 1035–1044.

59. Chen, Y.; Song, S.; Yan, Z.; Fenniri, H.; Webster, T. J. *Int. J. Nanomed.* **2011**, *6*, 101–107.

60. Chen, Y.; Song, S.; Yan, Z.; Fenniri, H.; Webster, T. J. *Int. J. Nanomed.* **2011**, *6*, 101–107.

61. Chhabra, R.; Moralez, J. G.; Raez, J.; Yamazaki, T.; Cho, J.-Y.; Myles, A. J.; Kovalenko, A.; Fenniri, H. *J. Am. Chem. Soc.* **2010**, *132*, 32–33.

62. Choi, J. K.; Jin, M. L.; An, C. J.; Kim, D. W.; Jung, H.-T. *ACS Appl. Mater. Interfaces* **2014**, *6*, 11047–11053.

63. Chun, A. L.; Moralez, J. G.; Fenniri, H.; Webster, T. J. *Nanotechnology* **2004**, *15*, S234–S239.

64. Chun, A. L.; Moralez, J. G.; Webster, T. J.; Fenniri, H. *Biomaterials* **2005**, *26*, 7304–7309.

65. Clarke, T. M.; Durrant, J. R. *Chem. Rev.* **2010**, *110*, 6736–6767.

66. Cogdell, R. J.; Gall, A.; Köhler, J. *Q. Rev. Biophysics* **2006**, *39*, 227–324.

67. Cogdell, R. J.; Gall, A.; Köhler, J. *Q. Rev. Biophysics* **2006**, *39*, 227-324.

68. Collman, J. P.; McDevitt, J. T.; Yee, G. T.; Leitner, C. R.; McCullough, L. G.; Little, W. A.; Torrance, J. B. *Proc. Natl. Acad. Sci. U.S.A.* **1986**, *83*, 4581–4585.

69. Compton, R. G.; Banks, C. E. *Understanding Voltammetry* 2nd ed.; Imperial College Press: London, 2011.

70. Conant, J. B.; Chow, B. F.; Dietz, E. M. *J. Am. Chem. Soc.* **1934**, *56*, 2185–2189.

71. Coropceanu, V.; Cornil, J.; da Silva Filho, D. A.; Olivier, Y.; Silbey, R.; Brédas, J. L. *Chem. Rev.* **2007**, *107*, 926–952.

72. Croce, R.; van Amerongen, H. *Nat. Chem. Biol.* **2014**, *10*, 492–501.

73. Croce, R.; van Amerongen, H. *Nat. Chem. Biol.* **2014**, *10*, 492–501.

74. D'Andrade, B. W.; Datta, S.; Forrest, S. R.; Djurovich, P.; Polikarpov, E.; Thompson, M. E. *Org. Electron.* **2005**, *6*, 11–20.

75. Dang, M. T.; Hirsch, L.; Wantz, G.; Wuest, J. D. *Chem. Rev.* **2013**, 113, 3734–3765.

76. Darden, T.; York, D.; Pedersen, L. *J. Chem. Phys.* **1993**, *98*, 10089–10092.

77. De Greef, T. F. A.; Smulders, M. M. J.; Wolffs, M.; Schenning, A. P. H. J.; Sijbesma, R. P.; Meijer, E. W. *Chem. Rev.* **2009**, *109*, 5687–5754.

78. De Luca, G.; Romeo, A.; Scolaro, L. M.; Ricciardi, G.; Rosa, A. Inorg. Chem. 2007, 46, 5979–5988.

79. Dennler, G.; Scharber, M. C.; Brabec, C. J. *Adv. Mater.* **2009**, *21*, 1323–1338.

80. Department of Astronomy, University of Washington. Astronomy 150: Light. http://www.astro.washington.edu/users/smith/Astro150/Tutorials/EM/ (accessed Oct 10, 2014.)

81. DeRose, J. A.; Revel, J.-P. *Thin Solid Films* **1998**, *331*, 194−202.

82. DeRose, J. A.; Revel, J.-P. *Thin Solid Films* **1998**, *331*, 194−202.

83. Di Maria, F.; Olivelli, P.; Gazzano, M.; Zanelli, A.; Biasiucci, M.; Gigli, G.; Gentili, D.; D'Angelo, P.; Cavallini, M.; Barbarella, G. *J. Am. Chem. Soc.* **2011**, *133*, 8654–8661.

84. Dimitrakopoulos, C. D.; Malenfant, P. R. L. *Adv. Mater.* **2002**, *14*, 99–117.

85. Djurovich, P. I.; Mayo, E. I.; Forrest, S. R.; Thompson, M. E. *Org. Electron.* **2009**, *10*, 515–520.

86. Drain, C. M.; Varotto, A.; Radivojevic, I. *Chem. Rev.* **2009**, *109,* 1630–1658.

87. Eaton, P. and West, P. *Atomic Force Microscopy* 1st ed.; Oxford University Press: Oxford, 2010.

88. Eisfeld, A.; Briggs, J. S. *Chem. Phys.* **2006**, *324*, 376–384.

89. Elemans, J. A. A. W.; van Hameren, R.; Nolte, R. J. M.; Rowan, A. E. *Adv. Mater.* **2006**, *18*, 1251–1266.

90. Ellis, A. M.; Feher, M.; Wright, T. G. *Electronic and Photoelectron Spectroscopy: Fundamentals and Case Studies* 1st ed.; Cambridge University Press: London, 2005.

91. Evans, D. H.; O'Connell, K. M.; Petersen, R. A.; Kelly, M. J. *J. Chem. Educ.* **1983**, *60*, 290–293.

92. Farah, A. A.; Bravo-Vasquez, J. P.; Alvarez-Puebla R. A.; Cho, J.-Y.; Fenniri, H. *Small* **2009**, *5*, 1283–1286.

93. Fassioli, F.; Olaya-Castro, A.; Scheuring, S.; Sturgis, J. N.; Johnson, N. F. *Biophys. J.* **2009**, *97*, 2464–2473.

94. Fathalla, M.; Neuberger, A.; Li, S. C.; Schmehl, R.; Diebold, U.; Jayawickramarajah, J. *J. Am. Chem. Soc.* **2010**, *132*, 9966–9967.

95. Fendt, L.; Bouamaied, I.; Thoni, S.; Amiot, N.; Stulz, E. *J. Am. Chem. Soc.* **2007**, *129*, 15319–15329.

96. Fenniri, H.; Deng, B. L.; Ribbe, A. E. *J. Am. Chem. Soc.* **2002**, *124*, 11064–11072.

97. Fenniri, H.; Deng, B.-L.; Ribbe, A. E.; Hallenga, K.; Jacob, J.; Thiyagarajan, O. *Proc. Natl. Acad. Sci. U.S.A.* **2002**, *99*, 6487–6492.

98. Fenniri, H.; Mathivanan, P.; Vidale, K. L.; Sherman, D. M.; Hallenga, K.; Wood, K. V.; Stowell, J. G. *J. Am. Chem. Soc.* **2001**, *12*, 3854–3855.

99. Fuhrhop, J.-H. *Langmuir* **2014**, *30*, 1–12.

100. Gao, Y. Interface Electronic Structure and Organic Photovoltaic Devices. In *Optical Science and Engineering*; Sun, S.-S. and Sariciftci, N. S. Eds.; CRC Press: Boca Raton, FL, 2005; Vol. 99, pp 421–448.

101. Gaussian 09, Revision D.01, Frisch, M. J.; Trucks, G. W.; Schlegel, H. B.; Scuseria, G. E.; Robb, M. A.; Cheeseman, J. R.; Scalmani, G.; Barone, V.; Mennucci, B.; Petersson, G. A.; Nakatsuji, H.; Caricato, M.; Li, X.; Hratchian, H. P.; Izmaylov, A. F.; Bloino, J.; Zheng, G.; Sonnenberg, J. L.; Hada, M.; Ehara, M.; Toyota, K.; Fukuda, R.; Hasegawa, J.; Ishida, M.; Nakajima, T.; Honda, Y.; Kitao, O.; Nakai, H.; Vreven, T.; Montgomery, J. A., Jr.; Peralta, J. E.; Ogliaro, F.; Bearpark, M.; Heyd, J. J.; Brothers, E.; Kudin, K. N.; Staroverov, V. N.; Kobayashi, R.; Normand, J.; Raghavachari, K.; Rendell, A.; Burant, J. C.; Iyengar, S. S.; Tomasi, J.; Cossi, M.; Rega, N.; Millam, N. J.; Klene, M.; Knox, J. E.; Cross, J. B.; Bakken, V.; Adamo, C.; Jaramillo, J.; Gomperts, R.; Stratmann, R. E.; Yazyev, O.; Austin, A. J.; Cammi, R.; Pomelli, C.; Ochterski, J. W.; Martin, R. L.; Morokuma, K.; Zakrzewski, V. G.; Voth, G. A.; Salvador, P.; Dannenberg, J. J.; Dapprich, S.; Daniels, A. D.; Farkas, Ö.; Foresman, J. B.; Ortiz, J. V.; Cioslowski, J.; Fox, D. J. Gaussian, Inc., Wallingford CT, 2009.

102. Goetzberger, A.; Hebling, C.; Schock, H.-W. *Mater. Sci. Eng. R-Rep.* **2003**, *40*, 1–46.

103. Gosser, D. K. Cyclic Voltammetry: Simulation and Analysis of Reaction Mechanisms 1st ed.; Wiley-VCH: New York, 1993.

104. Gouterman, M. *J. Chem. Phys.* **1959**, *30*, 1139–161.

105. Gouterman, M. *J. Mol. Spectrosc.* **1961**, *6*, 138–163.

106. Gouterman, M.; Wagniere, G.; Snyder, L. R. *J. Mol. Spectrosc.* **1963**, *11*, 108–127.

107. Gritzner, G.; Kuta, J. *Pure Appl. Chem.* **1984**, *56*, 461–466.

108. Halik, M.; Klauk, H.; Zschieschang, U.; Schmid, G.; Ponomarenko, S.; Kirchmeyer, S.; Weber, W. *Adv. Mater.* **2003**, *15*, 917−922.

109. Hasobe, T.; Fukuzumi, S.; Kamat, P. V. *J. Am. Chem. Soc.* **2005**, *127*, 11884–11885.

110. Hasobe, T.; Saito, K.; Kamat, P. V.; Troiani, V.; Qiu, H.; Solladié, N.; Kim, K. S.; Park, J. K.; Kim, D.; D'Souza, F.; Fukuzumi, S. *J. Mater. Chem.* **2007**, *17*, 4160–4170.

111. Hatano, J.; Obata, N.; Yamaguchi, S.; Yasuda, T.; Matsuo, Y. *J. Mater. Chem.* **2012**, *22*, 19258–19263.

112. Hau, S. K.; Yip, H.-L.; Acton, O.; Baek, N. S.; Ma, H.; Jen, A. K.-Y. *J. Mater. Chem.* **2008**, *18*, 5113–5119.

113. He, Y.; Chen, H.-Y.; Hou, J.; Li, Y. *J. Am. Chem. Soc.* **2010**, *132*, 1377–1382.

114. He, Y.; Li, Y. *Phys. Chem. Chem. Phys.* **2011**, *13*, 1970–1983.

115. Hemraz, U. D.; El-Bakkari, M.; Yamazaki, T.; Cho, J.-Y.; Beingessner, R. L.; Fenniri, H. *Nanoscale* **2014**, *6*, 9421–9427.

116. Heo, J. H.; Im, S. H.; Noh, J. H.; Mandal, T. N.; Lim, C. S.; Chang, J. A.; Lee, Y. H.; Kim, H. J.; Sarkar, A.; Nazeeruddin, M. K. *Nat. Photonics* **2013**, *7*, 487–492.

117. Hiorns, R. C.; De Bettignies, R.; Leroy, J.; Bailly, S.; Firon, M.; Sentein, C.; Khoukh, A.; Preud'homme, H.; Dagron-Lartigau, C. *Adv. Funct. Mater.* **2006**, *16*, 2263–2273.

118. Hoeben, F. J. M.; Jonkheijm, P.; Meijer, E. W.; Schenning, A. P. H. J. *Chem. Rev.* **2005**, *105*, 1491−1546.

119. Honda, T.;Kojima, T.; Fukuzumi, S.; *Chem. Common.***2009**, 4994–4996.

120. Hong, X.; Weng, Y.-X.; Li, M. *Biophys J.* **2004**, *86*, 1082–1088.

121. Hoppe, H.; Sariciftci, N. S. *J. Mater. Res*. **2004**, *19*, 1924–1945.

122. Horowitz, G. *Adv. Mater.* **1999**, *10*, 365−377.

123. Hu, W.; Bai, F.; Xiong, G.; Zhan, X.; Fu, H.; Bjornholm, T. *Organic optoelectronics* 1st ed.; Wiley-VCH: Weinheim, Germany, 2013.

124. Huang, X.; Han, S.; Huang, W.; Liu, X. *Chem. Soc. Rev.* **2013**, *42*, 173–201.

125. Huang, Y.; Li, L.; Peng, X.; Peng, J.; Cao, Y. *J. Mater. Chem.* **2012**, *22*, 21841–21844.

126. Hüfner, S. *Photoelectron Spectroscopy: Principles and Applications* 3rd ed.; Springer: Bridgewater, 2003.

127. Hummelen, J. C.; Knight, B. W.; LePeq, F.; Wudl, F.; Yao, J.; Wilkins, C. L. *J. Org. Chem.* **1995**, *60*, 532–538.

128. Humphrey, W.; Dalke, A.; Schulten, K. *J. Molec. Graphics* **1996**, *14*, 33–38.

129. Imahori, H.; Fukuzumi, S. *Adv. Funct. Mater.* **2004**, *14*, 525–536.

130. Imaoka, T.; Ueda, H.; Yamamoto, K. *J. Am. Chem. Soc.* **2012**, 134, 8412–8415.

131. Iranpoor, N.; Firouzabadi, H.; Nowrouzi, N.; Khalili, D. *Tetrahedron* **2009**, *65*, 3893–3899.

132. Jelley, E. E. *Nature* **1936**, 1009–1010.

133. Johansson, T.; Mammo, W.; Svensson, M.; Andersson, M. R.; Inganäs, O. *J. Mater. Chem.* **2003**, *13*, 1316–1323.

134. Journeay, W. S.; Suri, S. S.; Moralez, J. G.; Fenniri, H.; Singh, B. *Small*, **2009**, *5*, 1446–1452.

135. Jurow, M.; Farley, C.; Pabon, C.; Hageman, B.; Dolor, A.; Drain, C. M. *Chem. Commun.* **2012**, *48*, 4731–4733.

136. Jurow, M.; Schuckman, A. E.; Batteas, J. D.; Drain, C. M. *Coord. Chem. Rev.* **2010**, 254, 2297–2310.

137. Kasumov, A. Y.; Klinov, D. V.; Roche, P.-E.; Guéron, S.; Bouchiat, H. *Appl. Phys. Lett.* **2004**, *84*, 1007−1009.

138. Kawano, S.-I.; Fujita, N.; Shinkai, S. *Chem.—Eur. J.* **2005**, *11*, 4735–4742.

139. Kengthanomma, T.; Thamyongkit, P.; Gasiorowski, J.; Ramil, A. M.; Sariciftci, N. S. *J. Mater. Chem. A* **2013**, *1*, 10524–10531.

140. Kim, I.; Haverinen, H. M.; Wang, Z. X.; Madakuni, S.; Li, J.; Jabbour, G. E. *Appl. Phys. Lett.* **2009**, *95*, 023305.

141. Kim, J. Y.; Lee, K.; Coates, N. E.; Moses, D.; Nguyen, T.-Q.; Dante, M.; Heeger, A. J. *Science* **2007**, *317*, 222−225.

142. Kissinger, P. T.; Heineman, W. R. *J. Chem. Educ.* **1983**, *60*, 702–706.

143. Kittel, C. *Introduction to Solid State Physics* 8th ed.; Wiley: Hoboken, 2005.

144. Kobashi, M.; Takeuchi, H. *Macromolecules* **1998,** *31*, 7273−7278.

145. Koezuka, H. S.; Tsumuta, A.; Ando, T. *Synth. Met.* **1987**, *18*, 699–704.

146. Koo, J.; Cho, J.-J.; Yang, J. H.; Yoo, P. J.; Ph, K. W.; Park, J. *Bull. Korean Chem. Soc.* **2012**, *33*, 636–640.

147. Kruper, W.J.; Chamberlin, T.A.; Kochanny, M. *J. Org. Chem.* **1989**, *54*, 2753–2756.

148. Kumar, R. J.; MacDonald, J. M.; Singh, T. B.; Waddington, L. J.; Holmes, A. B. *J. Am. Chem. Soc.* **2011**, *133*, 8564–8573.

149. Lauer, M. E.; Fuhrhop, J.-H. *Langmuir* **2004**, *20*, 8321–8328.

150. Leclere, P.; Surin, M.; Viville, P.; Lazzaroni, R.; Kilbinger, A. F. M.; Henze, O.; Feast, W. J.; Cavallini, M.; Biscarini, F.; Schenning, A. P. H. J.; Meijer, E. W. *Chem. Mater.* **2004**, *16*, 4452–4466.

151. Lee, S. J.; Hupp, J. T.; Nguyen, S. T. *J. Am. Chem. Soc.* **2008**, *130*, 9632–9633.

152. Li, C.; Liu, M.; Pschirer, N. G.; Baumgarten, M.; Müllen, K. *Chem. Rev.* **2010**, *110*, 6817–6855.

153. Li, C.-Z.; Yip, H.-L.; Jen, A. K. Y. *J. Mater. Chem.* 2012, *22*, 4161–4177.

154. Li, C.-Z.; Yip, H.-L.; Jen, A. K. Y. *J. Mater. Chem.* **2012**, *22*, 4161–4177.

155. Li, F.; Yager, K. G.; Dawson, N. M.; Jiang, Y.-B.; Malloy, K. J.; Qin, Y. *Chem. Mater.* **2014**, *26*, 3747–3756.

156. Li, G.; Zhu, R.; Yang, Y. *Nat. Photonics* **2012**, 6, 153–161.

157. Li, H. P.; Martin, R. B.; Harruff, B. A.; Carino, R. A.; Allard, L. F.; Sun, Y. P. *Adv. Mater.* **2004**, *16*, 896–900.

158. Li, L.-L.; Diau, E. W.-G. *Chem. Soc. Rev.* **2013**, *42*, 291–304.

159. Liang, Y.; Wu, Y.; Feng, D.; Tsai, S. T.; Son, H. J.; Li, G.; Yu, L. *J. Am. Chem. Soc.* **2009**, *131*, 56–57.

160. Liu, Y.; Chen, C. C.; Hong, Z.; Gao, J.; Yang, Y. M.; Zhou, H.; Dou, L.; Li, G.; Yang, Y. *Sci. Rep.* **2013**, *3*, 1616.

161. Lin, Y. Z.; Li, Y. F.; Zhan, X. W. *Chem. Soc. Rev.* **2012**, *41*, 4245–4272.

162. Liu, Y.; Zhou, J.; Wan, X.; Chen, Y. *Tetrahedron* **2009**, 65, 5209–5215.

163. Loi, M. A.; Denk, P.; Hoppe, H.; Neugebauer, H.; Winder, C.; Meissner, D.; Brabec, C.; Sariciftci, N. S.; Gouloumis, A.; Vazquez P.; Torres, T. *J. Mater. Chem.* **2003**, *13*, 700–704.

164. Lovell, J. F.; Jin, C. S.; Huynh, E.; Jin, H.; Kim, C.; Rubinstein, J. L.; Chan, W. C. W.; Cao, W.; Wang, L. V.; Zheng, G. *Nat. Mater.* **2011**, *10*, 324–332.

165. Lu, G., Tang, H., Qu, Y., Li, L.; Yang, X. *Macromolecules* **2007**, *40*, 6579–6584.

166. Lu, G.; Zhang, X.; Cai, X.; Jiang, J. *J. Mater. Chem.* **2009**, *19*, 2417–2424.

167. Lu, H.; Zhang, X. P. *Chem. Soc. Rev.* **2011**, *40*, 1899–1909.

168. Luechai, A.; Gasiorowski, J.; Petsom, A.; Neugebaurer, H.; Sariciftci, N. S.; Thamyongkit, P. *J. Mater. Chem.* **2012**, *22*, 23030–23037.

169. Luguya, R.; Jaquinod, L.; Fronczek, F. R.; Vicente, M. G. H.; Smith, K. M. *Tetrahedron* **2004**, *60*, 2757–2763.

170. Ma, C. Q.; Fonrodona, M.; Schikora, M. C.; Wienk, M. M.; Janssen, R. A. J.; Bauerle, P. *Adv. Funct. Mater.* **2008**, *18*, 3323–3331.

171. Ma, C.; Xing, D.; Zhai, C.; Che, J.; Liu, S.; Wang, J.; Hu, W. *Org. Lett.* **2013**, *15*, 6140–6143.

172. Ma, Y.-P.; He, S.-G.; Ding, X.-L.; Wang, Z.-C.; Xue, W.; Shi, Q. *Phys. Chem. Chem. Phys*. **2009**, *11*, 2543–2552.

173. MacroModel, version 9.9. Schrödinge , LLC: New York, NY, USA, 2011.

174. Mahmoud, A. M.; Bergren, A. J.; Pekas, N.; McCreery, R. L. *Adv. Funct. Mater.* **2011**, *21*, 2273–2281.

175. Maibach, J.; Mankel, E.; Mayer, T.; Jaegermann, W. *J. Mater. Chem. C* **2013**, *1*, 7635–7642.

176. Maiti, N. C.; Mazumdar, S.; Periasamy, N. *J. Phys. Chem. B* **1998**, 102, 1528 –1538.

177. Marsh, A.; Silvestri, M.; Lehn, J.-M. *Chem. Commun.* **1996**, *13*, 1527–1528.

178. Martin, R. E.; Diederich, F. *Angew. Chem., Int. Ed.* **1999**, *38*, 1350–1377.

179. Martínez-Díaz, M. V.; de la Torre, G.; Torres, T. *Chem. Commun.* **2010**, *46*, 7090–7108.

180. Matsuo, Y.; Sato, Y.; Niinomi, T.; Soga, I.; Tanaka, H.; Nakamura, E. *J. Am. Chem. Soc.* **2009**, *131*, 16048–16050.

181. McCullough, R. D. *Adv. Mater.* **1998**, *10*, 93–116.

182. McCullough, R. D.; Lowe, R. D.; Jayaraman, M.; Anderson, D. L. *J. Org. Chem.* **1993**, *58*, 904–912.

183. Mcdermott, G.; Prince, S. M.; Freer, A. A.; Hawthornthwaite-Lawless, A. M.; Paplz, M. Z.; Cogdell, R. J. *Nature*, **1995**, *374*, 517–521.

184. McGehee, M. D.; Topinka, M. A. *Nat. Mater.* **2006**, 5, 675–676.

185. McHale, J. L. *J. Phys. Chem. Lett.* **2012**, *3*, 587–597.

186. Mei, J. G.; Graham, K. R.; Stalder, R.; Tiwari, S. P.; Cheun, H.; Shim, J.; Yoshio, M.; Nuckolls, C.; Kippelen, B.; Castellano, R. K.; Reynolds, J. R. *Chem. Mater.* **2011**, 23, 2285–2288.

187. Mei, J.; Diao, Y.; Appleton, A. L.; Fang, L.; Bao, Z. *J. Am. Chem. Soc.* **2013**, *135*, 6724–6746.

188. Melucci, M.; Gazzano, M.; Barbarella, G.; Cavallini, M.; Biscarini, F.; Maccagnani, P.; Ostoja, P. *J. Am. Chem. Soc.* **2003**, *125*, 10266–10274.

189. Meng, H.; Wudl, F. *Macromolecules* **2001**, *34*, 1810–1816.

190. Mercier, L. G.; Mishra, A.; Ishigaki, Y.; Henne, F.; Schulz, G.; Bäuerle, P. *Org. Lett.* **2014**, *16*, 2642–2645.

191. Messmore, B. W.; Hulvat, J. F.; Sone, E. D.; Stupp, S. I. *J. Am. Chem. Soc.* **2006**, *126*, 14452–14458.

192. Mete, E.; Uner, D.; Çakmak, M.; Gülseren, O.; Ellialtıoğlu, Ş. *J. Phys. Chem. C* **2007**, *111*, 7539–7547.

193. Mishra, A.; Ma, C.-Q.; Bäuerle, P. *Chem. Rev.* **2009**, *109*, 1141–1276.

194. Moralez, J. G.; Raez, J.; Yamazaki, T.; Motkur, K.; Kovalenko, A.; Fenniri, H. *J. Am. Chem. Soc.* **2005**, *127*, 8307–8309.

195. Nagayama K. *Eur. Biophys. J.* **2008**, *37*, 345–358.

196. Nagayama, K. *J. Electron Microsc.* **2011**, *60*, S43–S62.

197. Naito, K.; Sakurai, M.; Egusa, S. *J. Phys. Chem. A* **1997**, *101*, 2350−2357.

198. Nakanishi, T. *Supramolecular Soft Matter: Applications in Materials and Organic Electronics* 1st ed.; Wiley: Hoboken, USA, 2011.

199. Nakayama, J.; Konishi, T.; Hoshino, M. *Heterocycles* **1988**, *27*, 1731–1754.

200. Nelson, R. C. *J. Opt. Soc. Am.* **1956**, *46*, 13–16.

201. Ng, K. K.; Lovell, J. F.; Vedadi, A.; Hajian, T.; Zheng, G. *ACS NANO*, **2013**, *7*, 3484–3490.

202. Nguyen, L. H.; Hoppe, H.; Erb, T.; Günes, S.; Gobsch, G.; Sariciftci, N. S. *Adv. Funct. Mater.* **2007**, *17*, 1071–1078.

203. Nishino, T.; Ito, T.; Umezawa, Y. *Proc. Natl. Acad. Sci. U.S.A.* **2005**, *102*, 5659–5662.

204. O'Regan, B.; Grätzel, M. *Nature* **1991**, *353*, 737–740.

205. O'Shea, D. F.; Miller, M. A.; Matsueda, H.; Lindsey, J. S. *Inorg. Chem.* **1996**, *35*, 7325–7338.

206. Ogawa, K.; Kobuke, Y. *Angew. Chem., Int. Ed.* **2000**, *39*, 4070–4073.

207. Ohno, O.; Kaizu, Y.; Kobayashi, H.; J. Chem. Phys.**1993**, *99*, 4128–4139.

208. Okada, S.; Segawa, H. *J. Am. Chem. Soc.* **2003**, *125*, 2792–2796.

209. Ong, B. S.; Wu, Y.; Liu, P.; Gardner, S. *J. Am. Chem. Soc.* **2004**, *126*, 3378–3379.

210. Ostroverkhova, O. *Handbook of Organic Materials for Optical and (Opto)Electronic Devices: Properties and Applications* 1st ed.; Woodhead Publishing Limited: Cambridge, UK, 2013.

211. Otsuki, J. *Coord. Chem. Rev.* **2010**, *254*, 2311–2341.

212. Ozawa, H.; Tanaka, H.; Kawao, M.; Unoa, S.; Nakazato, K. *Chem. Commun.* **2009**, *47*, 7411–7413.

213. Park, H. H.; Lee, Y.; Jo, J. W.; Jo, W. H. *Polym. Chem.* **2012**, *3*, 2928–2932.

214. Park, S. H.; Roy, A.; Beaupre, S.; Cho, S.; Coates, N.; Moon, J. S.; Moses, D.; Leclerc, M.; Lee, K.; H., A. J. *Nat. Photonics* **2009**, *3*, 297–302.

215. Perepichka, I. F.; Perepichka, D. F.; Meng, H.; Wudl, F. *Adv. Mater.* **2005**, *17*, 2281−2305.

216. Pratihar, P.; Ghosh, S.; Stepanenko, V.; Patwardhan, S.; Grozema, F. C.; Siebbeles, L. D. A.; Wurthner, F. *Beilstein J. Org. Chem.* **2010**, *6*, 1070–1078.

217. Price, S. C.; Stuart, A. C.; Yang, L.; Zhou, H.; You, W. *J. Am. Chem. Soc.* **2011**, *133*, 4625–4631.

218. Qi, B.; Wang, J. *J. Mater. Chem.* **2012**, *22*, 24315–24325.

219. Ra, C. S.; Yim, S.; Park, G. *Bull. Korean Chem. Soc*. **2008**, *29*, 891–893.

220. Reinert, F.; Hüfner, S. *New J. Phys.* **2005**, *7*, 97.

221. Rich, C. C.; McHale, J. L. *Phys. Chem. Chem. Phys.* **2012**, *14*, 2362–2373.

222. Richards, B. S. *Sol. Energy Mater. Sol. Cells* **2006**, *90*, 2329–2337.

223. Roncali, J. *Adv. Energy Mater.* **2011**, *1*, 147–160.

224. Rosa, A.; Ricciardi, G.; Baerends, E. J.; Romeo, A.; Monsù Scolaro, L. *J. Phys. Chem. A* **2003**, *107*, 11468–11482.

225. Rose, E.; Andrioletti, B.; Zrig, S.; Quelquejeu-Etheve, M. *Chem. Soc. Rev.* **2005**, *34*, 573–583.

226. Rudine, A. B.; DelFatti, B. D.; Wamser, C. C. J. Org. Chem. 2013, 78, 6040–6049.

227. Ruoff, R. S.; Tse, D. S.; Malhotra, R.; Lorents, D. C. *J. Phys. Chem.* **1993**, *97*, 3379–3383.

228. Ryckaert, J. P.; Ciccotti, G.; Berendsen, H. J. C. *J. Comput. Phys.* **1977**, *23*, 327–341.

229. Sakai, J.; Taima, T.; Saito, K. *Org. Electron.* **2008**, *9*, 582–590.

230. Sakata, A.; Kobuke, Y. *Org. Biomol. Chem.* **2007**, *5*, 1679–1691.

231. Samuelsen, E. J.; Mårdalen, J. The Structure of Polythiophenes. In *Handbook of Organic Conductive Molecules and Polymers*; Nalwa, H. S., Ed.; Wiley: Chichester, UK, 1997; Vol. 3, pp 87–120.

232. Sariciftci, N. D.; Braun, D.; Zhang, C.; Srdanov, V. I.; Heeger, A. J.; Stucky, G.; Wudl, F. *Appl. Phys. Lett.* **1993**, *62*, 585–587.

233. Sariciftci, N. S.; Smilowitz, L.; Heeger, A. J.; Wudl, F. *Science* **1992**, *258*, 1474–1476.

234. Sayed, S. Y.; Fereiro, J. A.; Yan, H.; McCreery, R. L.; Bergren, A. J. *Proc. Natl. Acad. Sci. U.S.A.* **2012**, *109*, 11498–11503.

235. Scharber, M. C.; Mühlbacher, D.; Koppe, M.; Denk, P.; Waldauf, C.; Heeger A. J.; Brabec, C. J. *Adv. Mater.* **2006**, *18*, 789–794.

236. Schenning, A. P. H. J.; Meijer, E. W. *Chem. Commun.* **2005**, *26*, 3245–3258.

237. Schillinger, E.-K.; Mena-Osteritz, E.; Hentschel, J.; Börner, H. G.; Bäuerle, P. *Adv. Mater.* **2009**, *21*, 1562–1567.

238. Schmid, S.; Mena-Osteritz, E.; Kopyshev, A.; Bäuerle, P. *Org. Lett.* **2009**, *11*, 5098–5101.

239. Schmidt-Mende, L.; Fechtenkötter, A.; Müllen, K.; Moons, E.; Friend, R. H.; MacKenzie, J. D. *Science* **2001**, *293*, 1119–1122.

240. Scholes, G. D.; Fleming, G. R.; Olaya-Castro, A.; van Grondelle R. *Nature Chem.*, **2011**, *3*, 763–774.

241. Schulz, G. L.; Urdanpilleta, M.; Fitzner, R.; Brier, E.; Mena-Osteritz, E.; Reinold, E.; Bäuerle, P. *Beilstein J. Nanotechnol.* **2013**, *4*, 680–689.

242. Scudiero, L.; Barlow, D. E.; Mazur, U.; Hipps, K. W. *J. Am. Chem. Soc.* **2001**, *123*, 4073–4080.

243. Sengupta, S.; Ebeling, D.; Patwardhan, S.; Zhang, X.; von Berlepsch, H.; Böttcher, C.; Stepanenko, V.; Uemura, S.; Hentschel, C.; Fuchs, H.; Grozema, F. C.; Siebbeles, L. D. A.; Holzwarth, A. R.; Chi, L.; Würthner, F. *Angew. Chem., Int. Ed.* **2012**, *51*, 6378–6382.

244. Seo, J. H.; Nguyen, T.-Q. *J. Am. Chem. Soc.* **2008**, *130*, 10042–10043.

245. Shaw, S. J.; Shanmugathasan, S.; Clarke, O. J.; Boyle, R. W.; Osborne, A. G.; Edwards, C. *J. Porphyrins Phthalocyanines* **2001**, *5*, 575–581.

246. Shen, S.; Jiang, P.; He, C.; Zhang, J.; Shen, P.; Zhang, Y.; Yi, Y.; Zhang, Z.; Li, Z.; Li, Y. *Chem. Mater.* **2013**, *25*, 2274–2281.

247. Shockley, W.; Queisser, H. J. *J. Appl. Phys.* **1961**, *32*, 510–519.

248. Shoute, L. C. T.; Wu, Y.; McCreery, R. L. *Electrochim. Acta* **2013**, *110*, 437–445.

249. Sirringhaus, H.; Brown, P. J.; Friend, R. H.; Nielen, M. M.; Bechgaard, K.; Langeveld-Voss, B. M. W.; Spiering, A. J. H.; Janssen, R. A. J.; Meijer, E. W.; Herwig, P.; de Leeuw, D. M. *Nature*, **1999**, *401*, 685−688.

250. Sirringhaus, H.; Tessler, N.; Friend, R. H. *Science* **1998**, *280*, 1741–1744.

251. Sista, S.; Park, M.-H.; Hong, Z.; Wu, Y.; Hou, J.; Kwan, W. L.; Li, G.; Yang, Y. *Adv. Mater.* **2010**, *22*, 380–383.

252. Smulders, M. M. J.; Nieuwenhuizen, M. M. L.; de Greef, T. F. A.; van der Schoot, P.; Schenning, A. P. H. J.; Meijer, E. W. *Chem.—Eur. J.* **2010**, *16*, 362–367.

253. Sonar, P.; Ng, G.-M.; Lin, T. T.; Dodabalapur, A.; Chen, Z.-K. *J. Mater. Chem.* **2010**, *20*, 3626–3636.

254. Spada, G. P.; Lena, S.; Masiero, S.; Pieraccini, S.; Surin, M.; Samorì, P. *Adv. Mater.* **2008**, *20*, 2433–2438.

255. Spanggaard, H.; Krebs, F. C. *Sol. Energy Mater. Sol. Cells* **2004**, *83*, 125−146.

256. Sternberg, E. D.; Dolphin, D, Brückner, C. *Tetrahedron* **1998**, *54*, 4151–4202.

257. Stone, A.; Fisher, E. B. *J. Am. Chem. Soc.***, 1968**, *90*, 2735–2748.

258. Stone, D. A.; Tayi, A. S.; Goldberger, J. E.; Palmer, L. C.; Stupp, S. I. *Chem. Commun.* **2011**, *47*, 5702–5704.

259. Suga, S.; Sekiyama, A. "*Photoelectron Spectroscopy: Bulk and Surface Electronic Structures*" in *Springer Series Optical Sciences Volume 176*; Springer: Heidelberg, 2014.

260. Sun, D.; Tham, F. S.; Reed, C. A.; Boyd, P. D. W. *Proc. Natl. Acad. Sci. U.S.A.* **2002**, *99*, 5088−5092.

261. Sun, Y. M.; Welch, G. C.; Leong, W. L.; Takacs, C. J.; Bazan, G. C.; Heeger, A. J. *Nat. Mater.* **2012**, *11*, 44–48.

262. Sun, Y.; Takacs, C. J.; Cowan, S. R.; Seo, J. H.; Gong, X.; Roy, A.; Heeger, A. J. *Adv. Mater.* **2011**, *23*, 2226–2230.

263. Sun, Y.; Welch, G. C.; Leong, W. L.; Takacs, C. T.; Bazan, G. C.; Heeger, A. J. *Nat. Mater.* **2012**, *11*, 44–48.

264. Suri, S. S.; Rakotondradany, F.; Myles, A. J.; Fenniri, H.; Singh, B. *Biomaterials* **2009**, *30*, 3084–3090.

265. Tada, A.; Geng, Y.; Wei, Q.; Hashimoto, K.; Tajima, K. *Nat. Mater.* **2011**, *10*, 450–455.

266. Tamayo, A. B.; Tantiwiwat, M.; Walker, B.; Nguyen, T.-Q. *J. Phys. Chem. C* **2008**, *112*, 15543–15552.

267. Tan, Z.; Hou, J.; He, Y.; Zhou, E.; Yang, C.; Li, Y. *Macromolecules* **2007**, *40*, 1868–1873.

268. Tang, C. W. *Appl. Phys. Lett.* 1986, *48*, 183–185.

269. Tang, C. W.; VanSlyke, S. A. *Appl. Phys. Lett.* **1987**, *51*, 913–915.

270. Taniguchi, M.; Cramer, D. L.; Bhise, A. D.; Kee, H. L.; Bocian, D. F.; Holten, D.; Lindsey, J. S. *New J. Chem.* **2008**, *32*, 947–958.

271. ten Hoeve, W.; Wynberg, H. *J. Am. Chem. Soc.* **1991**, *113*, 5887–5889.

272. Tevis, I. D.; Palmer, L. C.; Herman, D. J.; Murray, I. P.; Stone, D. A.; Stupp, S. I. *J. Am. Chem. Soc.* **2011**, *133*, 16486–16494.

273. Thompson, B. C.; Fréchet, J. M. J. *Angew. Chem., Int. Ed.* **2008**, *47*, 58–77.

274. Tikhomirov, G.; Oderinde, M.; Makeiff, D.; Mansouri, A.; Weibing, L.; Heirtzler, F. R.; Kwok, D. Y.; Fenniri, H. *J. Org. Chem.* **2008**, *73*, 4248–4251.

275. Tikhomirov, G.; Yamazaki, H.; Kovalenko, A.; Fenniri, H. *Langmuir* **2008**, *24,* 4447–4450.

276. Tour, J. M. *Chem. Rev.* **1996**, *96*, 537–554. (b) Fichou, D. *J. Mater. Chem.* **2000**, *10*, 571–588.

277. Tsujimura, T. *OLED Display Fundamentals and Applications* 1st ed.; Wiley: Hoboken, USA, 2012.

278. Tsumura, A.; Koezuka, H.; Ando, T. *Appl. Phys. Lett.* **1986**, *49*, 1210–1212.

279. Tu, S. Y.; Kim, S. H.; Joseph, J.; Modarelli, D. A.; Parquette, J. R. *J. Am. Chem. Soc.* **2011**, *133*, 19125–19130.

280. Tu, S.; Kim, S.-H.; Joseph, J.; Modarelli, D. A.; Parquette, J. R. *ChemPhysChem* **2013**, *14*, 1609–1617.

281. Umeyama, T.; Watanabe, Y.; Oodoi, M.; Evgenia, D.; Shishido, T.; Imahori, H. *J. Mater. Chem.* **2012**, *22*, 24394–24402.

282. University of California, Davis ChemWiki: The Dynamic Chemistry E-textbook. http://chemwiki.ucdavis.edu/Physical_Chemistry/Spectroscopy/Photoelectron_Spectroscopy/Photoelectron_Spectroscopy%3A_Application (Accessed Sept. 25, 2014).

283. Van der Heide, P. *X-ray Photoelectron Spectroscopy: An Introduction to Principles and Practices* 1st ed.; Wiley: Hoboken, 2012.

284. van Hameren, R.; Schön, P.; Van Buul, A. M.; Hoogboom, J.; Lazarenko, S. V.; Gerritsen, J. W.; Engelkamp, H.; Christianen, P. C. M.; Heus, H. A.; Maan, J. C.;

Rasing, T.; Speller, S.; Rowan, A. E.; Elemans, J. A. A. W.; Nolte, R. J. M. *Science* **2006**, *314*, 1433–1436.

285. Vanlaeke, P.; Swinnen, A.; Haeldermans, I.; Vanhoyland, G.; Aernouts, T.; Cheyns, D.; Deibel, C.; D'Haen, J.; Heremans, P.; Poortmans, J.; Manca, J. V. *Sol. Energy Mater. Sol. Cells* **2006**, *90*, 2150–2158.

286. Walter, M. G.; Rudine, A. B.; Wamser, C. C. *J. Porphyrins Phthalocyanines* **2010**, *14*, 759–792.

287. Walter, R. I.; Ojadi, E. C. A.; Linschitz, H. *J. Phys. Chem.* **1993**, *97*, 13308–13312.

288. Wang, C.; Dong, H.; Hu, W.; Liu, Y.; Zhu, D. *Chem. Rev.* **2011**, *112*, 2208–2267.

289. Wang, J.; Wolf, R. M.; Caldwell, J. W.; Kollman, P. A.; Case, D. A. *J. Comput. Chem.* **2004**, *25*, 1157–1174.

290. Wang, P.; Yao, K.; Chen, L.; Chen, Y.; Li, F.; Wang, H.; Yu, S. *Sol. Energy Mater. Sol. Cells* **2012**, *97*, 34–42.

291. Wang, Q.; Chen, Y.; Ma, P.; Lu, J.; Zhang, X.; Jiang, J. *J. Mater. Chem.* **2011**, *21*, 8057–8065.

292. Wang, Z.; Medforth, C. J.; Shelnutt, J. A. *J. Am. Chem. Soc.* **2004**, *126*, 15954–15955.

293. Wienk, M. M.; Kroon, J. M.; Verhees, W. J. H.; Knol, J.; Hummelen, J. C.; van Hal, P. A.; Janssen, R. A. J. *Angew. Chem., Int. Ed.* **2003**, *42*, 3371–3375.

294. Wilson, J. D.; Buffa, A. J.; Lou, B. *College Physics* 7th ed.; Addison-Wesley: San Francisco, 2010.

295. Würthner, F. *Nat. Chem.* **2014**, *6*, 171–173.

296. Xin, H.; Kim, F. S.; Jenekhe, S. A. *J. Am. Chem. Soc.* **2008**, *130*, 5424–5425.

297. Xu, Z.; Chen, L.-M.; Chen, M.-H.; Li, G.; Yang, Y. *Appl. Phys. Lett.* **2009**, *95*, 013301.

298. Yaffe, O.; Qi, Y.; Scheres, L.; Puniredd, S. R.; Segev, L.; Ely, T.; Haick, H.; Zuilhof, H.; Vilan, A.; Kronik, L.; Kahn, A.; Cahen, D. *Phys. Rev. B* **2012**, *85*, 045433.

299. Yamamoto, T.; Hatano, J.; Nakagawa, T.; Yamaguchi, S.; Mastsuo, Y. *Appl. Phys. Lett.* **2013**, *102*, 013305.

300. Yamamoto, Y.; Zhang, G. X.; Jin, W. S.; Fukushima, T.; Ishii, N.; Saeki, A.; Seki, S.; Tagawa, S.; Minari, T.; Tsukagoshi, K.; Aida, T. *Proc. Natl. Acad. Sci. U.S.A.* **2009**, *106*, 21051–21056.

301. Yan, L.; Watkins, N. J.; Zorba, S.; Gao, Y. L.; Tang, C. W. *Appl. Phys. Lett.* **2001**, *79*, 4148−4150.

302. Yang, C.-J.; Jenekhe, S. A.; *Macromolecules* **1995**, *28*, 1180–1196.

303. Yang, X. N.; Loos, J.; Veenstra, S. C.; Verhees, W. J. H.; Wienk, M. M.; Kroon, J. M.; Michels, M. A. J.; Janssen, R. A. J. *Nano Lett.* **2005**, *5*, 579–583.

304. Yang, X.; Loos, J.; Veenstra, S. C.; Verhees, W. J. H.; Wienk, M. M.; Kroon, J. M.; Michels, M. A. J.; Janssen, R. A. J. *Nano Lett.* **2005**, *5*, 579–583.

305. Yassar, A.; Horowitz, G.; Valat, P.; Wintgens, V.; Hmyene, M.; Deloffre, F.; Srivastava, P.; Lang, P.; Garnier, F. *J. Phys. Chem.* **1995**, 99, 9155–9159.

306. Yella, A.; Lee, H.-W.; Tsao, H. N.; Yi, C.; Chandiran, A. K.; Nazeeruddin, M. K.; Diau, E. W.-G.; Y, C.-Y.; Zakeeruddin, S. M.; Grätzel, M. *Science* **2011**, *334*, 629–634.

307. Yin, B.; Yang, L.; Liu, Y.; Chen, Y.; Qi, Q.; Zhang, F.; Yin, S. *Appl. Phys. Lett.* **2010**, 97, 023303.

308. Yoo, S.; Domerq, B.; Kippelen, B. *Appl. Phys. Lett.* **2004**, *85*, 5427–5429.

309. Yoon, D.; Lee, S.; Yoo, K.; Kim, J.; Lim, J.; Aratani, N.; Tsuda, A.; Osuka, A.; Kim, D. *J. Am. Chem. Soc.* **2003**, *125*, 11062–11064.

310. You, J.; Dou, L.; Yoshimura, K.; Kato, T.; Ohya, K.; Moriarty, T.; Emery, K.; Chen, C.; Gao, J.; Li, G.; Yang, Y. *Nat. Commun.* **2013**, *4*, 1446.

311. Yu, G.; Gao, J.; Hummelen, J. C.; Wudl, F.; Heeger, A. J. *Science* **1995**, *270*, 1789–1791.

312. Zhang, G.; Musgrave, C. B. *J. Phys. Chem. A* **2007**, *111*, 1554–1561.

313. Zhang, L.; Ramsaywack, S.; Fenniri, H.; Webster, T. J. *Tissue Eng. Pt. A* **2008**, *14*, 1353–1364.

314. Zhang, L. J.; Rodriguez, J.; Raez, J.; Myles, A. J.; Fenniri, H.; Webster, T. J. *Nanotechnology* **2009**, *20*,175101.

315. Zhang, L.; Rakotondradany, F.; Myles, A. J.; Fenniri, H.; Webster, T. J. *Biomaterials* **2009**, *30*, 1309–1320.

316. Zhang, Y.; Basel, T. P.; Gautam, B. R.; Yang, X. M.; Mascaro, D. J.; Liu, F.; Vardeny, Z. V. *Nat. Commun.* **2012**, *3*, 1043.

317. Zhao, G.; He, Y.; Li, Y. *Adv. Mater.* **2010**, *22*, 4355–4358.

318. Zhao, Q.; Wang, Y.; Qiao, Y.; Wang, X.; Guo, X.; Yan Y.; Huang J. *Chem. Commun.* **2014**, *50*, 13537–13539.

319. Zheng, M.; Sarker, A. M.; Gurel, E. E.; Lahti, P. M.; Karaz, F. E. *Macromolecules* **2000**, *33*, 7426–7430.

320. Zhou, T.; Jia, T.; Kang, B.; Li, F.; Fahlman, M.; Wang, Y. *Adv. Energy Mater.* **2011**, *1*, 431–439.

321. Zimmermann, Y.-S.; Schaffer, A.; Hugi, C.; Fent, K.; Corvini, P. F.-X.; Lenz, M. *Environ. Int.* **2012**, *49*, 128–140.